SOME PROPERTIES OF S AND D–WAVE 2 DIMENSIONAL SUPERCONDUCTORS

By

MOHAMED MANSOR, B.SC., M.SC.

A Thesis
Submitted to the School of Graduate Studies
in Partial Fulfillment of the Requirements
for the Degree
Doctor of Philosophy

McMaster University
September 1994

Copyright Mohamed A. Mansor, 1994

SOME PROPERTIES OF S AND D–WAVE 2 DIMENSIONAL SUPERCONDUCTORS

DOCTOR OF PHILOSOPHY (1994) McMASTER UNIVERSITY
(Physics) Hamilton, Ontario

TITLE: Some Properties of S and D–Wave 2 Dimensional Superconductors

AUTHOR: Mohamed Mansor, B.Sc., M.Sc.
(Laurentian University)

SUPERVISOR: Professor Jules Carbotte

NUMBER OF PAGES: vii, 208

Abstract

We utilize Eliashberg theory, up to the Migdal approximation, to study some properties of two dimensional superconductors. The mechanism of superconductivity in this thesis is bosonic, either caused by phonons or by spin fluctuations. The order parameter is an s–wave for the phonon mechanism or a d–wave when considering spin fluctuations.

The two dimensional (2D) superconductor is modeled by a stack of conducting sheets and coupling between the sheets is neglected for simplicity. The electronic density of states (EDOS) of a 2D electron gas on a lattice possesses a singular peak usually called a van Hove singularity (vHs). The presence of a vHs near the Fermi level is shown to enhance the superconducting transition temperature, T_c, for both mechanisms as well as reduce the isotope effect, β, from its standard value of 0.5 (predicted by BCS theory).

The Eliashberg equations (EE) on the imaginary axis are handled in two ways i) the EDOS is used directly when integrating out the energy dependence of the EE to get analytical expressions that can be solved numerically ii) the k–sum is handled numerically from the start and the whole 2D Brillouin zone is used. In the first approach, infinite band models of EDOS are used, in the second only the dispersion of the electron gas has to be specified.

Some of the properties calculated in this thesis are the critical temperature, the isotope effect (for phonons only), the specific heat difference and its jump at T_c, the thermodynamic critical field, the upper critical field and the London penetration depth. Impurity scattering is also considered, in Born approximation and in resonance scattering (for d–wave only).

Experimental comparison with our results show that the isotope effect and the specific heat jump at T_c correlate very well with an s–wave order parameter, while the low temperature dependence of the London penetration depth and some superconducting specific heat results are best described by a d–wave order parameter.

Acknowledgements

I would like first to thank my parents for their patience and support, this thesis is dedicated to them. I also thank my wife, FATMA, for her moral support. My sincere thanks to my supervisor, Prof. Jules P. Carbotte, for his leadership and care – he has been a great teacher and a magnificent person. Much of this work was motivated by him. My special thanks also to Drs. Catherine Kallin and Tom Timusk, and to my committee members, Drs. Rajat Bhaduri and John Preston.

I am also grateful to a few other people with whom I had interesting discussions. Some that come to mind are Drs. Stephan Lenck, Dimitry Basov, Richard Akis, Chao Jiang, Elisabeth Nicol, Pekka Soininen, Mark Kvale and Tom Szeredi, and the very fine company of Yong Zhang, Bill Minor, Jennifer Rendell, Hamish Johnston, Charles Curry, Rachid Ouyed, Chris O'Donovan, Bill Atkinson, Dwayne Branch and Peter Arberg.

I would like to acknowledge the financial support I received from the Secretary of Scientific Research (SSR) of my country, Libya. I also appreciate the hospitality of Canada and McMaster University.

Mrs. Jackie Collin, who type this manuscript, deserves my sincere gratitude.

Lastly, I thank the Lord for my children, Arwa and Amre – they have brought me much joy.

Table of Contents

Chapter 2 **Formalism**

Chapter 3 **The Critical Temperature, the (3) Free Energy and the Gap**

Chapter 4 **The London Penetration Depth**

Chapter 5 **The Specific Heat**

Chapter 6 **The Upper Critical Field, Hc_2**

Chapter 1

Introduction

Superconductivity was first discovered in mercury (Hg) by Kammerlingh–Onnes [Kammerlingh–Onnes 1911]. Below the transition (or critical) temperature, T_c (~4 K in Hg), a superconductor has zero dc resistivity. It also expels magnetic field and becomes a perfect diamagnet [Meissner 1933]. Since 1911, many other metals (eg. Al, Pb, V, Ta, Sn, Tl, In, Mo, Ga, Bi, La and Nb) and alloys (eg. V_3Si, V_3Ge, Nb_3Al, Nb_3Sn, Pb_xBi_{1-x} (x=0.9, 0.8, 0.75, 0.7, 0.54, 0.5) and many others) have been discovered to superconduct. The highest T_c was ~23 K for Nb_3Ge. Early attempts to find higher T_c materials were concentrated on cubic transition alloys, especially those containing niobium Nb, as well as materials that possess lattice instabilities. These are called "Matthias's Rules", which were based on the fact that superconductivity is closely linked to the electron–phonon interaction. Further explanation is given in the next section. It took quite a long time to break out of these rules and look for superconductivity somewhere else.

The break through came in 1986 when Bednorz and Müller discovered a 30°K superconductor in a copper oxide based material (La–Ba–Cu–O) [Bednorz and Müller 1986]. Soon after, a host of the new superconductors the cuprates were discovered (T_c~20–40°K and chemical formulae $La_{2-x}M_xCuO_{4-y}$, M=Ba, Sr, and Ca). These materials are usually denoted as La214, and the individual members assigned LSCO, LBCO and LCCO according to their metallic substitution M=Sr, Ba and Ca respectively. Application of large pressure on the LSCO system raises T_c to just above 50 K. In 1987, a substitution of La by Y (to induce internal pressure [Pickett 1989]) resulted in a 90 K superconductor and later identified as $YBa_2Cu_3O_{7-y}$ (to be denoted Y123 or YBCO). To date, one of the highest T_c cuprates discovered so far, is $Tl_2Ba_2CaCu_2O_{8-y}$ (denoted Tl2212 or TBCCO) with a T_c of ~120 K. All of these high temperature superconductors exhibit strange electrical properties both in the normal and the superconducting states. The parent compounds (x=y=0 and y=1 for Y123) are antiferromagnetic insulators, and after a few percent doping, an insulator–metal transition takes place beyond which a superconducting transition occurs. The superconducting transition curve in the phase diagram is a parabola: T_c increases as the doping increases until it reaches a maximum (optimum doping) and decreases afterwards to zero at doping level of 20% to 40%. Other anomalies include their linear resistivity with temperature at optimal doping above T_c as well as non–constant Hall angle and coefficient in the normal state.

I. The Theory of Conventional Superconductivity

Early attempts to describe superconductivity were phenomenological and coined "super"–conductors in analogy with (charged) superfluids. The two–fluid model [Gorter and Casimir 1934 a,b] separates electrons in a material into superconducting and normal fractions. This proved useful in explaining the Meissner effect [London 1948]. Further development in second order phase transitions led to a macroscopic quantum theory of superconductors in which the order parameter is the superfluid density [Ginsburg and Landau 1950]. This is called Ginzburg–Landau theory and is still very useful in many calculations and is used, even at present day, to explain various superconducting properties, especially near T_c. Hints of the microscopic interaction that caused superconductivity in electrons became apparent only after an experimental connection between T_c and the isotope mass M of the material was established, for example, for mercury $T_c{}^*M^{1/2}\sim$ constant [Fröhlich, Maxwell and Reynolds 1950]. Fröhlich proposed that phonons, play a major role in superconductivity. Soon after Cooper calculated an instability for two electrons on the Fermi surface, with opposite spin and momenta $\mathbf{k}\uparrow, -\mathbf{k}\downarrow$), towards pair formation [Cooper 1956]. Finally, Bardeen, Cooper and Schrieffer came up with a new microscopic theory (BCS theory) based on an attraction between electrons which is mediated by phonons and causes electrons to condense into a highly correlated superconducting state [Bardeen, Cooper and Schrieffer 1957]. In BCS theory, an attractive constant potential, V, between a pair of electrons of opposite spin and momentum causes them to pair up and form a Cooper pair. The average size of a Cooper pair (correlation length), ξ is roughly of the order of thousands of Angstroms, while the average interelectron distance is about 1–2 Angstroms. Obviously, there is a great deal of overlap between the pairs in real space which, in turn, gives the wave function high rigidity, reflected in zero dc resistivity. Furthermore, this constant potential V extends, in momentum space, to momentum states of energies ω_D in an inner and outer rim of the Fermi surface, where ω_D is the characteristic Debye frequency associated with the lattice specific heat. It turns out in BCS theory that the transition temperature T_c is given by

$$T_c = 1.13\ \omega_D \exp\left[-\frac{1}{N(E_f)V}\right] \tag{1.1}$$

and that the excitation spectrum, reflected in the specific heat of the superconducting state at low temperature, is gapped by $2\Delta_0$,

$$\Delta_0 = 2\ \omega_D \exp\left[-\frac{1}{N(E_f)V}\right] \tag{1.2}$$

where $N(E_f)$ is the electronic density of states at the Fermi surface. It is quite apparent that equation (1.1) leads to $T_c/\omega_D \sim$ constant, and hence, $T_c\, M^{1/2} \sim$ constant, since for phonons $\omega \propto M^{-1/2}$.

BCS theory is a universal theory and has been highly successful in a qualitative sense, and sometimes quantitative sense as in aluminum. Lead and mercury, on the other hand, are poorly described by BCS theory. For materials with small ω_D it is necessary to take into account the retarded nature of the electron–phonon interaction. Even in the normal state, the electronic properties are slightly modified by the electron–phonon interaction. The theory of electron–phonon interaction in the normal state was first developed by Migdal [Migdal 1958]. Eliashberg extended Migdal formalism to the superconducting state [Eliashberg 1960]. The Eliashberg theory explained deviations from BCS theory for most materials to within a few percent, excluding the recent high temperature superconductors, making it one of the most attractive and successful theories known at the present time [Carbotte 1990]. Eliashberg theory has two microscopic parameters $\alpha^2F(\omega)$ and μ^*. The spectral function $\alpha^2F(\omega)$ is obtained from an electron–phonon coupling $\alpha(\omega)$ and the phonon frequency distribution $F(\omega)$. The parameter μ^* represents the effective Coulomb repulsion between two electrons in a Cooper pair. Extension of Eliashberg theory to other boson mediated interactions is quite trivial, since phonons are bosons, and the only requirement is to make sure that only retarded three body, interactions (e,e,ph.) are included (Migdal approximation). Higher order interactions should be of smaller magnitude and can be neglected. This is not so obvious for the spin fluctuation mediated superconductivity. Furthermore, Eliashberg theory is generally formulated for metals with large Fermi surfaces and, consequently, a constant density of states at the Fermi level. However, for materials like high T_c superconductors with narrow bands and rapidly varying densities of states near the chemical potential, Eliashberg theory needs to be modified. There is little theoretical literature on the various properties of these materials. This is the prime motivation for the work presented in this thesis. In this thesis, we would like to calculate some thermodynamic properties and compare them with recent experiments on the cuprates and, eventually, try to draw some conclusions from our calculations.

II. Structure of High T_c Materials and their Electrical Properties

Crystal structure characterization of all the cuprates have yielded that they are made of Cu–O_2 layers separated by salt (ionic) layers (i.e. La_2O_3 in the case of La214) and sometimes these ionic layers are threaded by Cu–O chains (Y123). The Cu–O bond length in the Cu–O_2 layers is too short to give it a meaningful ionic character. Initially, most researchers believed that this bond is covalent as a result of hybridization of oxygen p–orbital with a $d_{x^2-y^2}$–orbital of Cu^{2+} ion. Band calculations, however, predict a half filled valence band for the parent compounds (i.e. metals) while in actual fact they are insulators. Others think the hybridization is not complete and results in a Mott insulator. The third view, and most popular, is the Hubbard model. In the Hubbard model there is one electron on each Cu site in the $Cu–O_2$ layer, from $3d^9$ shell of Cu^{2+} ion, and these electrons are strongly localized. The localization is a result of an on–site Coulomb repulsion U to any other electron that happens to hop and fill the hole on the Cu^{2+} ion. It is only when these $Cu–O_2$ sheets are chemically doped with holes (electrons) that electron hoping may cost no extra potential energy, they become conducting sheets. It has been argued that this on–site repulsion U results directly in an insulating gap at half filling (parent compounds) as well as favouring the antiferromagnetic state by lowering its ground state energy by a factor of $\sim t^2/U$, where t is the kinetic hopping energy of an electron between two Cu sites. It was first proposed by Emery [Emery 1987] that the 3d–Cu orbitals are split into two bands separated by the Hubbard gap U (the on–site repulsion) and the valence band for the cuprates is σ–antibonding of the oxygen $2p_{x,y}$ orbitals in the Cu–O layer. Since the vacuum consists of Cu^{2+} ions with their 3d–electrons strongly localized, the valence band is completely filled. The idea here is that the 3d–Cu states do not hybridize with the oxygen orbitals, and hence, for the half filling case, the cuprates are insulators. Band calculations with strongly localized 3d–Cu states, using linear augmented–plane–wave (LAPW) method, indeed showed filled valence bands [Mattheiss and Hamann 1989]. According to these calculations, the doped holes initially depopulate the antibonding σ bands that point along Cu–O bond directions, with π and $2p_z$ sub–bands entering only at larger hole concentration.

The last model that we would like to mention is due to Anderson [Anderson 1987]. Anderson argues that the on–site repulsion limits the phase space available for other electrons with opposite spin, similar to the Pauli exclusion principle of parallel spin electrons, and, in turn, leads to different spin statistics from that of the normal Fermi liquids. The single particle picture is not adequate to describe the excitation spectrum or the dispersion for that matter. The ground state is a highly correlated state and non–perturbative, and the quasi–particles are drastically different from the usual particle–hole excitations. There are two kinds of quasi–particles in this theory, spinons (no charge) and holons (no spin), and the spin and charge of electrons are separated. This last theory is called the Resonating Valence Bond (RVB) theory. The RVB theory is outside the scope of this thesis, although we might make a comment or two about it as events unfold. Experimentally, we still await hard and clear evidence for the existence of these two kinds of quasi–particles. There is not enough experimental evidence to discriminate against any of the aforementioned views.

In this thesis, we will adopt the Fermi liquid picture generally accepted for large doping. This is consistent with Eliashberg theory in which the quasi–particles are Fermions. The only thing left to decide is what kind of dispersion or density of states we should use for the electrons. This is explained in the next section.

The last structural aspect of the hole doped cuprates, which we would like to emphasize, is the existence of apex oxygen coordination for the Cu ions in the layers. Apex oxygen ion coordination for Cu in the hole doped cuprates turns out to be very important and necessary for superconductivity, and maybe even for metalicity. Recently made, the so–called infinite layer cuprates $Ca_{1-x}Li_xCuO_2$

and $Ca_{0.86}Sr_{0.14}CuO_2$ are both semiconductors and nonsuperconductors [Kubo and Yamauchi 1994]. Their resistances at room temperature are two orders of magnitude higher than the superconducting cuprates. Both of these compounds contain only four–coordinated Cu ions (planar). To shed some light on the matter, we will discuss the difference between 4^-, 5^- or 6^{-th} coordination of Cu according to the third model (Hubbard) which utilizes the Jahn–Teller effect [for a short review see O'Brien 1993]. The on–site repulsion of the $3d^9$ shell of Cu^{2+} splits the $3d_{x^2-y^2}$ orbital into two orbitals separated by an energy gap U_1. The upper (lower) orbital is a spin up (down) orbital and reverses its spin for the nearest neighbour Cu ion. This split decreases monotonically with doping. Furthermore, the $3d_{z^2}$ orbital splits into two orbitals separated by another Hubbard gap U_2, this gap is zero for zero doping and increases in magnitude as a function of doping [Kubo and Yamauchi 1994]. In the sixth or fifth coordination of Cu ions in the Cu–O_2 planes, the Jahn–Teller gaps, separating $3d_{x^2-y^2}$ and $3d_{z^2}$ states, are much smaller than the gap in the fourth coordination. It seems that the $3d_{z^2}$ orbital plays a significant role in charge transport in the high temperature superconductors (HTSC). The upper $3d_{z^2}$ may hybridize or strongly overlap with the lower $3d_{x^2-y^2}$ as well as the antibonding σ bands of the oxygen. Band renormalization have been observed recently in $Bi_2Sr_2Ca_{1-x}Y_xO_{8+\delta}$ as a function of doping. X–ray photoelectric spectroscopy on this compound showed that the chemical potential shifts from between the upper and lower Hubbard bands at half filling, to the top of the valence band, and is associated with a considerable spectral weight shift from the higher energy band above the Hubbard gap to that below the Hubbard gap [van Veenendaal and Sawatzky 1994]. In conventional metals, the spectral weights of the electronic bands are independent of filling (single particle picture).

The complexity of the electronic bands of the HTSC is still a hot subject for research involving different kinds of electron spectroscopies. Theoretically, it is still a challenging field and some, like Anderson, think resolving it is essential to sort out the mechanism for the high temperature superconductors.

III. Dispersion and Electron Density of States Models for the Cuprates

As mentioned in the previous section, electron dispersions in the high temperature superconductors are not well known. We still, however, get a good approximation by using tight binding dispersions. A typical dispersion for a square lattice is

$$\epsilon_k = -2\bar{t}[\cos k_x a + \cos k_y a - 2B \cos k_x a \cos \cos k_y a] - \mu \tag{1.3}$$

k_i is the momentum in the ith direction, μ is the chemical potential, $\bar{t}$ is a kinetic energy hopping parameter between nearest neighbours, B is the relative strength of next nearest neighbour hopping, and a is the lattice spacing in the plane. Equation (1.3) is only applicable to high hole (electron) doping, where the Fermi liquid picture is plausible. We have chosen the z–axis to be perpendicular to $Cu{-}O_2$ sheets and assumed equal bond distances in the x and y directions. The latter assumptions hold extremely well for all the cuprates. Photoemission intensity experiments [see the discussions in Schneider 1990 and Wermbter 1992] support the applicability of tight binding approximation. The electronic density of states (EDOS) is shown in Figure (1.1) for the dispersion in equation (1.3), dotted line is appropriate for LSCO (B=0.16) and the long dashed line (B=0.48) is appropriate for Y123.

The common feature of these EDOS's is that they all contain sharp peaks called van Hove singularities which are characteristic of electronic bands in two dimensions. Early formulation of BCS and Eliashberg theories considered only a constant EDOS at the Fermi level and later on Eliashberg theory was modified to include a Lorentzian peaked density of states [Mitrovic 1983] to explain the high transition temperature for A15 compounds (chemical formula A_3B). After the discovery of the HTSC, many researchers modeled a van Hove singularity with a logarithmically divergent electronic density of states and incorporated it into the BCS theory [Dzyaloshinskit 1988; Xing 1991; Newns 1992]. Part of the work presented here includes these model density of states with logarithmic divergencies in the Eliashberg formalism. These model density of states are i) an undamped logarithmic singularity

$$N(\epsilon) = N_b\left[r - s\ln\left|\frac{\epsilon-\delta}{Ef}\right|\right] \tag{1.4}$$

and ii) a damped logarithmic singularity

$$N(\epsilon) = N_b\left[r - \frac{s}{(\epsilon-\delta)^2+D^2}\ln\left|\frac{\epsilon-\delta}{Ef}\right|\right] \tag{1.5}$$

where N_b is a background density of states similar to $N(E_f)$ in equations (1.1) and (1.2), r and s control how much strength the logarithmic part has, E_f is the width of the logarithmic singularity, δ gives the position of the peak away from the Fermi surface, and finally, D is a Lorentzian damping for the logarithmic part. Figure (1.2) and (1.3) show the EDOS for these two models, undamped in the upper frame and damped in the lower frame for both figures. In Figure (1.2), E_f is 500 meV and the upper frame shows a negative density of states for the solid line (see figure caption for parameters) which is unphysical. Increasing E_f to 1500 meV in Figure (1.3), overcomes this difficulty. In the damped case (lower frames) with D~40 meV, both density of states, E_f=500 and 1500 meV, are positive definite and very physical. The parameter D sets the actual width of the peaks as can be clearly seen from both figures.

IV. Scope and Outline of Thesis

In Chapter 2, we present the necessary theoretical background to modify Eliashberg formalism to take into account the EDOS variations and derive some specific formulae needed to compute the properties presented in Chapters 3, 4, 5 and 6. In Chapter 3, we study the transition temperature, the isotope effect, the gap ratio and the termodynamic critical field associated with phonon mediated superconductors. In Chapter 4, we study the London penetration depth utilizing finite bands and concentrating on d–wave superconductivity stabilized by antiferromagnetic spin fluctuations. In Chapter 5, we study the specific heat for both models described in Chapters 3 and 4. In Chapter 6, we study the upper critical field for both types of order parameters, s–wave and d–wave, but utilizing the Fermi surface approximation. Finally, we provide a short summary in Chapter 7.

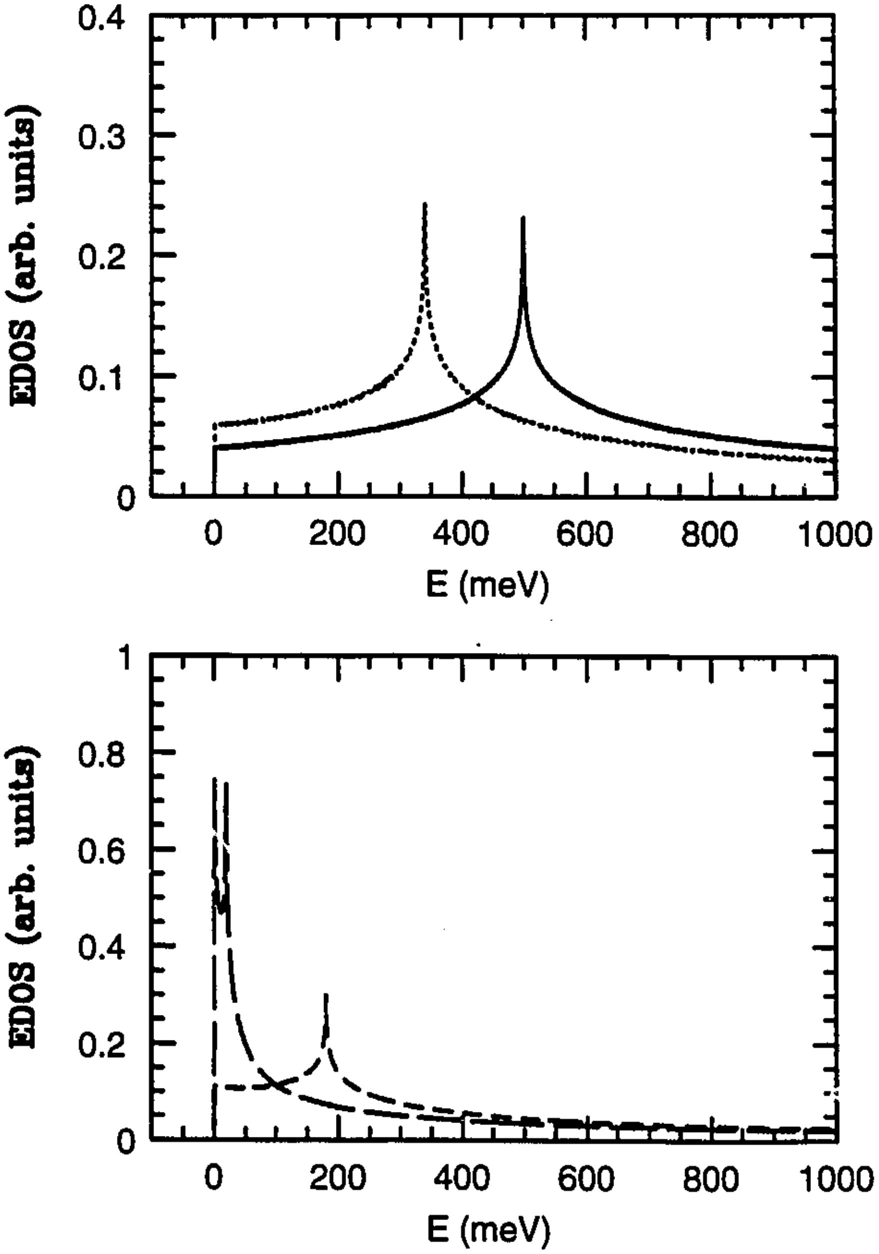

Figure 1.1: Electronic density of states (EDOS) for tight binding dispersion given in equation 1.3, solid (B=0), dotted (B=0.16), short dashed (B=0.32), and long dashed (B=0.48), see text for explanation.

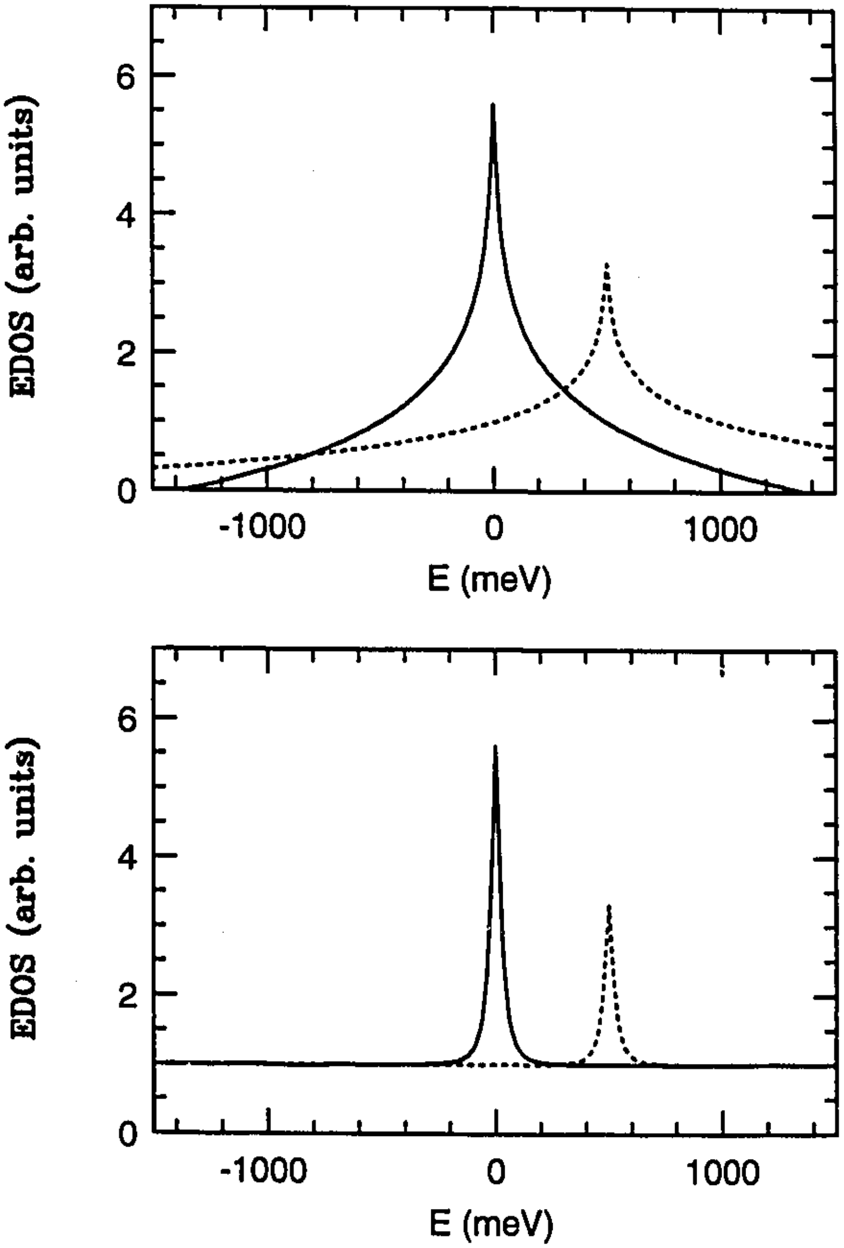

Figure 1.2: Density of states; (upper frame) for equation 1.4 r=1.0, E_f=500 solid line (s=1.0, δ=0.0) and dotted line s=0.5 and δ=500). (Lower frame) for equation 1.5 r=1.0, E_f=500 and D=40 solid line (s=1600, δ=0.0) and dotted line (s=800 and δ=500).

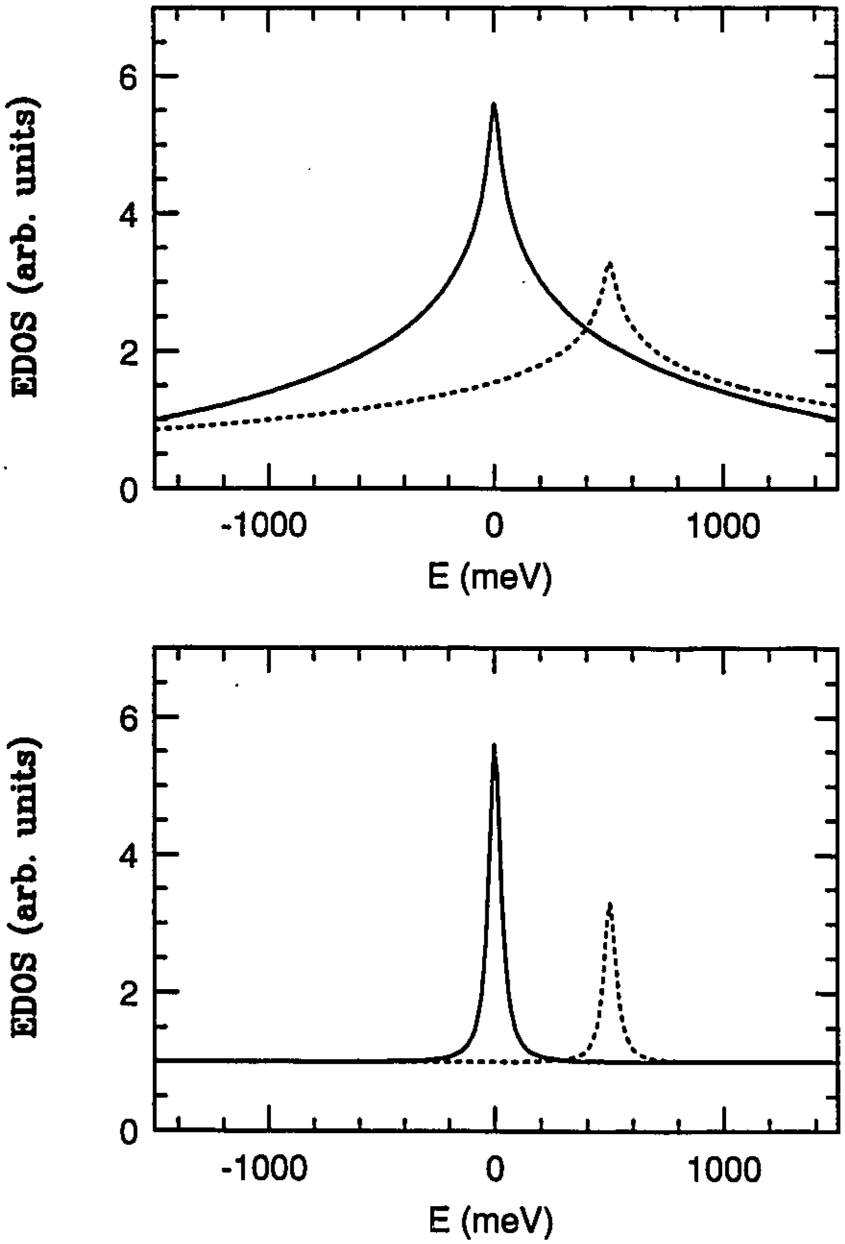

Figure 1.3: Density of states; Upper frame for equation 1.4 and lower frame for equation 1.5 E_f=1500 for both frames and other parameters are identical to those of figure 1.2.

Chapter 2

Formalism

I) Introduction

In this chapter, we will list the Eliashberg equations as well as derive the thermodynamic potential for an electron gas interacting with a background of phonons (or spin fluctuations) and a dilute concentration of normal impurities. Following this, we will derive a new formula for the London penetration depth for a finite band superconductor applicable to Eliashberg formalism. Finally, we will show how to treat the upper critical field so as to include a general density of electronic states in two or three dimensions.

II) The Eliashberg Equations on the Imaginary Axis

A) Pure and Born Approximation Limits

The Eliashberg equations are a set of self consistent equations that describe the superconducting (or normal) state, and from which several thermodynamic properties can be calculated. The Eliashberg equations are analytically derived from the self energy, $\hat{\Sigma}$, of a particle–hole propagator, $\hat{G}$, called a Green's function [Eliashberg 1960]. In quantum field theory [Mandle and Shaw 1984], the self energy $\hat{\Sigma}$, of the propagator $\hat{G}$, is calculated from a set of Feynman diagrams, shown in Figure (2.1). The interaction of electrons (or holes) with bosons (phonons or spin fluctuations) is given by the first diagram in Figure (2.1a). Migdal has shown that in the case of phonons, the vertex corrections are of the order of $(\omega_D/\epsilon_F)^{1/2} \sim 10^{-2}$ [Migdal 1958], where ω_D is the Debey frequency and ϵ_F is the Fermi energy. However, it is still debatable whether or not the same situation can be extended to include spin fluctuations. In the absence of instabilities like spin (or charge) density waves SDW (CDW), it is safe to assume that only first order interactions are of significant importance, and higher order corrections (Figure (2.1b)) can be neglected. The solid line in Figure (2.1a) denotes the Gor'kov Green's functions $\hat{G}(p)$ which is a 4×4 matrix [Maki 1969], and its inverse $\hat{G}(p)^{-1}$ is related to the self energy matrix $\hat{\Sigma}(p)$ by the so called Dyson equation,

$$\hat{G}(p)^{-1} = \hat{G}^{0}(p)^{-1} - \hat{\Sigma}(p) \tag{2.1}$$

here, $\hat{G}^{0}(p)^{-1}$ is the inverse of the noninteracting Green's function $\hat{G}^{0}(p)$, $p \equiv (\mathbf{k}, i\omega_n)$, with $\omega_n = \pi T(2n+1)$, n=0, ±1, ±2, ..., etc., T is the temperature of the system, and $\mathbf{k}$ is the momentum of the quasiparticle (the propagator). The inverse of the noninteracting Green's function is given by

$$\hat{G}^{0}(p)^{-1} = i\omega_n - \epsilon_k \hat{\beta}, \tag{2.2}$$

where ϵ_k is the dispersion of free electrons in the band, and $\hat{\beta}$ is a diagonal matrix formed from the tensor product of two Pauli matrices, $\hat{\beta}=\tau_3 \times \sigma_0$, and has the following form

$$\hat{\beta} = \begin{bmatrix} 1 & 0 & 0 & 0 \\ 0 & 1 & 0 & 0 \\ 0 & 0 & -1 & 0 \\ 0 & 0 & 0 & -1 \end{bmatrix} . \tag{2.3}$$

The inverse of the Green's function $\hat{G}(p)^{-1}$ in the superconducting state is written as follows

$$\hat{G}(p)^{-1} = i\tilde{\omega}_n(p) - \tilde{\epsilon}(p)\,\hat{\beta} + \phi(p)\,\hat{\alpha}, \tag{2.4}$$

the superscript ~ indicates a self consistent renormalization of the Matsubara frequency ω_n as well as the dispersion ϵ_k, and $\hat{\alpha}=\tau_2 \times \sigma_2$ has the following form,

$$\hat{\alpha} = \begin{bmatrix} 0 & 0 & 0 & -1 \\ 0 & 0 & 1 & 0 \\ 0 & 1 & 0 & 0 \\ -1 & 0 & 0 & 0 \end{bmatrix} . \tag{2.5}$$

The order parameter in the superconducting state is given by the off diagonal component $\phi(p)$ of $\hat{\Sigma}(p)$. The parameter $\phi(p)$ plays the role of the energy gap in the superconducting state. The normal to superconducting phase transition is characterized by the onset of a non–zero value for $\phi(p)$. Eliashberg equations describe both the normal state ($\phi(p)=0$) as well as the superconducting state ($\phi(p)\neq 0$). There is still a normal state solution of the Eliashberg equations below the transition temperature and this solution, of course, has a higher free energy. The wiggly line in Figure (2.1a) is the boson propagator, B, inducing the interaction

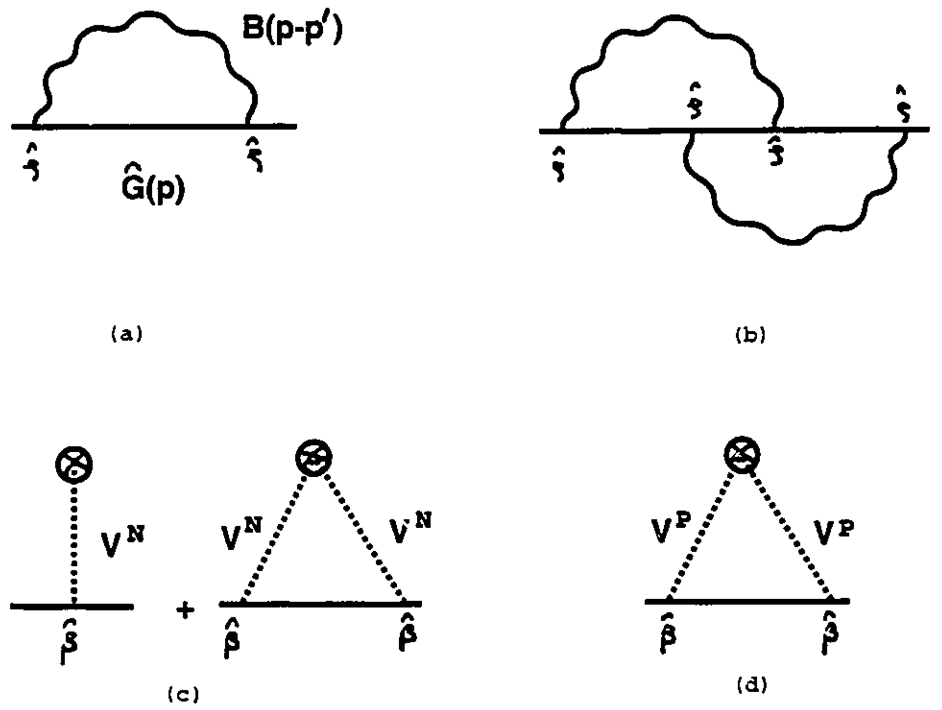

Figure 2.1: Feynman diagrams of a,b) electron self energy; c) normal impurity scattering; d) paramagnetic impurity scattering.

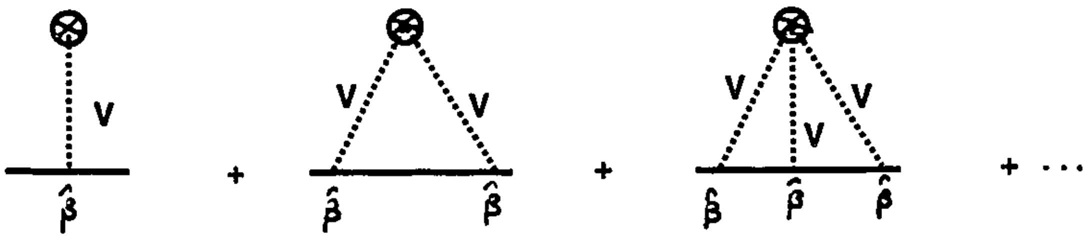

Figure 2.2: Feynman diagrams for normal resonance impurity scattering.

responsible for superconductivity, and the self energy $\hat{\Sigma}_b(p)$ from this boson interaction [Allen and Mitrovic 1982] is given by

$$\hat{\Sigma}_b(\mathbf{k},n) = \frac{T}{N_b}\sum_{\mathbf{k}',m}\int_0^{\infty} d\Omega\, \frac{\alpha^2F(\mathbf{k},\mathbf{k}',\ \Omega)2\Omega}{\Omega^2+(\omega_n-\omega_m)^2}\ \hat{\rho}\ \hat{G}(k',m)\hat{\rho}, \tag{2.6}$$

where N_b is a background average of the electronic density of states (EDOS) near the Fermi surface, the boson propagator is written in terms of spectral representation α^2F and $\hat{\rho}=\hat{\beta}$ or the identity for phonons or spin fluctuations, respectively. Inverting equation (2.4) to get

$$\hat{G}(p) = -\frac{i\tilde{\omega}(p)+\ \tilde{\epsilon}(p)\hat{\beta}-\phi(p)\hat{\alpha}}{D(p)} \tag{2.7}$$

where

$$D(p) = \tilde{\omega}^2(p) + \tilde{\epsilon}^2(p) + \phi^2(p) \tag{2.8}$$

and using Dyson equation (2.1), we can write down the self energy $\hat{\Sigma}_b(p)$, component wise as

$$\tilde{\omega}_n(k,n) = \omega_n + \frac{T}{N_b}\sum_{\mathbf{k}',m} \lambda(\mathbf{k},\mathbf{k}';n-m)\,\frac{\tilde{\omega}(\mathbf{k}',m)}{D(\mathbf{k}',m)}, \tag{2.9a}$$

and

$$\phi(k,n) = \pm\frac{T}{N_b}\sum_{\mathbf{k}',m} \lambda(\mathbf{k},\mathbf{k}';n-m)\,\frac{\phi(\mathbf{k}',m)}{D(\mathbf{k}',m)}, \tag{2.9b}$$

– sign for spin fluctuations and,

$$\chi(\mathrm{k,n}) = -\frac{\mathrm{T}}{\mathrm{N_b}} \sum_{\mathrm{k',m}} \lambda(\mathbf{k},\mathbf{k}';\mathrm{n-m})\, \frac{\tilde{\epsilon}(\mathbf{k}',\mathrm{m})}{\mathrm{D}(\mathbf{k}',\mathrm{m})}, \tag{2.9c}$$

where we defined χ and λ as

$$\chi(\mathrm{k,n}) = \tilde{\epsilon}(\mathbf{k},\mathrm{n}) - \epsilon_{\mathrm{k}}, \tag{2.10}$$

$$\lambda(\mathbf{k},\mathbf{k}',\mathrm{n-m}) = \int_0^\infty d\Omega\ \alpha^2\mathrm{F}(\mathbf{k},\mathbf{k}',\Omega)\, \frac{2\Omega}{\Omega^2+(\omega_{\mathrm{n}}-\omega_{\mathrm{m}})^2}. \tag{2.11}$$

Elastic impurity scattering up to a second order in the impurity potential (Born approximation) is included by adding the contributions of Feynman diagrams in Figure (2.1c) for normal impurities and the diagram of Figure (2.1d) for paramagnetic impurities. Assuming potentials that are momentum independent for this elastic process, the self energy due to impurities is given by [Allen and Mitrovic 1982],

$$\hat{\Sigma}_{\mathrm{B}}(\mathrm{n}) = \mathrm{t}^0\, \hat{\beta} + \frac{\mathrm{t}^+}{\pi \mathrm{N_b}} \sum_{\mathbf{k}'} \hat{\beta}\, \hat{\mathrm{G}}(\mathrm{k',n})\hat{\beta} + \frac{\mathrm{t}^-}{\pi \mathrm{N_b}} \sum_{\mathbf{k}'} \hat{\mathrm{G}}(\mathrm{k',n}) \tag{2.12}$$

where t^0 and t^+ are proportional to normal impurity scattering in first order and second order, respectively, and t^- gives the strength of the paramagnetic impurity scattering to second order. Eliashberg equations that include elastic impurity scattering up to second order can be written as

$$\tilde{\omega}(\mathbf{k},\mathrm{n}) = \omega_{\mathrm{n}} + \frac{\mathrm{T}}{\mathrm{N_b}} \sum_{\mathbf{k}',\mathrm{m}} \lambda(\mathbf{k},\mathbf{k}';\mathrm{n-m})\, \frac{\tilde{\omega}(\mathbf{k}',\mathrm{m})}{\mathrm{D}(\mathbf{k}',\mathrm{m})} + \frac{\mathrm{t}^+ + \mathrm{t}^-}{\pi \mathrm{N_b}}\, \mathrm{G_0}(\mathrm{n}), \tag{2.13a}$$

$$\phi(\mathbf{k},n) = \pm \frac{T}{N_b} \sum_{\mathbf{k}',m} \lambda(\mathbf{k},\mathbf{k}';n-m) \frac{\phi(\mathbf{k}',m)}{D(\mathbf{k}',m)} + \frac{t^+ - t^-}{\pi N_b} G_2(n), \qquad (2.13b)$$

note that the reason of the – sign with t^- is the same as that for the – sign associated with spin fluctuations,

$$\chi(\mathbf{k},n) = -\frac{T}{N_b} \sum_{\mathbf{k}',m} \lambda(\mathbf{k},\mathbf{k}';n-m) \frac{\tilde{\epsilon}(\mathbf{k}',m)}{D(\mathbf{k}',m)} + t^0 - \frac{t^+ + t^-}{\pi N_b} G_1(n). \qquad (2.13c)$$

Where we defined $G_i(n)$, i=0, 1, 2 as follows

$$G_0(n) = \sum_{\mathbf{k}} \frac{\tilde{\omega}(\mathbf{k},n)}{D(\mathbf{k},n)}, \qquad (2.14a)$$

$$G_1(n) = \sum_{\mathbf{k}} \frac{\tilde{\epsilon}(\mathbf{k},n)}{D(\mathbf{k},n)}, \qquad (2.14b)$$

$$G_2(n) = \sum_{\mathbf{k}} \frac{\phi(\mathbf{k},n)}{D(\mathbf{k},n)}. \qquad (2.14c)$$

Besides the electron–boson interactions, there is also a screened Coulomb repulsion between two electrons in a Cooper pair. In the normal state, the repulsion exchange between electrons modifies the bands of electrons through the Hartree and Fock terms. As pairing takes place, on average there will be extra repulsion between two paired electrons. This is only an off diagonal effect and only modifies the gap equation ($\phi(p)$ equation). The range of the Coulomb repulsion is of the order of the Fermi–Thomas length q_{FT} which is also comparable to the Fermi momentum k_F.

It is very hard to get any quantitative measure of the Coulomb repulsion μ for any material because it is a many body problem that involves the long range Coulomb force. The most dominant contribution to the repulsion comes from $\mu(E_f)$ at the Fermi surface. In Eliashberg theory $\mu(E_f)$ is an adjustable parameter that can be used to fix T_c for example. It is shown [Morel and Anderson 1962] that the cutoff can be scaled down to $\omega_c \sim$ several ω_{max} by renormalizing $\mu(E_f)$ to $\mu^*(\omega_c)$ with ω_{max} being the maximum boson frequency and

$$\mu^*(\omega_c) = \frac{\mu(E_f)}{1+\mu(E_f)\, \ell n\left[\frac{E_f}{\omega_c}\right]}. \tag{2.15}$$

For isotropic interactions in the absence of particle–hole asymmetry ($\chi(n)=0$), the Eliashberg equations in the clean limit reduce to [Rainer and Bergmann 1974]

$$\Delta(i\omega_n)Z(i\omega_n) = \pi T \sum_{m=-\infty}^{\infty} [\lambda(i\omega_m - i\omega_n) - \mu^*(\omega_c)\theta((\omega_c) - |\omega_m|)] \times \frac{\Delta(i\omega_m)}{\sqrt{\omega_m^2 + \Delta^2(i\omega_m)}} \tag{2.16a}$$

and

$$Z(i\omega_n) = 1 + \frac{\pi T}{\omega_n} \sum_{m=-\infty}^{\infty} \lambda(i\omega_m - i\omega_n) \frac{\omega_m}{\sqrt{\omega_m^2 + \Delta^2(i\omega_m)}} \tag{2.16b}$$

where we used $\phi_n = \Delta_n Z_n$, $\tilde{\omega}_n = Z_n\, \omega_n$, and performed the sum over the momentum states by using $N(\epsilon) \sim N_b$ and

$$\sum_{\mathbf{k}} = \int_{-\infty}^{\infty} d\epsilon\, N(\epsilon) \int \frac{d\Omega_{\mathbf{k}}}{4\pi} \tag{2.17}$$

where $d\Omega_{\mathbf{k}}$ is an element of solid angle. The isotropic $\lambda(z)$ is given by

$$\lambda(z) = \int_0^{\infty} \frac{2\nu\alpha^2F(\nu)}{\nu^2+z^2}\, d\nu \tag{2.18}$$

and $\theta(x)$ is a step function defined by

$$\theta(x) = \begin{cases} 1 & x \geq 0 \\ 0 & x<0 \end{cases}. \tag{2.19}$$

In Eliashberg theory, the strength of the electron–boson coupling is related to the spectral function of the bosons by a dimensionless parameter λ

$$\lambda = 2 \int_0^{\infty} \frac{d\omega}{\omega}\, \alpha^2F(\omega). \tag{2.20}$$

The larger λ is, the stronger the coupling. Conventional superconductors have λ values which may reach as large as 2.76 [Carbotte 1990]. The quantity $1+\lambda$ is the mass enhancement factor usually inferred from the slope of the normal specific heat at small temperatures. Another useful parameter is $T_c/\omega_{\ell n}$ which is used to gauge the electron–boson coupling strength. The parameter $\omega_{\ell n}$ is defined by

$$\omega_{\ell n} = \exp\left\{\frac{2}{\lambda} \int_0^{\infty} \frac{d\omega}{\omega}\, \alpha^2F(\omega)\ell n\omega\right\} \tag{2.21}$$

and was first introduced by Allen and Dynes [Allen and Dynes 1975]. The larger $T_c/\omega_{\ell n}$ ratio is, the stronger the coupling. Many approximate formulas for strong coupling corrections to BCS quantities have been derived using only the ratio $T_c/\omega_{\ell n}$ [Mitrovic, Zarate and Carbotte 1984; Marsiglio and Carbotte 1986]. Many of our numerical results in the next chapters will be gauged by the strong coupling parameter $T_c/\omega_{\ell n}$.

B) Normal Impurity Resonance Scattering Limit

Normal impurity resonance scattering is calculated from Figure (2.2) which includes higher order Feynman diagrams. The contribution of Figure (2.2)to the resonance impurity self energy $\hat{\Sigma}_r(k,n)$, for a given concentration η of scattering centres is

$$\hat{\Sigma}_r(n) = \eta\hat{T}(n) = \eta\left\{V\hat{\beta}+V^2\sum_{\mathbf{k}}\hat{\beta}\,\hat{G}(\mathbf{k}',n)\hat{\beta}+\right.$$

$$\left.V^3\sum_{\mathbf{k}'\mathbf{k}''}\hat{\beta}\,\hat{G}(k',n)\hat{\beta}\,\hat{G}(\mathbf{k}'',n)\hat{\beta}+\ldots\right\}. \tag{2.22}$$

Equation (2.22) is a simplified version of the T–matrix scattering equation, where the momentum dependence of the scattering potential V is dropped reducing it to an isotropic short range scattering potential. The solutions for $\hat{T}(n)$ in equation (2.22) is quite simple and written as

$$\hat{T}(n) = \frac{-iG_0(n)+C(n)\hat{\beta}-G_2(n)\hat{\alpha}}{L(n)} \tag{2.23}$$

with

$$L(n) = G_0^2(n) + C^2(n) + G_2^2(n), \tag{2.24}$$

and

$$C(n) = C + G_1(n), \tag{2.25}$$

$$C = \frac{1}{V} \tag{2.26}$$

Eliashberg equations then take the following form for normal impurity resonance scattering,

$$\tilde{\omega}(\mathbf{k},n) = \omega_n + \frac{T}{N_b} \sum_{\mathbf{k}',m} \lambda(\,\mathbf{k},\mathbf{k}',n-m)\, \frac{\tilde{\omega}(\mathbf{k}',m)}{D(\mathbf{k}',m)} + \eta \frac{G_0(n)}{L(n)}, \tag{2.27a}$$

$$\phi(\mathbf{k},n) = \pm \frac{T}{N_b} \sum_{\mathbf{k}',m} \lambda(\,\mathbf{k},\mathbf{k}',n-m)\, \frac{\phi(\mathbf{k}',m)}{D(\mathbf{k}',m)} + \eta \frac{G_2(n)}{L(n)}, \tag{2.27b}$$

$$\chi(\mathbf{k},n) = -\frac{T}{N_b} \sum_{\mathbf{k}',m} \lambda(\,\mathbf{k},\mathbf{k}',n-m)\, \frac{\tilde{\epsilon}(\mathbf{k}',m)}{D(\mathbf{k}',m)} + \eta \frac{C(n)}{L(n)}. \tag{2.27c}$$

III) Thermodynamic Potential and Free Energy Difference

A) Pure and Born Approximation Limits

The thermodynamic potential Ω for an electron gas interacting with a gas of bosons up to the Migdal approximation [Migdal 1958] is given by [Luttinger and Ward 1960]:

$$\Omega = \Omega' - \frac{T}{2} \sum_{p} \left\{ \ln(+|\hat{G}^{-1}_{(p)}|) + \mathrm{Tr}\, \hat{\Sigma}(p)\, \hat{G}(p) \right\}, \tag{2.28}$$

where Ω' is the contribution of Feynman diagram shown in Figure 2.3, $\mathrm{Tr}\hat{O}$ is short

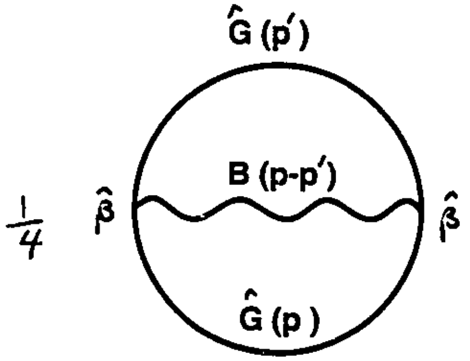

Figure 2.3

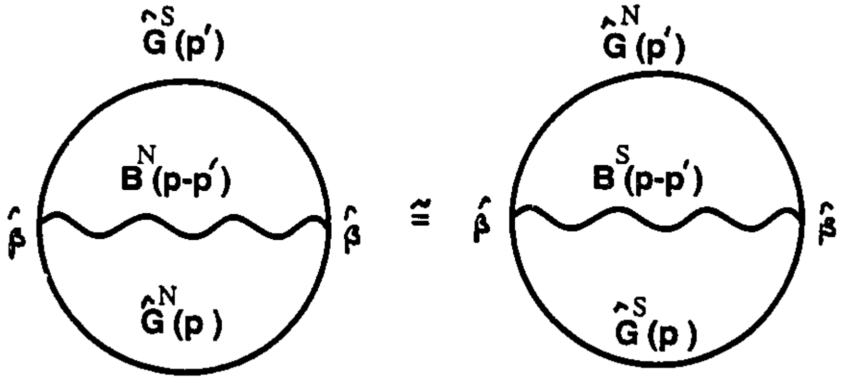

Figure 2.4

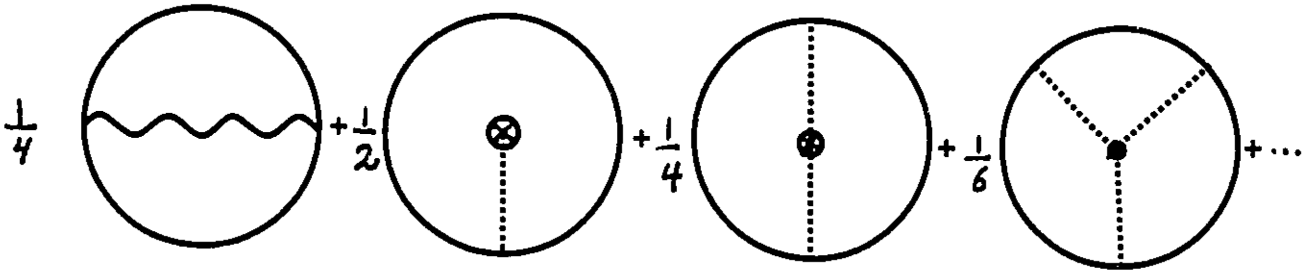

Figure 2.5

for the taking the trace of the matrix $\hat{O}$, and $|\hat{O}|$ is the determinat of $\hat{O}$. The contribution of Figure (2.3) to Ω' is

$$\Omega' = \frac{T}{4}\,\mathrm{Tr}\sum_{p} \hat{\Sigma}_b(p)\,\hat{G}(p), \tag{2.29}$$

and using $|\hat{G}^{-1}(p)| = D^2(p)$, we can rewrite equation (2.28) as:

$$\Omega = -T\sum_{p}\left\{\ln D(p) + \frac{\mathrm{Tr}}{4}\hat{\Sigma}_b(p)\,\hat{G}(p)\right\}. \tag{2.30}$$

The thermodynamic potential Ω is a divergent quantity, however the free energy difference $\Omega_S-\Omega_N$ between the superconducting and the normal state is finite and can be calculated quite easily from equation (2.30).

$$\Delta\Omega = \Omega_S-\Omega_N = T\sum_{p}\left\{\ln\frac{D(p)^N}{D(p)^S} + \frac{\mathrm{Tr}}{4}\left[\hat{\Sigma}_b^N(p)\,\hat{G}(p)^N-\hat{\Sigma}_b^S(p)\hat{G}(p)^S\right]\right\} \tag{2.31}$$

The superscripts S and N refer to the superconducting and normal state, respectively. It is a standard practice to compute the Bardeen–Stephan formula $\Delta\Omega_{BS}$ for the free energy difference between the normal state and the superconducting state and use it to compute the specific heat difference between the two states instead of $\Delta\Omega$. The Bardeen–Stephan formula is derived by adding and subtracting the contribution of Feynman diagrams on Figure (2.4) to equation (2.31). The contribution of Figure (2.4) Ω_1 is given by

$$\Omega_1 = \frac{T}{4}\sum_{p}\mathrm{Tr}\,\hat{\Sigma}_b^N(p)\,\hat{G}(p)^S \cong \frac{T}{4}\sum_{p}\mathrm{Tr}\,\hat{\Sigma}_b^S(p)\,\hat{G}(p)^N \tag{2.32}$$

i.e., add and subtract the left and right hand side of equation (2.32), respectively, to the right of equation (2.31) to get

$$\Delta\Omega_{BS} = T \sum_{p} \left\{ \ln \frac{D(p)^{N}}{D(p)^{S}} + \frac{Tr}{4} \left[\hat{\Sigma}^{N}(p) - \hat{\Sigma}^{S}(p) \right] \left[\hat{G}(p)^{N} + \hat{G}(p)^{S} \right] \right\}. \qquad (2.33)$$

We have dropped the subscript b (for boson) because equation (2.33) applies equally to the case of Born scattering by normal or magnetic impurities [Mitrovic and Carbotte 1983], where the self energy $\hat{\Sigma}(p)$ is the total self energy $\hat{\Sigma}_b + \hat{\Sigma}_B$. The self energy can be written in terms of $\tilde{\omega}$, $\tilde{\epsilon}$ and ϕ by using equations (2.1), (2.2) and (2.4) to get the following form

$$\hat{\Sigma}(p) = i(\omega_n - \tilde{\omega}(p)) + \chi(p)\hat{\beta} - \phi(p)\hat{\alpha} \qquad (2.34)$$

and, as before, $p = (k;i\omega_n)$.

The calculable form of $\Delta\Omega_{BS}$ in terms of the parameters given by Eliashberg equations $(\tilde{\omega}, \chi, \phi)$ is

$$\Delta\Omega_{BS} = T \sum_{p} \left\{ \ln \frac{D(p)^{0}}{D(p)} + [\tilde{\omega}(p) - \tilde{\omega}(p)^{0}] \left[\frac{\tilde{\omega}(p)^{0}}{D(p)^{0}} + \frac{\tilde{\omega}(p)}{D(p)} \right] \right.$$

$$\left. [\chi(p) - \chi(p)^{0}] \left[\frac{\tilde{\epsilon}(p)^{0}}{D(p)^{0}} + \frac{\tilde{\epsilon}(p)}{D(p)} \right] + \frac{\phi(p)^{2}}{D(p)} \right\}. \qquad (2.35)$$

We have dropped the superscript S for the superconducting state and replaced the N by 0 to denote the normal state.

In the case of particle–hole symmetry, $\chi(p)=\chi^0(p)=0$, and constant background EDOS, equation (2.35) can be further reduced to

$$\Delta\Omega_{BS} = N(0)T \sum_{n} \left\langle \int_{-\infty}^{\infty} d\epsilon \left\{ \ln \left[\frac{\epsilon^2+\tilde{\omega}_k^0(n)}{\epsilon^2+\tilde{\omega}_k^2(n)+\tilde{\Delta}_k^2(n)} \right] \right.\right.$$

$$+ \left[\tilde{\omega}_k(n)-\tilde{\omega}_k^0(n)\right] \left[\frac{\tilde{\omega}_k^0(n)}{\epsilon^2+\tilde{\omega}_k^{02}(n)} + \frac{\tilde{\omega}_k(n)}{\epsilon^2+\tilde{\omega}_k^2(n)+\tilde{\Delta}_k^2(n)} \right]$$

$$\left.\left. + \frac{\tilde{\Delta}_k^2(n)}{\epsilon^2+\tilde{\omega}_k^2(n)+\tilde{\Delta}_k^2(n)} \right\} \right\rangle \tag{2.36}$$

where <...> denotes the average over the Fermi surface and N(0) is the EDOS at the Fermi surface. With the aid of the equation (A.1) and (A.5) in Appendix A, equation (2.36) can be written as

$$\Delta\Omega_{BS} = \pi T\, N(0) \sum_{n} \left\langle \left\{ 2\left[|\tilde{\omega}_k^0(n)| - \sqrt{\tilde{\omega}_k^2(n)+\tilde{\Delta}_k^2} \right] \right.\right.$$

$$\left[\tilde{\omega}_k(n)-\tilde{\omega}_k^0(n)\right] \left[\frac{\tilde{\omega}_k^0(n)}{|\tilde{\omega}_k^0(n)|} + \frac{\tilde{\omega}_k(n)}{\sqrt{\tilde{\omega}_k^2(n)+\tilde{\Delta}_k^2(n)}} \right]$$

$$\left.\left. \frac{\tilde{\Delta}_k(n)}{\sqrt{\tilde{\omega}_k^2(n)+\tilde{\Delta}_k^2(n)}} \right\} \right\rangle \tag{2.37}$$

and utilizing the identity $\tilde{\omega}=|\tilde{\omega}|$ sign $\tilde{\omega}$ and few mathematical rearrangements, we get

$$\Omega_{\mathrm{BS}} = 2\pi\, \mathrm{N}(0) \sum_{n\geq 0} \left\langle \left[\tilde{\omega}_{\mathbf{k}}(n) - \sqrt{\tilde{\omega}_{\mathbf{k}}^{2}(n) + \tilde{\Delta}_{\mathbf{k}}^{2}} \right] \left[1 - \frac{\tilde{\omega}_{\mathbf{k}}^{0}(n)}{\sqrt{\tilde{\omega}_{\mathbf{k}}^{2}(n) + \tilde{\Delta}_{\mathbf{k}}^{2}(n)}} \right] \right\rangle \tag{2.38}$$

Equation (2.38) is the same as equation (27) in [Schachinger and Carbotte 1991] and equation (20) in [Prohammer, Perez–Gonzalez and Carbotte 1993] for the Bardeen–Stephan free energy expression in an anisotropic superconductor.

B) Normal Impurity Resonance Scattering Limit

There is a constraint on the thermodynamic potential Ω of an interacting system, namely, the self energy $\hat{\Sigma}(p)$ of the propagator $\hat{G}(p)$ is defined by requiring that the variation of Ω with respect to $\hat{\Sigma}(p)$ is identically zero. The application of the stationary condition to equation (2.28), i.e. $\partial\Omega/\partial\hat{\Sigma}(p)=0$, results in the proper definition of $\Omega'(p)$, i.e. $\hat{\Sigma}(p)=2\,\partial\Omega'/\partial\hat{G}(p)/T$, and from which we demand that Ω' has to be the contribution of the set of Feynman diagrams given in Figure (2.5). The first diagram is the same one as in Figure (2.3), and its contribution was evaluated earlier (equation (2.29)), however, the contribution of the rest of the diagrams, denoted by S, can be evaluated quite easily by the following procedure.

$$\begin{aligned} S = \frac{\eta T}{2}\, \mathrm{Tr} \sum_{n} \Big\{ & V_{\beta} \sum_{\mathbf{k}} \hat{G}(\mathbf{k},n) + \tfrac{1}{2} V^{2} \big(\hat{\beta} \sum_{\mathbf{k}} \hat{G}(\mathbf{k},n)\big)^{2} \\ & + \tfrac{1}{3} V^{3} \big(\hat{\beta} \sum_{\mathbf{k}} \hat{G}(\mathbf{k},n)\big)^{3} + \dots \Big\} \end{aligned} \tag{2.39}$$

Everywhere factors of the form 1/n are replaced by $\int_0^1 dx\, x^{n-1}$, so now S can be written as,

$$S = \frac{\eta T}{2} \mathrm{Tr} \sum_n \int_0^1 \frac{dx}{x} \Big\{ xV\, \hat{\beta} + (xV)^2 \sum_{\mathbf{k}} \hat{\beta}\, \hat{G}(\mathbf{k},n)\, \hat{\beta}$$

$$+ (xV)^3 \Big(\sum_{\mathbf{k}} \hat{\beta}\, \hat{G}(\mathbf{k},n)\Big)^2 \hat{\beta} + ... \Big\} \sum_{\mathbf{k}} \hat{G}(\mathbf{k},n). \tag{2.40}$$

The form inside brackets in equation (2.40) is the same one inside brackets in equation (2.22), except now xV replaces V.

We now define $\hat{T}(x,n)$ to be identical in form to $\hat{T}(n)$, and each V in $\hat{T}(n)$ is replaced by xV with $\hat{T}(1,n)=\hat{T}(n)$. Equation (2.40) is easily rewritten as

$$S = \frac{\eta T}{2} \sum_n \int_0^1 \frac{dx}{x} \mathrm{Tr} \Big\{ \hat{T}(x,n) \sum_{\mathbf{k}} \hat{G}(\mathbf{k},n) \Big\}. \tag{2.41}$$

The integration over k can be performed (consult equations (2.14a) to (2.14c)) and after taking the trace we get

$$S = -2\eta T \sum_n \int_0^1 \frac{dx}{x} \Big\{ \frac{xVG_1(n) + (xV)^2 [G_0^2(n) + G_1^2(n) + G_2^2(n)]}{1 + 2xVG_1(n) + (xV)^2 [G_1^2(n) + G_2^2(n)]} \Big\}. \tag{2.42}$$

The integration over x is trivial and we end up with

$$S = -\, \eta T \sum_n \ln[V^2 L(n)], \tag{2.43}$$

and L(n) is defined by equation (2.24).

The contribution Ω' of Figure (2.5) is now given by

$$\Omega' = \frac{T}{4}\,\mathrm{Tr}\sum_{p}\,[\hat{\Sigma}(p)-\eta\hat{T}(n)]\,\hat{G}(p) - \eta T\sum_{n}\ln[V^2L(n)], \tag{2.44}$$

where we have used the expression for the total self energy of resonance scattering, i.e. $\hat{\Sigma}(p)=\hat{\Sigma}_b(p)+\eta\hat{T}(n)$.

The free energy difference between the superconducting and normal state $\Delta\Omega$ is now easily calculated and is equal to

$$\Delta\Omega = \Delta\Omega_{BS} + \Delta\Omega_r \tag{2.45}$$

with

$$\Delta\Omega_r = \eta T\left\{\sum_{n}\ln\left[\frac{L^N(n)}{L^S(n)} + \frac{\mathrm{Tr}}{4}\sum_{p}\,[\hat{T}^S(n)+\hat{T}^N(n)][\hat{G}^N(p)-\hat{G}^S(p)]\right]\right\}, \tag{2.46}$$

which can be reduced further, after doing the **k** integration and taking the trace to

$$\Delta\Omega_r = \eta\,T\sum_{n}\left\{\ln\left[\frac{L^0(n)}{L(n)}\right] + [G_0(n)G_0^0(n)+C(n)C^0(n)][L^0(n)^{-1}-L(n)^{-1}]\right\}, \tag{2.47}$$

where the superscript 0 refers to the normal state. Again for the case of constant EDOS which is particle–hole symmetric $G_1(n)=0$ and $C(n)=C$ and

$$G_0^0(n) = \pi N(0)\ \mathrm{sign}\ \tilde{\omega}_k^0(n), \tag{2.48a}$$

$$G_0(n) = \pi N(0) \left\langle \frac{\tilde{\omega}_k(n)}{\sqrt{\tilde{\omega}_k^2(n)+\tilde{\Delta}_k^2(n)}} \right\rangle = \pi N(0) G_0'(n), \qquad (2.48b)$$

$$G_2(n) = \pi N(0) \left\langle \frac{\tilde{\Delta}_k(n)}{\sqrt{\tilde{\omega}_k^2(n)+\tilde{\Delta}_k^2(n)}} \right\rangle = \pi N(0) G_2'(n), \qquad (2.48c)$$

$$C = \pi N(0) C', \qquad (2.48d)$$

$$L(n) = \pi^2 N^2(0)\, [G_0'^2(n) + C'^2 + G_2'^2(n)] \qquad (2.48e)$$

$$L^0(n) = \pi^2 N^2(0) [1+C'^2], \qquad (2.48f)$$

$$\Omega_r = 2\eta\, T \sum_{n\geq 0} \left\{ \ln \left[\frac{1+C'^2}{C'^2+G_0'^2(n)+G_2'^2(n)} \right] \right.$$

$$\left. + [G_0'(n)+C'^2] \left[\frac{1}{1+C'^2} - \frac{1}{C'^2+G_0'^2(n)+G_2'^2(n)} \right] \right\}. \qquad (2.49)$$

By eliminating C'^2 from $G_0'(n)+C'^2$, we can rewrite equation (2.59) into

$$\Omega_r = 2\pi^2 N(0)\, T\Gamma \sum_{n\geq 0} \left\{ \ln \left[\frac{1+C'^2}{C'^2+G_0'^2(n)+G_2'^2(n)} \right] \right.$$

$$+ [G_0'(n)-1] \left[\frac{1}{1+C'^2} - \frac{G_0'(n)}{C'^2+G_0'^2(n)+G_2'^2(n)} \right]$$

$$+ \frac{G_2'^2(n)}{C'^2+G_0'^2(n)+G_2'^2(n)}\Bigg\} \tag{2.50}$$

where we defined Γ by

$$\Gamma = \frac{\eta}{\pi^2 N(0)}. \tag{2.51}$$

Equation (2.5) is the same as equation (21) in [Prohammer, Perez–Gonzalez and Carbotte 1993].

IV) The London Penetration Depth

In this fourth section, we will derive a new strong coupling formula [Arberg, Mansor and Carbotte 1993] for the London penetration depth applicable to finite bands as well as energy dependent electronic density of states valid for all impurity scattering limits. The basic idea [Nam 1967] is to calculate the response function $\underline{K}(q,\omega)$ for a paramagnetic current density $J(q,\omega)$,

$$J_\mu^p(q,\omega) = \frac{-1}{4\pi}\left\{K_{\mu\nu}^{sp}(q,\omega) - K_{\mu\nu}^{np}(q,0)\right\} A^\nu(q,\omega), \tag{2.52}$$

the superscripts s and n refer to the superconducting and normal state, respectively, and p stands for paramagnetic. The Greek indices specify the component of the vector potential, A. The penetration depth $\lambda(T)$ is calculated from [Nam 1967],

$$\lambda_{\mu\nu}(T) = \frac{2}{\pi}\int_0^\infty \frac{dq}{q^2+K_{\mu\nu}(q,0)}, \tag{2.53}$$

where

$$K_{\mu\nu}(q,\omega) = K^{sp}_{\mu\nu}(q,\omega) - K^{np}_{\mu\nu}(q,0). \qquad (2.54)$$

The London penetration depth $\lambda_{\mu\nu}(T)$ is evaluated from equation (2.53) by using $K_{\mu\nu}(0,0)$ instead of $K_{\mu\nu}(q,0)$ and is equal to

$$\lambda_{\mu\nu}(T) = K_{\mu\nu}(0,0)^{-1/2}. \qquad (2.55)$$

The paramagnetic response function $\underline{K}(0,0)$ is given by

$$K^{sp}_{\mu\nu}(0,0) = 4\pi e^2\, T \sum_{\mathbf{k},n} \mathrm{Tr}\left\{(\nabla_k \epsilon_k)_\mu\, \hat{G}(\mathbf{k},n)(\nabla_k \epsilon_k)_\nu\, \hat{G}(\mathbf{k},n)\right\} \qquad (2.56)$$

and simplifies to

$$K^{sp}_{\mu\nu}(0,0) = 16\pi e^2\, T \sum_{p} v_\mu v_\nu \frac{\tilde{\epsilon}^2(p)+\phi^2(p)-\tilde{\omega}^2(p)}{D^2(p)} \qquad (2.57)$$

where $v_\mu = (\nabla_k \epsilon_k)_\mu$ is e^- velocity. The final expression for $K_{\mu\nu}(0,0)$ to be used in equation (2.55) is

$$K_{\mu\nu}(0,0) = T \sum_{p} v_\mu v_\nu \left\{\frac{\tilde{\epsilon}^2(p)+\phi^2(p)-\tilde{\omega}^2(p)}{D^2(p)} - \frac{\tilde{\epsilon}^{02}(p)-\tilde{\omega}^{02}(p)}{D^{02}(p)}\right\}, \qquad (2.58)$$

and again the superscript 0 refers to the normal state.

Equation (2.58) is very general and applicable to superconductors with finite bands as well as clean or dirty superconductors including resonance impurity scattering. In chapter 4, we will utilize equation (2.58) to compute the London penetration depth for a d–wave superconductor and compare it to a recent microwave measurement of $\lambda_L(T)$. In the constant EDOS and particle–hole symmetry, we can utilize equation (A.7) in appendix A to show that equation (2.58) reduces to

$$K(0,0) = \frac{16\pi^2}{3} e^2 T \quad N(0)\, v_F^2 \sum_n \frac{\tilde{\Delta}^2(n)}{[\tilde{\omega}^2(n) + \tilde{\Delta}^2(n)]^{3/2}} \tag{2.59}$$

where we used $<v_i^2> = v_F^2/3 =$ constant, which is the same as equation (1.11) in [Nam 1967]. It is important to note that the contribution from the normal state part of equation (2.58) to equation (2.59) is identically zero only in the infinite band approximation with constant EDOS. In a finite band, however, the contribution is less than zero. In the clean limit BCS $\tilde{\omega}(p)=\omega_n$ for both the normal and superconducting states, and it matters whether the integration over ϵ is done first or the summation of the Matsubara frequencies is done first. To do the summation over n first, we will use the following identities;

$$\tanh\left(\beta\frac{x}{2}\right) = \sum_{n\geq 0}^{\infty} \frac{4\beta x}{\pi^2(2n+1)^2+\beta^2 x^2} \tag{2.60}$$

and

$$\tanh\left(\beta\frac{x}{2}\right) = 1 - 2\, f(x) \tag{2.61}$$

where

$$f(x) = \frac{1}{1+e^{\beta x}}$$

is the Fermi function and β is T^{-1}. It can be shown quite easily that

$$\frac{\partial f(x)}{\partial x} = -\frac{1}{2}\frac{\partial}{\partial x}\tanh\left(\beta\frac{x}{2}\right) = \frac{1}{\beta}\sum_{n}\frac{x^2-\omega_n^2}{[x^2+\omega_n^2]^2}. \tag{2.62}$$

The summation over n in equation (2.62) is unrestricted, and hence equation (2.58) for clean a BCS superconductor becomes

$$\underline{K}_{\mu\nu}(0,0) = 16\,\pi\,e^2 \sum_{\mathbf{k}} v_\nu v_\mu \left\{\frac{\partial f(E_k)}{\partial E_k} - \frac{\partial f(\epsilon_k)}{\partial \epsilon_k}\right\} \tag{2.63}$$

which corresponds to formula (32) in [Marsiglio and Hirsch 1990].

V) The Upper Critical Field Hc_2

The calculation of the upper critical field Hc_2 for a strong coupling superconductor reduces to solving the linearized version of the Eliashberg equations in the presence of a magnetic field $\underline{H}$. The linearized forms for $\tilde{\omega}$ and $\tilde{\epsilon}$ are not functions of the order parameter ϕ and only when considering the Pauli limited case (strong magnetic field) are they functions of the magnetic field. Pauli limiting is beyond the scope of this thesis and will not be discussed further. The order parameter, however, is dependent on the magnetic field. The formalism adapted here to treat the order parameter, is closely related to that of Scharnberg and Klemm [Scharnberg and Klemm 1980] in which the pairing potential is not a delta function (contact potential) in real space. The order parameter is given by [Prohammer and Carbotte 1990]

$$\Phi(R,\mathbf{k};i\omega_n) = -T\sum_{q,m} I^2\chi(\mathbf{k}-q;\omega_n-\omega_m)\xi(R,q,i\omega_m) \times \Phi(R,q;i\omega_m), \tag{2.64}$$

where $I^2\chi(\mathbf{k}-\mathbf{q};\omega_n-\omega_m)$ plays the role of the boson pairing potential previously labeled $\lambda(\mathbf{k},\mathrm{q},\mathrm{n}-\mathrm{m})$ and ξ is given by

$$\xi(\mathrm{R},\mathrm{q},i\omega_n) = \int d^w y \int d^w z\, e^{iq\cdot(y-z)}\, G^0(y;i\omega_n) \times G^{0*}(z;i\omega_n)\, e^{iz.\Pi(R)} \tag{2.65}$$

and $\Pi(\mathbf{R})$ is related to the magnetic field $\mathbf{H}$ through the vector potential $\mathrm{A}(\mathbf{R})$ and is given by

$$\Pi(\mathrm{R}) = \frac{1}{i}\nabla_R + 2eA(R), \tag{2.66}$$

e is the change of the electron. The dimensionality of the system is w, in equation (2.65), and $G^0(y,i\omega_m)$ refers to the one particle Green's function in the normal state defined by

$$G^0(y;i\omega_m) = \sum_{\mathbf{k}} \frac{e^{i\,\mathbf{k}.\mathbf{y}}}{i\tilde{\omega}_m-\tilde{\epsilon}_k}. \tag{2.67}$$

At this stage, we will deviate from the standard procedure generally followed in manipulating equation (2.64) to reach an eigenvalue equation for the upper critical field Hc_2. The new approach is as follows: first, we rewrite equation (2.65) as,

$$\xi(\mathbf{R},\mathrm{q};i\omega_m) = \sum_{\mathbf{k}\mathbf{k}'} \int d^w y \int d^w z\, e^{iq\cdot(y-z)}$$

$$\times \frac{e^{i\mathbf{k}\cdot\mathbf{y}}}{\tilde{\epsilon}_k-i\tilde{\omega}_m}\, \frac{1}{\tilde{\epsilon}_{k'}+i\tilde{\omega}_m}\, e^{-\nabla_{\mathbf{k}'}.\Pi(R)}\, e^{-i\mathbf{k}'.z} \tag{2.68}$$

and we use the identity $\int_0^\infty dt\, e^{-zt}=z^{-1}\ \forall\ \mathrm{Re}\ z>0$, to write $(\epsilon_{k'}+i\tilde{\omega}_m)^{-1}=-is_m$

$\int_0^\infty dt\, e^{(-|\tilde{\omega}_m|+is_m\epsilon_{k'})t}$, and s_m=sign $\tilde{\omega}_m$. Second, we integrate by parts with respect to k′ to switch positions among the exponents $-i\mathbf{k}'.\mathbf{z}$ and $-is_m\, \bar{\epsilon}_{k'}t$, and ignore the surface part since it is equal to zero, see [Scharnberg and Klemm 1980, appendix B].

$$\xi(\mathrm{R},\mathrm{q};i\omega_m) = \sum_{\mathbf{kk}'} \int d^w y \int d^w z\, e^{i\mathbf{q}.(\mathbf{y}-\mathbf{z})} \frac{e^{i\mathbf{k}\,.\,\mathbf{y}}}{\bar{\epsilon}_k - i\tilde{\omega}_m}$$

$$\times\; e^{-i\mathbf{k}'.\mathbf{z}}\, e^{\nabla_{\mathbf{k}'}.\Pi(\mathrm{R})} \left(-is_m \int_0^\infty dt\, e^{(-|\tilde{\omega}_m|+is_m\bar{\epsilon}_{k'})t}\right). \tag{2.69}$$

Last, we operate with $\nabla_{k'}$ on $\epsilon_{k'}$ and do the spatial integrations followed by the summations over **k** and **k**′, then equation (2.69) becomes,

$$\xi(\mathrm{R},\mathrm{q};i\omega_m) = \frac{-is_m}{\tilde{\epsilon}_q - i\tilde{\omega}_m} \int_0^\infty dt\, e^{-is_m t\nabla_q\tilde{\epsilon}_q.\Pi(\mathrm{R})}\, e^{(-|\tilde{\omega}_m|+is_m\tilde{\epsilon}_q)t}, \tag{2.70}$$

noting that we took advantage of some symmetries like $\tilde{\epsilon}_{-q} = \tilde{\epsilon}_q$ and $\nabla_q\tilde{\epsilon}_q = -\nabla_{-q}\tilde{\epsilon}_q$.

The procedure carried out so far is independent of dimensionality w as well as parity. The sum over q in equation (2.64) can be converted into an energy integral $\Sigma_q = \int d\Omega/\Omega_0 \times \int N(\epsilon)d\epsilon$, and hence only the energy integral can be done independent of the parity of the order parameter provided a separable model for the pairing potential and the order parameter is used. We will not work out this problem in this chapter. Instead, we will treat it generally, independent of parity and dispersion choices, for a magnetic field **H** along, say, the z–direction which in two dimensions is perpendicular to the conducting plane. The vector potential is calculated from $\mathbf{A}=1/2\ \mathbf{H}\times\mathbf{R}$ and applies only to continuous systems. A stack of conducting sheets cannot be handled this way, and are outside the scope of this thesis. For a constant field $\mathbf{H}=H\hat{z}$ equations (2.64) and (2.70) combine into

$$\Phi(R,k;i\omega_n) = +\,T \sum_{q,m} \frac{is_m}{\tilde{\epsilon}_q - i\,\tilde{\omega}_m}\, I^2\chi(k-q;n-m) \int_0^\infty dt\, e^{-\frac{\alpha_1}{2}t^2(\nu_1^2(q)+\nu_2^2(q))}$$

$$\times\, e^{(-|\tilde{\omega}_m|+is_m\tilde{\epsilon}_q)t}\ \times\, e^{-is_m t a_q^* B^+}\ e^{-is_m t a_q B}\ e^{is_m t\nu_3(q)}\ \frac{\partial}{\partial R_3} \times \Phi(\mathbf{R},q;i\omega_m), \qquad (2.71)$$

with $\alpha_1=eH$, $a_q=[\nu_1(q)+i\nu_2(q)]\sqrt{\alpha_1}$, $\nu_i(q)=\partial/\partial q_i\epsilon_q$ $i=1,2,3$ such that 1 and 2 are labels for two orthogonal vectors in the x–y plane, $\nu_3=0$ for two dimensions, and finally $B(B^+)$ is a lowering (raising) operator for an harmonic oscillator in two dimensions. It is natural to express the order parameter in terms of generalized Abrikosov solutions Φ_N [Abrikosov 1957] and to separate its frequency and parity dependence (implicit in **q**) from the spatial varying part. The order parameter is expanded as follows:

$$\Phi(\mathbf{R},\mathbf{k};i\omega_m) = \sum_{Nk} b_N^{k_3}\, \Delta(k;i\omega_m)\Phi_N(R_1,R_2)\, e^{ik_3R_3}\ , \qquad (2.72)$$

and for largest eigenvalue, we choose $k_3=0$, and equation (2.71) now becomes

$$b_L^0\,\Delta(\underline{k};i\omega_n) = +\,T\sum_{q,m}\frac{is_m}{\bar{\epsilon}_q - i\tilde{\omega}_m}\,I^2\chi(\mathbf{k}-\mathbf{q};n-m)$$

$$\times\int_0^{\infty} dt\; e^{\frac{-\alpha_1}{2}t^2(\nu_1^2(q)+\nu_2^2(q))}\; e^{(-|\tilde{\omega}_m|+is_m\bar{\epsilon}_q)t}$$

$$\times\,\Delta(q;i\omega_m)\left\{\sum_{N=0}^{\infty}\;\sum_{j=\max(N-L,0)}^{j=N}\frac{(-is_m t\,a_q^{*})^{L-N+j}}{(L-N+j)!}\,\frac{(-is_m\,t\,a_q)^{j}}{j!\,(N-j)!}\right.$$

$$\left.\times\,(L!N!)^{1/2}\,b_N^0\right\}. \qquad (2.73)$$

To get Hc_2, one has to solve equation (2.73) for its highest eigenvalue. The symmetries of the pairing potential, order parameter, and the system (i.e. crystal of particular structure) which is usually reflected in the type of the dispersion can reduce the number of integrals by a great number, for example in the free electron gas model with an s–wave order parameter equation (2.73) is diagonal, since when performing the angular integration of q, only the diagonal integrals are nonzero.

VI) Summary

We have given a derivation of the Eliashberg equations on the imaginary axis for both the normal and superconducting states appropriate to finite bands, equation (2.9a–c). We have also included impurity scattering up to Born approximation for both normal and magnetic impurities, equations (2.13a–c). We have considered normal impurity resonance scattering for which the Eliashberg equations take the form presented in equations (2.26a–c). We have also presented analytic derivation of the free energy difference between the normal and superconducting states for all the cases mentioned above. The free energy difference is given by the Bardeen–Stephan formula, equation (2.35), for all the cases except for the normal impurity resonance scattering. With resonance scattering, an extra term is added to the Bardeen–Stephan formula and this extra term is given by equation (2.47). We have also developed a new formula for the London penetration depth, equation (2.58), which is appropriate to finite bands and all types of impurity scatterings considered above. We have derived a new formula for the eigenvalue value problem for Hc_2 which is also very different in form from previous treatments and is very general as well, equation (2.73). We have shown that the free energy and penetration depth formulas reduce to the known ones appropriate for infinite band with constant EDOS. Similar reductions for equation (2.73) are shown in detail in Appendix B.

Chapter 3

Critical Temperature, Free Energy and the Gap

I) Introduction

After the discovery of the high temperature superconductors (HTSC) and the determination of large anisotropy in the electric conductivity tensor, there have been several attempts to correlate the high transition temperature T_c to an anomalously large, two–dimensional (2D), electronic density of states (EDOS) near the Fermi level of these cuprates. As mentioned in Chapter 1, a 2D tight binding conductor has a van Hove singularity (vHs) in its EDOS. This vHs diverges logarithmically near the peak and, hence, can be approximated by a logarithmic function. Early band structure calculations showed that the Fermi level of these cuprates crosses antibonding p–oxygen bands and, hence, most of the electronic properties are dominated by the oxygen character in the CuO_2 layers, apart from strong correlation effects coming from the copper ions [L. Mattheis 1987; A.J. Freeman 1987]. Several authors utilized the vHs in the EDOS within the BCS formalism to calculate T_c [Labbe and Bok 1987; Friedel a,b 1987; Combescat and Labbe 1988; Labbe 1989; Markiewic and Giessen 1989; Markiewic 1990; Tsuei et al.

1990; Newns et al. 1992; Tsuei et al. 1992]. Combescot and Labbe showed that T_c correlates with part of the EDOS (coming from the CuO_2 layers) at the Fermi level N(0). They compared L214 (T_c=37K) with Y123 (T_c=93K) and assumed that the coupling strength, V, is the same for both of them. The CuO_2 layer, one in L214 and two in Y123, has a tight binding dispersion of the form,

$$\epsilon_k = 2\, t_1\, (2 - \cos k_x a - \cos k_y a) \tag{3.1}$$

with $t_1 \sim 0.5$ eV, while the CuO chain in Y123 has a dispersion of the form,

$$\epsilon_k = 2\, t_2\, (1 - \cos k_x a) + 2\, t_3 \tag{3.2}$$

with $t_3 > t_2 \sim t_1$.

The EDOS near the vHs in the planes is

$$N_p(\epsilon) \sim \frac{N}{2\pi^2 t_1}\, \ell n \left| \frac{16 t_1}{\epsilon - 4 t_1} \right| , \tag{3.3}$$

where N is the number of copper atoms in the plane, and for the chain the EDOS (near the chain's vHs) is

$$N_c(\epsilon) \sim \frac{N}{2\pi t_2} \left[\frac{\epsilon - 2t_3}{t_2} \right]^{-1/2} . \tag{3.4}$$

Combescot and Labbe showed that the higher total EDOS, N_t, for Y123 leads to higher T_c~94K, independent of the pairing interaction V [Combescot and Labbe 1988], where N_t is given by

$$N_t = 2\,N_p(\epsilon) + N_c(\epsilon). \tag{3.5}$$

Another group (IBM Research Division) used a different type of dispersion with saddle points in the energy surface for the band structure to get a logarithmic vHs. This dispersion has the following form

$$\epsilon_k = \frac{k_x k_y}{m}, \quad |k_x|, |k_y| < k_c. \tag{3.6}$$

This type of vHs, at $k_x = k_y = 0$, does not have the nesting problems associated with the simple tight binding dispersion, equation (3.1). The EDOS near the saddle point can be approximated by

$$N(\epsilon) = \frac{1}{2D}\,\ln\left|\frac{D}{\epsilon-\delta}\right|, \quad \text{with} \quad D = \frac{k_c^2}{m} \tag{3.7}$$

and δ is the chemical potential. Analytic calculations of T_c and the isotope effect β gave very encouraging results. The isotope effect has a minimum at $\delta=0$ which corresponds to a maximum in T_c. The shape of the T_c versus hole doping curve is Gaussian–like and is given by

$$T_c(\delta) = 1.36\,D\,\exp\left\{-\left[a+\delta^2\left[\frac{1}{8T_c^2} + \frac{1}{\omega_D^2}\right]\right]^{1/2}\right\} \tag{3.8}$$

where

$$a = \frac{4D}{V} + \left[\ln\frac{D}{\omega_D}\right]^2 - 1, \tag{3.9}$$

which is a constant independent of doping. These results correlate very well with the shape of T_c and β vs hole doping in the HTSC's [Newns et al. 1992].

The density of states effect is not the only route to high T_c. In principle, there is no upper limit on T_c within the framework of Eliashberg theory. In the asymptotic limit where the electron phonon coupling λ is very high, T_c is directly proportional to $\sqrt{\lambda}$ [Carbotte 1990]. Yet there is no reason to believe that the HTSC's have large λ simply because of the low density of carriers. Furthermore, calculations within the Eliashberg formalism with a constant EDOS do not show any agreement between theory and experiment, especially for the specific heat jump $\Delta\ C_v(T_c)$, the slope of the jump at T_c, the isotope effect, and the shape of T_c curve vs doping [Akis 1991]. This scenario is unusual considering the fact that Eliashberg theory is very accurate and well suited to conventional superconductors [Carbotte 1990]. Extension of the vHs model in the EDOS, equation (3.7), to the Eliashberg formalism seems to be the next logical step to account for other effects such as retardation and realistic pairing potential. It turns out that the mere inclusion of retardation has a profound effect on both T_c and the isotope effect. It was found that T_c is reduced by a factor of ~1–3 and the minimum isotope effect β gets pushed up to a much higher value by retardation effects [Carbotte and Akis 1992; Newns et al. 1992].

Retardation smears out the vHs in EDOS, giving a smaller and a broader effective density of states. This point will be further clarified at the end of the next section. In conventional BCS theory β is one half and with a vHs in the EDOS β_{min} is about 0.2 at maximum T_c [Tsuei et al. 1990]. For our particular vHs model, β_{min} is about 0.35 for a reasonably weak coupling case. The minimum experimental isotope effect is –0.1 [J. P. Franck 1994]. Inspite of this poor agreement, we nevertheless investigate the vHs model further and study its effects on T_c and β, as well as extend it to $T<T_c$ to study the gap ratio $2\Delta/T_c$, the free energy and the thermodynamic critical field. In the next section, we will present our model of EDOS which is appropriate for this. We will present all the formulas used to calculate our results, including the Eliashberg equations for both the normal and superconducting states and the free energy formula. We will present our calculations on T_c and β in Section III, including normal impurity effects. Section IV contains the gap ratio results and our results on the thermodynamic critical field. Experimental comparison will be made in Sections III and IV, and conclusions in Section V.

II) The model of EDOS and the appropriate Eliashberg equations

In Eliashberg theory, the EDOS is considered to be a constant around the Fermi energy and, because of damping effects from the Green's functions, this constant value N(0) is extended over the whole energy range. In normal metals, the width of the electronic energy band is large compared to the scale of energy inducing superconductivity, ω_D or ω_E. The general practice is to integrate the energy from $-\infty$ to ∞ in equations (2.9a–c), making use of equation (2.17) to convert the sum over $\underline{k}$ to an energy integration. The pairing interaction $\lambda(n-m)$ is assumed to be isotropic, so the angular integration is normalized to unity. We need a model for the density of states $N(\epsilon)$ to be used in equation (2.17). Our choice of the EDOS $N(\epsilon)$ is slightly different from equation (3.7) and has the following form:

$$N(\epsilon) = N_b \left[r - \frac{s}{(\epsilon-\delta)^2+D^2} \ln \left| \frac{\epsilon-\delta}{E_f} \right| \right]. \tag{3.10}$$

We have introduced a background EDOS proportional to r, in addition to the vHs which is proportional to s. The width of the logarithmic divergence is scaled to E_f. We introduce a damping function, Lorentzian with a width of 4D, to ensure that $N(\epsilon) \geq 0 \ \forall \ \epsilon$ and to be able to change the width of the peaked EDOS. Recall that Y123 has CuO chain which has a square root singularity of width less than the width of the simple logarithmic singularity of the CuO_2 planes. Equation (3.10) models Y123 for $D<<E_f$ and L214 for $D \lesssim E_f$. In all of our calculations presented in this chapter, the values assumed for the parameters in equation (3.10) are D=40 meV, E_f=500–800 meV, r=0.5–1.0 and in most cases, s=1600 meV. A typical plot of equation (3.10) was shown in the lower frame of Figure (1.2). Carrying out the energy integration in Eliashberg equations (2.13a–b), we get

$$\tilde{\omega}_n = \omega_n + \pi T \sum_{m=-\infty}^{\infty} \lambda(n-m) \frac{\tilde{\omega}_m}{x_m} \hat{N}(x_m,\delta)$$

$$+ \pi (t^{+}+t^{-}) \frac{\tilde{\omega}_n}{x_n} \hat{N}(x_n,\delta) \tag{3.11}$$

$$\phi_n = \pi T \sum_{m=-\infty}^{\infty} [\lambda(n-m) - \mu^{*} \theta(\omega_c - |\omega_m|)] \frac{\phi_m}{x_m} \hat{N}(x_m,\delta)$$

$$\pi (t^{+}-t^{-}) \frac{\phi_n}{x_n} \hat{N}(x_n,\delta) \tag{3.12}$$

where

$$x_n = \begin{cases} |\tilde{\omega}_n| & \text{normal state and } T_c \text{ equation} \\ \sqrt{\tilde{\omega}_n^2+\phi_n^2} & \text{superconducting state} \end{cases} \tag{3.13}$$

and

$$\hat{N}(a,b) = r - \frac{s}{2D}\left\{\frac{(a+D)\ell n\left[\frac{D\sqrt{b^2+a^2}}{Ef^2}\right] + b\ \tan^{-1}\left[\frac{b}{a}\right]}{b^2 + (a+D)^2}\right.$$

$$\left. - \frac{(a-D)\ell n\left[\frac{D}{\sqrt{b^2+a^2}}\right] - b\ \tan^{-1}\left[\frac{b}{a}\right]}{b^2 + (a-D)^2}\right\} \tag{3.14}$$

where

$$\theta(x) = \begin{cases} 1 & x \geq 0 \\ 0 & x < 0 \end{cases} \tag{3.15}$$

and

$$\lambda(n-m) = \int_0^{\infty} d\Omega\, \frac{2\Omega\ \alpha^2F(\Omega)}{\Omega^2+(\omega_n-\omega_m)^2}\,. \tag{3.16}$$

We have ignored the effect of the chemical potential equation, equation (2.13c). This is because self–consistent calculations with this equation modify the chemical potential, denoted by δ. The change of chemical potential implies a change in the number of particles for a fixed volume.

Physically then, as the temperature changes the density of particles changes. To prevent this from happening we must introduce a constraint on the chemical potential. In practice, in a self consistent calculation the difference in number densities between fully interacting and non–interacting particles is held constant and referenced to its value at zero temperature. This is more complicated than just using equations (3.11) and (3.12) alone. We choose to ignore this effect especially at T_c and absorb its effects in δ, since δ is a variable. Furthermore, for our particular model of $N(\epsilon)$, the particle hole symmetry is valid for $\delta=0$ and $\delta>>E_f$ or D, so this effect is zero. The free energy difference between the superconducting state and the normal state is easily calculated from equation (2.36). The free energy difference for our particular model of $N(\epsilon)$, given by equation (3.10), has the following form

$$\Delta\Omega_{BS} = \frac{-2N_b}{\beta} \sum_{n=1}^{\infty} \Bigg\{ 2\pi \left[\sqrt{\tilde{\omega}_n{}^2 + \phi_n^2} - \tilde{\omega}_n^0 \right]$$

$$-s \int_{-\infty}^{\infty} \frac{\ell n \left| \frac{\epsilon-\delta}{E_f} \right|}{(\epsilon-\delta)^2+D^2} \, \ell n \left[\frac{\epsilon^2 + \tilde{\omega}_n^2 + \phi_n^2}{\epsilon^2 + \tilde{\omega}_n^{0\,2}} \right] d\epsilon$$

$$- \pi \frac{\tilde{\omega}_n(\tilde{\omega}_n - \tilde{\omega}_n^0) + \phi_n^2}{\sqrt{\tilde{\omega}_n + \phi_n^2}} \hat{N} \left(\sqrt{\tilde{\omega}_n + \phi_n^2}, \delta \right)$$

$$+ \pi (\tilde{\omega}_n^0 - \tilde{\omega}_n) \hat{N}(\tilde{\omega}_n^0, \delta) \Bigg\} , \qquad (3.17)$$

and the energy integration is handled numerically.

The generalization of the imaginary axis Eliashberg equations to include a nonconstant EDOS was done previously in an attempt to explain some properties of the A15 compounds. A Lorentzian peak, with adjustable height and width, superimposed on a constant background was utilized as a model for the EDOS [Lie and Carbotte 1978, a,b, 1980; Lie, Daams and Carbotte 1978; Mitrovic and Carbotte a,b 1983; Picket 1980; Schachinger, Mitrovic and Carbotte 1982]. Also recently, only the linearized (normal state) Eliashberg equations were generalized to include an undamped vHs, equation (1.4), where it was found that strong coupling effects and high temperature conspire to reduce the effective density of states $\hat{N}$ in the imaginary axis equations compared to its value at zero temperature. To see this clearly, consider $\hat{N}(\tilde{\omega}_n)$ for $N(\epsilon)$ coming from equation (1.4), which has the form

$$\hat{N}(\tilde{\omega}_n) = r - \frac{s}{2} \ln \left[\frac{\tilde{\omega}_n^2+\delta^2}{E_f^2}\right] \tag{3.18}$$

and peaks for small values of $\tilde{\omega}_n$. We notice here that $\tilde{\omega}_n \sim \pi T(2n+1)[1+\lambda(n)]$, and even if one chooses to take $\lambda(n)=0$, the BCS case, then the smallest $\tilde{\omega}_n$ is $\omega_0=\pi T$ and the next higher value is $\omega_1=3\pi T$ etc. . $\hat{N}$ is a decreasing function in both T and retardation ,i. e. the inclusion of all n up to the cut off actually reduces the effective density of states. In other words, the peak in the density of states is blurred and lowered in magnitude by high temperature. Retardation effects are smaller near T=0, and hence the EDOS effects are strongly reflected in quantities evaluated at zero temperature like the gap Δ_0 and the thermodynamic field $H_c(0)$, as we will show in this chapter.

III) The transition temperature T_c and the isotope effect β

In this section, we present our calculations of T_c and β on two different types of spectral densities: $\alpha^2F(\omega)$ of lead and a delta function at an Einstein frequency ω_E. Both calculations are done numerically where we solve for the largest eigenvalue associated with the eigenvector ϕ_n of the normal state Eliashberg equations, equations (3.11) and (3.12). The isotope effect β is given by

$$\beta = \frac{d\ \ell n\ T_c}{d\ \ell n\ M}, \tag{3.19}$$

where we vary the ion mass M by varying $\alpha^2F(\omega)$.

In the lower frame of Figure (3.1), we show that the isotope effect β is minimum when the Fermi level is on the vHs, δ=0, rises to a higher value than in BCS theory (β=1/2), and finally drops to a saturated value close to the BCS value as the chemical potential sweeps away from the centre of the vHs. A scaled lead spectrum for $\alpha^2F(\omega)$ was used to calculate T_c and β in Figure (3.1) with the following EDOS parameters: D=40 meV, Ef=1500 meV, s=1600 $(\mathrm{meV})^2$ and r=1.0. The T_c curves are Gaussian shaped, centred on δ=0, and superimposed on a constant background. The variation of δ is achieved experimentally by chemical doping, substitution, or even by applying hydrostatic pressure. The asymptotic limit $\delta\rightarrow\infty$ for the T_c curves comes directly from the constant background of density of states. The widths of the Gaussian peaks in Figure (3.1) depend strongly on the coupling strengths. The coupling strength is given by λ or $T_c/\omega_{\ell n}$ where $\omega_{\ell n}$ is called the Allen–Dyne parameter and is given by

$$\omega_{\ell n} = \exp\left\{\frac{2}{\lambda}\int_0^\infty d\Omega\,\frac{\ell n\Omega}{\Omega}\,\alpha^2F(\Omega)\right\} \tag{3.20}$$

with

$$\lambda = \lambda(0) = 2\int_0^\infty d\Omega\,\frac{\alpha^2F(\Omega)}{\Omega}\,. \tag{3.21}$$

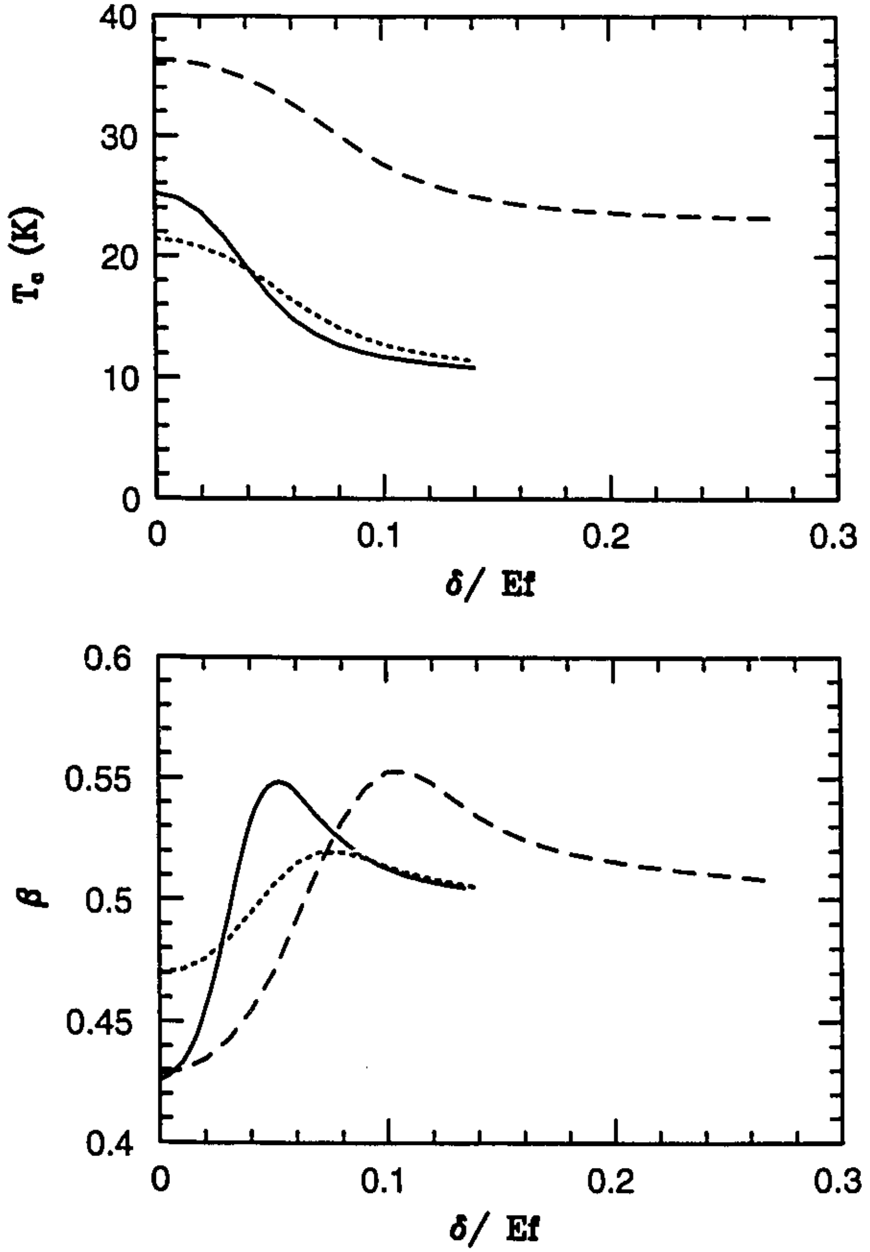

Figure 3.1: Upper frame, critical temperature T_c vs. chemical potential δ for a lead spectrum $\alpha^2F(\omega)$ (solid curve) and with t^+=5 meV (dotted curve) and $3\alpha^2F(\omega)$ (dashed curve). The lower frame shows the isotope effect β vs. δ for the same set of curves in the upper frame. EDOS parameters are: s=1600, r=1.0, D=40, δ=0, and E_f=1500.

In the BCS limit both λ and $T_c/\omega_{\ell n} \to 0$.

Our particular choice of $T_c/\omega_{\ell n}$ for all the calculations is $T_c^a/\omega_{\ell n}$, where T_c^a is the asymptotic ($\delta \to \infty$) limit of the transition temperature T_c. The solid curve, $T_c^a/\omega_{\ell n}=0.2$, shows an enhancement of T_c at $\delta=0$ of 150% over the asymptotic value, $T_c^a=10.5$ K. Upon scaling $\alpha^2F(\omega)$ by a factor of 3, λ is increased by the same factor and T_c^a doubles (dashed curve, $T_c^a/\omega_{\ell n}=0.4$) and the width of the Gaussian peak of the T_c curve increases. The maximum enhancement of T_c is only 53%, however. The flatness of the dashed curve in the upper frame of Figure (3.1) is qualitatively consistent with the universal relationship between T_c and the hole content in p–type cuprates [Zhang and Sato 1993]. Such an experimental effect might arise, however, from pinning of the Fermi level to the vHs associated with strong correlation effects. The isotope effect at δ=o increases only slightly for $T_c^a/\omega_{\ell n}=0.4$ over that for $T_c^a/\omega_{\ell n}=0.2$, yet the value of δ at which $\beta=1/2$ is much higher and roughly corresponds to the width of the Gaussian peak in the T_c curve. These isotope effect curves are not universal and it would be more meaningful to plot them against T_c. Another point is that if real materials are not pure and contain nonmagnetic defects, such as impurities or some other type of disorder, then the vHs effect is modified for both T_c and β. The parameters of the dotted line in Figure (3.1) are identical to those of the solid line in the same figure but with some normal impurities added, $t^+=5$ meV. The maximum enhancement of T_c is only 110%, compared to 150% in the pure case (solid line). The width of the T_c peak is increased and the T_c curve crosses that of the pure case at large δ. This is a sign of EDOS smearing, where the peak in the vHs gets reduced and the background far away from the singularity gets increased. The local minimum and maximum in the isotope effect curve are pushed up and down respectively, and at sufficiently high

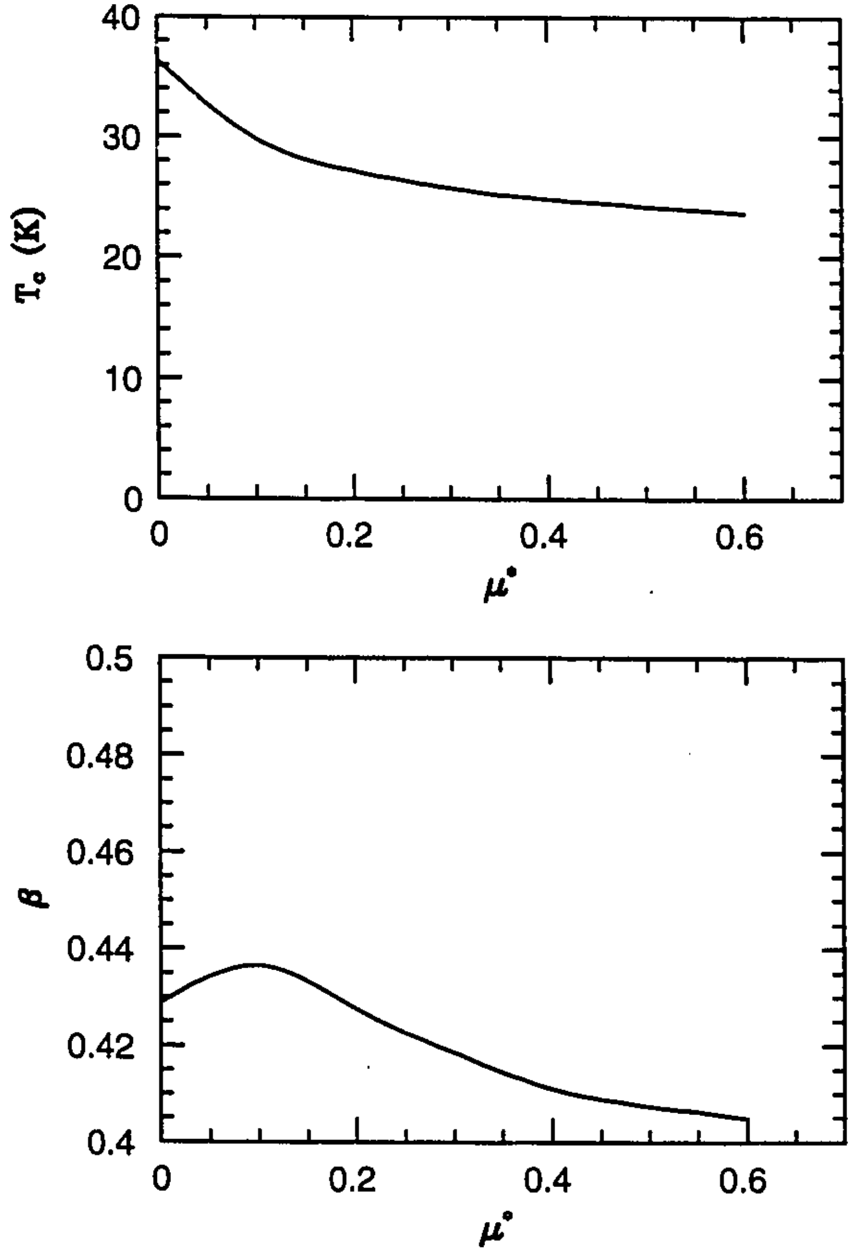

Figure 3.2: The critical temperature T_c (upper frame) and isotope effect β (lower frame) vs μ^* for $\alpha^2F(\omega)$ equals three times that of lead. EDOS parameters are: s=1600, D=40, r=1.0, δ=0, and E_f=1500.

impurity concentration both will collapse to $\beta=1/2$. The calculations presented in Figure (3.1) are for $\mu^*=0.0$ where as typically in real systems there is a finite positive μ^* on the order of 0.1–0.2. This value could be even higher in the cuprates because of less screening. In Figure (3.2), we calculate T_c and β for one point at $\delta=0$ from the dashed curve in Figure (3.1). We notice only small effects on T_c and β upon increasing μ^*; the largest drop in T_c occurs in the interval $0\leq\mu^*\leq 0.2$. The isotope effect changes slowly to reach a minimum value of 0.405 at $\mu^*=0.6$. The β dependence of Figure (3.2) is qualitatively different from the behaviour of that given by the McMillan equation [Allen and Dynes 1975];

$$\beta = \frac{1}{2}\left[1 - \frac{1.04(1+\lambda)(1+0.62\lambda)}{[\lambda-\mu^*(1+0.62\lambda)]^2}\,\mu^{*2}\right], \tag{3.22}$$

which has a maximum β for $\mu^*=0$. This is not surprising since equation (3.22) is only an approximation for Eliashberg theory with no vHs. Since the effect of μ^* is very small, we will adopt a zero value for μ^* in all our calculations.

We can use functional derivative techniques to achieve a better understanding of the isotope effect. The isotope effect β can be calculated from the following expression

$$\beta = \int_0^\infty \beta(\omega)\mathrm{d}\omega, \tag{3.23}$$

where $\beta(\omega)$ is the differential isotope effect given by [Rainer and Culetto 1979]

$$\beta(\omega) = \alpha^2 F(\omega)\, R(\omega) \tag{3.24}$$

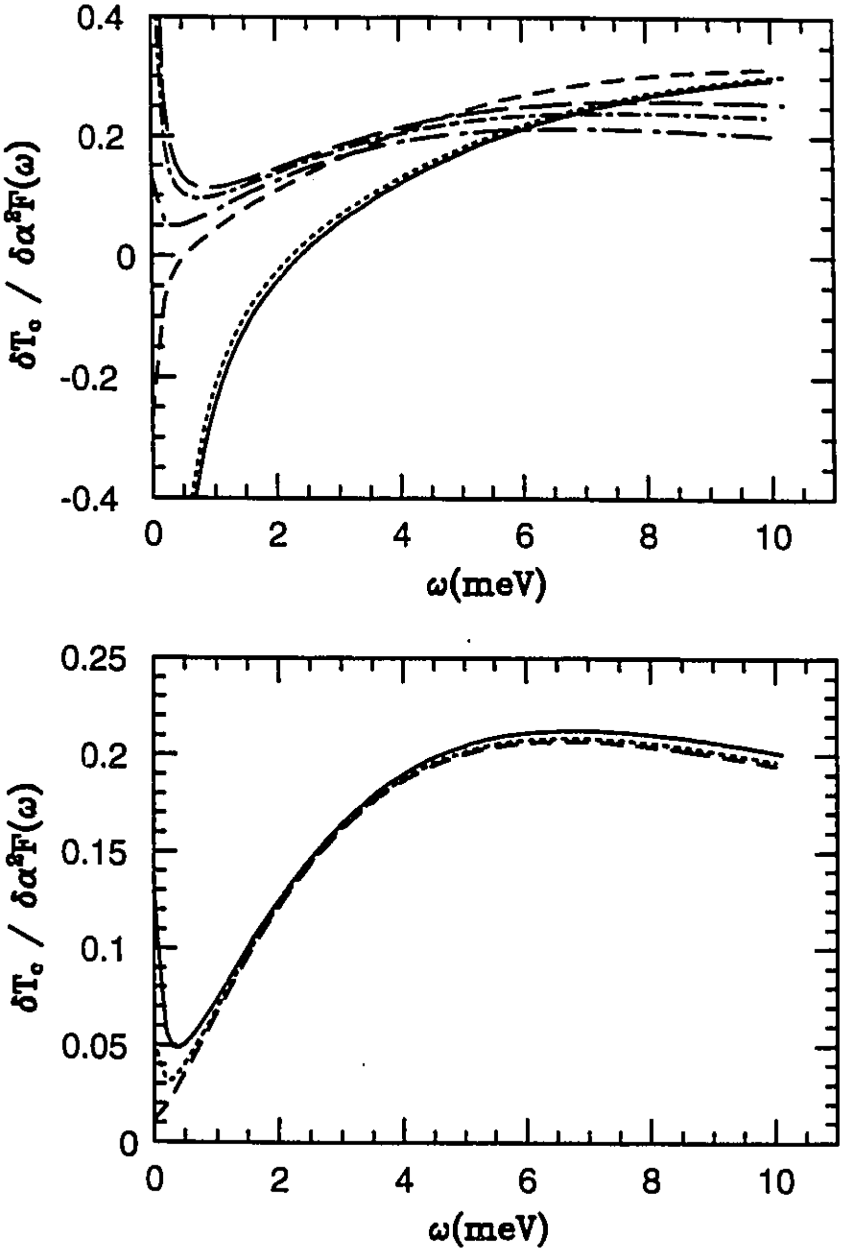

Figure 3.3: Functional derivative of T_c w.r.t. $\alpha^2F(\omega)$. In the upper frame, δ=0 (solid), δ=1.0 (dotted), δ=40 (dashed), δ=80 (long dashed), δ=100 (dotted dashed), and δ=200 meV for (dotted long dashed curve). In the lower frame, δ=200 (solid), δ=300 (dotted), and δ=500 meV (dashed curve). EDOS parameters are s=800, r=1.0, D=40 and E_f=1500.

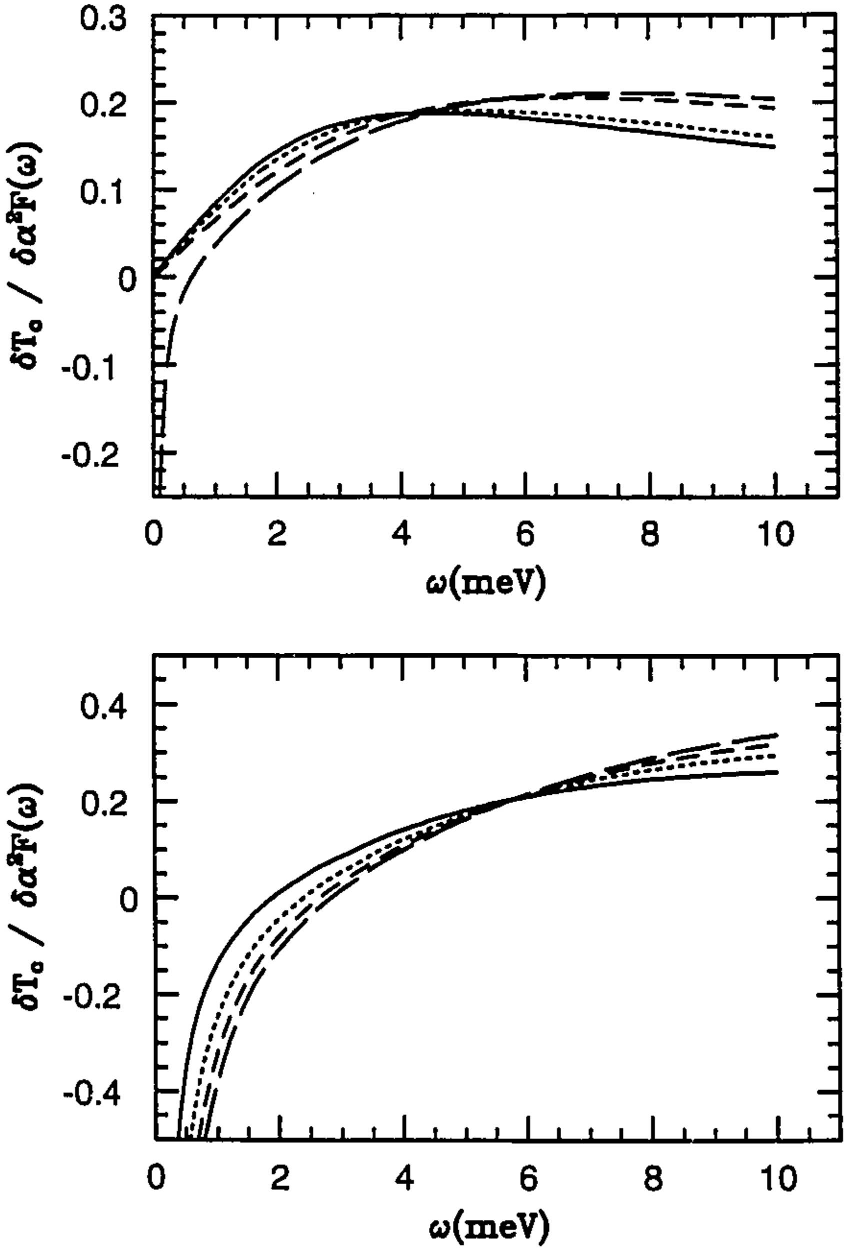

Figure 3.4: Functional derivative of T_c w.r.t. $\alpha^2F(\omega)$. In the upper frame, s=0 and $\mu^*=0.1438$ (solid), s=0.0 and $\mu^*=0.1$ (dotted), s=0 (dashed), and s=40 (long dashed curve) and $\mu^*=0$ for both curves. In the lower frame ($\mu^*=0$), s=400 (solid), s=800 (dotted), s=1200 (dashed), and s=1600 (long dashed curve), all with EDOS parameters of 4=1.0, D=40, $\delta=0$ and $E_f=1500$.

with

$$R(\omega) = \frac{1}{2T_c} \frac{\delta T_c}{\delta \alpha^2 F(\omega)} + \frac{\omega}{2T_c} \frac{d}{d\omega} \frac{\delta T_c}{\delta \alpha^2 F(\omega)} \, . \tag{3.25}$$

In Figure (3.3), we show the functional derivative of T_c with respect to $\alpha^2F(\omega)$ of lead, $\delta T_c/\delta\alpha^2F(\omega)$, with EDOS parameters r=1.0, E_f=1500 meV, D=40 meV, and s=800 $(\text{mev})^2$. If we neglect the second term in equation (3.25), we can see that there will be a net reduction of the isotope effect for δ=0 (solid curve) because $\delta T_c/\delta\alpha^2F(\omega) < 0$ for small ω. For δ=10 meV, $\delta T_c/\delta\alpha^2F(\omega)$ is slightly displaced to the left (dotted curve) and hence the isotope effect β should increase slightly which is in agreement with the results presented in Figure (3.1). For δ=80 meV, $\delta T_c/\delta\alpha^2F(\omega)$ develops a positive peak near small ω and hence the isotope effect exceeds the BCS value in accordance with Figure (3.1) (solid curve at $\delta/\text{Ef} \sim 0.05$.) As δ increases further (upper and lower frames of Figure (3.3)), the value of the peak in $\delta T_c/\delta\alpha^2F(\omega)$ near small ω gets even smaller and we expect β to decrease further, approaching the appropriate strong coupling value given by the constant background of the EDOS. In Figure (3.4), we show the evolution of $\delta T_c/\delta\alpha^2F(\omega)$ as the weight s of the vHs in the EDOS is varied. As s is switched on, a negative well in $\delta T_c/\delta\alpha^2F(\omega)$ develops near $\omega \to 0$. The well becomes wider and deeper as s increases. It is clear that the reduction of β is dominated by the small–frequency behaviour of $\delta T_c/\delta\alpha^2F(\omega)$. This may stem from a higher effectiveness for the low frequencies in $\alpha^2F(\omega)$ to increase λ, and hence produce more retardation effects. Retardation is expected to reduce the peak, smear it out and, decrease T_c. Similarly, when δ is outside the peak of the EDOS, retardation increases the effective local density of states at the Fermi level and T_c increases as a result.

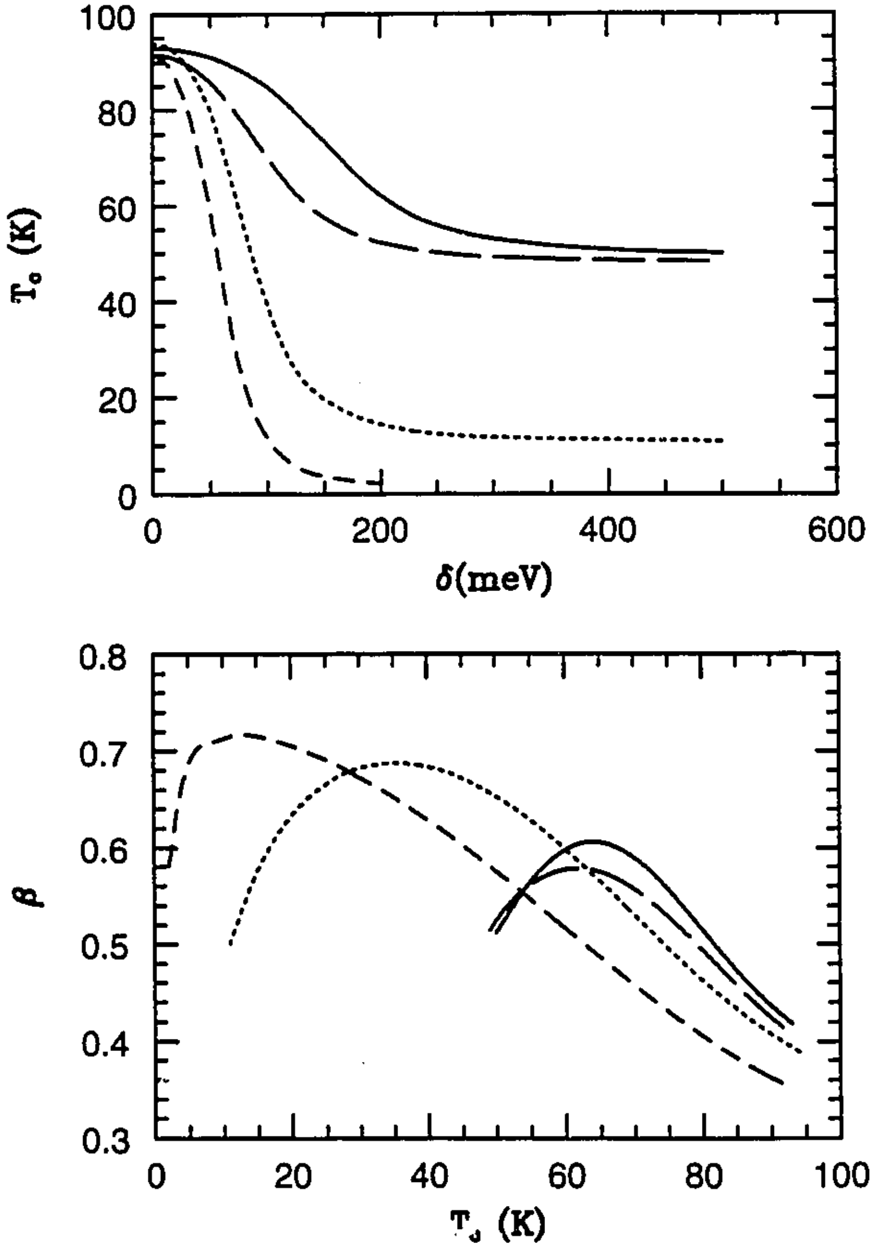

Figure 3.5: Critical temperature vs chemical potential δ (upper frame) and the isotope effect vs critical temperature (lower frame) for Einstein spectra centred on ω_E=20 (solid), ω_E=40 (dotted), ω_E=60 (dashed) with r=0.5 and E_f=800 and ω_E=30 meV (long dashed curve) with r=1.0 and E_f=500. The common EDOS parameters are s=1600 and D=40.

In Figure (3.5), we plot T_c and β for an Einstein spectral function. Density of states parameters are specified in the figure caption. The upper frame of Figure (3.5) clearly shows that enhancement of T_c is greatest for $T_c^a/\omega_{\ell n}$=0.0019 (dashed line) and is of the order of 71 times T_c^a, while for an intermediate case $T_c^a/\omega_{\ell n}$=0.0226 (dotted line) is only 8 times T_c^a, despite the fact that these two lines and the solid line have the same EDOS parameters. On the other hand, the enhancement of T_c^a for the strong coupling cases is ~ 85% for both the solid curve, $T_c^a/\omega_{\ell n}$=0.215 and long dashed curve, $T_c^a.\omega_{\ell n}$=0.135. Any isotropic mechanism invoked to explain the high T_c must be associated with weak coupling strengths so as to take full advantage of non–smeared EDOS. In the lower frame of Figure (3.5), we plot the isotope effect against the transition temperature T_c for the same set of curves shown in the upper frame. It is clear that the isotopic effect is minimized at maximum T_c and is lowered for weaker couplings. The isotope shift increases at higher values as we dope away from optimal doping, and even exceeds the BCS value of 1/2 to reach a maximum which is higher for weaker coupling strengths. The isotope shift then drops to β=1/2 again which is a direct consequence of the constant background EDOS. The final point to notice is that the maximum of the isotope effect is band–dependent as well. This is clearly seen from the long dashed curve, which has higher background EDOS than the solid curve and lower $T_c^a/\omega_{\ell n}$. This would make β–T_c curves less universal than one might hope.

Next, we consider the effect of normal impurities on the transition temperature and the isotope effect. Zinc substitution in CuO_2 planes is believed to introduce physical defects without changing the number of carriers of the Fermi level. For small enough concentrations of zinc, we can use the Born approximation to study normal impurity substitution within the framework of Eliashberg theory.

For a constant density of states, normal impurities do not affect T_c at all. According to the BCS theory of dirty superconductors [Anderson 1959], the pairing is between an electron and its time reversed counterpart. For dirty superconductors, the momentum of an electron is not a good quantum number and cannot be used to describe Cooper pairs. Anderson argued that the elastic scattering due to chemical and physical impurities does not affect the energy of the electrons, and that by diagonalizing the normal state Hamiltonian including the impurity effects, one can recast the reduced BCS Hamiltonian for pairs between $\mathbf{k}\uparrow$ and $-\mathbf{k}\downarrow$ to pairs of time reversed electrons with constant energy. If there exist a small initial anisotropy in V, characteristic of pure systems, then the new pairing potential V is reduced only slightly compared to that of the clean limit. Normal impurities kill this anisotropy and reduce T_c with a very steep initial slope. The transition temperature then saturates quickly and becomes invariant to impurity concentration. The Eliashberg equations used in this chapter are very isotropic and, in a sense, they describe time reversed pairing because the averaging over momentum states was carried out (angular integration) to favour energy labeling only,i.e. $\tilde{\omega}$. The dotted long dashed line in the upper frame of Figure (3.6), $T_c/\omega_{\ell n}=0.135$, is a T_c curve calculated with constant EDOS and shows no variation of T_c with normal impurity concentration t^+, in accordance with Anderson's theory for dirty superconductors. Normal impurities have a profound effect on T_c when the EDOS is not constant. In Figure (3.6), we show that T_c drops significantly from its maximum value with an initial linear dependence on the impurity concentration and later saturates to a constant value, given by the constant background in the EDOS. The drop in T_c is more dramatic than that due to anisotropy effects for conventional superconductors. This linear drop of T_c for small

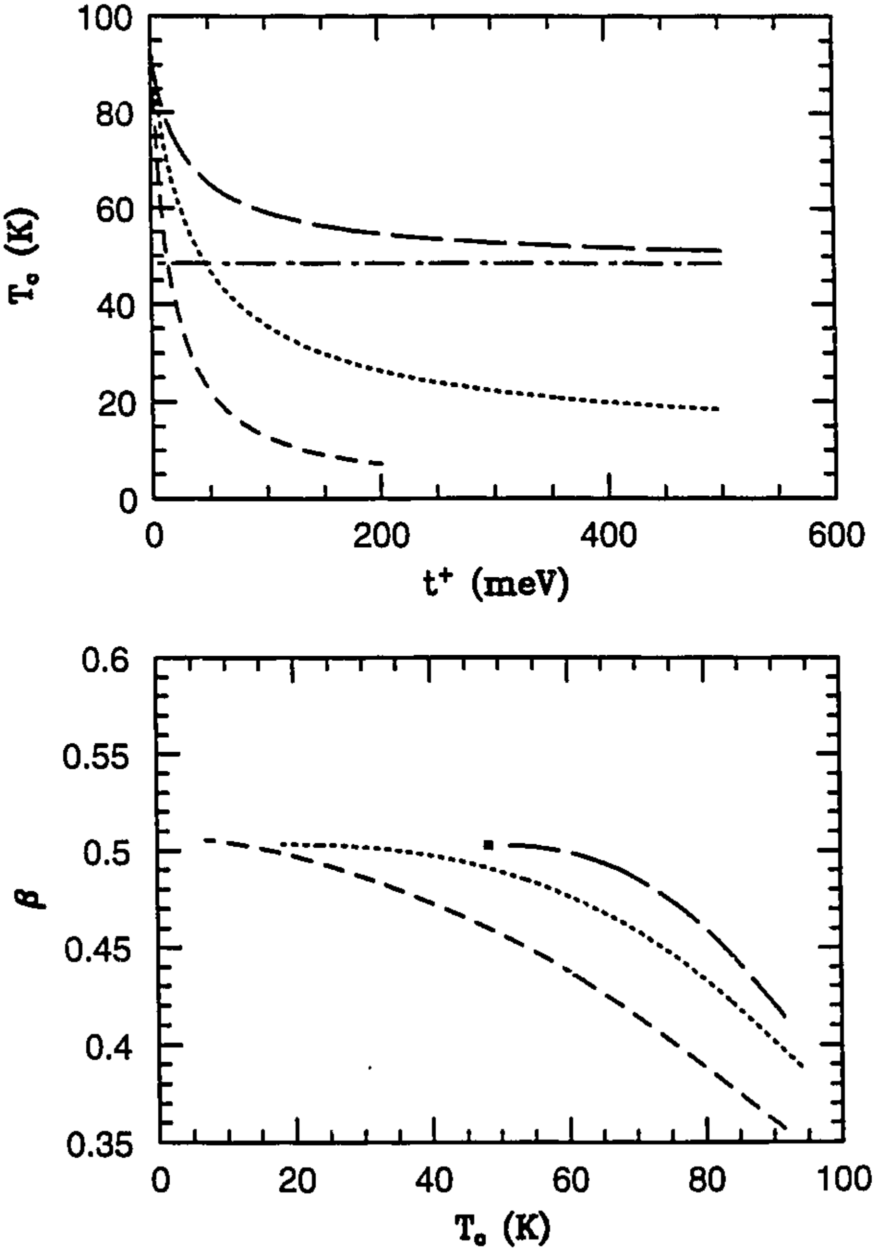

Figure 3.6: Critical temperature vs normal impurity concentration t^+ (upper frame) and the isotope effect vs critical temperature (lower frame) for Einstein spectra centred on ω_E=30 with r=1.0, E_f=500 and s=0 (dotted long dashed), s=1600 (long dashed); r=0.5, s=1600 and E_f=800 for ω_E=40 (dotted), ω_E=60 (dashed curve). D=40 and δ=0 for all of the curves.

t^+ should not be confused with similar linear drops of T_c with paramagnetic impurities, t^-, shown in Figure (3.7), which are pair breaking. The reduction of T_c with t^+ is related to a reduction of the effective EDOS at the Fermi level. Potential scattering is generally overlooked by experimentalists (often they just state Anderson's theorem) when trying to explain Zn substitution for Cu in the CuO_2 layers in HTSC. Zn^{2+} is a filled 3d shell and can be an extremely good scatterer, and when coupled with low dimensionality and perhaps weak coupling superconductivity, it is not surprising that the superconducting temperature is greatly reduced by small doping concentrations of zinc. In other words, there is no reason to consider zinc to be a paramagnetic pair breaker. This in fact has some experimental support in a 2:2:1:2 system. .Maeda et. al. 1990 found that Zn is nonmagnetic in single phase $Bi_2\,(Sr_{0.6}Ca_{0.4})\,(Cu_{1-x}M_{x2})O_4$ which has Cu sites only in the planes and the cation M substitutes for Cu only. The same authors also found that Zn and Ni dopings suppress T_c at the same rate. Remschnig et. al. 1991 also found that Zn and Ni dopings suppress T_c in the 25–K $Bi_{1.2}Pb_{0.8}La_{0.5}Sr_{1.5}CuO_6$ phase at approximately the same rate (8K/at .%). This leads to the conclusion that potential scattering is far more important in the hole doped cuprates that have small coherence lengths. The 25–K Nd–Ce–Cu–O, which is electron doped and is identical in structure to the Bi– based phases, has a much larger coherence length in the ab plane and it was found that magnetic impurities depress T_c at a faster rate than the nonmagnetic ones [Remschnig et al. 1991]. The lower frame of Figure (3.6) shows the isotope effect calculated for the upper frame T_c curves. The isotope curves are plotted vs transition temperature T_c and show a linear dependence near the maximum T_c's. This is quite remarkable, since it was shown that the isotope effect of oxygen in the Zn–doped 123 system is linear with

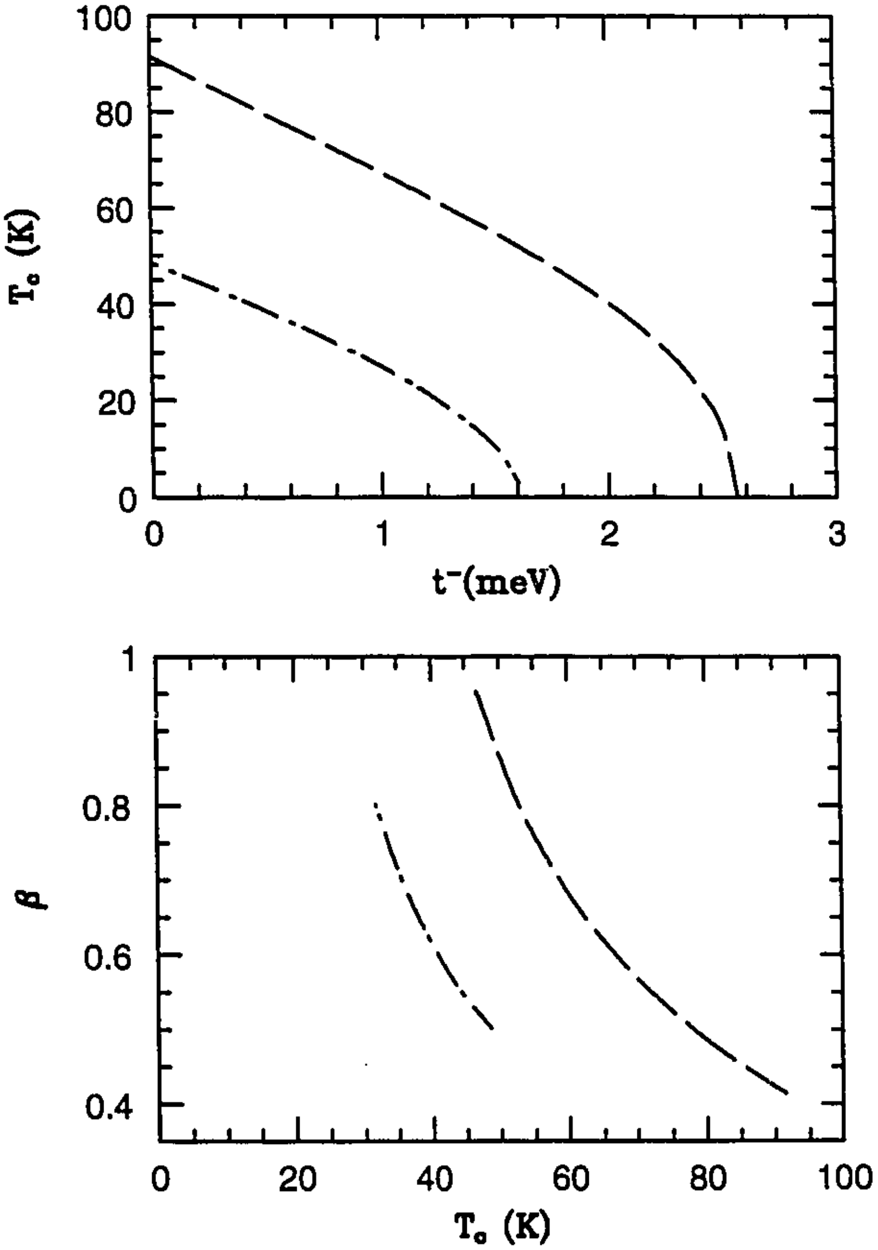

Figure 3.7: Critical temperature vs paramagnetic impurity concentration t^- (upper frame) and the isotope effect vs critical temperature (lower frame) for an Einstein spectrum centred on ω_E=30 meV with EDOS parameters of r=1.0, s=1600, D=40, δ=0 and E_f=500.

T_c. Nickel doping has a similar effect to that of Zn, but has higher β and more downward curvature [Bornemann et al. 1991]. We suspect that aside from the potential scattering, which might be much lower with Ni, there would be a Fermi level shift associated with Ni doping.

The isotope effect β for paramagnetic impurities is shown in the lower frame of Figure (3.7). For both the vHs scheme (long dashed curve) and constant EDOS (dotted long dashed curve), β has an upward curvature and does not saturate to a specific value for low T_c. We take this as evidence against a pair breaking role for Ni. The effect of paramagnetic impurities on T_c within the vHs scenario is shown in Figure (3.8). The long dashed curve is for an intermediate strong coupling (ω_E=30 meV) and the dashed curve is for a weak coupling case (ω_E=60 meV). The dotted long dashed curve has the same parameters as the long dashed curve but the vHs peak is switched off. The three curves are almost identical when plotted in a normalized fashion, T_c is renormalized to its pure value, and t^- is normalized to the critical impurity strength t_c^- for which T_c is zero, as is clearly seen in the lower frame of Figure (3.8). There have been some attempts to model pair breaking effects with realistic phonon spectral densities, $F(\omega)$, and constant density of states. These claimed success in explaining the T_c dependence on paramagnetic impurity concentration [Nakamura et al. 1991]. We do not expect the inclusion of the vHs in the EDOS to be any different except that much smaller λ's are required to obtain the high transition temperatures. We would like to caution the reader that an appropriate treatment of paramagnetic impurities should be included in a model that treats antiferromagnetic spin fluctuations. All of the HTSC have peaked spin susceptibilities at or near $(\pm\pi,\pm\pi)$ which are pair breaking for an isotropic or anisotropic s–wave superconductors. The paramagnetic impurity treatment

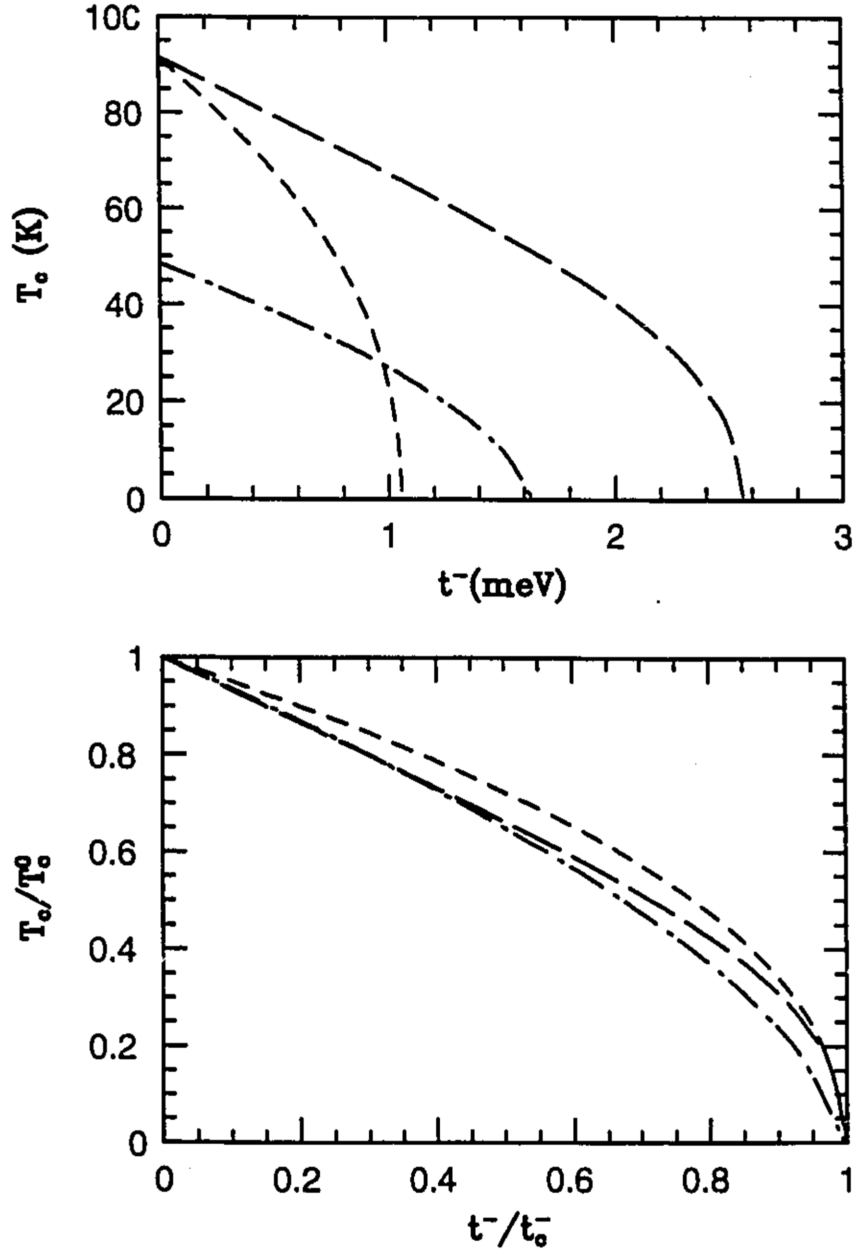

Figure 3.8: The critical temperature vs paramagentic impurity concentration t^- (upper frame). The long dashed curves are for ω_E=30, r=1.0, E_f=500, D=40, δ=0 and s=1600, while the dotted long dashed curve is for s=0. The dashed curve is for ω_E=60, r=0.5, E_f=800, s=1600, δ=0 and D=40. The lower frame contains the same curves normalized to maximum T_c and t^-.

presented in this chapter and Chapter 5 are only valid for the dilute limit [Abrikosov and Gor'kov 1961] where spin correlations are absent. Overall, experiments on the isotope effect β in HTSC show small partial isotope effects near optimal dopings. The isotope effect increases as T_c is reduced by decreasing the hole concentration. The minimum isotope effect for oxygen in Y123 is about 0.02 and in La214 is ~ 0.16. In the overdoped La214, β stays roughly constant and does not increase, which is quite anomalous. Negative isotope shifts are observed in some cuprates with values as low as –0.1. In $Bi_2Sr_2CaCu_{2-x}Fe_xO_8$, β decreases from 0.08 to –0.1 for T_c=74.1 and 65.7 K respectively [ref. 171 in Franck 1994].

IV) The Gap Ratio and the Thermodynamic Critical Field

The energy gaps in the excitation spectrum of most conventional superconductors are measured experimentally from infrared conductivities or tunneling curves. The energy gap Δ_0 to the transition temperature T_c is a universal ratio in BCS. The gap ratio, defined by $2\Delta_0/T_c$, is easily calculated from equations (1.1) and (1.2) to be

$$\frac{2\Delta_0}{T_c} = 3.53. \tag{3.26}$$

Almost all conventional superconductors, except for $A\ell$, deviate from equation (3.26). The calculated gap ratios from Eliashberg theory, however, agree very well with those from experiment [Carbotte 1990]. Furthermore, an approximate equation for the gap ratio using strong coupling corrections has been derived and fitted to experimental ratios [Mitrovic, Zarate and Carbotte 1984]. This analytic expression is a one parameter fit in terms of $T_c/\omega_{\ell n}$, and is given by

$$\frac{2\Delta_0}{T_c} = 3.53\left[1+12.5\left[\frac{T_c}{\omega_{\ell n}}\right]^2 \ell n\left[\frac{\omega_{\ell n}}{2T_c}\right]\right]. \tag{3.27}$$

Equation (3.27) gives good results for the gap ratios of almost all conventional superconductors. Our numerical calculations in this section will show that the gap ratio is modified by the inclusion of a peak in the EDOS. In particular, the gap ratio is increased over its asymptotic limit value given by equation (3.27). There will be no attempt in this work to quantify the enhancement of $2\Delta_0/T_c$ at $\delta=0$ over its asymptotic value. From the numerical solutions of equation (3.11–3.13) in the superconducting state, we can find ϕ_0 and $\tilde{\omega}_0$, which are used to define the gap ratio. The gap ratio is simply defined as

$$\frac{2\Delta_0}{T_c} = \frac{2\pi}{T_c} \lim_{T\to 0} \frac{\phi_0}{\tilde{\omega}_0} T \,. \tag{3.28}$$

In the upper frame of Figure (3.9), we show the gap ratio plotted for three cases of coupling strengths. The Einstein frequencies ω_E for the curves are 20 meV, 40 meV, and 60 meV. The T_c curves were shown in the upper frame of Figure (3.5). Figure (3.9) shows an overall enhancement of $2\Delta_0/T_c$ over its value in the absence of the vHs. Unlike the T_c results, the enhancement of $2\Delta_0/T_c$ is not monotonic in strong coupling. These enhancement are 40, 53 and 33% for the solid, dotted and dashed curves, respectively. The widths of the $2\Delta_0/T_c$ curves are less than those of the T_c curves. This is can be understood in terms of effective smearing of the peak in the EDOS. The amount of smearing in the density of states is proportional to λT for the electron–phonon interaction. The smearing in the effective EDOS is

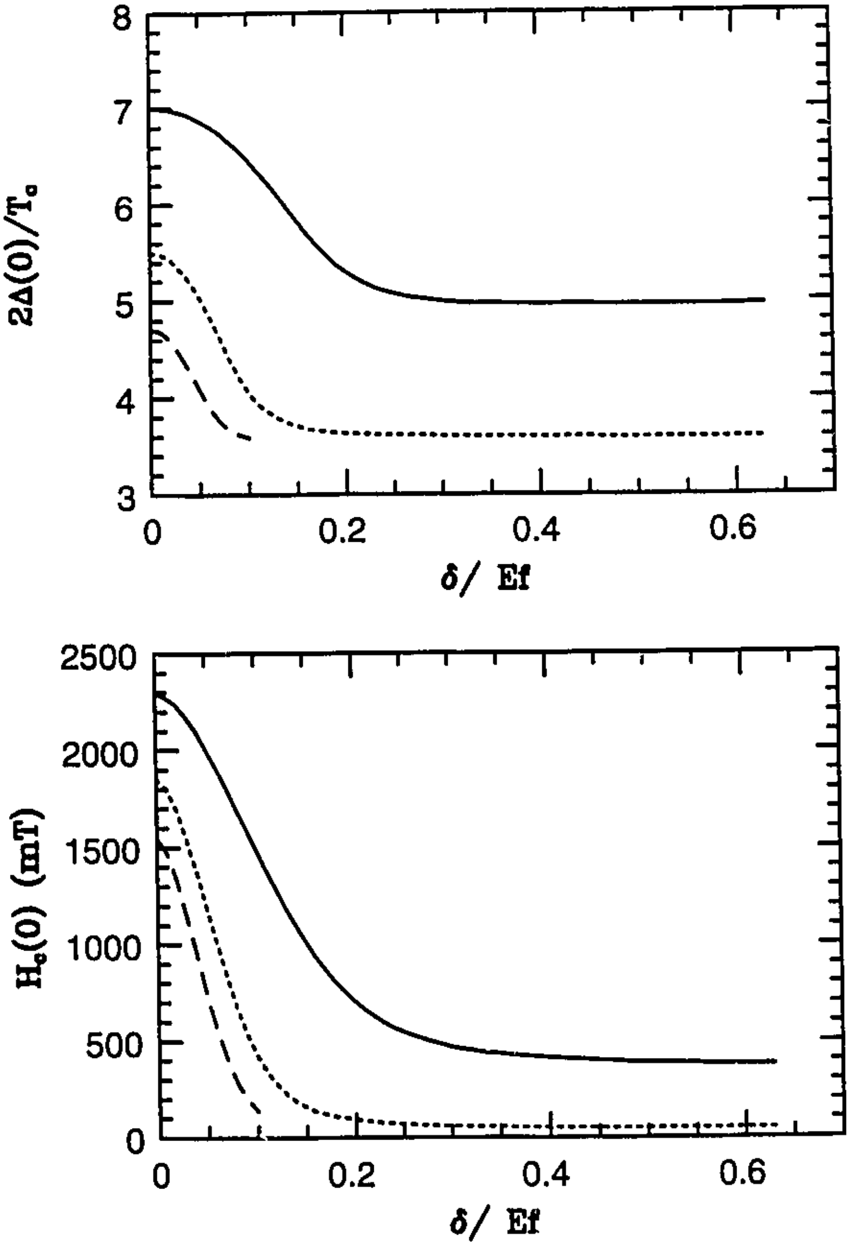

Figure 3.9: The gap ratio (upper frame) and thermodynamic critical field (lower frame) for three Einstein spectra with roughly the same T_c^{max}. EDOS parameters are r=0.5, E_f=800, s=1600, D=40 and ω_E=20 (solid), ω_E=40 (Dotted) and ω_E=60 meV (dashed curve).

smallest at T=0, resulting in a sharp peak in the energy gap as a function of chemical potential δ. A similar effect is expected for the thermodynamic critical field at zero temperature. The thermodynamic critical field H_c is formally defined as

$$H_c^2 = -8\pi\, \Delta\Omega_{BS} \tag{3.29}$$

and signifies the stored energy density in a magnetic field H_c just capable of killing superconductivity. The lower frame of Figure (3.9) shows the thermodynamic field at zero temperature $H_c(0)$ for the same three cases shown in the upper frame of the same figure. The values of $H_c(0)$ at $\delta=0$ clearly reflect the strong coupling dependence, similar to the $2\Delta_0/T_c$ behaviour. Since it is not our aim to find exact fits to any experimental data, and because of the large parameter space available in choosing the EDOS and $\alpha^2F(\omega)$, we only want to show here that the relatively sharp peak in $H_c(0)$ as a function of electron doping is a clear indication of a van Hove singularity in the EDOS.

In the next three figures, Figs. (3.20, 3.11, 3.12), we show the critical field at all temperature ranges for the three curves in Figure (3.9). A useful plot is the normalized critical field $H_c(T)/H_c(0)$ as a function of its deviation D(t) from the normalized critical field of the two fluid model, where $t=T/T_c$. The temperature dependence of the two fluid models' critical field is given by

$$H_c(t) = H_c(0)\,(1-t^2), \tag{3.30}$$

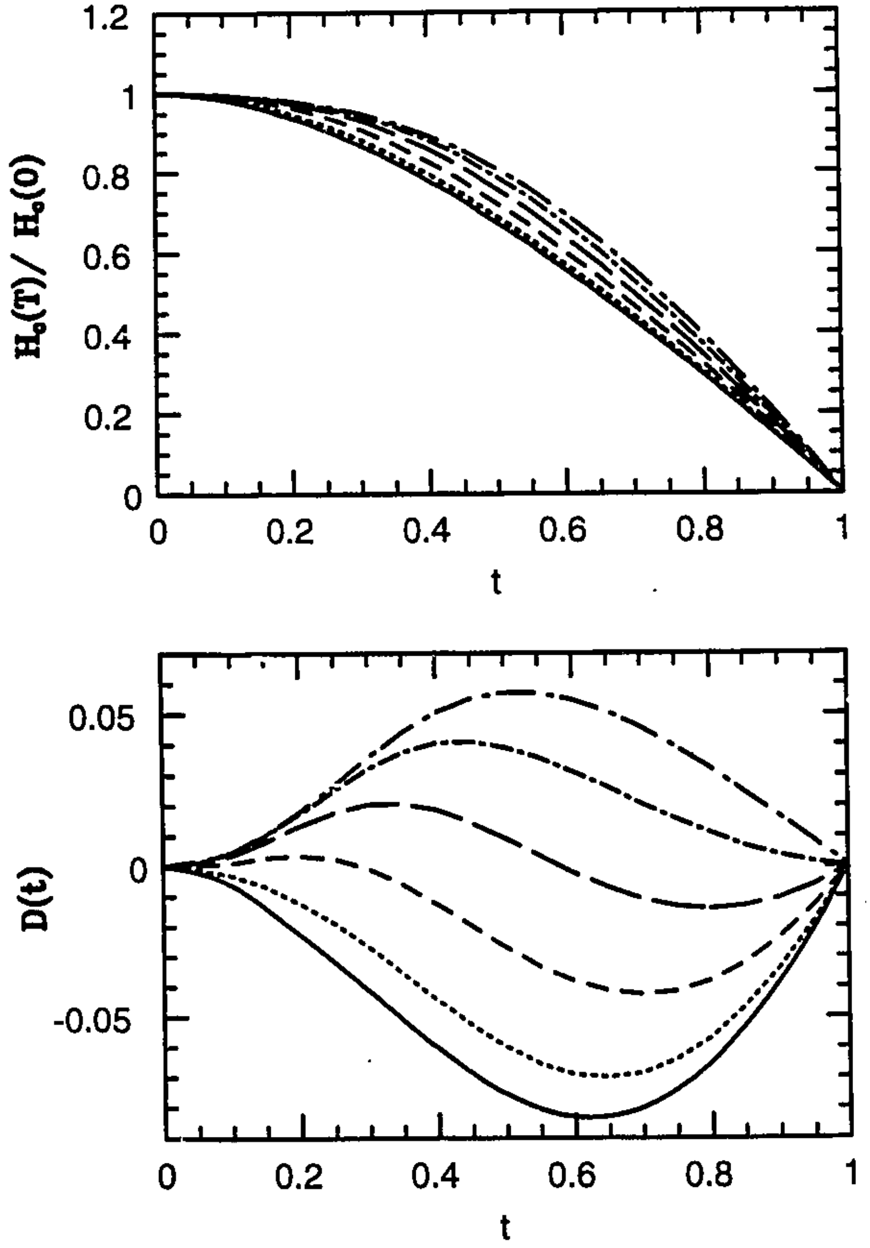

Figure 3.10: The normalized critical field (upper frame), and its deviation from the two fluid model (lower frame) vs reduced temperature t for the strong coupling case of ω_E=20 meV. The curves are for δ=0 (solid), 20 (dotted), 40 (dashed), 60 (long dashed), 80 (dotted dashed) and 100 meV (dotted long dashed).

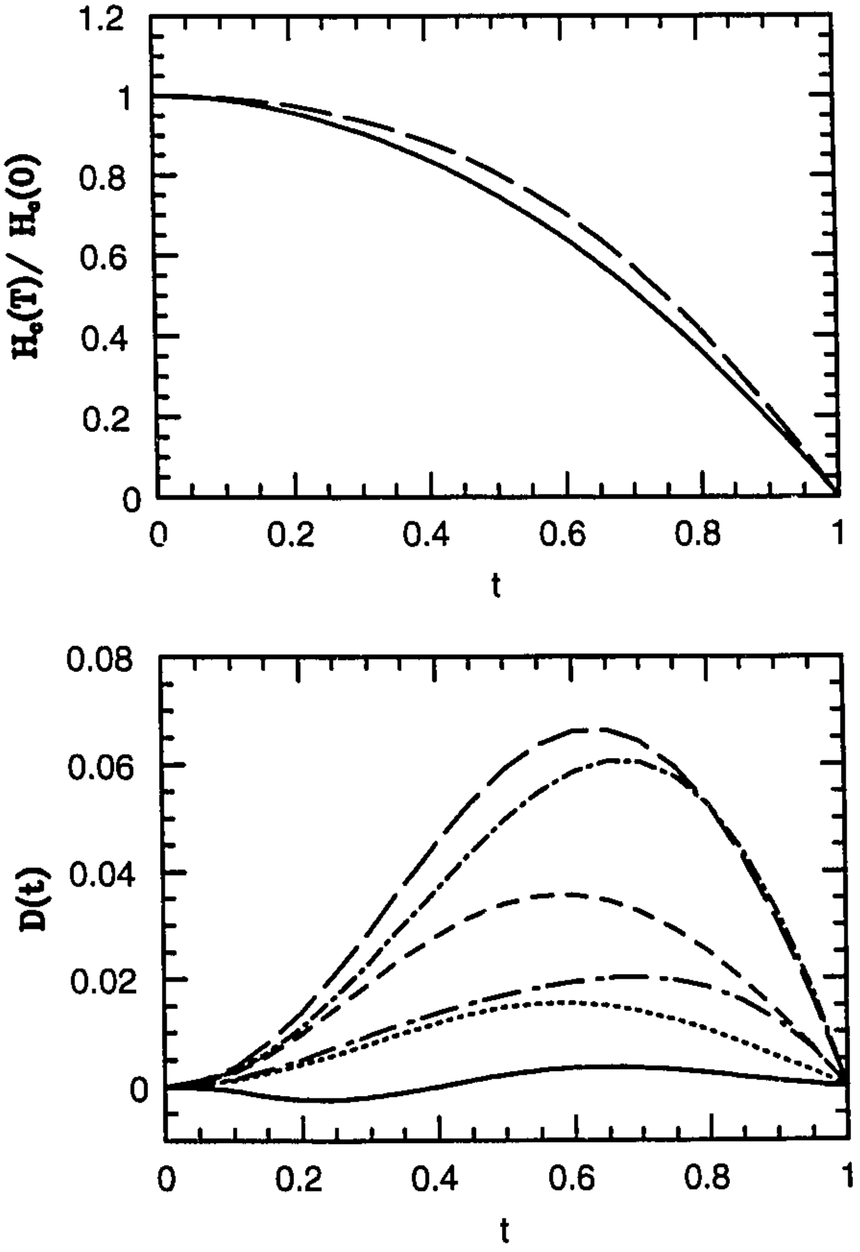

Figure 3.11: The same as in Fig. 3.10 but for an intermediate coupling ω_E=40 meV. The curves are δ=0 (solid), δ=10 (dotted), δ=20 (dashed) δ=40 (long dashed), δ=60 (dotted dashed) and δ=80 meV (dotted long dashed).

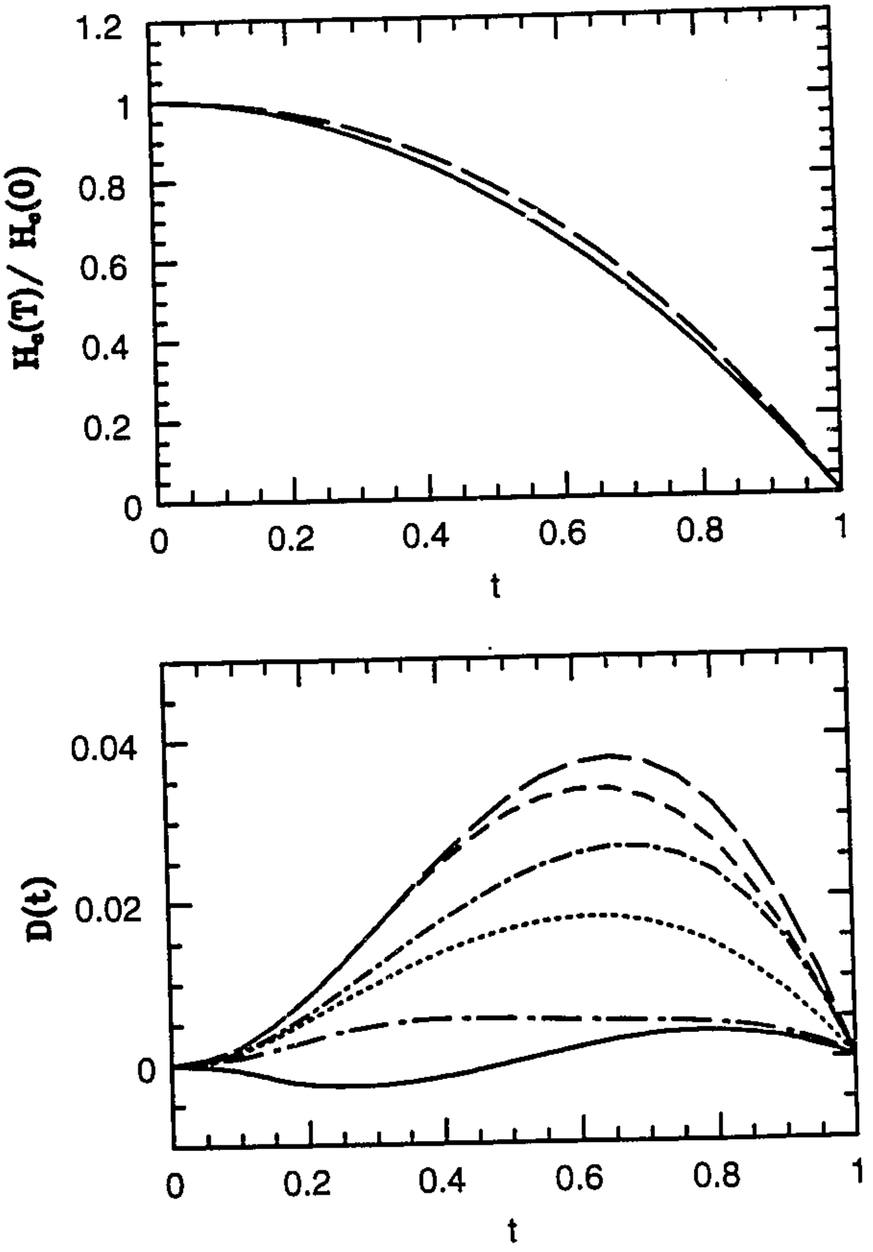

Figure 3.12: The same as in Fig. 3.10 but for weak coupling case of ω_E=60 meV. The curves are δ=0 (solid), δ=10 (dotted), δ=20 (dashed), δ=30 (long dashed), δ=40 (dotted dashed) and δ=50 meV (dotted long dashed).

and so the deviation function is defined as

$$D(t) = \frac{H_c(t)}{H_c(0)} - (1-t^2). \tag{3.31}$$

The lower frame of Figure (3.10) shows D(t) for the strong coupling case ω_E=20 meV (solid line in Fig. (3.9)). The solid curve in Fig. (3.10) is for the critical field at δ=0 meV. It shows quite unusual behaviour; the D(t) curve is negative definite with a minimum deviation of $\simeq -0.08$. Strong coupling superconductors have generally positive deviation and BCS has a universal negative D(t) with minimum deviation of $\simeq -0.036$. As we move δ away from the vHs, D(t) increases towards the strong coupling regime, positive D(t), with a maximum of 0.02–0.03, and eventually exceeds it to about 0.055. The particular values of δ are included in the figure caption. D(t) decreases upon further change in δ to saturate to all positive deviation with a maximum of 0.04, not shown. For the intermediate case of ω_E=40 meV, the dotted curve in Figure (3.9), the lower frame of Figure (3.11) shows that D(t) has only small negative deviation near small T for δ=0 (solid curve). As δ increases, the deviation of $H_c(t)/H_c(0)$ is pushed up to the very high strong coupling limit and drops back again to a maximum of 0.02 (long dashed dotted curve). The weakest case of ω_E=60 meV (dashed curve in Figure (3.9)) shows a very similar effect in the lower frame of Figure (3.12). Deviation functions also have a very strong dependence on $\alpha^2F(\omega)$, which is not very useful to us here and will not be discussed further in this section.

In the previous section, we argued for the importance of normal impurity scattering, especially for Zn. We will continue the investigation here. In Figure (3.13), we show the dependence of $H_c(0)$ on potential scattering. The upper frame

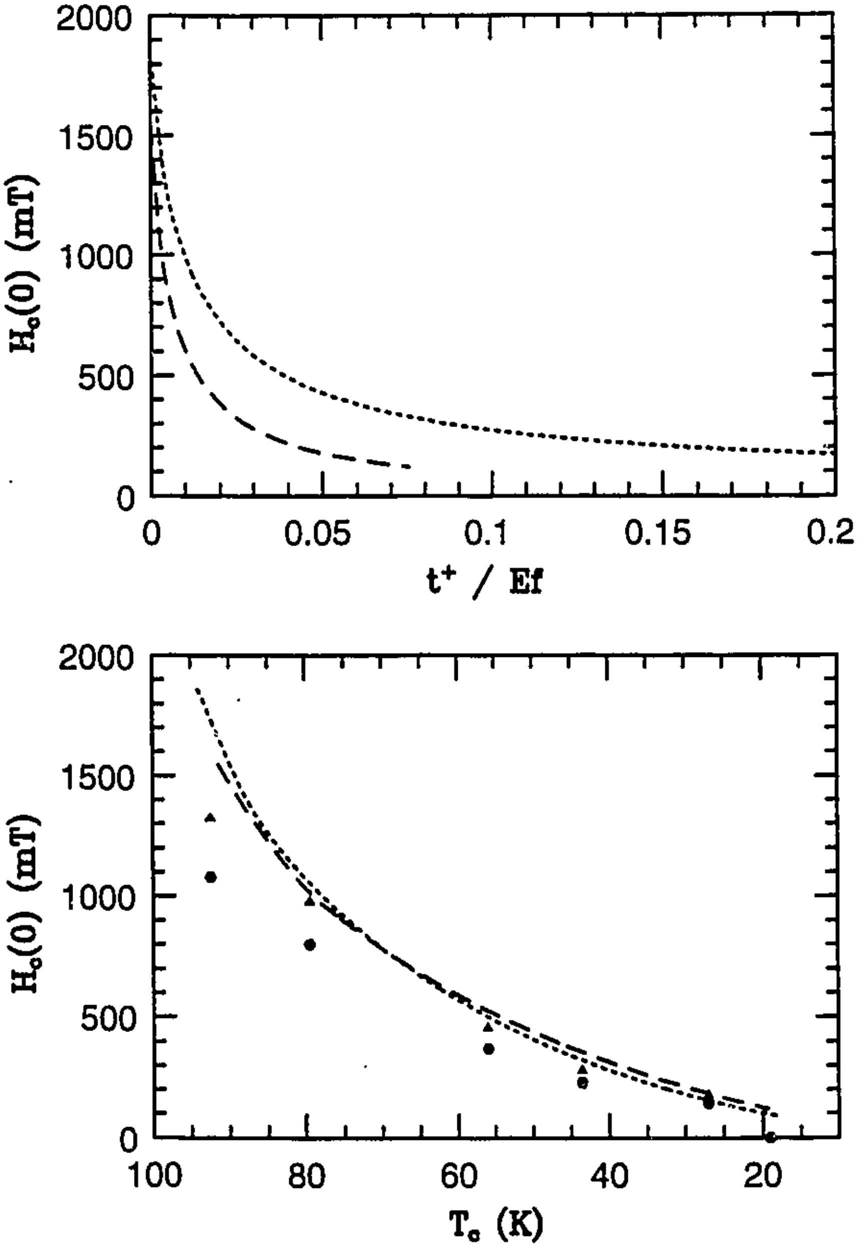

Figure 3.13: Thermodynamic critical field at zero temperature vs normal impurity concentration t^+ (upper frame) and vs critical temperature (lower frame) for $\omega_E=40$ (dotted curve) and $\omega_E=60$ (dashed curve). The EDOS parameters are r=0.5, s=1600, D=40, $E_f=800$ and $\delta=0.0$. The hexagons are experimental data for Zn substituted Y123 taken from Loram et al. 1990.

shows how $H_c(0)$ drops with increased impurity concentration for $\omega_E=40$ (dotted curve) and $\omega_E=60$ (dashed curve). The chemical potential is pinned to the vHs and the EDOS parameters are r=0.5, s=1600, and $E_f=800$. In the lower frame of the same figure, we plot $H_c(0)$ vs T_c and compare it to the experimental data for $YBa_2(Cu_{1-x}Zn_x)_3O_7$ [Loram et al. 1990]. The actual data are the filled hexagons; the triangles are the same data scaled up by a constant factor. We actually have the freedom to scale our calculated curves by any factor, because N_b in equation (3.17) can be adjusted to scale ΔF or the specific heat jump $\Delta C(T_c)$ to fit experiment. We decided to scale the $\Delta C(T_c)$ values and hence this fixes the $H_c(0)$ values as well. The experimental values (solid triangles) were adjusted so that the experimental $\Delta C(T_c)$ values best–fit the specific heat calculations, Figure (5.9). Experimentally, the $H_c(0)$ values are calculated from the specific heat difference between super and normal states through two consecutive integration steps, i.e. specific heat to entropy and then to free energy differences. Needless to say, there are still large uncertainties in these $H_c(0)$ values which, unfortunately, are not quoted. In any case, our calculations clearly capture the trend of the experiment. Paramagnetic impurities in this theory have quite different effects from the normal impurities. Figure (3.14) shows the dependence of $H_c(0)$ on T_c from variation of the paramagnetic impurity concentration t^-. The $H_c(0)$ curves are approximately linear and have extremely small negative curvature. This dependence is similar to that in regular Eliashberg theory.

V) Conclusion

We have incorporated a damped van Hove singularity into the Eliashberg equations using the Fermi level approximation and calculated the

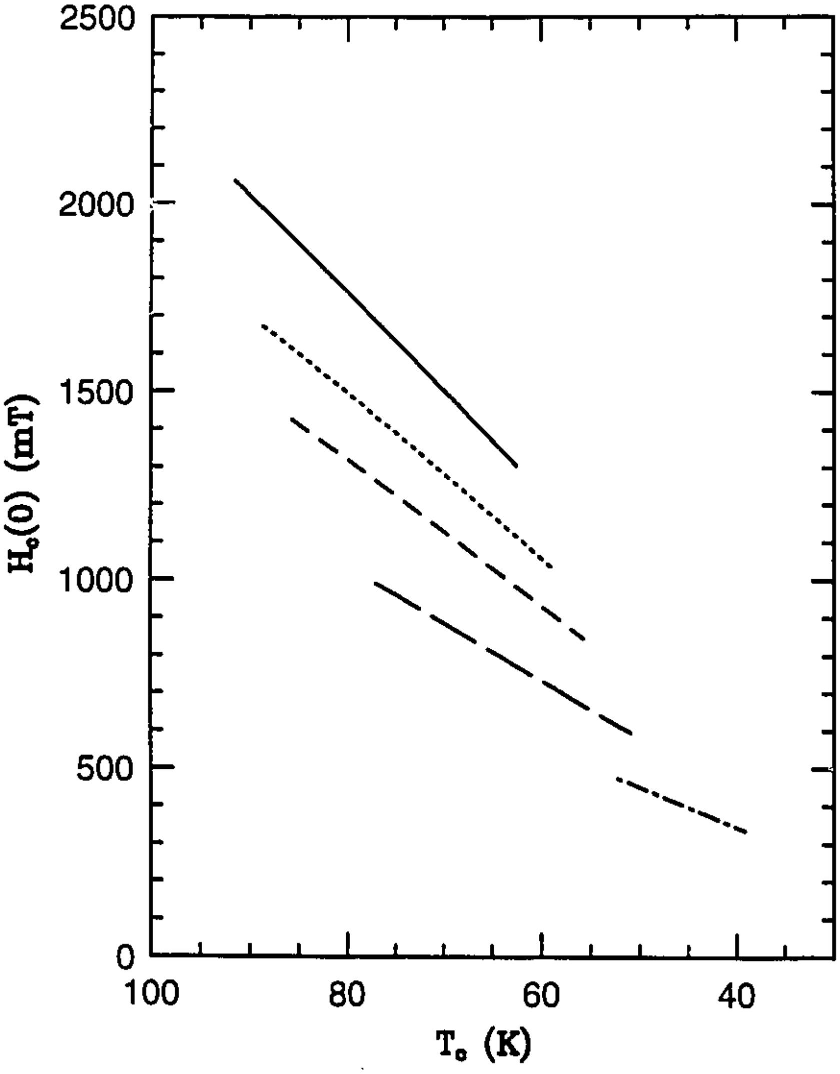

Figure 3.14: Thermodynamic critical field at zero temperature vs critical temperature resulting from a variation of paramagnetic impurity concentration t^-.These curves are for ω_E=20 meV and EDOS parameters of r=0.5, s=1600, D=40, E_f=800 and δ=0 (solid), 35 (dotted), 50 (dashed), 80 (long dashed) and 200 meV (dotted dashed).

the transition temperature and the isotope effect. We have found that the effect of a peak in the EDOS is greatest on both T_c and β for the weak coupling condition and is weaker (washed out) for very strong coupling. When the Fermi level is very close to a vHs, there is an enhancement of T_c by a factor of up to 71 in the weakest case considered in Figure (3.5) and a decrease of β to about 3/4 of the BCS value. To be able to explain the data from some of the cuprates, the minimum value of β should be near or even slightly below zero. Within the approximations considered in this chapter, this is not possible. We have discussed, however, the presence of some correlations between the calculated and the experimentally measured isotope effect for hole and impurity doping. The good agreement between our calculated $H_c(0)$ vs T_c curve, obtained by varying t^+, and the experimental data for Zn doped Y123 is striking. This might be interpreted as evidence for density of states smearing by normal impurities.

Chapter 4

The London Penetration Depth

I) Introduction and Formalism

In this chapter, we will calculate the temperature dependence of the London penetration depth for a planar s–wave and d–wave model superconductor with a simple tight binding band within the CuO_2 plane and also with a saddle point singular band derived from photoemission experiments for Y123. Initial experiments on the London penetration depth favoured BCS theory and the two fluid model. Later, new experiments on thin films showed anamolous quadratic temperature dependence at low T interpreted as evidence for an unconventional pairing order parameter, namely d–wave. This provided the motivation to study the penetration depth of d–wave superconductors. Others have suggested that large anisotropy in the electronic dispersion might give similar temperature anomalies for regular s–wave superconductors. Our work on d–wave superconductors showed that the London penetration depth is quite linear in temperature at low T [Arberg, Mansor and Carbotte 1993]. Shortly after this was experimentally confirmed by Hardy. Hardy [1993] found that the London penetration depth of a well characterized single crystal of Y123 exhibits a linear temperature dependence in the range of 25 – 4 K. The thin film results, however, give T^2 dependence [Lee and Lemberger 1993; Annett et al. 1991; Anlage et al. 1992; Pond et al. 1991]. These two power laws arise naturely in the d–wave picture. The linear law is for pure d–wave superconductor and the quadratic results from strong impurity scattering [Gross et al. 1986; Hirschfeld et al. 1988; Prohammer and Carbotte 1991; Arberg, Mansor and Carbotte 1993; Hirschfeld and Goldenfeld 1993]. We will show that the linear temperature dependence can not arise from an s–wave superconductor, and this result is independent of the type of electronic band.

Some experimental evidence in support of $d_{x^2-y^2}$ gap in the CuO_2 layers in the HTSC is reviewed by Annett and Goldenfeld [Annett 1992]. The key experiments are i) NMR and Knight shift [Martinalal et al. 1993; Ishida et al 1993; and Hotta 1993] ii) some tunnelling data [Jiang 1993] and SQUID experiments [Wallman et al 1993; and Sigrist 1992] iii) thermal conductivity [Yu et al. 1992] and optical conductivity [Remero et al. 1992] iv) microwave scattering rate [Bonn et al. 1992; and Nass et al. 1991] v) low temperature dependence of the London penetration depth [Hardy et al. 1993] vi) spin susceptibility [Mason et al. 1993] and angular resolved photoemission [Wells et al. 1992 and Shen et al. 1993].

In the following calculations, no Fermi surface approximation is introduced and a complete integration over the Brillouin zone is carried out at a fixed chemical potential μ. Impurity scattering in the Born and unitary limit are considered. A large amount of Born scattering is needed to change the low temperature dependence from a T to T^2 law, in the d–wave case, while unitary scattering shows this effect at the lowest concentration considered. The zero temperature penetration depth $\lambda_L(0)$ increases with impurity scattering while the transition temperature decreases in d–wave. These results are in qualitative agreement with heavy Fermion models, where it was shown that the temperature dependence of the London limit penetration depth of a cubic d–wave superconductor [Prohammer and Carbotte 1991] and p–wave one [Einzel et al. 1986] exhibit large deviations from a conventional s–wave BCS superconductor. Also the linear dependence of the penetration depth at low temperature for the pure case goes over to a quadratic dependence when sufficient impurity scattering is added [Hirschfeld et al. 1988, 1986; and Pethick and Pines 1986].

In this chapter, we model the superconductivity in CuO_2 planes with a square Brillouin zone and one of the following electronic dispersions i) a tight binding of the form

$$\epsilon_{\mathbf{k}} = -2\bar{t}[\cos k_xa + \cos k_ya - 2B \cos k_xa \cos k_ya] - \mu \tag{4.1}$$

where $\bar{t}$ is the nearest neighbour hopping integral, $\mathbf{k}$ the momentum in the plane, a is the lattice parameter, and μ is the chemical potential ii) or a saddle shaped band inferred from photoemission data [Liu et al. 1992; Deussau et al. 1993] with the following analytical form [Abrikosov et al. 1993]

$$\epsilon_{\mathbf{k}} = \begin{cases} \frac{1}{2m}[k_x^2 - a_1(k_y - \pi/a)^2] - \mu & k_{y_0} \leq k_y \leq \frac{\pi}{a} \\ \frac{1}{2m}[k_{y_0}^2 + k_x^2 - k_y^2] \quad -\mu & 0 \leq k_y \leq k_{y_0} \end{cases} \tag{4.2}$$

and $0<a_1\leq 1$ and for $a_1 \simeq 0.01$ this form is particular to Y123.

The vHs of equation (4.2) is a square root singularity if a_1 is very small. In Figure (4.1), we show the EDOS for the Abrikosov model, equation (4.2), for four

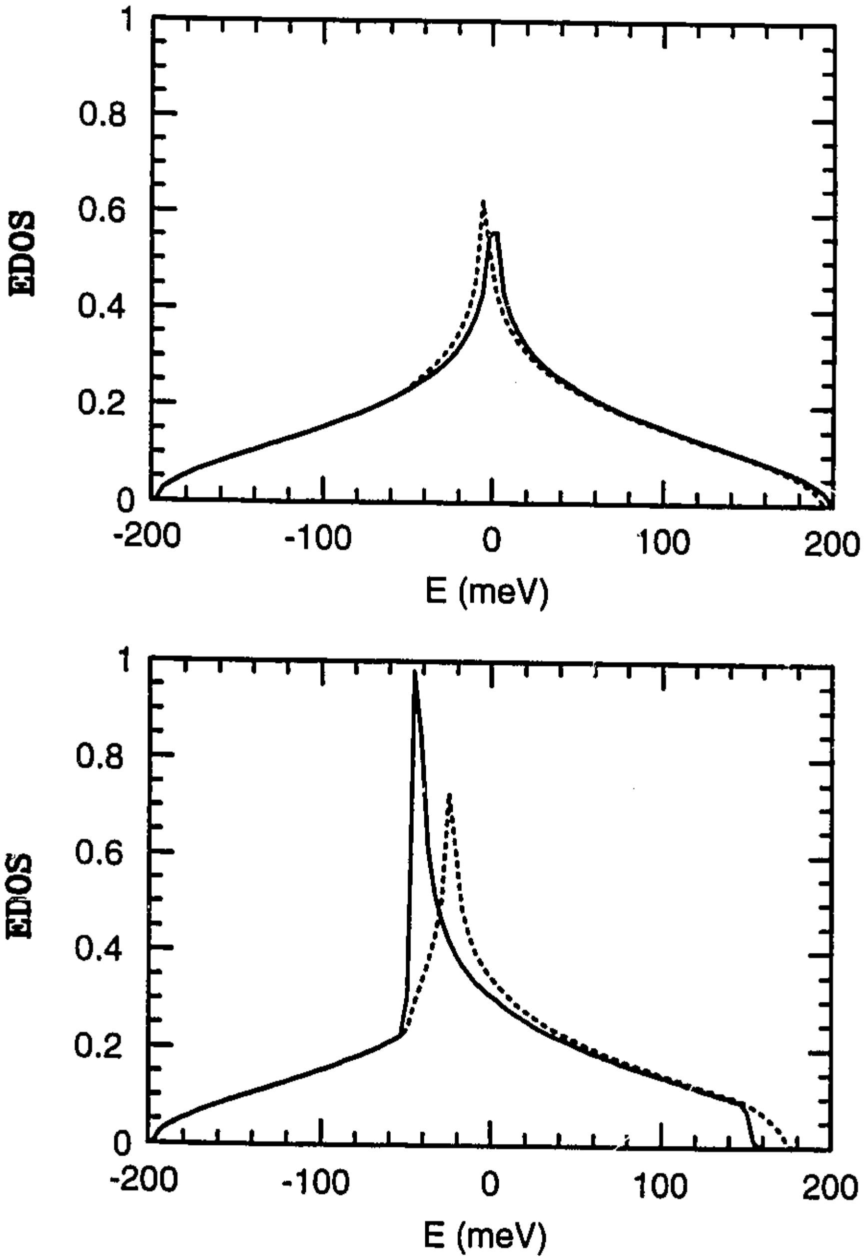

Figure 4.1: EDOS for the Abrikosov model, equation (4.2); the upper frame is for a_1=1.0 (solid curve) and a_1=0.5 (dotted curve); the lower frame is for a_1=0.05 (dotted curve) and a_1=0.01 (solid curve) and $k_{y_0} = \pi/2a$ for all the curves.

values of a, in the upper frame a_1=1.0 (solid curve) and a_1=0.5 (dotted curve) and in the lower frame a_1=0.05 (dotted curve) and a_1=0.01 (solid curve) where we fix k_{y_0} to be $\pi/2a$. Among the possible order parameter symmetries for the square lattice are s–wave, extended s–wave, d–wave and even higher harmonics in momentum space [Wenger and Öslund 1993; Yip and Garg 1993; Sigrist and Rice 1987; Hasegawa and Fukuyama 1987; and Volovik and Gor'kov 1985]. We will only use d–wave and s–wave symmetries in this work. The momentum dependence for the d–wave gap parameter is $\eta_{\mathbf{k}}=[\cos k_x a - \cos k_y a]$ [Emery 1987; Hirschfeld et al. 1986; Millis et al. 1990; Monthoux et al. 1991; Pines 1991; Scalapino and Bulut 1991; Schultz 1981; and Zhou and Schultz 1992]. For the pairing potential in the d–wave case, we use a separable model to project out the part responsible for pairing [Prohammer 1990a, 1991; Rieck et al. 1990; Millis 1992; and Norman 1988].

The generalized gap equation in Matsubara representation for the pairing energy $\phi_{\mathbf{k}}(n)$ and the normalized frequencies $\tilde{\omega}(n)$ at any $\mathbf{k}$ point in the first Brillouin zone take the form

$$\phi_{\mathbf{k}}(n) = g\pi T \sum_m \lambda(n-m) <\eta_{\mathbf{k}'}, \Phi_{\mathbf{k}'}(m)>' \eta_{\mathbf{k}} \tag{4.3}$$

and

$$\tilde{\omega}(n) = \omega_n + \pi T \sum_m \lambda(n-m) <\Omega_{\mathbf{k}}(m)> \tag{4.4}$$

where the notation $< > = 4\tilde{t}\, \Sigma_{\mathbf{k}}$, and

$$\Phi_{\mathbf{k}}(n) = \frac{\phi_{\mathbf{k}}(n)}{\tilde{\omega}^2(n)+\epsilon_{\mathbf{k}}^2+\phi_{\mathbf{k}}^2(n)} \qquad (4.5)$$

and

$$\Omega_{\mathbf{k}}(n) = \frac{\tilde{\omega}(n)}{\tilde{\omega}^2(n)+\epsilon_{\mathbf{k}}^2+\phi_{\mathbf{k}}^2(n)} \qquad (4.6)$$

Impurity scattering can be included here most easily by adding the following extra terms to equation (4.4);

i) for Born scattering of strength t^+

$$\pi t^+ <\Omega_{\mathbf{k}}(n)>,$$

ii) for resonant scattering of strength Γ

$$\pi \frac{\Gamma}{L(n)} <\Omega_{\mathbf{k}}(n)>,$$

and

$$L(n) = C^2 + <\Omega_{\mathbf{k}}(n)>^2 + <\Phi_{\mathbf{k}}(n)>^2.$$

We have explicitly ignored the particle–hole asymmetry. The parameter C is related to phase shifts and is zero for unitary scattering and infinite for Born scattering.

Finally, the expression for the penetration depth tensor $\lambda_{ij}(T)$ with ij Cartesian components, was derived in chapter two and is given by

$$\lambda_{ij}^{-2}(T) = \frac{8\pi e^2}{c' A c^2}\left[T \sum_{\mathbf{kn}} v_{ki}\, v_{kj} \left\{\frac{\epsilon_{\mathbf{k}}^2 + \phi_{\mathbf{k}}^2(n) - \tilde{\omega}^2(n)}{[\epsilon_{\mathbf{k}}^2 + \phi_{\mathbf{k}}^2(n) - \tilde{\omega}^2(n)]^2} - \frac{\epsilon_{\mathbf{k}}^2 - \tilde{\omega}^{02}(n)}{[\epsilon_{\mathbf{k}}^2 + \tilde{\omega}^{02}(n)]^2}\right\}\right] \tag{4.7}$$

e is the electron charge, c is the speed of light, A is the area of the plane and c′ is the lattice constant in the z–direction. Given a specific dispersion, we can evaluate the velocity vector and by integrating (4.7) numerically, we can evaluate the inverse square of the London penetration depth.

II) The Zero Temperature Limit

We will first consider the BCS clean limit of the penetration depth, in which case we can rewrite equation (4.7) as

$$\lambda_{ij}^{-2}(T) = \frac{8\pi e^2}{c' A c^2} \sum_{\mathbf{k}} v_{ki}\, v_{kj} \left[\frac{\partial f(E_{\mathbf{k}})}{\partial E_{\mathbf{k}}} - \frac{\partial f(\epsilon_{\mathbf{k}})}{\partial \epsilon_{\mathbf{k}}}\right] \tag{4.8}$$

$$\text{with } E_{\mathbf{k}} = \sqrt{\epsilon_k^2 + \Delta_{\mathbf{k}}^2} \text{ and } \Delta_{\mathbf{k}} = \frac{\phi_k(0)}{\tilde{\omega}(0)}\,\omega_0 .$$

The first term in equation (4.8) vanishes at T→0 and $-\partial f/\partial\epsilon$ becomes a delta function at the chemical potential μ

$$\lambda_{ij}^{-2}(\mu) = \frac{8\pi e^2}{c' A c^2} \sum_{\mathbf{k}} v_{ki}\, v_{kj}\, \delta(\epsilon_{\mathbf{k}} - \mu) \tag{4.9}$$

For simple tight binding (B=0), and coordinate transformation of the form $0 \le k_x, k_y \le \pi/a$ to $\cos(k_x a) = \epsilon - (1 - |\epsilon|)\cos\theta$ and $\cos(k_y a) = \epsilon + (1 - |\epsilon|)\cos\theta$

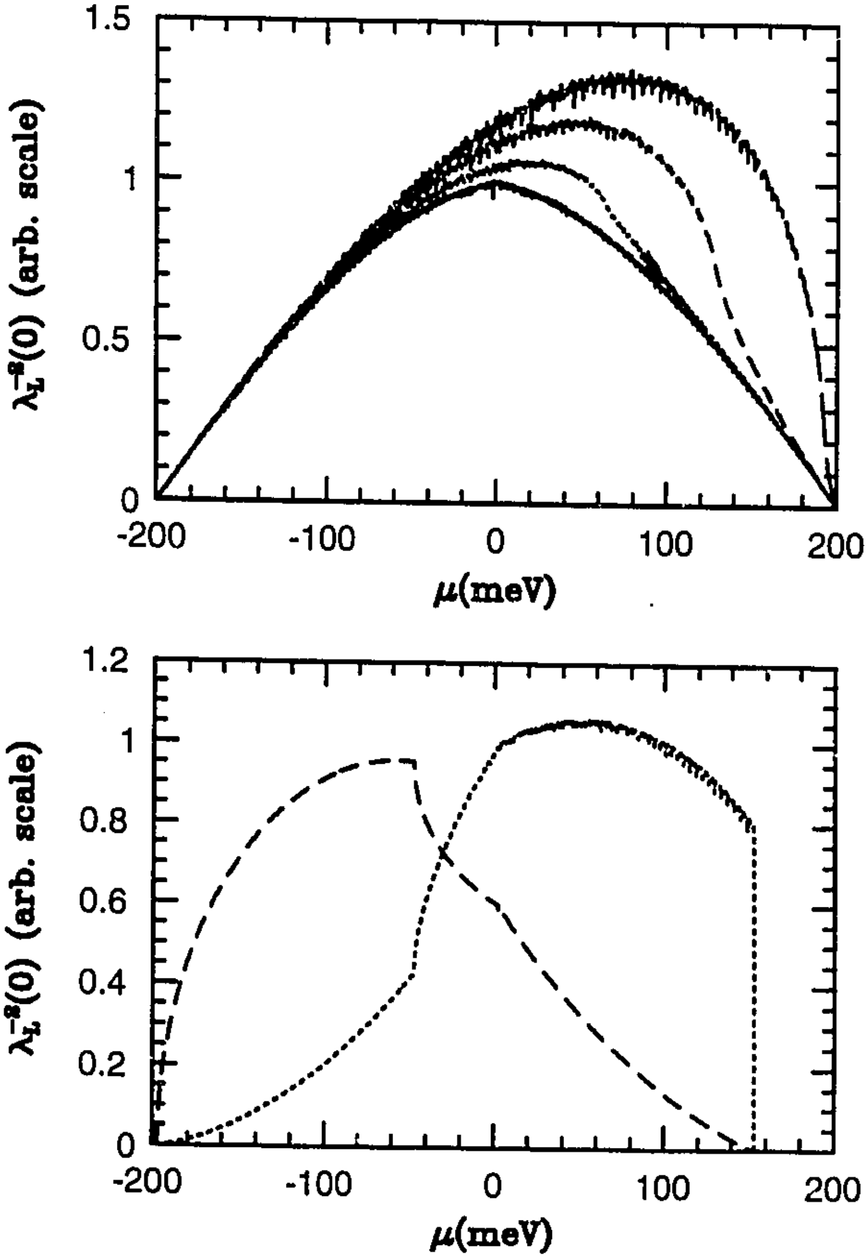

Figure 4.2: Numerical evaluation of the penetration depth at zero temperature from equation (4.9). The upper frame is for tight binding dispersion with B=0 (solid), B=0.16 (dotted), B=0.32 (dashed) and B=0.48 (long dashed). The lower frame is for Abrikosov dispersion with a_1=0.01; xx direction (dotted), yy direction (dashed).

with $-1\leq\epsilon\leq1$ and $0\leq\theta\leq\pi$, we can write

$$\lambda_{xx}^{-2}(\mu) = \frac{64e^2\bar{t}}{\pi c' c^2\hbar^2}\left[1-\left|\frac{\mu}{4\bar{t}}\right|\right] I\left(\left|\frac{\mu}{4\bar{t}}\right|\right) \tag{4.10}$$

where we used $\Sigma_{\mathbf{k}}=A/(2\pi)^2\int d^2k$, and finally defined I(x) by

$$I(x) = \int_0^{\pi/2} d\theta \cos^2\theta \sqrt{\frac{\sin^2\theta+x\ \cos^2\theta}{\cos^2\theta+x\ \sin^2\theta}} \tag{4.11}$$

where we can show that $I(0)=1/2$ and $I(1)=\pi/4$. Later we will provide a plot of $\lambda_{xx}^{-2}(\mu)$ from equation (4.10) normalized by $\lambda_{xx}^{-2}(0)$. The absolute value of $\lambda_L^2(0) \sim 2c'/\alpha\bar{t} \times 10^5$ Å^2 with c' in Å and $\bar{t}$ in meV and $\alpha=1/132.74$, in particular for $\bar{t}=50$ meV and $c'\sim5.5$Å , we get $\lambda(0)\sim1709$Å.

Equation (4.9) resembles that of the electronic density of states. Hence, we can construct a histogram for discrete values of μ and evaluate equation (4.9) numerically. The results are shown in Figure (4.2) for two types of electronic bands, tight binding in the upper frame and the Abrikosov band in the lower frame. Different curves in the upper frame are for different values of next nearest hopping integral B, see equation 4.1. The lower frame displays $\lambda_{xx}^{-2}(0)$ (dotted curve), $\lambda_{yy}^{-2}(0)$ (dashed curve). We should emphasis that the scale of the individual curves is arbitrary due to the numerical technique used to evaluate it. We also would like to mention that the solid curve in the upper frame of Figure (4.2) matches exactly the solid curve in the lower frame of Figure (4.3) which was evaluated from equations (4.10) and (4.11). Our exact calculations of $\lambda_L^{-2}(\mu)$ at zero temperature from equation (4.7), shown in Figure (4.3), exhibit the same shapes as shown in

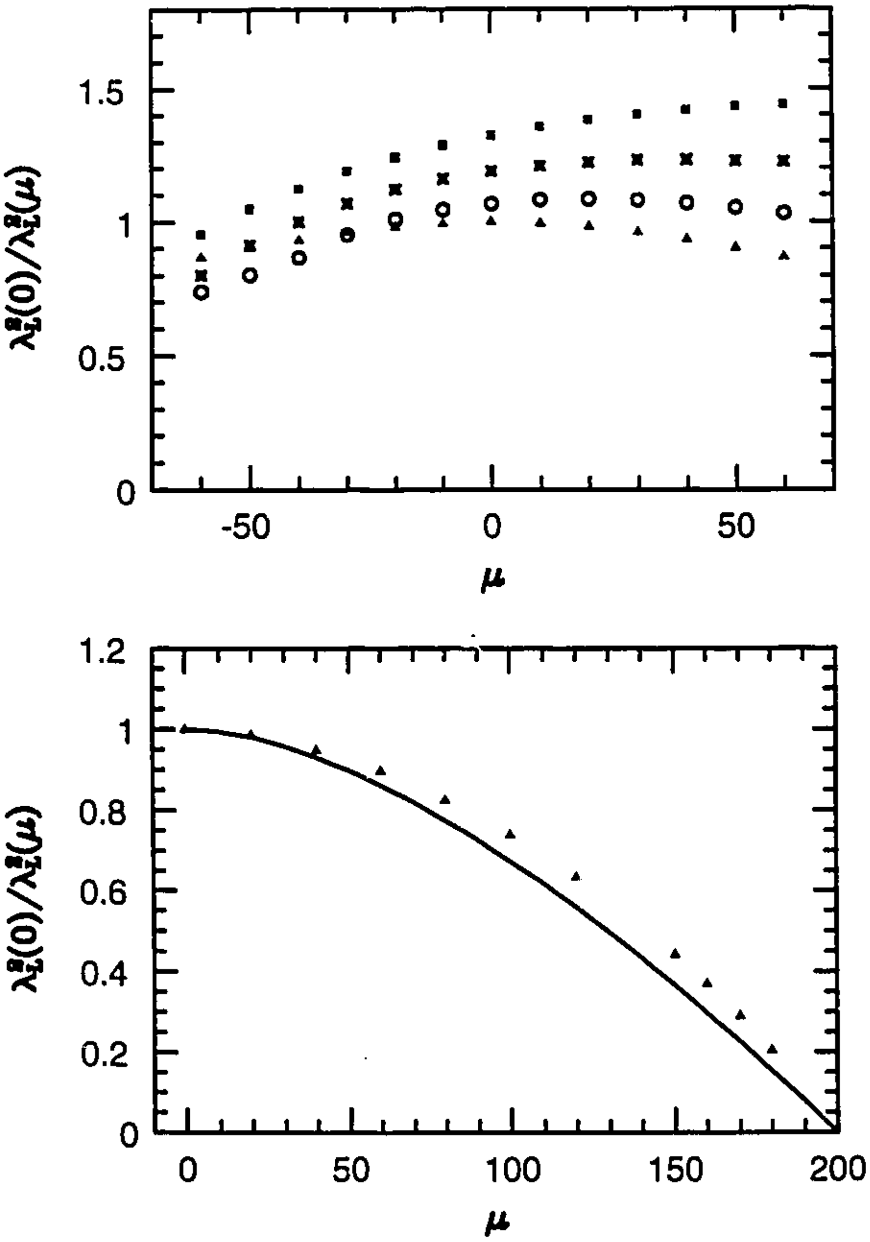

Figure 4.3: Exact calculations of $\lambda_L^{-2}(0)$ for d–wave (upper frame) and s–wave (lower frame) with tight binding dispersion. The B values are 0.0 (triangles), 0.16 (circles), 0.32 (crosses) and 0.48 (squares). The solid is numerical evaluation of equations (4.10) and (4.11).

Figure (4.2) independent of the order parameter symmetry and transition temperature. There is, however, a slight flattening of the curve due to the renormalization of the absolute value of $\lambda_L(\mu)$ by strong coupling effects which is more pronounced near the vHs. Equation (4.7) is not well suited for showing this effect explicitly. Instead we can use the Fermi surface approximation and constant EDOS (infinite band) to examine the effects of strong coupling on $\lambda_L(0)$. For such an approximation, we can write $\lambda_L(T)$ as

$$\lambda_L(T) = \left[\frac{4\pi}{3} N(0)\, e^2 v_F^2\, T \sum_{n=1}^{\infty} \frac{\Delta^2(\,i\,\omega_n)}{Z(i\omega_n)[\,\omega_n^2+\Delta^2(\,i\omega_n)]^{3/2}}\right]^{-1/2} \qquad (4.12)$$

If we use $Z(i\omega_n) \sim 1+\lambda$, we can see right away that $\lambda_L(0)$ is proportional to $\sqrt{1+\lambda}$ implying that the shortest penetration depth is that for BCS. The expectation is that λ (mass enhancement) varies with μ and is largest on the vHs near μ=0, which makes the $\lambda_L^{-2}(\mu)$ curves flatter near μ=0. In Figure (4.3), we show results of the exact calculation of the zero penetration depth squared as a function of chemical potential for d–wave (upper frame) and s–wave (lower frame). The spectral density used for these calculations is an Einstein spectrum centered at ω_E=30 meV with a cut off of 1200 meV. The hopping integral $\bar{t}$ is 50 meV so the band width is 400 meV. For the d–wave case, we set g=λ=1.0 and B=0.0 (solid triangles; T_c^0=129.5k at μ=0.0), B=0.16 (open circles; T_c^0=127.6 K at μ=–20 meV), B=0.32 (crosses; T_c^0=122 K at μ=–40 meV), B=0.48 (solid squares; T_c^0=114.6 K at μ=–75 meV). We have normalized all the values by $\lambda_L^{-2}(0)$ at B=0.0 at μ=0.0, which is about ~ 14342 Å and is 8.4 times larger than the BCS value. This is much larger than the observed values for HTSC's and is consequence of large λ. Such large values of

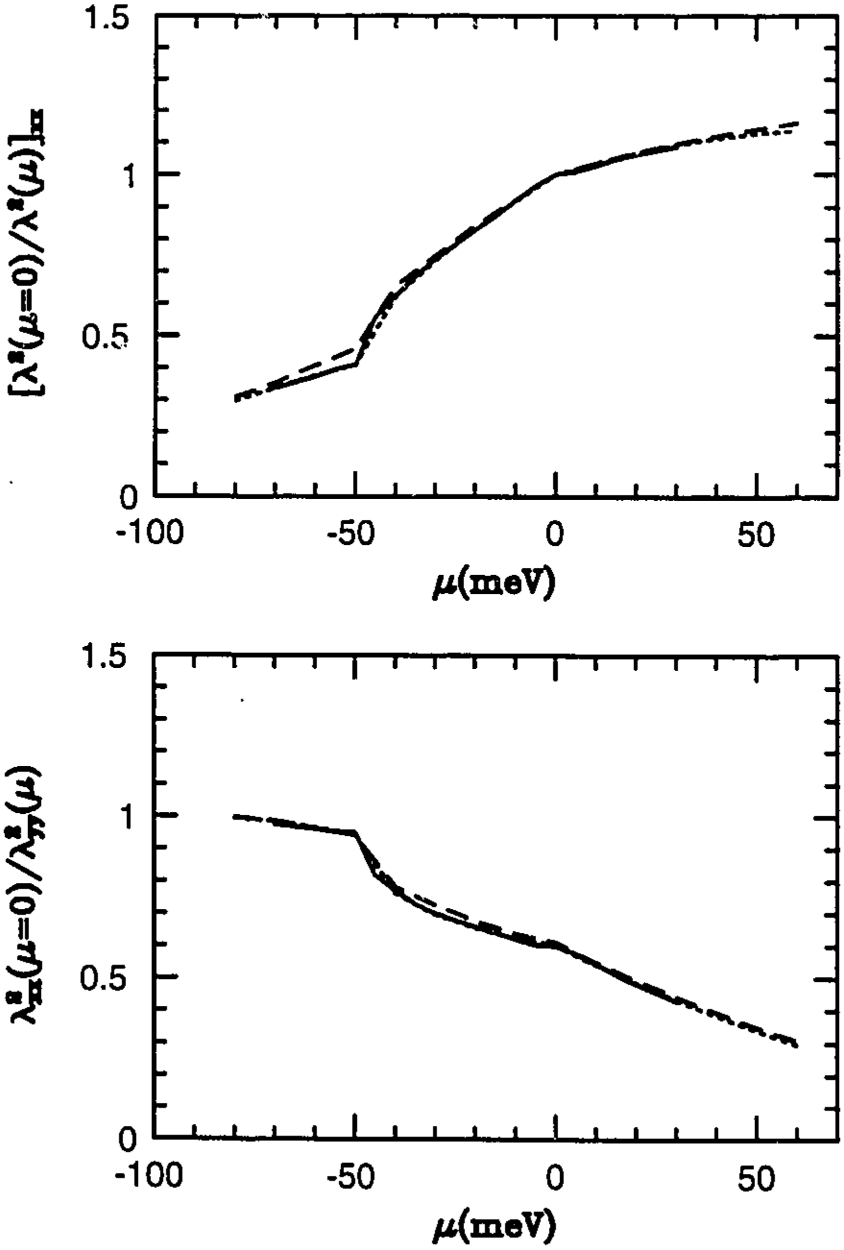

Figure 4.4: The zero temperature penetration depth tensors for d–wave (solid) and s–wave (dotted and dashed) for the Abrikosov model (see text for parameters).

$\lambda_L(0)$ can be reduced considerably by choosing higher values of the hopping integral, sacrificing numerical accuracy, and lower values of λ and larger values for ω_E. The solid triangles in the lower frame of Figure (4.3) are for an s–wave superconductor with B=0.0, g=1.0, λ=1.6 and the rest of the parameters the same as in the upper frame. The optimal value of T_c is 90.8 K and $\lambda_L(0)$ is larger by about 12% when compared to its counter part in the upper frame. This is in agreement with our simple analysis of $\lambda_L(0) \propto \sqrt{1+\lambda}$, where the expected increase is about 14%.

In Figure (4.4), we plot the normalized zero temperature penetration depth tensors for xx (upper frame) and yy (lower frame) of the Abrikosov band with a_1=0.01 and $(\hbar^2/ma^2)$=10 meV. The solid curve is d–wave with T_c^0=84.8 K at μ=–40 meV and the dotted curve is s–wave with T_c^0=54.8 K at μ=–40 meV. For both curves ω_E is 60 meV, the cut off is 1200 meV, λ is 1.0, and g is 1.0. The value of $\lambda_{xx}(0)$ for the s–wave case is only 0.45% larger than the d–wave case. The dashed curve is for an s–wave case with ω_E=30 meV and cut off of 1200 meV. $\lambda_{xx}(0)$ is larger in this case by about 41% compared with the previous s–wave . The rest of the parameters are λ=6.0, T_c^0=99.4 K at μ=–30 meV. The three curves shown have almost identical shapes even though they have different coupling strengths and T_c^0's and are independent of gap symmetry. We make the assertion that the zero temperature penetration depth is largely a normal state property which can be affected in magnitude by coupling strength, but its shape as a function of chemical potential can be obtained from the dispersion relations directly. The shortest zero temperature penetration depth is that for a BCS superconductor and depends only on the normal state dispersion. Strong coupling effects increase the penetration depth in magnitude.

III) The Finite Temperature Behaviour

To examine the low temperature behaviour of $\lambda_{ij}(T)$ near zero temperature, we have to figure out the contribution of the first term in equation (4.8). We will show that such a term is exponentially small for an s–wave superconductor and linear in temperature for the d–wave case. By using the same transformations used to arrive at equations (4.10) and (4.11), we can write the first term of equation (4.8) as

$$\frac{8\pi e^2}{Vc^2}\sum_{k}\left[-\beta\frac{e^{+\beta\sqrt{\epsilon_k^2+\Delta_k^2}]^2}}{\left[1+e^{\beta\sqrt{\epsilon_k^2+\Delta_k^2}}\right]^2}\right]v_{ki}v_{kj},$$

i) if the gap is isotropic with no zeros then the minimum of $\sqrt{\epsilon_k^2+\Delta_k^2}$ is $|\Delta|$, so the largest contribution is from the Fermi surface ($\epsilon_k=0$) and where we have $v_{ki}v_{kj}$ being regular and nonzero. So, such a term is of the order of $\exp(-|\Delta|/T)$ for small T. ii) if the gap is d–wave then it has a zero on the Fermi surface which will contribute the most and, after some tedious algebra, we can show that its contribution at small T is

$$-\frac{32e^2\bar{t}}{\pi c' c^2\hbar^2\beta\Delta}\int_0^\infty d\xi\int_0^\infty d\nu\,\frac{e^{\sqrt{\xi^2+\nu^2}}}{\left[1+e^{\sqrt{\xi^2+\nu^2}}\right]^2},$$

which is equal to $-16e^2\bar{t}/c'c^2\hbar^2\beta\Delta\,\ell n2$, which is clearly linear in T. So for simple tight binding and d–wave, we have

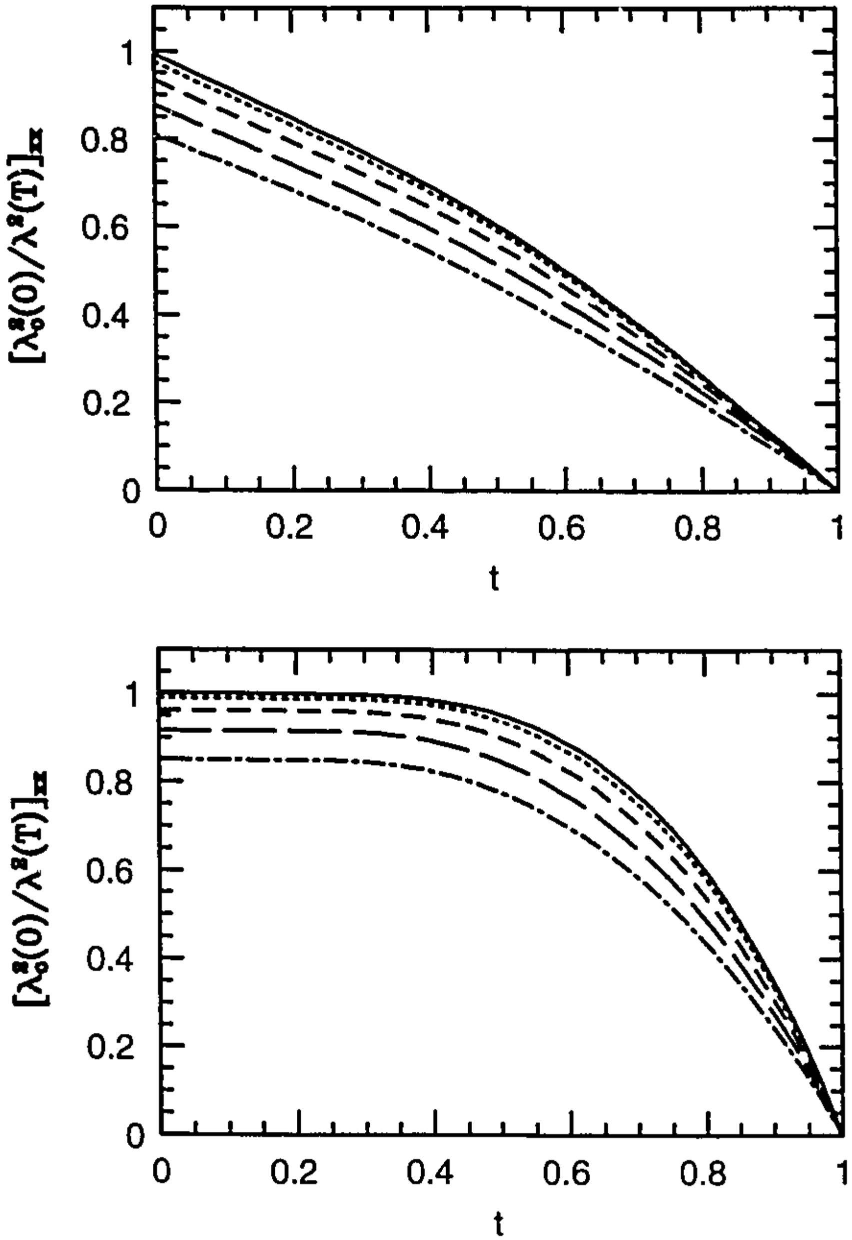

Figure 4.5: London penetration depth normalized to the optimal doping value for superconductors with simple tight binding dispersion (B=0.0). The upper frame is for d–wave and the lower frame is for s–wave.

$$\left[\frac{\lambda^2(0)}{\lambda^2(T)}\right]_{xx} = 1 - \frac{\pi \ell n 2}{4I(|\frac{\mu}{4\bar{t}}|)\left[1-|\frac{\mu}{4\bar{t}}|\right]}\,\frac{T}{\Delta}, \quad T\rightarrow 0 \qquad (4.13)$$

Armed with these low temperature limits for the penetration depth for both d– and s–wave, we now examine the whole temperature range up to T_c numerically.

In Figure (4.5), we show $\lambda(T)$ as a function of t for both d–wave (upper frame) and s–wave (lower frame) for a tight binding dispersion with $\bar{t}$=50 meV, ω_E=30 meV and cut off of 1200 meV, λ=0.7 and for the d–wave case g=0.82 . The optimal doping transition temperatures are 90.1 K and 61.4 for the d–wave and s–wave respectively, i.e. chemical potential μ=0.0. For both frames, the chemical potential is incremented by 20 meV for each curve where T_c decreases and $\lambda_L(0)$ increases both in a monotonic fashion. The ratios of T_c to T_c^0 in the upper frame are 0.95, 0.78, 0.53 and 0.25, and in the lower frame are 0.96, 0.88, 0.80 and 0.70. We notice no appreciable change in the shape of $\lambda_L^{-2}(T)$, furthermore, the slope of $(\lambda_L(0)/\lambda_L(T))^2$ with respect to the reduced temperature is roughly constant and independent of μ for $\mu<\bar{t}$ (hopping integral). For d–wave, this might seem, at first sight, to be in contradiction with equation (4.13) but, in fact, it is not. It turns out that $2\Delta/T_c$ increases monotonically with μ in such a way that it compensates for the decrease of (1–x)I(x) term with $x=|\mu/4\bar{t}|$ present in equation (4.13). For the s–wave curves, $\lambda_L(T)$ is only 3% larger than its zero temperature value at reduced temperature of 0.5, and the drop of $\lambda_L(T)$ with T is consistent with an exponential (flat) drop expected for an s–wave superconductor. For BCS, $\lambda_L(T)/\lambda_L(0)=1.03$ occurs at a reduced temperature of about 0.38, and the slope of $\lambda_L^2(T)/\lambda_L^2(0)$ at t=1 is ~ –2. The lower frame, however, shows a slope of –4 for the solid curve, which is the same as the slope predicted by the two fluid model. These curves do not deviate

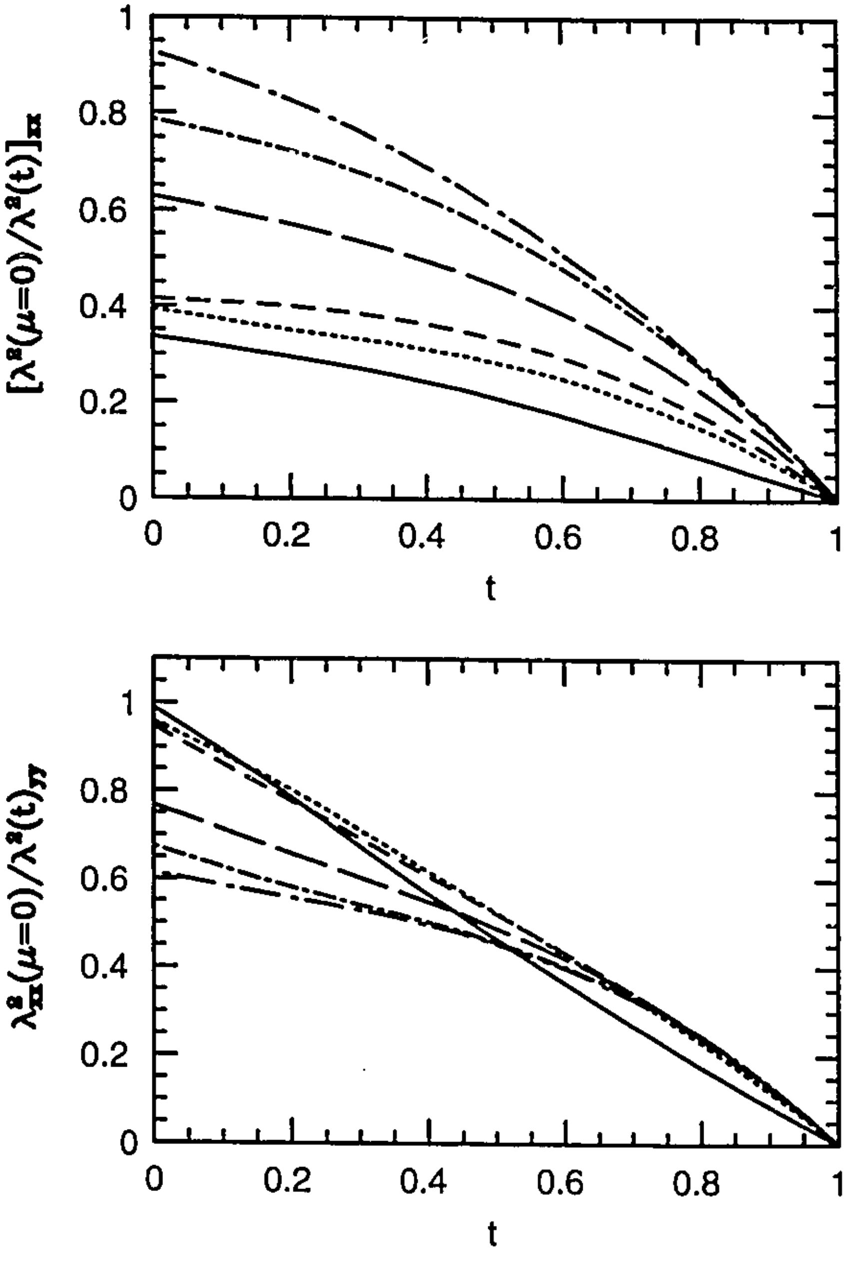

Figure 4.6: d–wave penetration depth with Abrikosov model, the curves are for T_c/T_c^0=0.40 (solid), 0.90 (dotted), 0.96 (dashed), 1.0 (long dashed), 0.92 (dotted dashed) and 0.70 (dotted long dashed).

strongly from those obtained with moderate strong coupling in ordinary Eliashberg theory with constant EDOS. Strong coupling effects initially increase the slope near T_c for both d–wave and s–wave and then decrease it considerably for high coupling strengths. We have tried many parameter variations in the hope of increasing the magnitude of the slope of $\lambda_L^2(T)/\lambda_L^2(0)$ near T_c for the d–wave case, ~ –1.33, to match it with experimental data, ~ –3 to –4 for Y123, but met with no success.

Next, we turn our attention to the Abrikosov model with a saddle point singularity at $\mu \sim -45$ meV and band width of ~390 meV, as shown in the solid line of the lower frame of Figure (4.1). We calculate $\lambda_{xx}(T)$ and $\lambda_{yy}(T)$ for a d–wave superconductor with ω_E set to 60 meV (cut off of 1200 meV) and coupling constants $g=\lambda=1.0$. Because of the asymmetry of the band, we study both the under doped and over doped cases. Optimal doping (long dashed curve in Figure (4.6)) for these parameters, λ and EDOS, is at ~ $\mu= -40$ meV with $T_c^0=84.9$ K. In Figure (4.6) we show the normalized penetration depth tensors for under doped cases with $\mu= -70$, –55 and –50 meV (solid, dotted and dashed curves respectively) and the over doped cases with $\mu= -25$ and –10 meV (dotted dashed and dotted long dashed curves respectively). All the curves exhibit linear behaviour at low temperature. One curve, however, exhibits a flat slope namely the one for $\mu= -50$ meV. This value of μ lies exactly on the vertical line of the saddle singularity in Figure (4.1). We think that there is a competition between the linear drop of $\lambda_L(T)$ due to a decrease in superfluid fraction and the linear increase in $\lambda_L(T)$ due to an increase in the effective mass coming from the proximity of the Fermi level to the flat portion of the band. This assertion can be further substantiated on close examination of $\lambda_{xx}(T)$ for an s–wave superconductor with the same EDOS parameters. The parameters used to calculate Figure (4.7) are the same as those used for Figure (4.6)

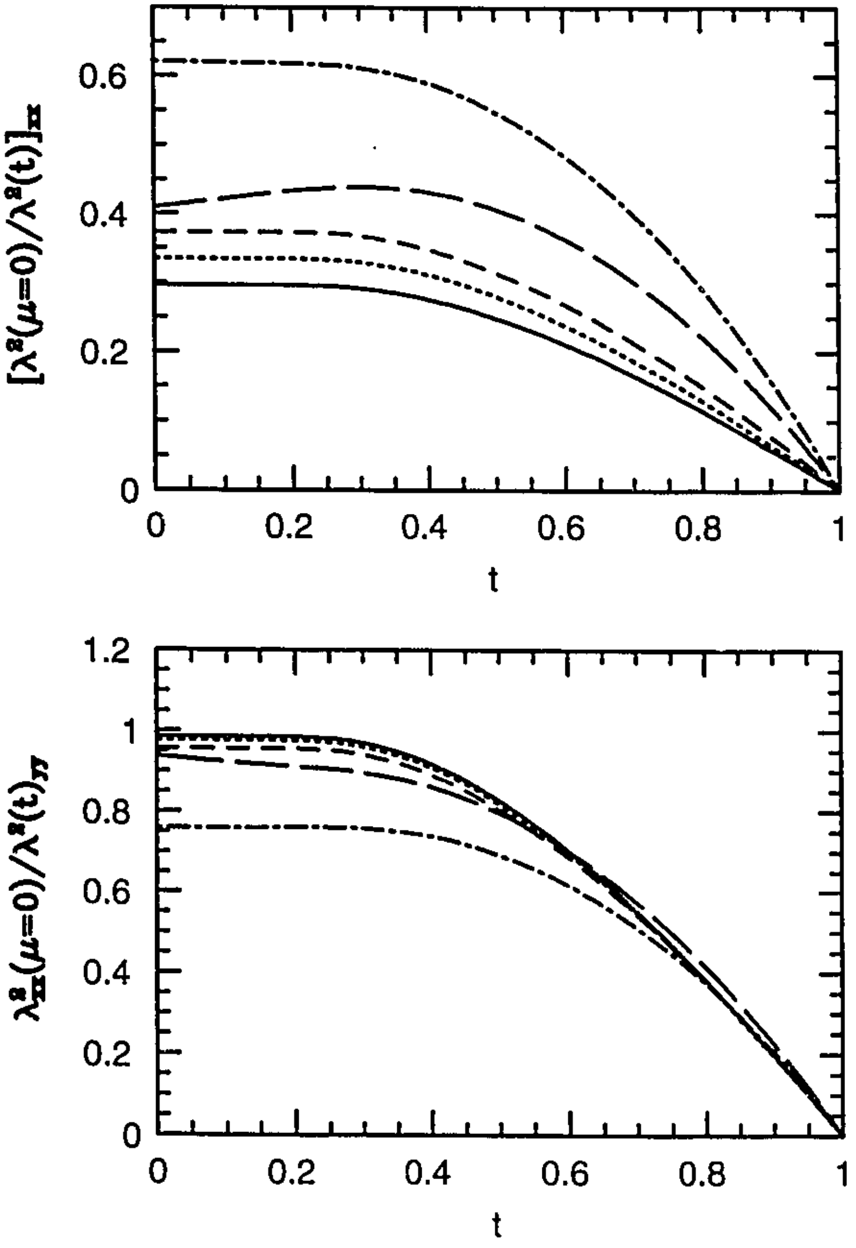

Figure 4.7: s–wave penetration depth for Abrikosov model, T_c/T_c^0 ratios are 0.24 (solid), 0.37 (dotted), 0.68 (dashed), 0.93 (long dashed) and 1.0 (dotted dashed).

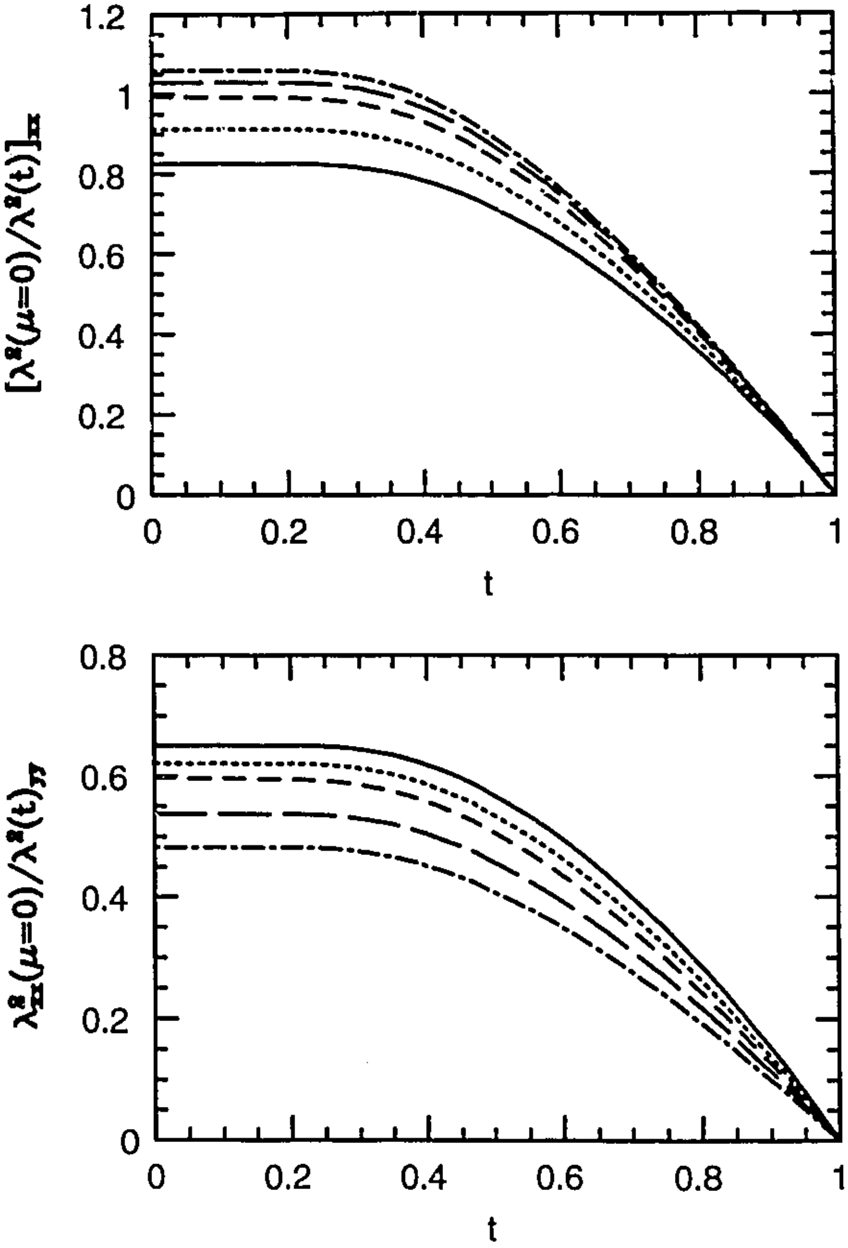

Figure 4.8: Similar to Figure (4.7) but for over doping with T_c/T_c^0 ratios of 0.85 (solid), 0.73 (dotted), 0.62 (dashed), 0.52 (long dashed) and 0.44 (dotted dashed).

except that the order parameter in this case is s–wave. The curves are for μ values of 80 (solid), –70 (dotted), –60 (dashed), –50 (long dashed) and –40 meV (dotted dashed curve). Except for the long dashed curve, all the curves exhibit the flat saturation below t≃0.25 which is clearly different from the tight binding results shown earlier in Figure (4.5), where it occurs below t~0.4. Optimal doping for this s–wave case is at μ= –40 meV with T_c^0=54.8 K. The long dashed curve in the upper frame of Figure (4.7) is different and drops with a decrease in t near small t. This corresponds to an increase of $\lambda_{xx}(T)$ as the temperature is lowered. This effect is only pronounced near the flat portion of the band (μ=–45 meV). In Figure (4.8), we show typical curves for $\lambda_{ii}(T)$ for the over doped cases. The curves are for μ values of –20 (solid), –10 (dotted), 0 (dashed), 10 (long dashed), and 20 meV (dotted dashed curve). All of $\lambda_{yy}(T)$ curves exhibit saturation at the same reduced temperature, t~0.3, as is also the case for the $\lambda_{xx}(T)$ curves. The two tensors are very much alike in their temperature dependencies.

IV Impurity Effects and Experiment Comparison

In this section, we will study the effect of impurity scattering on the London penetration depth of a d–wave superconductor. The calculations are for a superconductor with a simple tight binding dispersion and chemical potential of μ=0.0 meV. We should point out at this stage that the d–wave order parameter is not a fully consistent solution when the Abrikosov dispersion is used or, for that matter, for any orthorhombic 2D bands. This does not appreciably modify the clean limit results, showed in Figure (4.6), and leaves the linear law unchanged. Because of this complication, we will only use a tight binding dispersion (tetragonal symmetry). With tight binding dispersion, the full d–wave order parameter is self

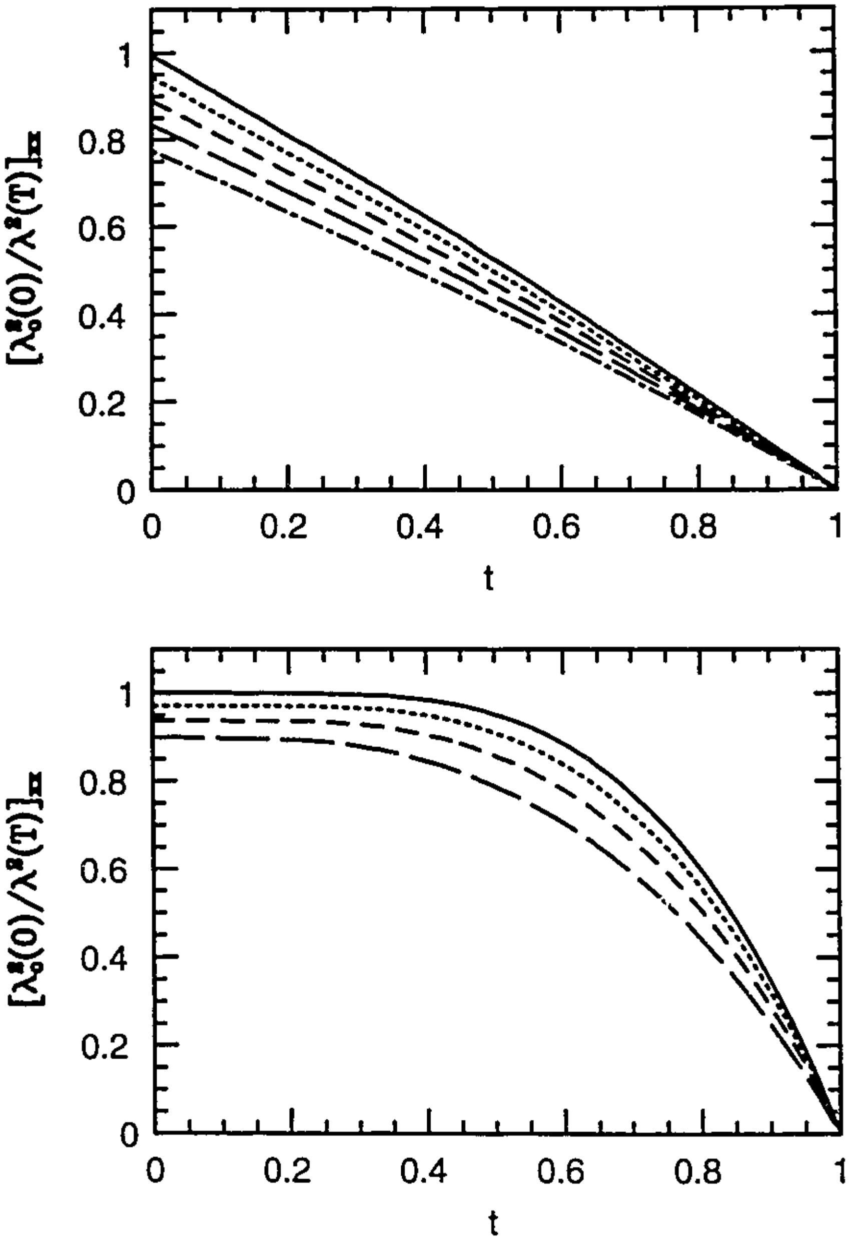

Figure 4.9: Effect of paramagnetic impurity scattering (Born approximation) on d–wave (upper frame) and s–wave (lower frame) superconductors. The solid curves are for the clean limit. See text for parameter.

consistent even in the dirty limit.

In the upper frame of Figure (4.9), we calculate the effect of normal (or paramagnetic) impurities on a d–wave superconductor with ω_E=30 meV, cut off of 1200 meV, hopping integral of 50 meV, g=183 and λ=0.001. Normal impurity doping causes a reduction in T_c proportional to the impurity concentration. The solid curve is for the pure limit with T_c^0=90.4 K and μ=0.0 meV and is held constant for all other curves. The ratios of T_c to T_c^0 are 0.95 (dotted), 0.90 (dashed), 0.85 (long dashed), and 0.80 (dotted dashed curve). The overall shape and temperature dependence does not change in any appreciable fashion and stays the same as that of the pure limit. The linear law is very stable for Born scattering and only for a huge reduction in T_c, of order of 56%, would there be significant deviations towards a quadratic law at low T [Arberg, Mansor and Carbotte 1993]. Next to reducing T_c, the most important effect of Born scattering is to decrease linearly the inverse square of the value of the zero temperature penetration depth with changing impurity concentration.

A similar increase in $\lambda_L^2(T)$ is observed when paramagnetic impurities are introduced in an s–wave superconductor. The lower frame of Figure (4.9) shows results for the only s–wave case considered in this section. The parameters are the same as used in the upper frame except that g=1.0 and λ=0.7. The curves are for T_c/T_c^0 equal to 0.90 (dotted), 0.80 (dashed), 0.68 (long dashed) and the solid curve is the optimal clean limit with $T_c^0 \simeq 61.4$ K. We note that besides the linear decrease in T_c and linear increase of $\lambda_L^2(T)$ with t^-, there is a reduction of the slope of $\lambda_L^{-2}(T)$ at T_c and a reduction of the reduced temperature at which $\lambda_L^{-2}(T)$ becomes flat, from t~0.4 for the pure case to t~0.25 for a 32% reduction in T_c.

Unitary scattering has a very different effect on $\lambda_L(T)$ than does Born

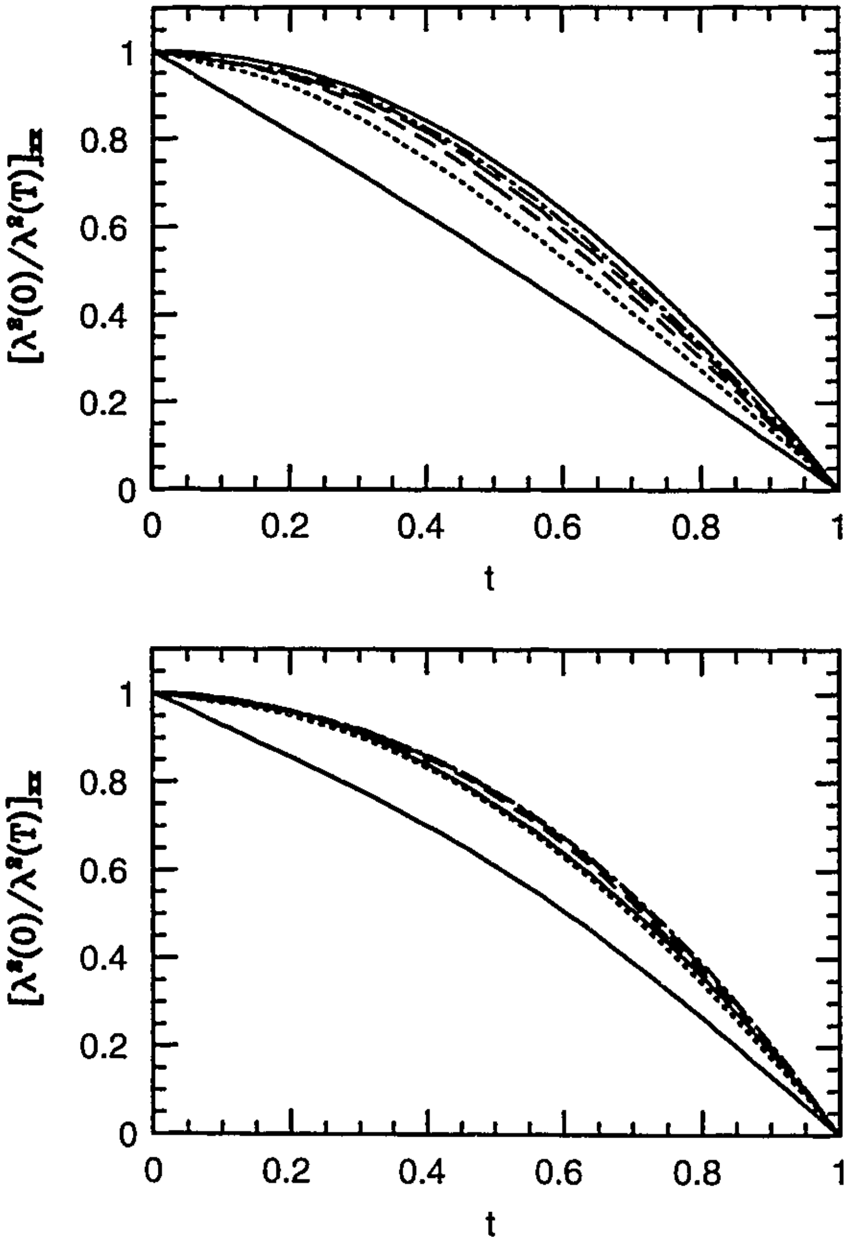

Figure 4.10: Effect of resonance impurity scattering on two d–wave superconductors; λ=0.001 (g=183) (upper frame) and λ=0.7 (g=0.82) (lower frame). See text for parameters.

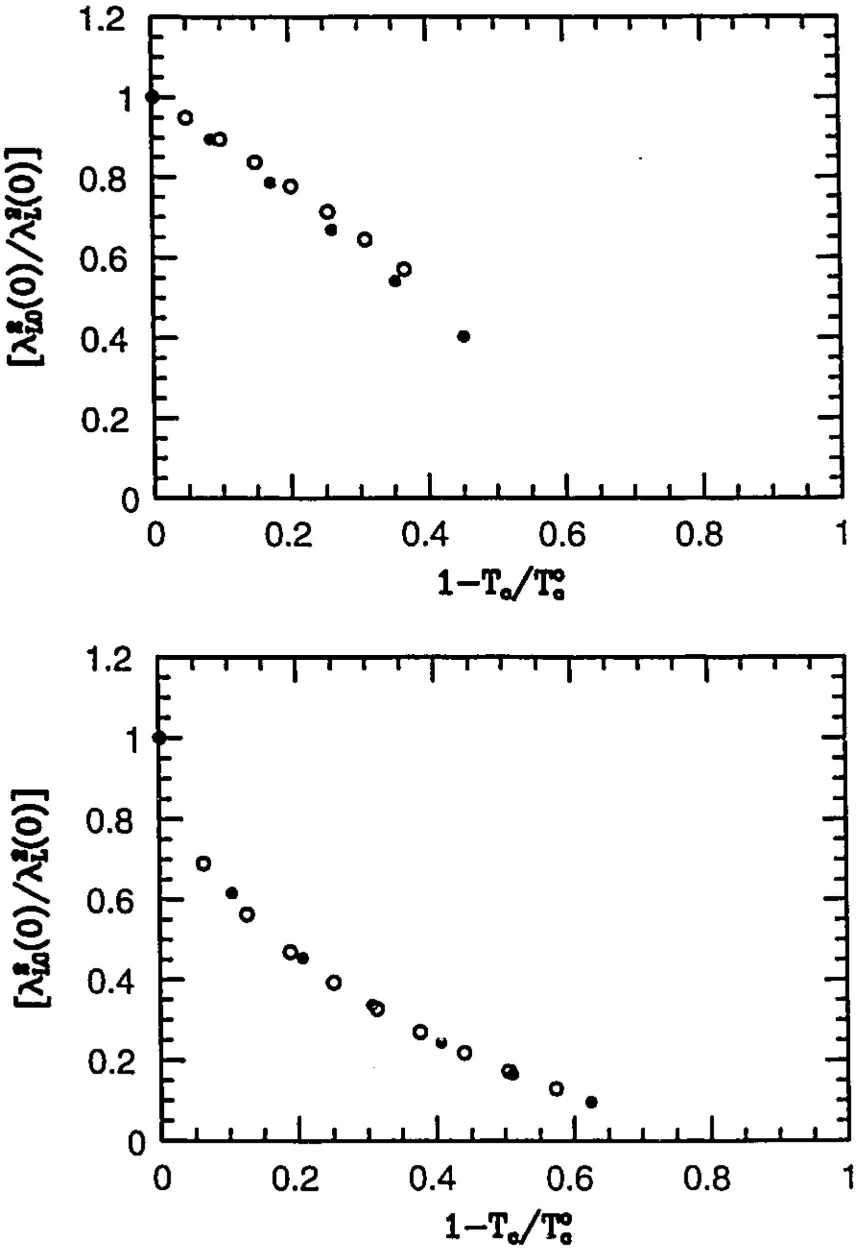

Figure 4.11: $\lambda_L^{-2}(0)$ normalized by the clean limit value vs $1-T_c/T_c^0$, where T_c^0 is the clean limit T_c. Both T_c and $\lambda_L(0)$ were reduced by increasing the impurity concentration, t^+ in the upper frame and Γ in the lower frame. Open circles are for $\lambda=0.001$ ($g=183$) and closed circles are for $\lambda=0.7$ ($g=0.82$).

scattering. The upper frame of Figure (4.10) has the same parameters as used in the upper frame of Figure (4.9). In this case, we plot $\lambda^{-2}(T)$ normalized to $\lambda_L^{-2}(0)$ versus the reduced temperature for varying the concentration of resonant scattering centres, Γ. There are two solid curves in this figure. The upper one is $1-t^2$ and is for comparison. The lower one is the pure limit. The percent reductions in T_c are 6.4% (dotted), 12.7% (dashed), 19.0% (long dashed) and 25.2% (dotted dashed curve). The top frame is for a case close to BCS in the sense that $\tilde{\omega}_n$ is very close to ω_n even though there are retardation effects in the pairing potential. Except for the dotted curve, all other curves obey $1-t^2$ law near small t. There is also a systematic increase of the slope of $\lambda_L^{-2}(T)$ normalized to $\lambda_L^{-2}(0)$ at T_c. As Γ increases, in each case the entire curve moves closer to the $1-t^2$ curve. This $1-t^2$ law, however, is never obeyed exactly over the entire temperature range.

If we consider a stronger coupling case with the same parameters but with $g=0.82$ and $\lambda=0.7$ and almost the same transition temperature, $T_c^0 \sim 90.1$ K, lower frame of Figure (4.10), we notice that the $[\lambda_L^2(0)/\lambda_L^2(T)]$ curves are pushed past the $1-t^2$ law (upper solid curve) as Γ increases and, of course, T_c decreases. The curves in increasing order of percent reduction of T_c (increase in Γ) are 10.6% for the dotted, 20.8% for the dashed, 30.7% for the long dashed, and 40.7% for the dotted dashed curve. The lower solid curve is the pure limit and is bent more toward the $1-t^2$ curve than the previous weaker coupling case, shown in the upper frame.

The reduction of T_c with impurity concentration Γ is linear for small Γ but the decrease of $\lambda_L^{-2}(0)$ with Γ is less than linear and much higher than for Born scattering with a similar reduction of T_c. This is shown in the next figure. In Figure (4.11), we show $\lambda_L^{-2}(0)$ normalized to the clean limit $\lambda_L^{-2}(0)$, denoted as

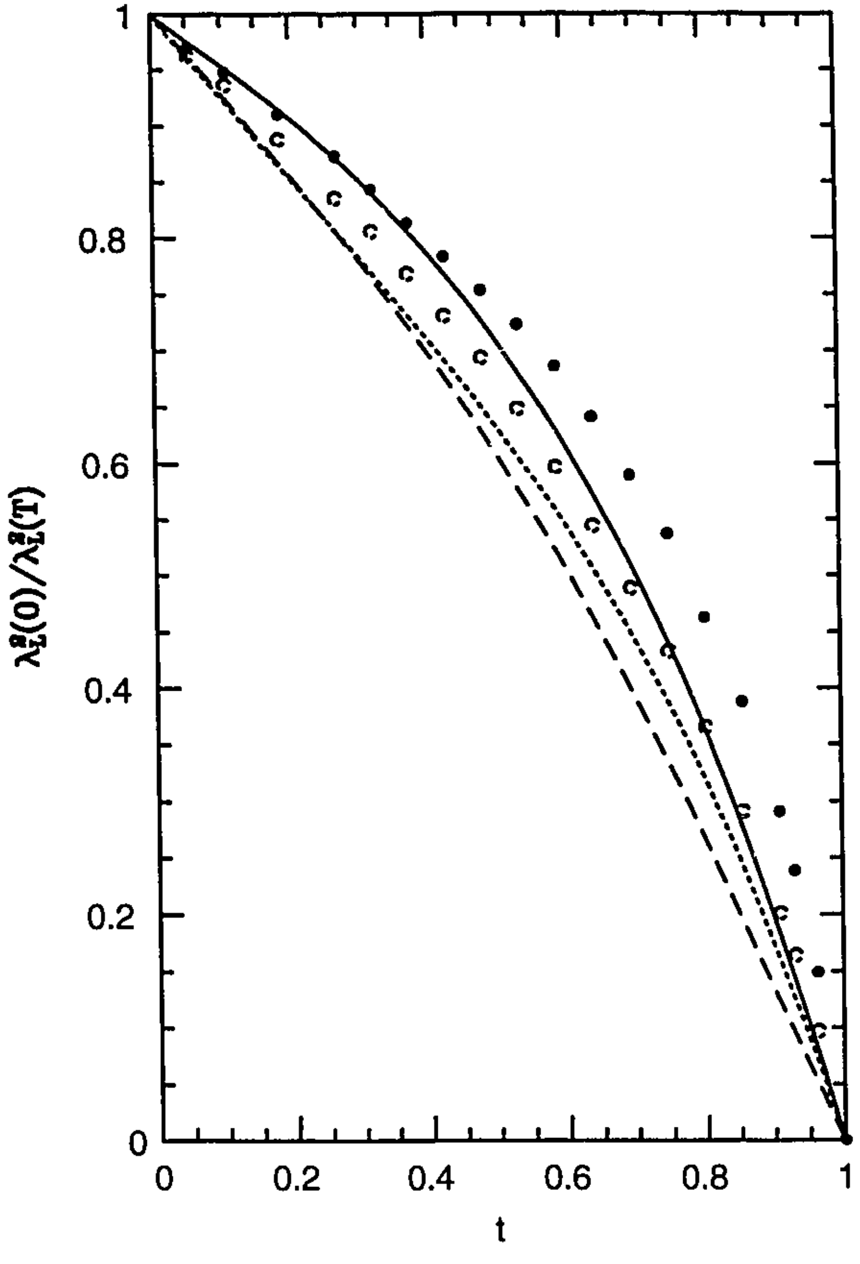

Figure 4.12: Inverse square penetration depth normalized to its zero temperature value for untwined Y123 single crystal, in a – (solid circles) and b – (open circles). The dashed curve is for d–wave and tight binding dispersion, λ=0.7 (g=0.82) and ω_E=30 meV. The solid and dotted curves are d–wave with Abrikosov dispersion at optimal doping with ω_E=60 meV and λ=1.0 (g=1.0) in x and y directions respectively.

$\lambda_{Lo}^{-2}(0)$, and plotted against $1-T_c/T_c^0$. The upper frame is for Born scattering and the lower frame is for unitary scattering. The open circles are for the BCS type case with g=183 and λ=0.001 and the solid circles are for the case of g=0.82 and λ=0.7. It is quite apparent that resonant scattering is more effective in increasing $\lambda_L(0)$ for small concentrations of impurities Γ than for large concentration. In a recent preprint by Ulm et al., it is shown that the increase of $\lambda_L(0)$ for thin films of Y123 is much higher than the predicted values of d–wave shown in Figure (4.11). We will list here some typical percent reductions of T_c and corresponding values of $\lambda_{Lo}^2(0)/\lambda_L^2(0)$; 1.8% and 0.25; 3.2% and 0.26; 31% and 0.15; 53% and 0.02; 54% and 0.026; 12% and 0.23; 32% and 0.033. Beside the scatter in these values, they lie much lower than our calculated values. These experimental values are not corrected for the contribution of grain boundaries which the authors believe to be small.

Our last figure, Figure (4.12), shows the famous London penetration depth results for a very clean untwined Y123 single crystal with T_c of 93.5K measured by Hardy et al. [Hardy 1993, 1994]. The open circles are for the yy direction and the solid circles are for the xx direction. We would like to mention that the measured data are denser than shown in this graph for the two ends near T_c and T=0. Because the experimental data show linear dependence on T near T_c and T=0, we took the liberty of omiting some of the points to make the graphs seem less crowded. One important feature of the data is the large value of the slope near t=1, –4 for xx–direction and –3.3 for yy direction, which is larger than that for BCS, namely –2, and is attributed to 2D fluctuations. The zero temperature London penetration depths were measured by Basov [Basov et al. 1994] to be $\lambda_{xx}(0)$=1600 Å and $\lambda_{yy}(0)$=1000 Å. This large anisotropy suggests that a substantial portion of the superconducting condensate is on the chains. We have not modeled the chains in the tight binding dispersion and hence $\lambda_{xx}(T)=\lambda_{yy}(T)$. The dashed curve in Figure (4.12) is the same as the solid curve in the lower frame of Figure (4.10). This tight binding curve compares well with the data. Apart from the obvious linear dependence at low T, the data points are slightly higher than this d–wave curve. One possible way of pushing this slope up is to change the dispersion (solid and dotted curves in Figure (4.12)). Another possibility is to have an anisotropic d–wave gap, this anisotropy might be derived from the presence of the chains that lead directly to anisotropy in the zero temperature limit of the penetration depth. This will affect the slopes of the gap along the node lines near the Fermi surface leading naturally to modified slopes for the penetration depth near T=0. We actually did not prove this, but quite generally, the linear drop of the inverse square of the penetration depth is related to the amount of phase space of the nodes on the Fermi surface. Band anisotropy, by itself, is also sufficient to introduce an anisotropy in the low temperature slope as shown by the solid, $\lambda_{xx}(T)$, and dotted, $\lambda_{yy}(T)$, curves in Figure (4.12). The solid and dotted curves are for the Abrikosov model at $\mu= -40$ meV shown earlier in Figure (4.6) as long dashed curves.

V) Conclusion

We have shown that the London penetration depth at zero temperature is a strong function of the type of electron dispersion as well as the effective mass renormalization. That is to say, it is a normal state property and independent of the symmetry of the order parameter. On the other hand, the slope of $\lambda_L^{-2}(T)$ near T=0 is a strong function of the symmetry of the order parameter, exponential decrease for s–wave and linear for d–wave, as well as the band type. In tight binding d–wave, this slope is insensitive to filling for $0 \leq |\mu| \leq \bar{t}$ (hopping integral), while for the Abrikosov model, it is sensitive to filling. We have noticed a strong temperature dependence of the effective mass only near the saddle point singularity in the Abrikosov model which is reflected strongly in the temperature dependence of $\lambda_L(T)$ for both types of order parameters. Our calculated values of $\lambda_L(0)$ as a function of impurity doping are much smaller than the thin films experimental results, but the low temperature dependence of $\lambda_L(T)$ can be reconciled with the resonance impurity scattering scheme and a d–wave order parameter.

Finally, if we consider that the true mean field transition temperature is probably higher than the measured one due to fluctuations, the magnitude of the slope of $\lambda_L^{-2}(T)$ will be reduced near small T and increased near T_c resulting in better agreement with the data at low T and near T_c. Furthermore, anisotropy in the dispersion and anisotropy in the d–wave gap itself, with perhaps some small extended s–wave, $[\cos k_x a + \cos k_y a]$, part mixed in it, will certainly result in slight modifications of both the slope of $\lambda_{ii}^{-2}(T)$ and its zero temperature value, $\lambda_{ii}(0)$.

Chapter 5

The Specific Heat

I) Introduction

In this chapter, we will examine the effect of a nonconstant EDOS on the specific heat difference ΔC between the normal and superconductor states. To start, we will review the specific heat of a normal metal and a superconductor. We will examine the effect of including a logarithmic singularity in the EDOS on the electronic specific heat of both states. We will also derive the low temperature asymptotic limit of the superconducting specific heat for a clean BCS superconductor with s– and d–wave order parameters. In the next section, we will provide a brief review of experimental results on the specific heat of quasi two dimensional superconductors and on the HTSC's outlining, in particular, some of the difficulties and controversy in interpretation of the experimental results. Our numerical results for $\Delta C(T)$ will be presented in Sections III and IV. Section III deals with an s–wave superconductor with the infinite band model, introduced earlier in Chapter 3. Section IV considers d–wave superconductors with only a tight binding dispersion. We will also make comparisons with results for an s–wave superconductor within the same finite band model. Some of our calculations of the specific heat jump, $\Delta C(T_c)$, will be compared to experimental results on Y123.

In our formalism, we can only calculate the specific heat difference between the superconducting and normal states and not each individually. This specific heat difference, $\Delta C = c_{es} - c_{en}$, can be calculated from the following thermodynamic relation

$$\Delta C = -T \frac{d^2 \Delta\Omega}{dT^2}$$

where $\Delta\Omega$ is the free energy difference between the superconducting and normal states derived earlier in Chapter 2 and given by equations (2.35) or (2.45) and (2.46) in case of resonant scattering. Later, we will demonstrate that when the Fermi level is pinned to the logarithmic singularity in the EDOS, the entropy of the normal state at low temperature is anomalous. This anomaly will be reflected in the numerical results for $\Delta C/T$ for both types of order parameters, d and s–wave.

In the normal state, the electronic contribution to the specific heat, c_{en}, for a constant EDOS varies linearly with temperature, i.e. $c_{en} = \gamma_n T$. The proportionality constant γ_n is equal to $2\pi^2 N(0)/3$ [Ashcroft and Mermin 1976]. The contribution of the phonons to the specific heat is $B_3 T^3$ at low temperature, this is also true in the superconducting state. The proportionality constant B_3 is related to the Debye temperature of the material. When the electron–phonon interaction is included, γ_n is amplified by a factor of order $(1+\lambda)$ where λ is called the mass enhancement factor for the electrons. This mass enhancement is attributed to the drag of the carriers caused by lattice vibrations. Other contributors to the specific heat at low temperature are magnetic impurities with a Schottky term C_{Sch} and in the presence of a magnetic field a hyperfine term proportional to T^{-2}. At higher temperatures, anharmonic effects for the phonons contribute terms with T^2 and T^5 temperature dependencies. Bulk measurements of the specific heat can also be complicated by contributions from impurity phases and phase transitions.

The disection of the various contributions to the specific heat in the normal state is only reasonable if the chemical potential is near a smooth part of the EDOS. Large variations of the EDOS on a small energy scale near the chemical potential may result in non–trivial modifications of the temperature dependence of γ_n. To get a flavour for this, consider the case where the chemical potential is pinned to a simple vHs for which the EDOS diverges logarithmically, as say $-\ell n|\epsilon|$. The excess specific heat, c^{ex}, coming from this extra piece in the EDOS, can be computed for a free electron gas from

$$c^{ex} = \frac{\partial U^{ex}}{\partial T} = \frac{\partial}{\partial T}\int_{-\infty}^{\infty} d\epsilon(-\ell n|\epsilon|)f(\epsilon)\epsilon,$$

where $f(\epsilon)$ is the Fermi function. c^{ex} is easily evaluated and found to be equal to $-(\pi^2/3\ T\ell nT - c'T)$ and $c' = 2\int_0^\infty x^2 \ell nx\ e^x/(1+e^x)^2 dx$, spin degeneracy is neglected. It is clear that the temperature derivative of the excess entropy, c^{ex}/T, approaches ∞ as $T \rightarrow 0^+$, i.e. a plot of c/T vs T should give a constant value with a logarithmic upturn for small T. This upturn is very different from that attributed to the Schottky anomaly. The electron–phonon interaction does not eliminate this upturn but rather enhances it. The presence of small but finite concentrations of impurities or physical defects will certainly supress such an upturn and regularize γ_n.

In the superconducting state for an s–wave superconductor, the electronic specific heat, c_{es}, vanishes exponentially at low temperature. It is simple to show that in this case [Rickayzen 1965],

$$c_{es} \sim 2\sqrt{2\pi}\, k_b\, N(0)\, \Delta \left[\frac{\Delta}{k_b T}\right]^{3/2} \exp\left[-\frac{\Delta}{k_b T}\right].$$

This is expected because the excitation spectrum is gapped by Δ for an s–wave superconductor. With a simple vHs in the EDOS and filling $\delta=0$, one can show that

$$c_{es} \sim 2\sqrt{2\pi}\, k_b\, N(0)\, \Delta \left[\frac{\Delta}{k_b T}\right]^{3/2} \left[r+s\, \ell n \left[\frac{Ef}{\Delta}\right] + \frac{1}{2} s\, \ell n \left[2e^{\gamma} \frac{\Delta}{k_b T}\right]\right] \exp\left[-\frac{\Delta}{k_b T}\right]$$

where $\gamma=0.577$ ..., Euler's constant. c_{es} is still exponentially damped for an s–wave superconductor even with the vHs in the EDOS.

For d–wave superconductors with simple tight binding dispersion (next neighbour hopping B=0), c_{es} is not exponentially gapped. With the same transformations presented earlier in Chapter 4 to derive the low temperature limit of the London penetration depth, we can show that c_{es} for a d–wave superconductor can be written as

$$c_{es} \sim \frac{2 k_b (k_b T)^2}{\pi^2 \bar{t}\, \Delta \left[1-\left[\frac{\mu}{4\bar{t}}\right]^2\right]} \int_0^{\infty} d\nu \int_0^{\infty} d\xi\, \frac{(\xi^2+\nu^2)\, e^{\sqrt{\xi^2+\nu^2}}}{\left[1+e^{\sqrt{\xi^2+\nu^2}}\right]^2}.$$

Evaluation of the integral yields

$$c_{es} \sim \frac{9}{2}\,\zeta(3)\,\frac{k_b^3\;T^2}{\pi\bar{t}\;\Delta\;\left[1-\left[\frac{\mu}{4\bar{t}}\right]^2\right]},$$

where $\zeta(z)$ is the Zeta function, $\zeta(3)\sim1.202057$. The quadratic dependence of c_{es} on T has a simple physical explanation. Everywhere in the Brillouin zone where the gap is large, c_{es} is still exponentially damped, but where the gap is zero on the Fermi surface, there exists a normal fluid component, caused by thermal excitations, that increase c_{es} by a factor of $\gamma(T)T$. Recall that the superconducting density fraction, $1-[\lambda_L(T)/\lambda_L(0)]^2$, decreases linearly with temperature for a d–wave superconductor, and hence the normal fluid component increases linearly with temperature, i.e. $\gamma(T)\propto T$. So the overall contribution of the thermally excited electrons around the zeros of the gap is quadratic. Born scattering leaves this dependence unaffected. Resonant scattering, however, changes this dependence to a linear one. The reason for this dependence is the creation of a finite normal fluid density at zero temperature.

At T_c, c_{es} has a finite jump, $\Delta C(T_c)$, and its ratio to c_{en} at T_c is a universal number in BCS theory and is equal to 1.43. This ratio is modified in Eliashberg theory and a correction due to strong coupling leads to [Marsiglio and Carbotte 1986]

$$\frac{\Delta C(T_c)}{c_{en}(T_c)} = 1.43\left[1+53\left[\frac{T_c}{\omega_{\ell n}}\right]^2 \ell n\left[\frac{\omega_{\ell n}}{3T_c}\right]\right].$$

In ordinary Eliashberg theory, $c_{en}(T_c)$ can easily be calculated from N(0) and $\alpha^2F(\omega)$, but with energy dependence in the EDOS, $c_{en}(T_c)$ is more complicated and is not easily calculated. Several schemes can be devised to calculate $\gamma_n(T)$ in this case. i) We can calculate $\gamma_n(T)$ for a noninteracting electron gas and then calculate the excess contribution from the interactions, or ii) calculate the difference ΔC for an s–wave superconductor with extremely large gap. At low T, the superconducting specific heat is exponentially small and hence $\Delta C(T) \sim -c_n(T)$. The first method is more difficult and is only applicable to pure superconductors. The second is less difficult but is not applicable with resonant impurity scattering. For this latter method, we will provide two examples. For a finite band with $\bar{t}$=50 meV and B=0, we calculate $\Delta C(T)$ for an s–wave superconductor with T_c=600 K, ω_E=200 meV and λ=1.0. We are certain that $\Delta C(T)$ is mainly $-c_{en}(T)$ at low T, i.e. up to 0.1 T_c. In Figure (5.1), we plot $-\Delta C(T)/T$ vs T. The curves are for different values of chemical potential μ. In the upper frame, μ is set to 0.0 (solid), 1.0 (dotted), 2.0 (dashed), 3.0 (long dashed), 4.0 (dotted dashed) and 5.0 meV (dotted long dashed). In the lower frame, μ is set to 8.0 (solid), 12 (dotted), 20 (dashed), 40 (long dashed), 100 (dotted dashed) and 200 meV (dotted long dashed). For μ=0.0 and 1.0 meV, $\gamma_n(T)$ has an upward curvature and anomalous negative slope at low T (solid and dotted curves in the upper frame). For μ=0.0, $\gamma_n(T)$ does not appear to saturate at low temperature. This upturn is expected in the case of a noninteracting electron gas where $\gamma_n \propto -\ln T$. As μ increases, a maximum develops at T higher than zero and shifts to higher T values as μ increases. For a very large μ, away from the vHs, the expected maximum in $\gamma_n(T)$ falls at $T \sim 0.1\ \omega_E$ and $\gamma_n(0)$ is a true local minimum [Grimvall 1981]. In Figure (5.2), we show the same calculations for the same parameters as in Figure (5.1) but with μ=0.0 meV, the chemical potential μ is

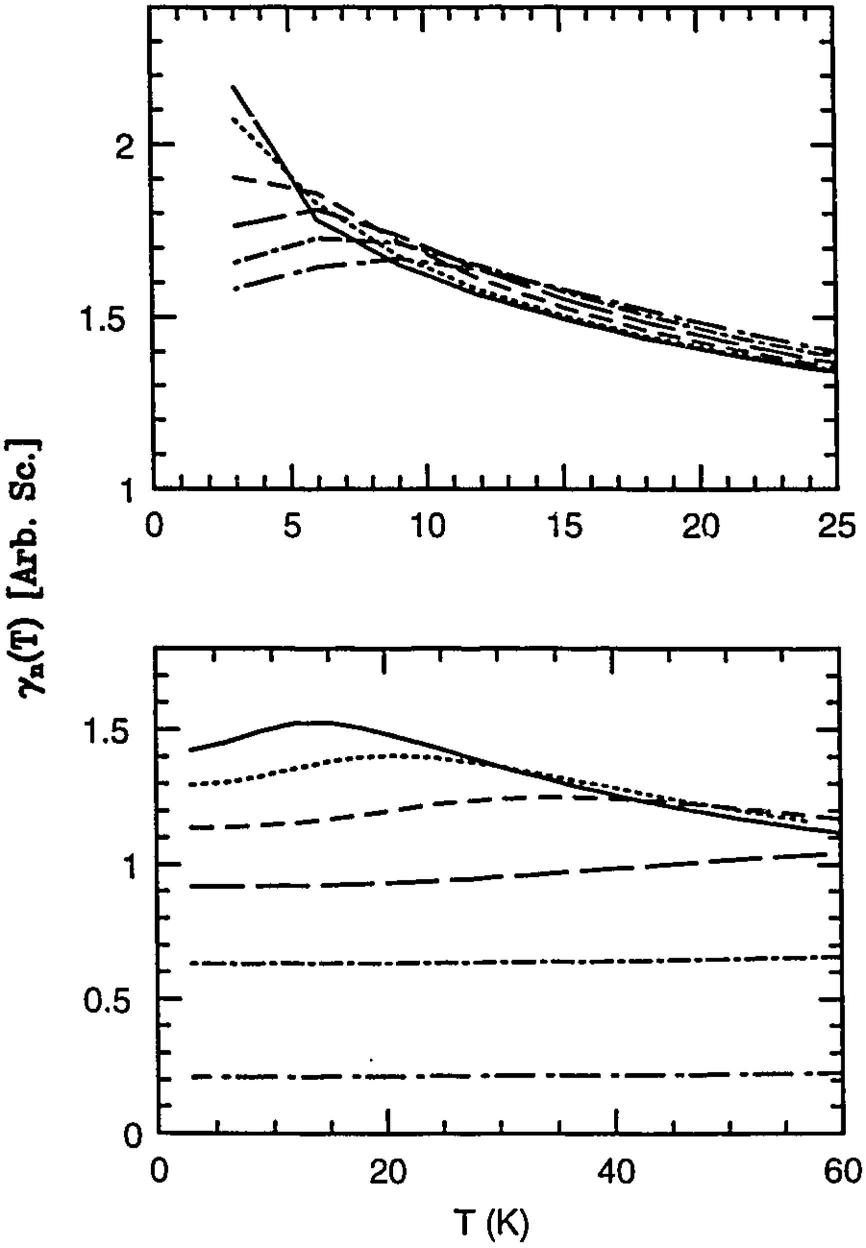

Figure 5.1: The linear coefficient of the normal specific heat γ_n vs. T for 2D tight binding metal ($\bar{t}$=50 meV and B=0). The curves are for different values of μ. In the upper frame, μ=0.0 (solid), 1.0, 2.0, 3.0, 4.0 and 5.0 meV (dotted large dashed). In the lower frame, μ=8.0 (solid), 12, 20, 40, 100 and 200 meV (dotted long dashed).

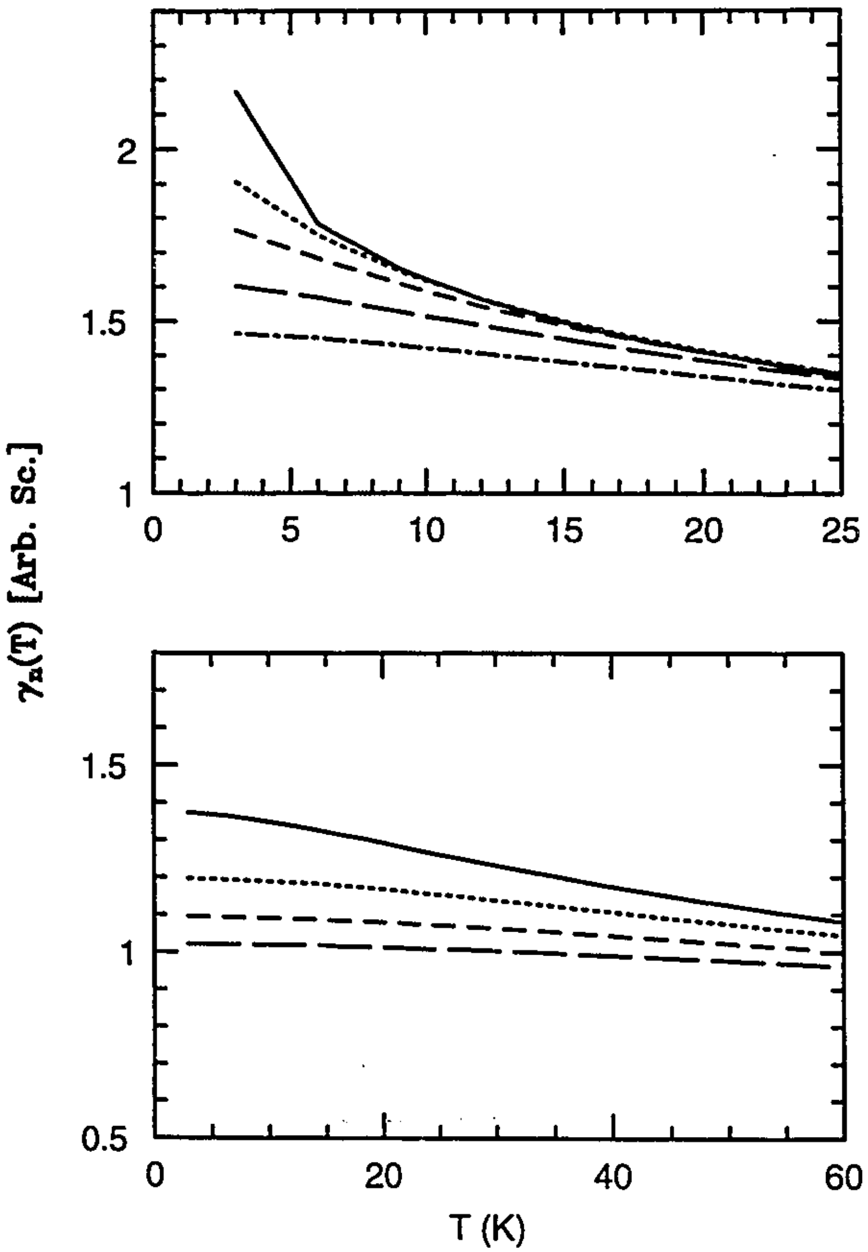

Figure 5.2: Similar to Fig. (5.1) but μ=0.0 meV and normal impurity concentration t^+ is varied. In the upper frame, t^+=0.0 (solid), 0.1, 0.2, 0.4 and 0.7 meV (dotted dashed). In the lower frame, t^+=1.0 (solid), 2.0, 30.0 and 4.0 meV (long dashed).

Similar results for ΔC and $\chi_\perp$ have been observed for most HTSC's except for fully oxygenated Y123. As an example, $\Delta C(T_c)/\gamma_n T_c$ for $La_{2-x}Sr_xCuO_4$ is 0.73, 1.14 and 0.88 for x=0.13, 0.115 (optimal doping) and 0.18 respectively [Loram et al. 1989]. The experimentally observed value of $\Delta C(T_c)/\gamma_n T_c$ for Y123 near optimal doping, on the other hand, is 2.37 for both polycrystals [Loram 1990] and pure single crystal [Liang et al. 1992]. For the single crystal, we have assumed γ_n to be ~ 1.6 $mJ/g_{at.}k^2$ adopted from [Loram 1990]. Even higher ratio values, ~ 2.5 – 2.75, are measured by Loram from the raw data that includes the critical fluctuations [Loram 1993]. This extra heat capacity for Y123 is definitely associated with the CuO chains. In Figure (5.3), we show some results for $\Delta C(T_c)/T_c$ vs T_c for some of the HTSC's [Mirza et al. 1990]. It is worth noting $\Delta C(T_c)/T_c$ decreases abruptly when CuO chains in Y123 are destroyed by the substitution of Cu ions by trivalent ions into the chains. This is shown in the upper frame of Figure (5.3) by the open circles which are for $YBa_2(Cu_{1-x}Co_x)_3O_{7-\delta}$. Increasing x from 0 to 1.5% results in an increase of T_c from 92.5 to 94 K and a decrease of ΔC_{T_c} from 3.4 to 1.8 $mJ/g_{at.}/K^2$. It is believed that Co dopes in the chains preferentially and hence destroys the order in the CuO chains and reduces their superconducting weight. At present, we do not have an explanation for the increase of T_c. For higher Co concentration, $\Delta C/T_c$ levels off and saturates to a constant value. It is not clear if Co is a pair breaker in the usual Abrikosov Gor'kov formalism or with higher order strength [Shiba 1968, 1973; Nagi 1983]. Another system shown in the lower frame of Figure (5.3) is $Y_{1-x}Ca_xSr_2Cu_2T\ell_{0.5}Pb_{0.5}O_7$. At optimal doping, $\Delta C/T_c$ is about 1.6 $mJ/g_{at.}k^2$ and is significantly smaller than that for Y123. This is attributed to the absence of CuO chains from this compound.

pinned to the vHs. The different curves are calculated for different normal impurity concentrations. In the upper frame, t^+ is set to 0.0 (solid), 0.1 (dotted), 0.2 (dashed), 0.4 (long dashed) and 0.7 meV (dotted dashed). In the lower frame, t^+ is set to 1.0 (solid), 2.0 (dotted), 3.0 (dashed) and 4.0 meV (long dashed). In this case, $\gamma_n(T)$ gets smaller with an increase in t^+ clearly indicating the EDOS is smeared and reduced by impurities. We also notice that $\gamma_n(T)$ does not develop a local minimum at T=0.

II) Experimental Results

In this section, we give a brief review of the experimental results on the specific heat of the HTSC. We will first outline some similarities between old quasi–two–dimensional superconductors and some of the cuprate superconductors, then discuss some specific heat measurements, some difficulties associated with their measurements, and the appropriate interpretation of the results.

One of the earliest quasi two–dimensional superconductors is $TaS_2(NC_5H_5)_{0.5}$. It is composed of 6Å thick metallic TaS_2 sheets with strong covalent bonds separated by 12Å thick ordered pyridine molecules. The transition temperature is 3.5 K while the nonintercalated parent, TaS_2, has a T_c equal to 0.7 K [Gamble et al. 1970]. The specific heat jump is broad, due to fluctuations, and reaches its maximum value at 0.4 K below the onset of the transition. The ratio $\Delta C(T_c)/\gamma_n\, T_{onset}$ is about 0.8 ± 0.1, which is roughly half the BCS value, [Di Salvo et al. 1971]. Apart from the deviation of $\Delta C/\gamma_n T_c$ from the BCS value, all other properties are in accord with Fermi liquid theory. The sole exception is the presence of an anomalous diamagnetic susceptibility $\chi_\perp$ extending much higher than even 10 T_c for a magnetic field ⊥ to the TaS_2 layers [Geballe 1971].

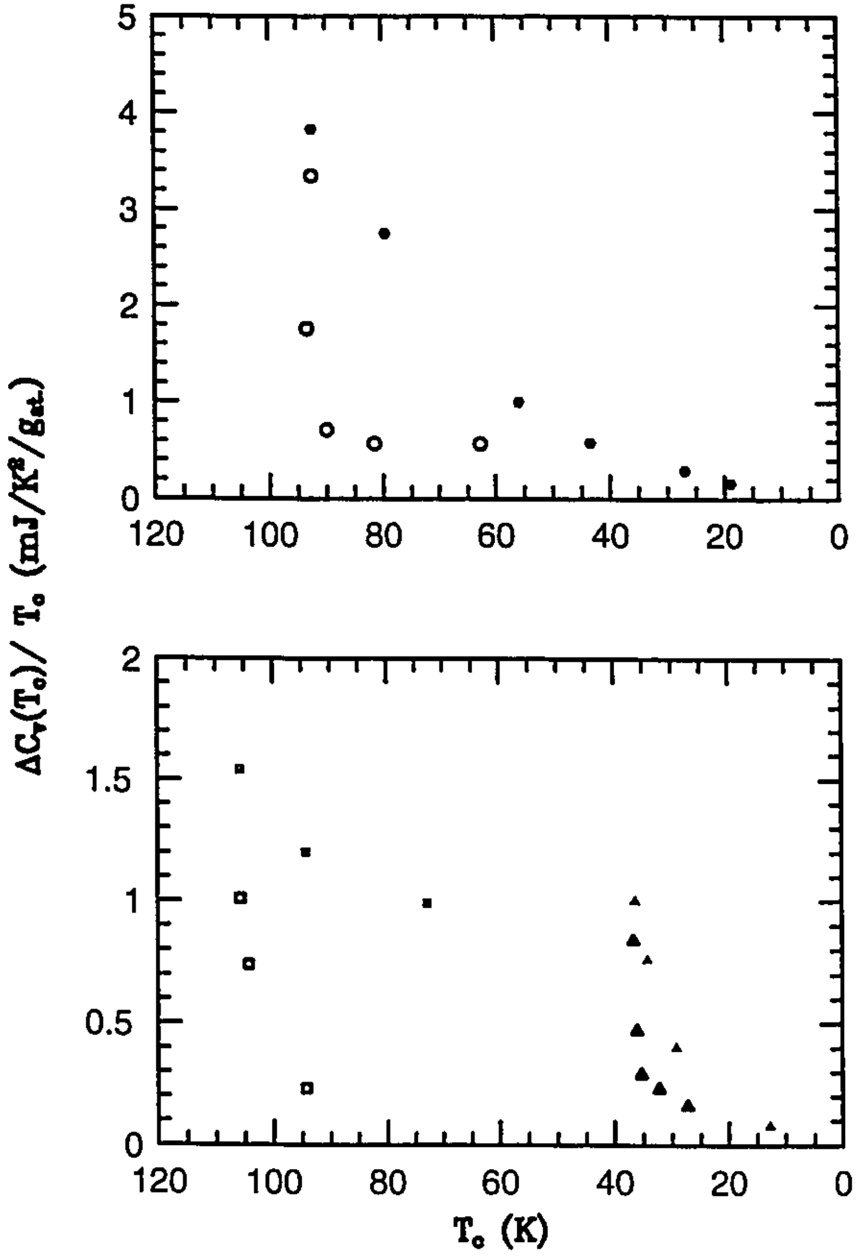

Figure 5.3: Experimental data of $\Delta C(T_c)/T_c$ vs T_c for $YBa(Cu_{1-x}Zn_x)_3O_7$(●), $YBa(Cu_{1-x}Co_x)_3O_{7-\delta}$(○), $Y_{1-x}Ca_xSr_2Cu_2T\ell_{0.5}Pb_{0.5}O_7$ (□underdoped, ■ overdoped) and $La_{2-x}Sr_xCuO_4$ (Δ underdoped, ▲ overdoped). The source of the data is Mirza et al. 1990.

Another trend evident in the lower frame of Figure (5.3) is that $\Delta C/T_c$ is higher for the overdoped samples than for the underdoped ones. The underdoped samples usually have broader $\Delta C(T_c)$ peaks implying higher fluctuations. A similar effect was also observed in underdoped Y123 by [Wühl et al. 1991]. Diamagnetic fluctuations in underdoped Y123 at oxygen concentration of 6.65 were also seen in $\chi_\perp$ up to a high temperature of order 6 T_c [Nakazawa and Ishikawa 1989]. Unfortunately most experimentalists look for Gaussian or critical fluctuations near T_c only and ignore diamagnetic fluctuations at higher temperatures [Loram 1992; Inderhees 1988, 1991; Ghiron 1992, 1993; Ernst 1993]. We feel that experimental values of $\Delta C/T_c$ may be under estimated for most HTSC's that consist of only CuO_2 planes and perhaps over estimated in the case of Y123.

Some of the other problems associated with specific heat measurements in these cuprates are the large and broad phonon contribution to the total specific heat and at low temperature contributions from impurities and impurity phases. The task of separating the electronic contribution to the superconducting specific heat is also complicated by the existence of a linear contribution at low T. For example, several measurements of the specific heat of L214, doped by Sr, [Mason et al.] and Y123 [Phillips 1987, 1990; Fisher 1988] show contradictory results regarding the existence of the linear term. The specific heat data show no intrinsic linear term for Y123 while there is such a term in L214 with a strength equal to about 20% of the normal state linear term, γ_n. More recent measurements on Y123 by Phillips show an intrinsic linear term in the superconducting specific heat which is attributed to a normal fraction associated with the CuO chains [Phillips et al. 1994]. A similar linear term is also observed in Hardy's high quality single crystals of Y123 in addition to the quadratic term characteristic of d–wave superconductivity [Moler et al. 1994]. Very recent experiments also on $La_{2-x}Sr_xCu_{1-y}Zn_yO_4$ by Momono show no intrinsic linear term in the superconducting state for y=0 [Momono et al. 1994], which contradicts the Mason result. A linear term develops for y>0.0 and increases monotonically with y until it saturates beyond a critical concentration of Zn, y_c, at which point superconductivity ceases to exist. Relations between $T_c/T_c(y=0)$ and $\gamma_s/\gamma_s(y=y_c)$ follow a single curve regardless of x. This is interpreted as qualitative evidence of resonance impurity scattering (by Zn impurities) in a d–wave superconductor.

III) The Infinite Band Numerical Results (s–wave)

In this section we will present numerical results for the specific heat difference, $\Delta C(T)$ of an s–wave superconductor with a vHs in the EDOS which was described earlier in Chapter 3. We will begin with a very strong coupling case and then consider weaker coupling. Effects of normal and paramagnetic impurities on $\Delta C(T)$ are also considered. At the end of the section, we will compare some experimental results to our calculations.

For all the calculations in this section, we fix the EDOS parameters, of equation (3.10), to be r=0.5, s=1600 $(meV)^2$, D=40 meV and E_f=800 meV. For these choices, the width and height of the peak in the EDOS correspond to those believed to model Y123. We will ignore the effect of μ^* by setting $\mu^*=0.0$. The main control parameter for these calculations is the optimal transition temperature T_c^0 obtained by varying the coupling constant λ and the frequency, ω_E, of the boson mediating electron pairing. Realistic values of ω_E are in the range of 20–80 meV for a phonon mechanism.

In Figure (5.4), we present $\Delta C(T)/\Delta C(T_c)$ versus the reduced temperature, t, for a superconductor with T_c^0=92.7k, ω_E=20 meV and $r\lambda$=2.0. The curves are for different filling factors namely δ=0.0 (incomplete solid), 20 (dotted), 40 (dashed), 60 (long dashed), 80 (dotted dashed) and 100 meV (dotted long dashed). There are considerable deviations for all the curves from the BCS curve, shown by the full solid curve in the same figure. Strong coupling effects for constant EDOS increase the normalized slope of the jump, defined as $R=T_c[d\Delta C(T)/dT]_{T=T_c}/\Delta C(T_c)$, and the crossover reduced temperature, t_0 defined by T at which $\Delta C(T)=0$. The magnitude of $\Delta C(T)/\Delta C(T_c)$ is also reduced at low T in comparison to that of BCS, as to conserve the entropy difference (entropy sum rule). The dotted long dashed curve in Figure (5.4) is very close to a strong coupling curve with constant EDOS. This is expected because the chemical potential (δ=100 meV) is far enough from the vHs. As the filling decreases from δ=100 to 0.0 meV, both R and t_0 decrease to values that are less than the BCS values. For δ=0.0 meV (incomplete solid curve) t_0 is about 0.43 while for the BCS (solid) curve, t_0 is about 0.514. There is also an increase in the magnitude of $\Delta C(T)/\Delta C(T_c)$ at low T and for δ=0.0 (incomplete solid curve) there is an anomalous kink caused by the coincidence of the chemical potential and the centre of the vHs in the EDOS. It is this anomaly that reflects the expected T ℓn T in the normal state specific heat which exists only when the chemical potential is at the vHs.

In Figure (5.5), we present $\Delta C(T)$ for the same parameters as in Figure (5.4) but for larger filling factors, $\delta \geq 150$ meV. In the upper frame, we show $\Delta C(T)/\Delta C(T_c)$ vs t, and in the lower frame, we show the same curves but normalized by the reduced temperature. The curves are for fillings of δ=150 (dotted), 200 (dashed), 300 (long dashed), 400 (dotted dashed) and 500 meV (dotted

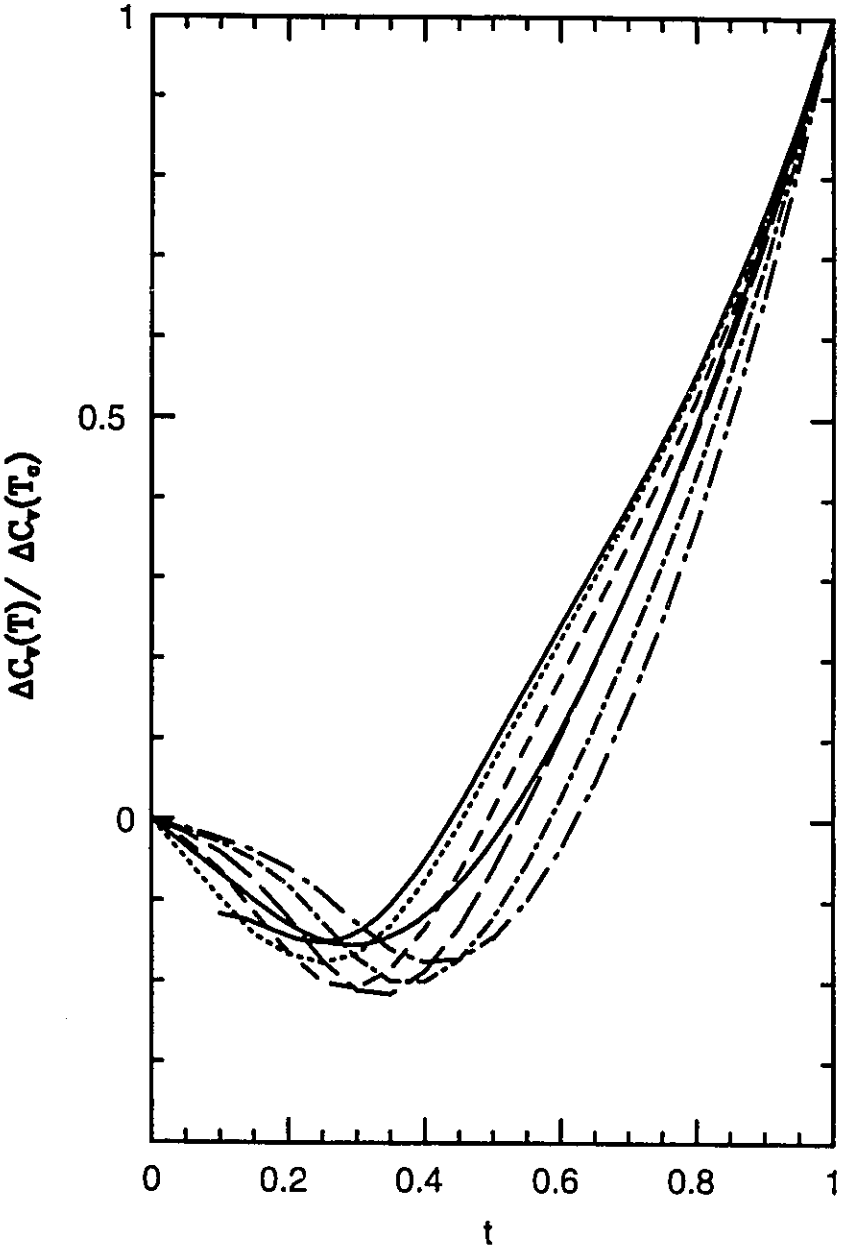

Figure 5.4: The specific heat difference normalized by the jump vs. reduced temperature for a strong coupling superconductor, ω_E=20 meV. The curves are for different chemical potentials, δ=0.0 (incomplete solid), 20 (dotted), 40 (dashed), 60 (long dashed), 80 (dotted dashed) and 100 meV (dotted long dashed). The complete solid curve in BCS.

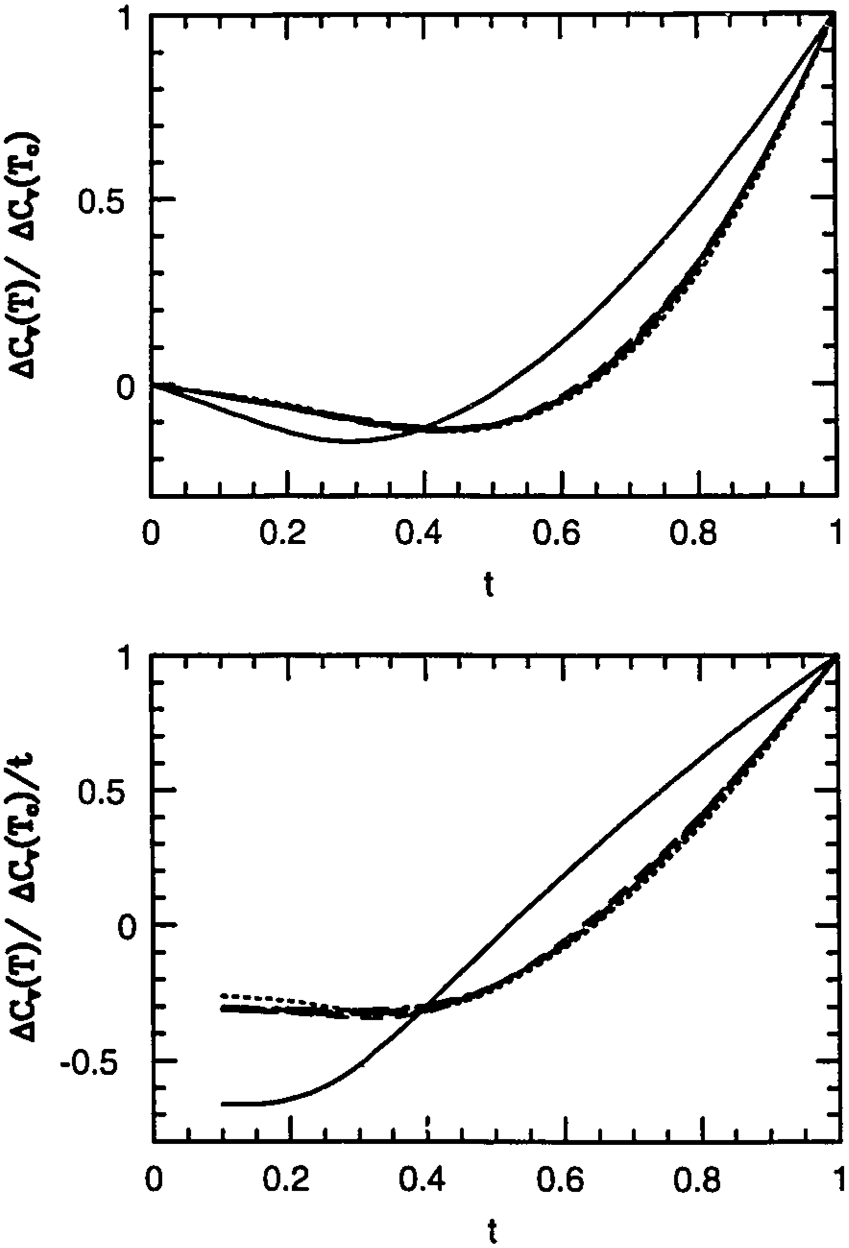

Figure 5.5: $\Delta C(T)/\Delta C(T_c)$ vs. t (upper frame) for the same superconductor in Fig. (5.4) but with higher δ values. The curves are for δ=150 (dotted), 200 (dashed), 300 (long dashed), 400 (dotted dashed) and 500 meV (dotted long dashed). The BCS curve is given by the solid curve. The same curves scaled by t are plotted in the lower frame.

long dashed). The solid curve is the BCS curve. Beyond a filling of 150 meV, ther is only a slight reduction of R and t_0 as δ increases. The maximum value of t_0 is 0.65 at δ=150 meV (dotted curve) and is only 5% larger than the corresponding strong coupling value given by the approximate formula [Akis 1991]

$$t_0 = 0.514\ [1+11.5\ (T_c/\omega_{\ell n})^2\ \ell n\ (\omega_{\ell n}/3.2\ T_c)],$$

where T_c was set to 50 K. All the curves in the upper frame Figure (5.5) are almost identical for δ larger than 150 meV except for a slight push to the left. At low t, the differences are smaller in the upper frame than in the lower frame due to enhancement of scale in the lower frame. For BCS (solid curve in the lower frame) $\Delta C(T)/T$ is flat near T=0 indicating a constant γ_n and an exponentially small γ_s. As T increases, larger t, γ_n is expected to remain constant in BCS but γ_s starts to increase beyond $t\sim0.511$ the value of $\gamma_s-\gamma_n$ is zero and for t larger than 0.514 the difference $(\gamma_s-\gamma_n)$ becomes positive, i.e. $\gamma_s>\gamma_n$. Upon including the electron-phonon interaction for an Einstein phonon model, γ_n initially increases with temperature from its zero temperature value, reaches a maximum arround 0.1 w_E and then decreases again to approach the unrenormalized Sommerfeld constant for $T\rightarrow\infty$ [Grimvall 1981]. This effect is seen in the downward curvature of $\Delta C(T)/\Delta C(T_c)$ at small t in the upper frame of Figure (5.5) and in the small negative slopes in the lower frame of the same figure.

In the upper frame of Figure (5.6), we plot $\Delta C(T)/\Delta C(T_c)$ of Figure (5.4) normalized by the reduced temperature against t. At δ=0.0 meV (solid curve), the maximum value of γ_n is at t=0 and shows no saturation. The maximum in γ_n is shifted to higher reduced temperature values as δ increases. This is

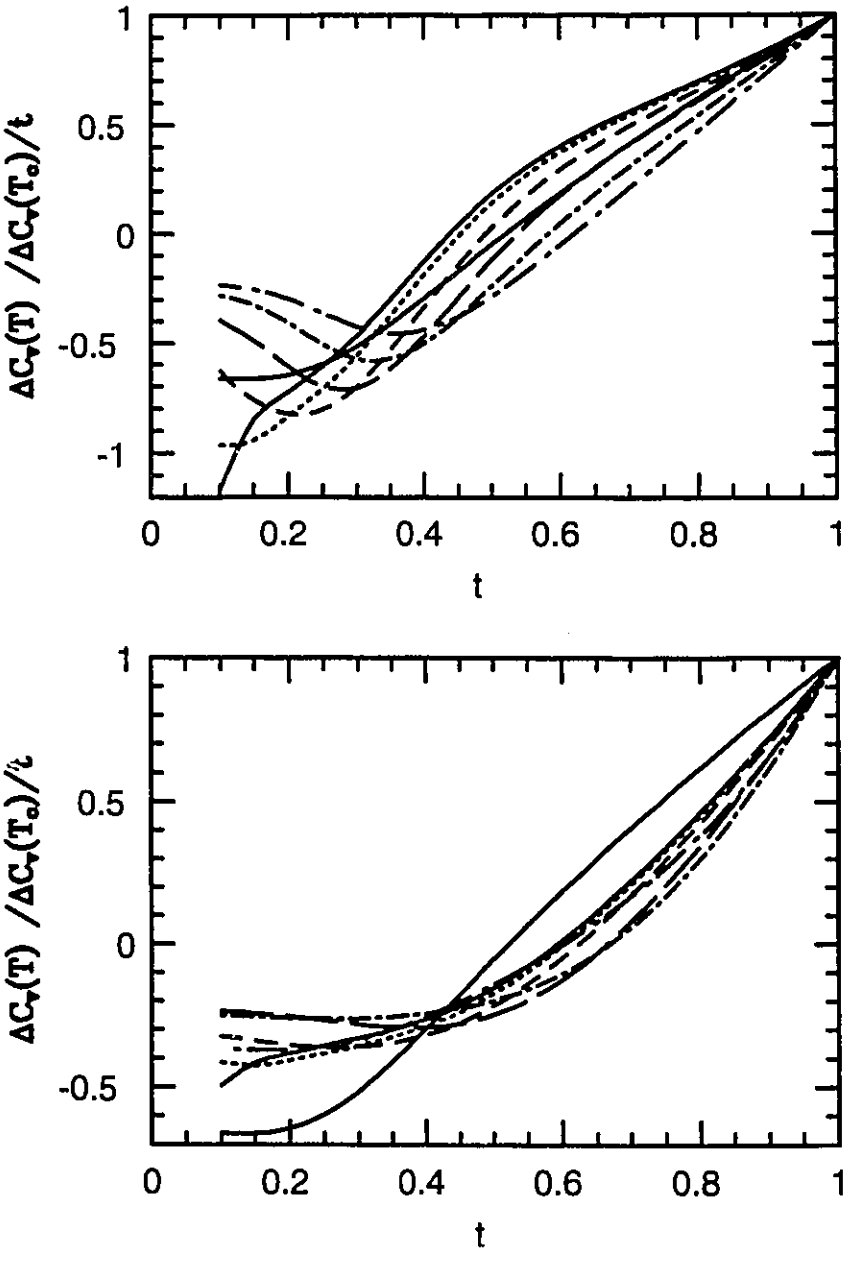

Figure 5.6: $\Delta C(T)/\Delta C(T_c)/t$ vs. t; the upper frame is for the same set of curves shown in Fig. (5.4); the lower frame is for the weaker coupling, ω_E=40 meV. The curves in the lower frame are for δ=0.0 (upper solid at t=0.2), 10 (dotted), 20 (dashed), 40 (long dashed), 60 (dotted dashed) and 80 meV (dotted long dashed). The BCS curve is shown by the lower solid curve at t=0.35 in both frames.

reflected in the shift of the minimum of $\Delta C(T)/\Delta C(T_c)/t$ to higher t values with the increase in δ. In the lower frame of the same figure we present similar calculations but, for a weaker coupling case. The coupling parameters are $r\lambda=0.4$, $\omega_E=40$ meV and $T_c^0=93.9$ K. Qualitatively, the results are similar to those in the upper frame but with smaller deviations. The curves are for filling factors, δ, of 0.0 (upper solid at t=0.2), 10 (dotted), 20 (dashed), 40 (long dashed), 60 (dotted dashed) and 80 meV (dotted long dashed). Again the lower solid curve at t=0.2 is the BCS case. For this particular case, R and t_0 are also both minimum at $\delta=0.0$ and increase as δ increases until $\delta=60$ meV. For $\delta=80$ meV, R and t_0 get reduced, but unlike the strong coupling case, the relative reduction is slightly larger. For much weaker coupling cases, R and t_0 initially start, at $\delta=0$, at values intermediate between the strong and the weak limits in normal Eliashberg theory, then increase as δ increases to reach maximum values (comparable to the two previous cases) and decrease again, past the $\delta=0$ values, to the characteristic weak coupling values. The maximum R and t_0 never exceed those established for regular Eliashberg theory, namely $R^{max}=5.0$ and $t_0^{max}=0.66$ [Akis 1991]. It was originally hoped that the inclusion of a vHs in EDOS might increase the upper limits of possible values of R and t_0. This would be important because initial experiments on Y123 have given R values slightly above 5.0 [Junod 1988; Loram 1988]. Even a larger value of R has been reported by Schilling, Ott and Hulliger for $Bi_{1.6}Pb_{0.4}Sr_2Ca_2Cu_3)_{10}$ [Schilling et al. 1989]. We now believe that these values may be exaggerated because the contribution of fluctuations is not taken into account. The specific heat jump ratio to T_c, however, may have less uncertainties and we will utilize it to compare theory to experiment. We now turn to a consideration of this quantity.

In Figure (5.7), we show typical curves of $\Delta C(T_c)$ versus δ (chemical

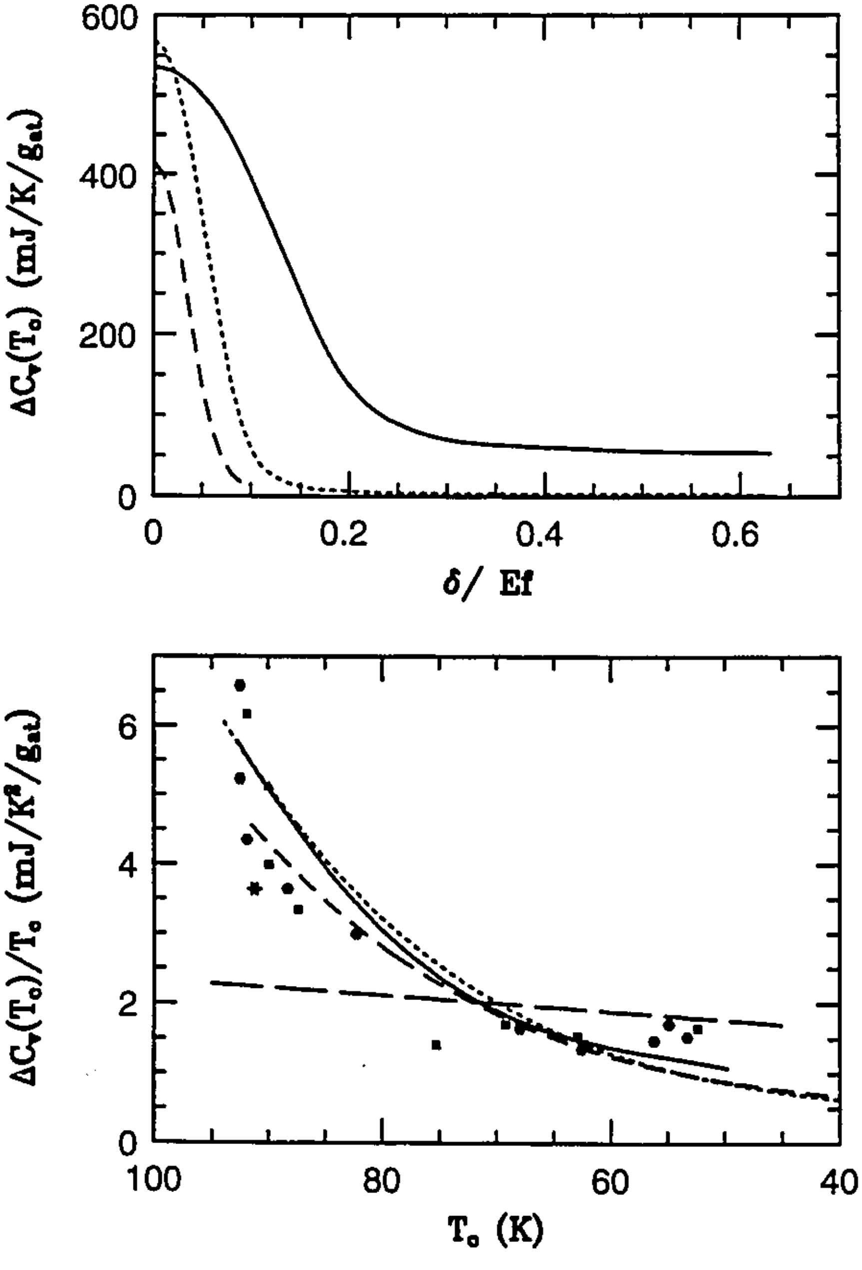

Figure 5.7: Upper frame; $\Delta C(T_c)$ vs. δ/E_f for three different coupling strengths, ω_E=20 (solid), 40 (dotted) and 60 meV (dashed). Lower frame; $\Delta C(T_c)/T_c$ vs T_c for the same three curves shown in the upper frame. The long dashed curve is BCS calculation with constant EDOS. The data points are for oxygen doped Y123 (see text for sources).

potential) for different coupling strengths but with roughly the same T_c. These specific heat jump curves have shapes similar to their corresponding T_c curves, see upper frame of Figure (3.5). The widths at half maximum, however, for $\Delta C(T_c)$ versus δ curves are smaller than those for T_c vs δ curves. In the upper frame of Figure (5.7), we show $\Delta C(T_c)$ vs δ/E_f for three different superconductors with ω_E set to 20 (solid), 40 (dotted) and 60 meV (dashed) respectively. The absolute values of $\Delta C(T_c)$ at $\delta=0$ are not monotonic in coupling strength. This is actually similar to regular Eliashberg theory where $\Delta C(T_c)$ increases with coupling strength to a maximum, then decreases again [Carbotte 1990]. In the lower frame, we show the same data as in the upper frame but plotted differently, $\Delta C(T_c)/T_c$ vs T_c. In the lower frame, the curves have very similar shapes and roughly overlap over a large interval of T_c values. The points shown in the same frame are experimental results for Y123 in which the oxygen concentration in the CuO chains was varied to achieve the variation in T_c. The data sources are Dumling et al. 1991 (hexagons), Junod et al. 1989 (a triangle), Inderhees et al. 1991 (a star) and Wühl et al. 1991 (squares). The qualitative agreement between the theory and experiment is quite impressive and is better than the results of BCS theory with a simple logarithmic singularity [Tsuei 1992]. It is worthwhile to note also that if BCS theory is used, varying only N(0) in a constant EDOS scenario, one cannot explain the data. Such a calculation is shown by the long dashed curve in the lower frame of Figure (5.7) with ω_0=65 meV and V=0.2.

In the next three figures, we will briefly examine the effect of impurity scattering on the specific heat in the presence of a vHs in the EDOS. The most interesting cases are for weak coupling. Normal impurity scattering in s–wave superconductors has no pair breaking effects and the superconducting specific heat is still exponentially activated. The effect of normal impurity scattering is to reduce and smear out the peak in the EDOS, which results in a decrease in T_c, $\Delta C(T_c)$ and $\gamma_n(T)$.

In Figure (5.8), we show $\Delta C(T_c)/T$ normalized by the same ratio at T_c evaluated for zero impurity concentration versus T normalized by the clean limit T_c^0, t^+=0.0 meV, for a superconductor with ω_E=60 meV and T_c^0=91.4 K. These curves are with δ=0.0 meV and normal impurity concentration of 0.0 (solid), 2.0 (dotted), 4.0 (dashed), 6.0 (long dashed), 8.0 (dotted dashed) and 10 meV (dotted long dashed). At t^+=2.0 meV (dotted curve), $\gamma_n(T)$ is roughly constant for small T and is reduced considerably in comparison to the clean limit case (solid curve). As t^+ increases, both $\Delta C(T_c)$ and $\gamma_n(T)$ get reduced but at a decreasing rate. For high enough values of t^+, both quantities saturate to a lower limit. For $\Delta C(T_c)$, the saturation behaviour is shown in the upper frame of Figure (5.9), this is similar to that of T_c shown in the upper frame of Figure (3.6). The two curves in Figure (5.9) are for two coupling strengths, ω_E= 40 meV with T_c^0=94 K (solid curve) and ω_E=60 meV with T_c^0=91 K (dashed curve). In the lower frame of Figure (5.9), we plot the same curves as in the upper frame but as $\Delta C(T_c)/T_c$ versus T_c. These curves are similar to those obtained by varying the chemical potential. The implication here again is that $\Delta C(T_c)$ vs t^+ curves have smaller widths than T_c vs t^+ curves. The experimental data (hexagons) are for Zn doped Y123 [Loram et al. 1990]. The asterisks are the same data but scaled up by a constant factor. These two curves and the experimental data correspond to the case presented earlier in Chapter 3 in the lower frame of Figure (3.13). The qualitative correspondence between theory and experiment is good. For the case of constant EDOS, normal impurities drop out of the problem and leave $\Delta C(T_c)/T_c$ unchanged. The large

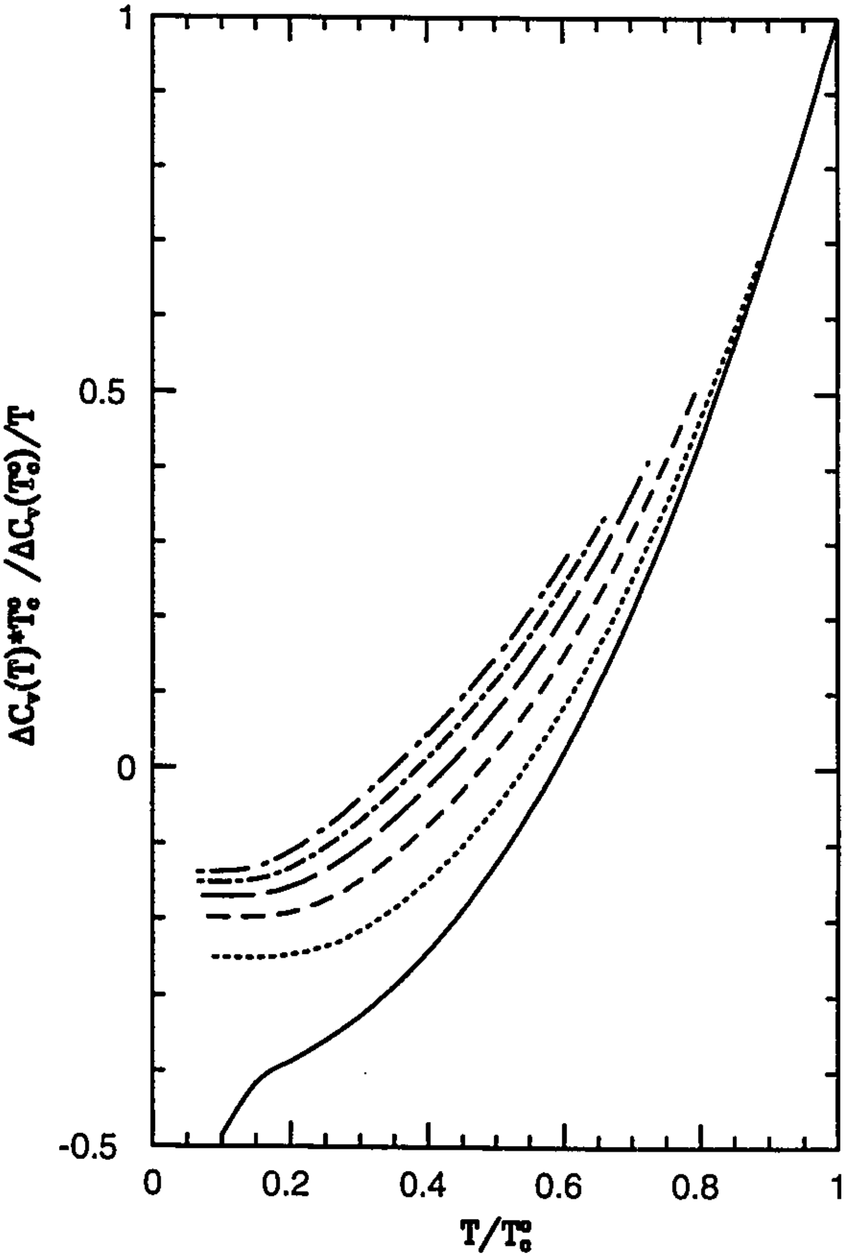

Figure 5.8: Variation of the specific heat difference with normal impurities. $\Delta C(T)/T$ normalized by $\Delta C(T_c^0)/T_c^0$, where T_c^0 is T_c for zero impurity concentration, plotted against T/T_c^0. The impurity concentrations for these curves are 0.0 (solid), 2.0 (dotted), 4.0 (dashed), 6.0 (long dashed), 8.0 (dotted dashed) and 10 meV (dotted long dashed).

variation found in Figure (5.9) finds a natural explanation in the van Hove model although other explanations might be possible.

For paramagnetic impurity scattering (pair breaking), the specific heat difference deviates only slightly from the conventional behaviour in ordinary Eliashberg theory. This deviation is only near T_c. Ordinarily, $\Delta C(T_c)/T_c$ is monotonic decreasing function of t^- and is almost a straight line. If the chemical potential is on or very close to a peak in the EDOS, then T_c drops faster than usual because the EDOS is being smeared in addition to the usual pair breaking effect. Hence, the ratio of $\Delta C(T_c)/T_c$ initially increases slightly as T_c decreases then starts to decrease in similar fashion to that in the absence of a vHs. This is illustrated in the lower frame of Figure (5.10), where we plot $\Delta C(T_c)/T_c$ normalized to the clean limit value versus T_c/T_c^0. The parameter of these calculations are $r=1.0$, $E_f= 500$ mev, $\omega_E=30$ meV and $\lambda=1.2$. The curves are for different chemical potentials, $\delta=0.0$ (solid), 35 (dotted), 50 (dashed), 80 (long dashed) and 200 meV (dotted dashed). These curves are quite different from $\Delta C(T_c)/T_c$ curves shown in Figures (5.7) and (5.9). Pair breaking is more effective in reducing T_c than reducing $\Delta C(T_c)$. In the upper frame of Figure (5.10), we show $\Delta C(T_c)/T$ vs T/T_c^0 for $\delta=0.0$ meV and the curves are for $t^-=0.0$ (solid), 0.2 (dotted), 0.4 (dashed), 0.6 (long dashed), 0.8 (dotted dashed) and 1.0 meV (dotted long dashed) respectively. At low T, these curves are not very different from those with normal impurities, except in this case the impurity concentrations are much lower.

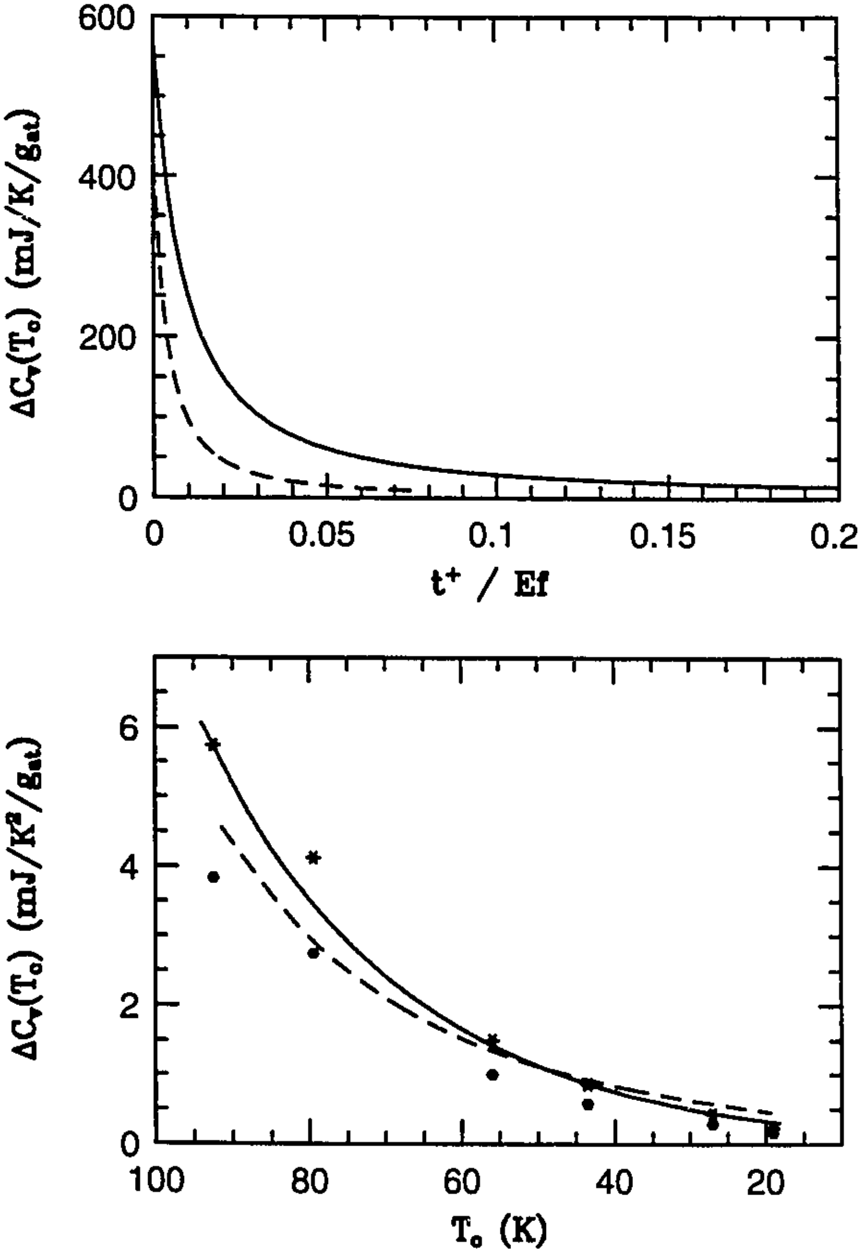

Figure 5.9: Upper frame; $\Delta C(T_c)$ vs. t^+/E_f for two different coupling strengths, ω_E=40 (solid) and 60 meV (dashed). Lower frame; $\Delta C(T_c)/T_c$ vs T_c for the same two curves shown in the upper frame. The hexagons are experimental data for Zn doped Y123 (see text for asterisks and source of data).

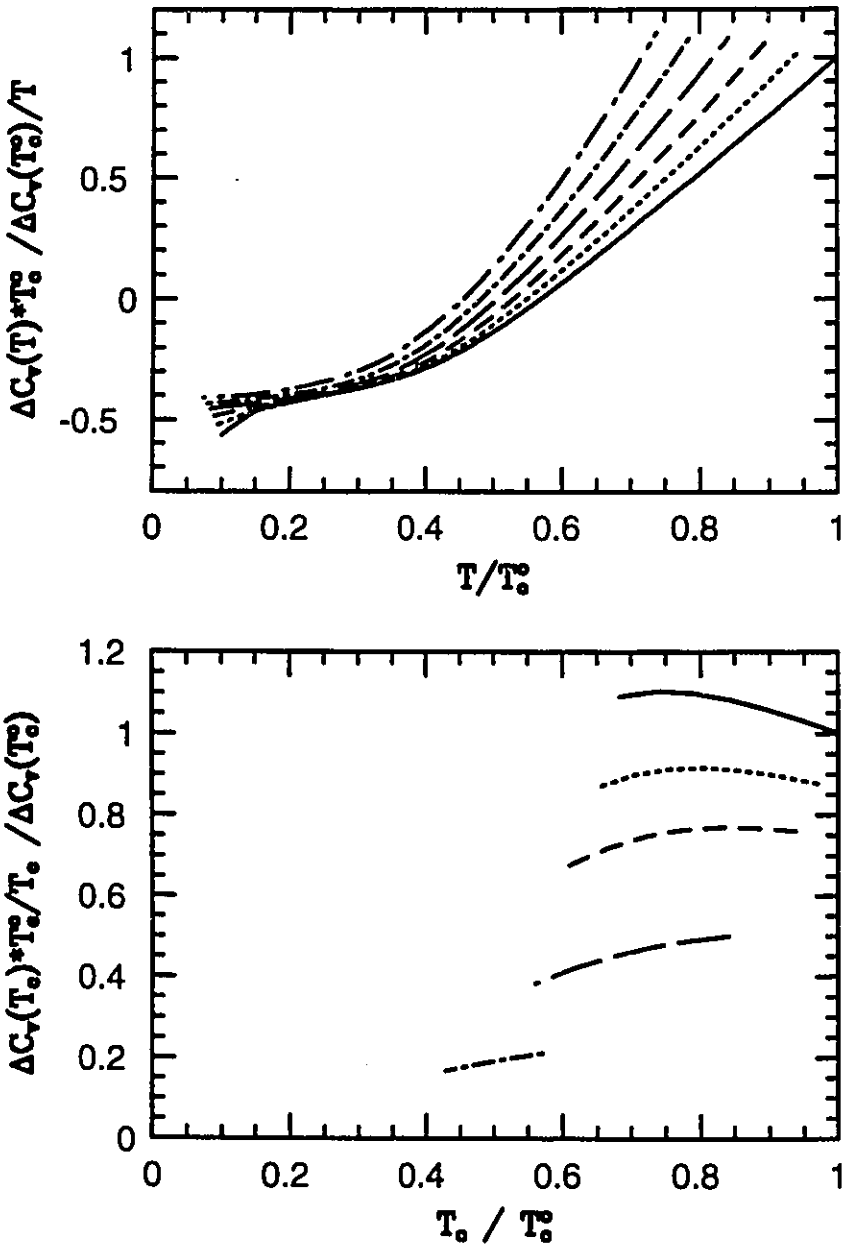

Figure 5.10: Effect of paramagnetic impurities on $\Delta C(T)$. Upper frame: similar to Fig. (5.8) and the curves are for $t^{-}=0.0$ (solid), 0.2 (dotted), 0.4 (dashed), 0.6 (long dashed), 0.8 (dotted dashed) and 1.0 meV (dotted long dashed). δ is set to zero. Lower frame: $\Delta C(T_c)/T_c$ normalized by its value at $t^{-}=\delta=0.0$ meV vs. T_c/T_c^0, T_c^0 is the optimal clean limit T_c. The chemical potentials for the various curves are $\delta=0.0$ (solid), 35 (dotted), 50 (dashed), 80 (long dashed) and 200 meV (dotted dashed).

IV) The Finite Band Numerical Results

In this section, we will present results for $\Delta C(T_c)$ using the tight binding model introduced earlier in Chapter 4. Both cases of s–wave and d–wave superconductors will be studied and compared, however for impurity scattering only the d–wave case will be emphasized. For simplicity, we will set B to be zero, no next nearest neighbour hopping. We will begin with results for T_c and $\Delta C(T_c)/T_c$ calculated for different hole doping levels, i.e. the chemical potential, μ, is being varied. Next, we will present $\Delta C(T)$ in the whole temperature range for both d–wave and s–wave superconductors. Third, we will study $\Delta C(T)$ for d–wave in the presence of impurities and compare to experimental results. The formalism needed for this section was described earlier in Chapter 4, for the Eliashberg equations, and in Chapter 2, for the free energy formula.

In the upper frame of Figure (5.11), we show the transition temperature plotted against the chemical potential for two d–wave superconductors (solid and dotted curves) and two d–wave superconductors (dashed and long dashed curves). For all of these curves, we set $\bar{t}$=50 meV, ω_E=30 meV and the cut off equal to 2100 meV. For the s–wave order parameter, T_c exhibits a broad maximum around μ=0.0 meV. The width of this maximum is larger for higher values of coupling strength λ, λ=0.7 for the long dashed curve and 1.6 for the dashed curve. This is similar to the results of Chapter 3 in which the T_c versus δ curves were much narrower due to the narrower EDOS. For the d–wave cases, the widths of the maximum of the T_c versus μ curve is higher for the stronger coupling case (solid curve, λ=0.7) than for the weaker coupling case (dotted curve, λ=0.001). The effect of coupling strength on the width of the maximum of T_c vs μ curves is similar for d–wave and s–wave.

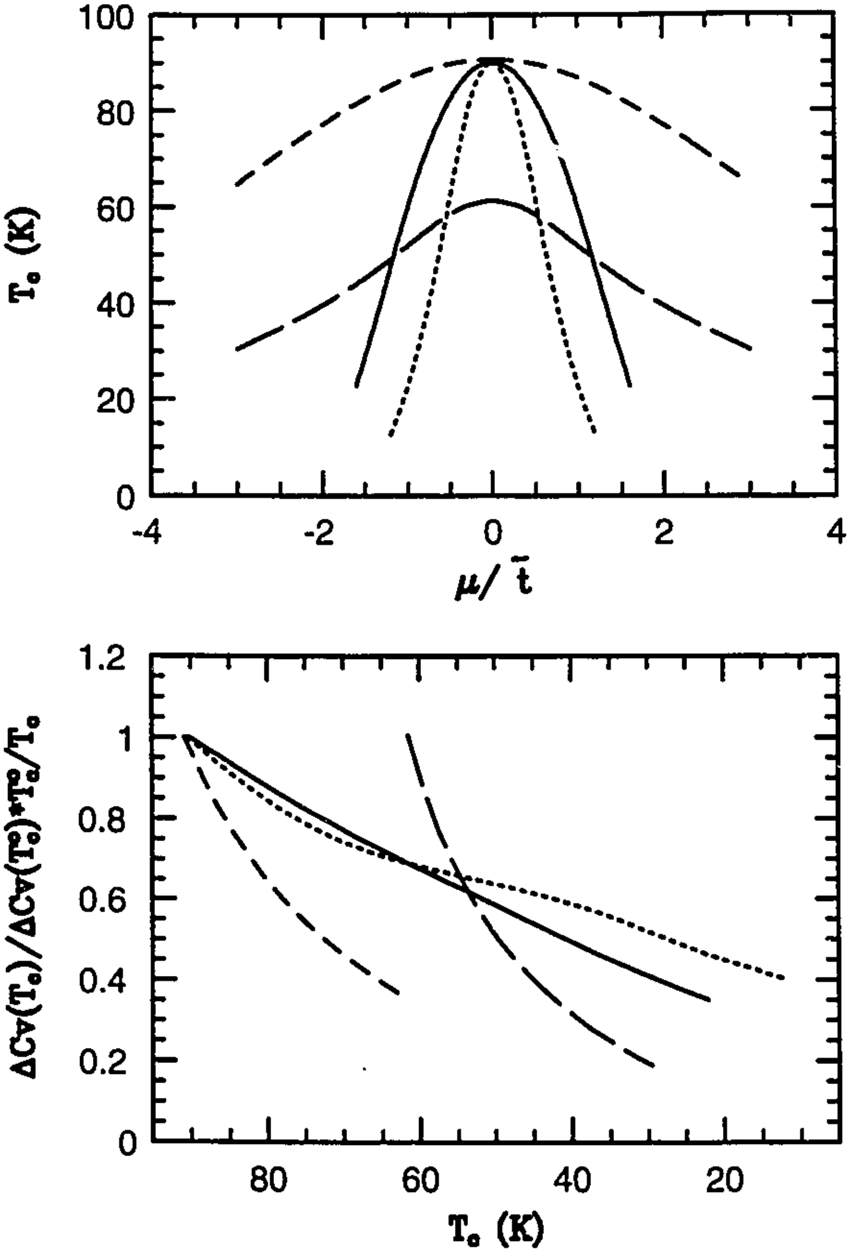

Figure 5.11: Upper frame; T_c vs. $\mu/\bar{t}$ (see text for parameters) for d–wave (solid and dotted) and s–wave (dashed and long dashed). Lower frame; $\Delta C(T_c)/T_c$ normalized to its value at μ=0.0 meV for the same curves shown in the upper frame.

The d–wave curves are much narrower than the s–wave curves. This effect has a simple explanation. For a separable model, the linearized gap equation (equation (4.3)) can be written as

$$\phi_n = g\,\pi\,T_c \sum_m \lambda(n-m)\,\phi_m \sum_{\mathbf{k}} \frac{\eta_{\mathbf{k}}^2}{\tilde{\omega}_m^2+\epsilon_{\mathbf{k}}^2},$$

and the most important contribution of the summation over **k** comes from on and around the Fermi surface. So as μ is varied, the effective value of $\eta_{\mathbf{k}}^2$ on the Fermi surface changes, i.e. its average changes with μ. The function $\eta_{\mathbf{k}}^2$ is peaked for $\mathbf{k}=(0,\pm\pi/a)$ and $(\pm\pi/a,0)$ and is zero for $\mathbf{k}=(0,0)$ and $(\pm\pi/a,\pm\pi/a)$. At half filling, μ=0.0 meV, the Fermi surface includes the maximum points of $\eta_{\mathbf{k}}^2$. This makes the effective pairing potential a maximum at μ=0.0 meV. As μ is swept away from zero, the average of $\eta_{\mathbf{k}}^2$ on the Fermi surface is reduced. The effective pairing potential then decreases as μ increases (decreases) from zero. This leads to further decrease in T_c compared with s–wave case, where $\eta_{\mathbf{k}}^2$ is replaced by a constant over the whole Brillouin zone.

In the lower frame of Figure (5.11), we show the ratio $\Delta C(T_c)/T_c$ normalized to its value at μ=0.0 meV plotted against T_c for the same set of curves as in the upper frame. For s–wave, $\Delta C(T_c)/T_c$ curves are similar to that obtained in the previous section (Infinite Band Model) and can nicely describe the experimental data for the oxygen doped Y123. For d–wave, however, this ratio, $\Delta C(T_c)/T_c$, deviates considerably from that of the s–wave. The experimental data on Y123 and LSCO, presented on triangles in the lower frame of Figure (5.3), cannot be explained with these d–wave results. This is not to suggest that d–wave is inconsistent with the data. The discrepancy between the experimental data and theory might be artificial because of assuming a separable model. In a separable model, T_c drops very fast with μ and hence gives a larger $\Delta C(T_c)/T_c$ ratio.

In figure (5.12), we show $\Delta C(T)/\Delta C(T_c^0)$, T_c^0 is T_c for $\mu=0$, for an s–wave (upper frame) and a d–wave (lower frame) superconductor plotted against T/T_c^0. These calculations are for two of the four curves shown in the previous figure, the long dashed curve (s–wave) and the solid curve (d–wave). The specific heat jump for $\mu=0.0$ meV, $\Delta C(T_c^0)$, for the s–wave is 54% larger than that of the d–wave. At optimal doping, $\Delta C(T)$ (unnormalized) at low T for the s–wave is only slightly larger (in absolute magnitude) than that of the d–wave evaluated at the same absolute temperature. This is because the normal state specific heats are equal for both of them. Note that the superconducting specific heat for d–wave is only slightly larger than that for the s–wave, which is exponentially activated at low temperature. The equality of the normal state specific heat follows from the equality in the EDOS parameters and equal coupling strength, λ, in the omega channel. The curves in the upper frame are for $\mu=0.0$ (solid), 20 (dotted), 40 (dashed), 60 (long dashed) and 80 meV (dotted dashed). The curves in the lower frame are for $\mu=0.0$ (solid), 30 (dotted), 40 (dashed), 50 (long dashed) and 60 meV (dotted dashed). The larger negative scale in the lower frame is a consequence of smaller $\Delta C(T_c^0)$ for the d–wave case. Away from the vHs, the low temperature part of $\Delta C(T)/T$ is quite flat and strong coupling corrections to γ_n are apparent for the s–wave superconductor (upper frame). For the d–wave superconductor (lower frame) and away from $\mu=0$, $\Delta C(T)/T$ curves have a linear slope below 0.15 T_c, as expected for d–wave. At $\mu=0.0$ meV (solid curve), $\gamma_n(T)$ has very large

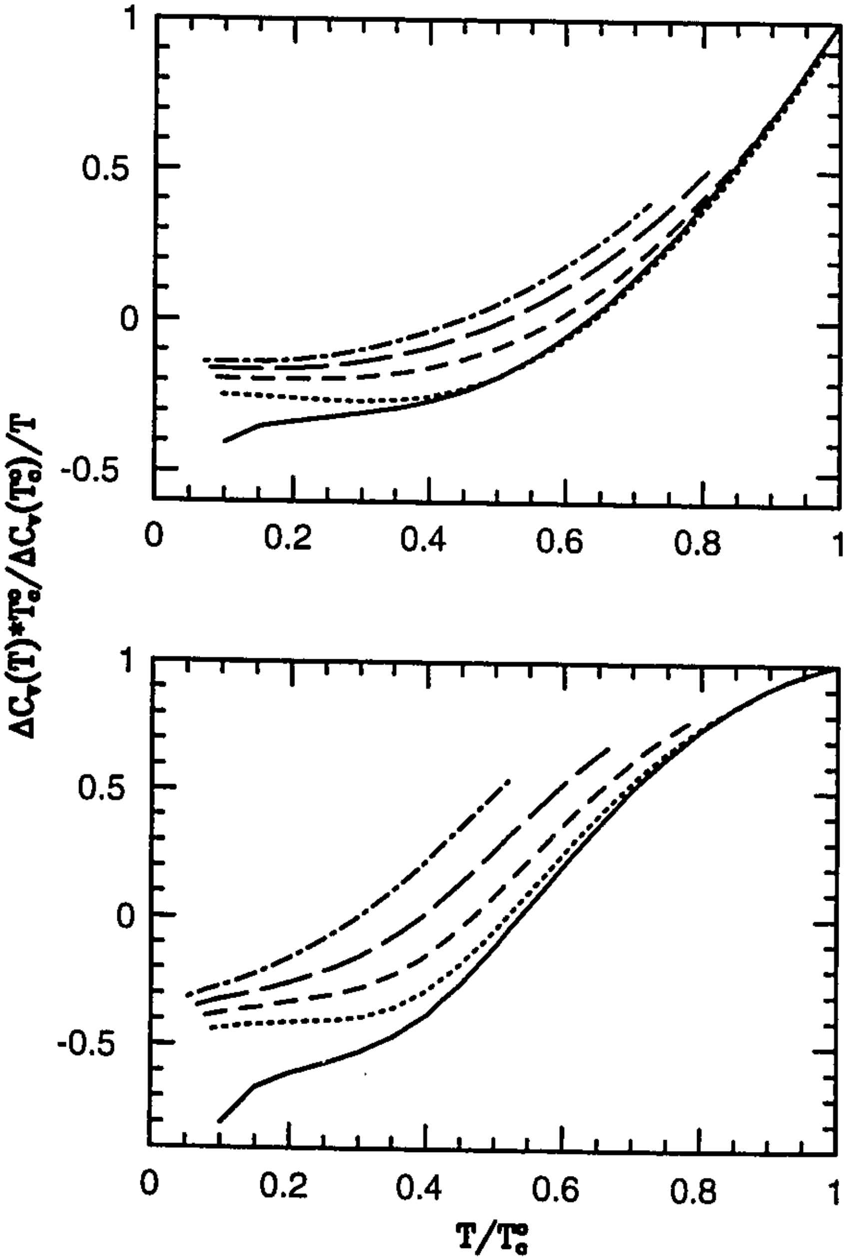

Figure 5.12: ΔC(T) normalized by ΔC(T_c) at μ=0.0 meV vs. T normalized by T_c at μ=0.0 meV. The curves in the upper frame (s–wave) are for μ=0.0 (solid), 20 (dotted), 40 (dashed), 60 (long dashed) and 80 meV (dotted dashed). In the lower frame (d–wave), the curves are for μ=0.0 (solid), 30 (dotted), 40 (dashed), 50 (long dashed) and 60 meV (dotted dashed).

temperature variation that masks the linear increase in c_{es}/T.

In Figure (5.13), we show $\Delta C(T)$ for a d–wave superconductor with T_c=30k plotted against absolute temperature (solid curve) and calculated with the following parameters, ω_E=70 meV, λ=1.0, cutoff =1050 meV, t=50 meV and μ=0.0 meV. The normal state specific heat (dotted curve) is calculated in the same way as in Figures (5.1) and (5.2). The dashed curve is the resultant superconducting specific heat of this 30 K d–wave superconductor. All the curves in the upper frame are normalized by the normal state specific heat at 30 K, $c_n(30)$. The lower frame of Figure (5.13) shows $\Delta C(T)/T$ normalized by $c_n(30)$. It is clear that the low T superconducting specific heat of this d–wave superconductor (dashed curve) is actually quadratic in temperature below 5 degrees and almost quadratic above that but with a different coefficient.

Next, we will consider the effect of impurity scattering on the specific heat of d–wave superconductors. Near T_c, both Born and resonance scattering have almost the same effect, both T_c and $\Delta C(T_c)$ drop linearly with increasing impurity concentration. For the same reduction of T_c from the pure limit, $\Delta C(T_c)$ is reduced a bit more in resonance scattering than in Born scattering. In Figure (5.14), we plot $\Delta C(T_c)/T_c$ normalized to its clean limit value versus T_c, obtained by increasing the impurity concentration of Born impurities (solid curve) or resonance scatters (dashed curve), for a d–wave superconductor with $\bar{t}$=50 meV, λ=0.7, g=0.82, ω_E=30 meV and a cutoff of 2100 meV. The hexagons are the experimental data for Zn doped Y123 [Loram et al. 1990]. The linear drop of T_c and $\Delta C(T_c)$ is independent of both μ and the sharpness of the vHs in the EDOS. The implication of this is that these experimental data can not be explained by a simple d–wave picture with short range s–wave resonance scattering.

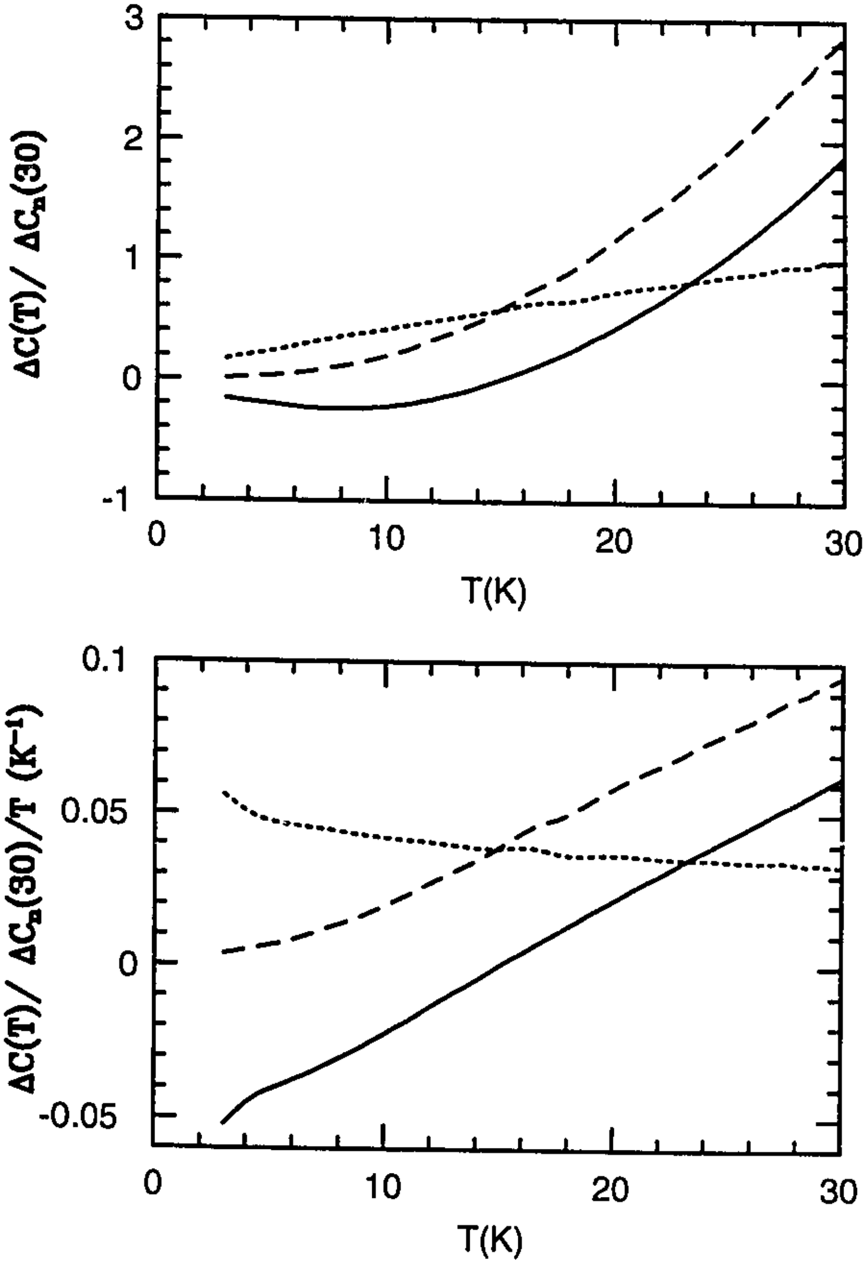

Figure 5.13: $\Delta C(T)$ (solid), $C_n(T)$ (dotted) and $C_s(T)$ (dashed) vs. T for a d–wave superconductor (μ=0.0 meV). The lower frame is for the same curves in the upper frame but divided by T.

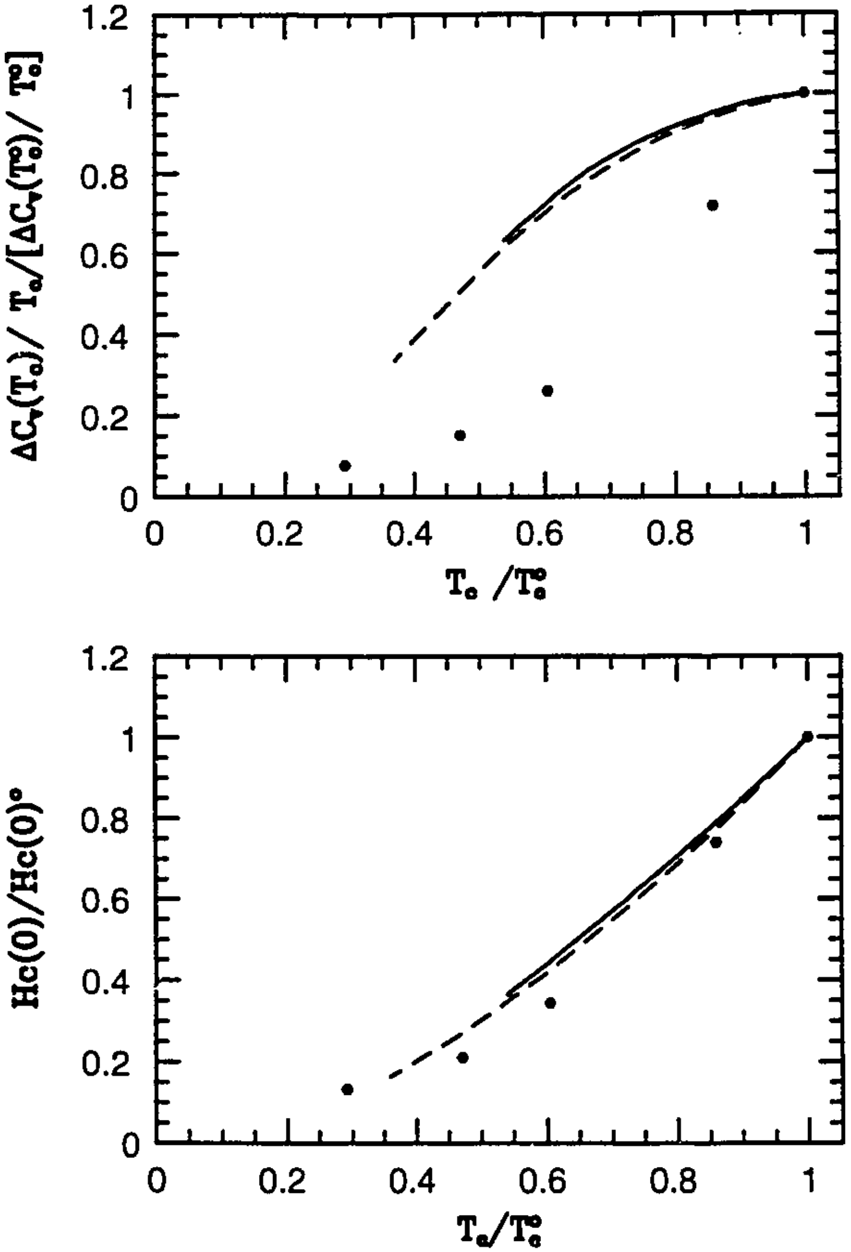

Figure 5.14: Upper frame; $\Delta C(T_c)/T_c$ normalized to its clean limit value vs. T_c normalized by the clean limite T_c for a d–wave superconductor. Lower frame; $H_c(0)$ normalized by its clean limit value vs T_c/T_c^0. The solid curve is for Born scattering and the dashed curve is for resonant scattering.

The thermodynamic critical field data, on the other hand, are much better described by this simple d–wave picture, lower frame of Figure (5.14).

As for the low temperature dependence of the London penetration depth described in Chapter 4, Born and resonant scattering have quite different effect on the low temperature dependence of the superconducting specific heat. Born scattering leaves the low temperature dependence unchanged (quadratic in T), while the smallest concentration of resonance impurities scattering changes the quadratic dependence to a linear one. In Figure (5.15), we show $\Delta C(T)/T$ normalized to its pure limit value for different impurity concentration t^+ (in the Born limit). In the upper frame, the percent reductions in T_c are 0% (solid), 4.5% (dotted), 9.1% (dashed) and 14% (long dashed curve). All the $\Delta C(T)/T$ curves in the upper frame extrapolate linearly to almost the same intercept at T=0. In the lower frame, we increase t^+ to get higher percent reductions of T_c, namely 19% (solid), 29% (dotted), 34% (dashed) and 40% (long dashed curve). The remaining parameters for these calculations are $\bar{t}$=50 meV, μ= –50 meV, λ=g=1.0, ω_E=90 meV, cutoff is 1350 meV and T_c for t^+=0 is 220 K. We now notice that $\Delta C(T)/T$ extrapolates to a higher value at T=0 evidence of density of states filling at high enough reductions in T_c. Notice that the reduction γ_n is expected to be very small because μ is far from the vHs (negligible smearing).

In Figure (5.16), we show the effect of resonance scattering on $\Delta C(T)$ for the same d–wave superconductor presented in Figure (5.15). In the upper frame, the percent reductions in T_c for the $\Delta C(T)/T$ curves are 0% (solid), 6.6% (dotted), 13% (dashed), 20% (long dashed) and 26% (dotted dashed curve). In the lower frame, the percent reductions in T_c for $\Delta C(T)/T$ curves are 32% (solid), 39% (dotted), 46% (dashed) and 53% (long dashed curve). Immediately, with very

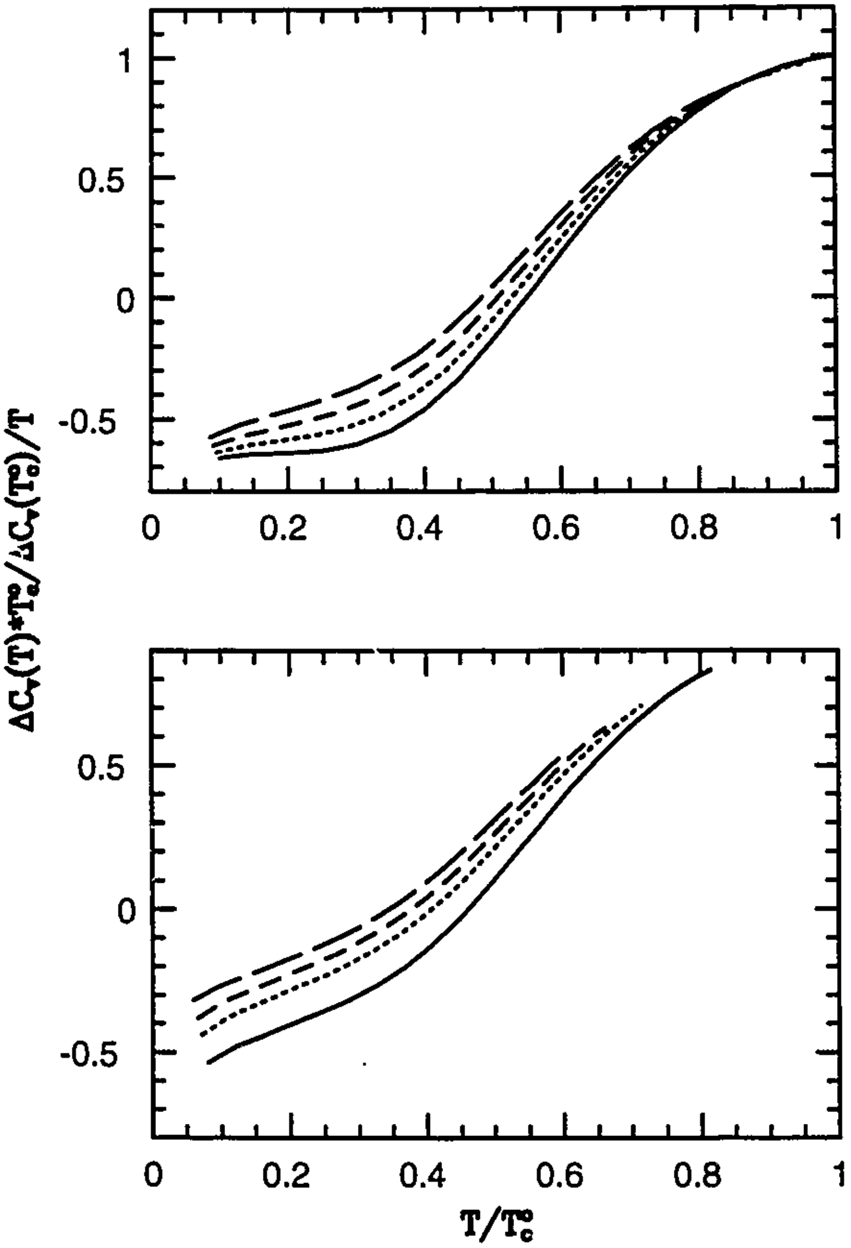

Figure 5.15: $\Delta C(T)/T$ normalized by $\Delta C(T_c^0)/T_c^0$ vs. T/T_c^0 for a d–wave superconductor with Born scattering. The curves in the upper frame are for $t^+=0.0$ (solid), 1.0 (dotted), 2.0 (dashed) and 3.0 meV (long dashed). The curves in the lower frame are for $t^+=4.0$ (solid), 5.0 (dotted), 6.0 (dashed) and 7.0 meV (long dashed).

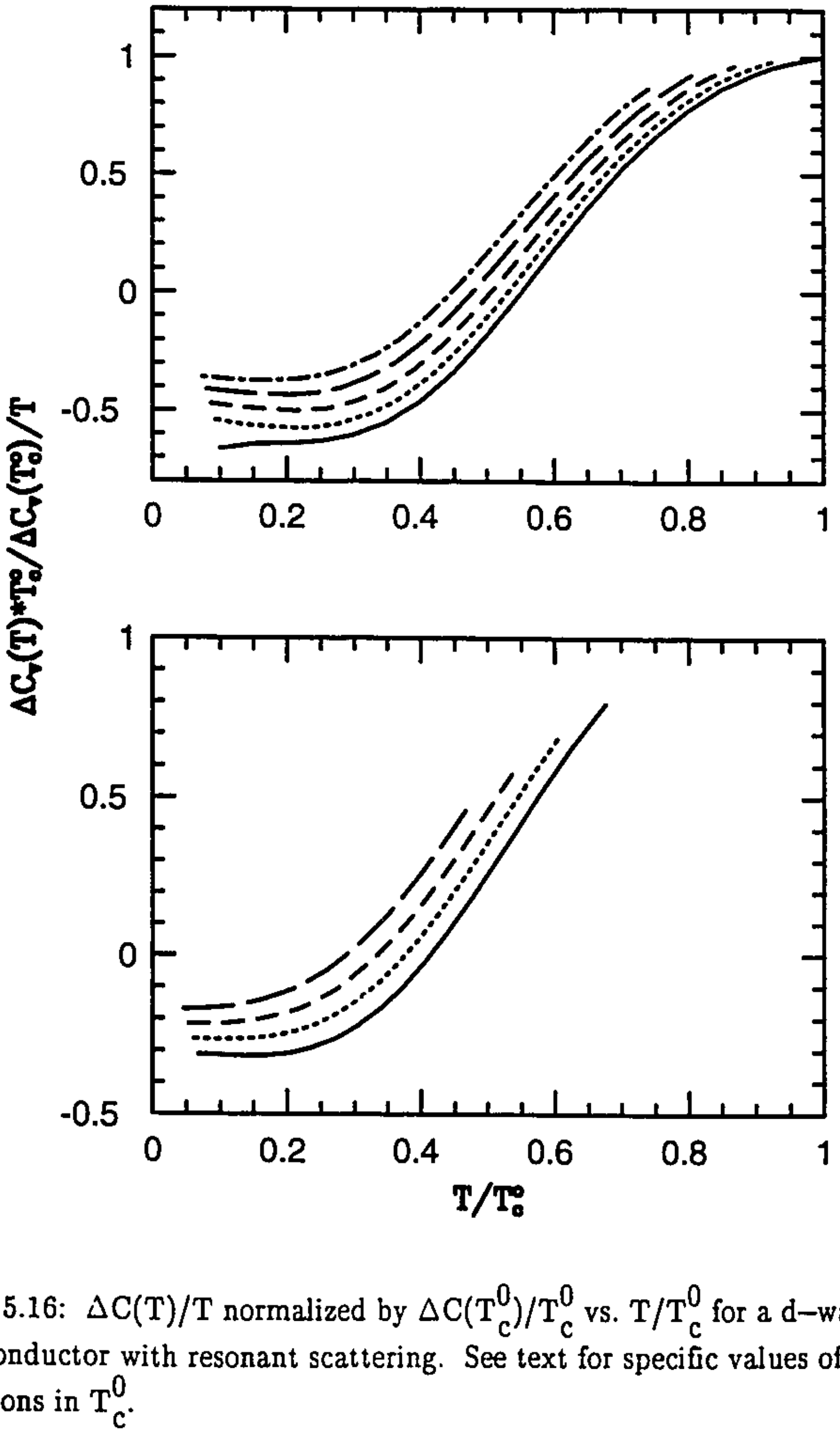

Figure 5.16: $\Delta C(T)/T$ normalized by $\Delta C(T_c^0)/T_c^0$ vs. T/T_c^0 for a d–wave superconductor with resonant scattering. See text for specific values of percent reductions in T_c^0.

small reductions in T_c, the quadratic dependence is replaced by a linear behaviour and $\Delta C(T)/T$ extrapolates to a higher value than for $\Gamma=0$ indicative of an enhancement of the low energy states in the superconducting states. This filling up of density of states is monotonic with the concentration of resonance scatterers, Γ, and resembles the experimental results for Zn doped LSCO described at the end of the experimental sections in this chapter.

IV) Conclusions

In regular metals and constant EDOS, $\gamma_n(T)$ has a local minimum at $T=0$ and a maximum at $T\sim 0.1\ \theta_D$, where θ_D is the Debye temperature. With a logarithmic singularity in the EDOS, the maximum in $\gamma_n(T)$ shifts to $T=0$. $\gamma_n(T)$ then becomes monotonic decreasing function of T. Our calculations do not establish unambiguously whether this peak is finite or not at $T=0$. In the absence of the electron–phonon interaction, we showed that $\gamma_n\sim -\ell n\ T$ and hence does not saturate at $T=0$. As the chemical potential moves away from the centre of the vHs, this peak shifts gradually to higher temperatures. Normal impurity doping, on the other hand, leaves the position of the peak at $T=0$ (unchanged). The magnitude of $\gamma_n(T)$ gets reduced with impurity concentration and for high enough concentration $\gamma_n(0)$ is finite and regular. In the infinite band model, $\gamma_n(T)$ saturates to a constant value in the limit $t^+\rightarrow\infty$, With finite bands $\gamma_n(T)$ does not saturate to a constant value.

The experimental data of $\Delta C(T_c)/T_c$ for oxygen doped Y123 could be explained by a vHs model as is shown by Figure (5.7). This is true irrespective of the coupling strength. This same ratio for Zn doped Y123 was also found to be reasonably accounted for by the vHs model (Figure (5.9)). This is taken as evidence for the existence of a sharp density of states at the Fermi level. The calculations for a d–wave superconductor with a finite band and seperable pairing potential did not agree with the experimental data for both types of dopings. This is not interpreted as evidence against the d–wave mechanism for two reasons. First, changing μ in a d–wave seperable model results in hole doping and also modifies the pairing potential. Second, T_c in this simple model is very sensitive to impurity concentration.

The low temperature behaviour of $\Delta C(T)$ in d–wave compares well with experiments by Moler [Moler et al. 1994] and Momono [Momono et al. 1994], particularly the development of a linear superconducting specific heat with the addition of Zn impurities (resonant scattering).

Chapter 6

Upper Critical Field Hc_2

I) Introduction

The Werthamer–Helfand–Hohenberg (WHH) theory [Helfand 1966] has been very successful in describing the temperature dependence of the upper critical field $Hc_2(T)$ for most conventional superconductors. Hc_2 is the magnetic field beyond which superconductivity ceases to exist. Some recent measurements of $Hc_2(T)$ for various HTSC, however, show an anomalous upward curvature that is not consistent with the WHH theory [Osofsky et. al. 1993 and Mackenzie et. al. 1993]. Schossmann and Schachinger (SS) have extended the WHH theory to include the full electron–phonon interaction [Schossmann 1986]. It is found in this new SS theory that for a larger ratio of $T_c/\omega_{\ell n}$ the $Hc_2(T)$ curve shows an upward curvature [Marsiglio and Carbotte 1987]. According to this model the reduced critical field $hc_2(T)$ is defined as

$$hc_2(T) = \frac{Hc_2(T)}{T_c \left| \frac{dHc_2(T)}{dT} \right|_{T_c}}. \qquad (6.1)$$

The normalized upper critical field hc_2 is a dimensionless quantity and is widely used in literature. For an isotropic s–wave gap the maximum $hc_2(0)$ is slightly less than 1.5. These new experiments show values of $hc_2(0)$ in excess of 1.6 in the HTSC. This is in disagreement with the maximum possible value in the SS theory.

There has been some early attempts to use lower dimensionality arguments and the WHH formalism to carry out calculations of $Hc_2(T)$ [Rieck 1991; Prohammer 1990b; Pint 1990]. These calculations do not show any anomalous upturn in $Hc_2(T)$ curves. Other attempts make use of spin fluctuation mechanisms within the SS model with anisotropic order parameters, for example, p–wave [Scharnberg 1980] and d–wave [Prohammer 1990a]. These calculations also do not show any different behaviour of the $Hc_2(T)$ curves from the regular s–wave SS model. The inclusion of thermal fluctuations, however, does result in an upward curvature of $Hc_2(T)$ near T_c [Reick et al. 1989]. This might be important if 2D fluctuations extend to a large temperature range below T_c.

Our approach to the $Hc_2(T)$ problem is to introduce in the formalism the energy dependence of the EDOS. The particular model that we will apply for $N(\epsilon)$ is that of a simple logarithmic van Hove singularity. We have followed the SS formalism closely and modified it to include the nonconstant EDOS in Section V of Chapter 2. In this chapter, we will calculate $Hc_2(T)$ for two types of order parameters, s–wave and d–wave. Next we will present the appropriate form of the equations necessary to carry out the numerical calculations for $Hc_2(T)$. In Section

III we will show our results and then compare them with experiment in Section IV. Section V contains asymptotic limits on $hc_2(0)$ and in Section VI we give a brief summary.

II) Formalism

In the absence of Pauli limiting the Eliashberg equation for the omega channel was given by equation (2.13a) and the order parameter equation was given by equation (2.73). Equation (2.13a) can be put in a form similar to equation (3.11) where the model for the electronic density of states $N(\epsilon)$ is taken to be a simple undamped van Hove singularity given by equation (1.4). Its particular $\hat{N}(\tilde{\omega}_n)$ is given by equation (3.18). This choice of $N(\epsilon)$ is convenient because it is the simplest choice and it has no poles in the upper and lower half of the complex ϵ–plane. The presence of poles would only complicate the mathematics. Furthermore, in all our calculations we will choose a large value of E_f such that we will stay within the physical regime, i.e. $\hat{N}>0 \ \forall \ \tilde{\omega}_n$ up to the cut off frequency. The last point to mention here about the omega equation is that only the linearized form is used to calculate Hc_2.

We now turn our attention to the gap equation, equation (2.73). Because we are using the infinite band model for these calculations, we have to make some approximations and adjustments to this equation. First of all, we will change the sum over q to an energy and an angular integration (consult equation (2.17)). The energy integration can be performed most easily and as a result the gap Δ, pairing interaction $I^2\chi$, and the Fermi velocities v_i, will all be pinned to the Fermi level. Our eigenvalue equations are described in some detail in Appendix B for both the d–wave and s–wave case. For the s–wave case, the equation for the largest eigenvalue with nonconstant density of states is

$$\tilde{\Delta}(i\omega_n) = \pi T \sum_m [\lambda(n-m)-\mu^*\theta(\omega_c-|\omega_m|)] \frac{\tilde{\Delta}(i\omega_m)}{\hat{N}^{-1}(\tilde{\omega}_m)X^{-1}(i\omega_n)-\pi(t^+-t^-)}, \quad (6.2)$$

where

$$\hat{N}(\tilde{\omega}_m) = r - \frac{s}{2} \ln\left[\frac{(\delta^2+\tilde{\omega}_m^2)}{E_f^2}\right], \quad (6.3)$$

$$\tilde{\omega}_n = \omega_n + \pi T \sum_m \lambda(n-m) \operatorname{sgn} \tilde{\omega}_m \hat{N}(\tilde{\omega}_m) + \pi(t^+ + t^-)\hat{N}(\tilde{\omega}_n), \quad (6.4)$$

and in 2D (see (B.18))

$$X(i\omega_m) = \frac{2}{\sqrt{\alpha}} \int_0^\infty dq\, e^{-q^2} H(\beta_m q), \quad (6.5)$$

with $\alpha=\alpha_1/2\, v_F^2$, $\alpha_1=eH$, v_F is the Fermi velocity and

$$\beta_m = \frac{\sqrt{\alpha}}{|\tilde{\omega}_m|}, \quad (6.6)$$

and

$$H(x) = \frac{x}{\sqrt{1+x^2}}. \quad (6.7)$$

In 3D, H(x) is replaced by F(x) while keeping the same arguments and

$F(x)=\tan^{-1}x$.

For the d–wave case, (see Appendix B) we have,

$$\Delta(i\omega_n) = \frac{1}{2}\,[c_1(n)+c_3(n)+[(c_1(n)-c_3(n))^2+4\,c_2^2(n)]^{1/2}], \tag{6.8}$$

and

$$c_i(n) = \pi gT \sum_m \lambda(n-m)\,\Delta(i\omega_m)\,\hat{N}(\tilde{\omega}_m)\,X_i(i\omega_m), \tag{6.9}$$

for i=1,2,3 and for X_i in 2D we have

$$X_1(i\omega_m) = \frac{2}{\sqrt{\alpha}}\int_0^\infty dq\, e^{-q^2}\, H(\beta_m q), \tag{6.10}$$

$$X_2(i\omega_m) = -\frac{4}{\sqrt{\alpha}}\frac{1}{\sqrt{6}}\int_0^\infty dq\, e^{-q^2}\, L_2^0(q^2)\, H(\beta_m q), \tag{6.11}$$

$$X_3(i\omega_m) = \frac{2}{\sqrt{\alpha}}\int_0^\infty dq\, e^{-q^2}\, L_4^0(2q^2)\, H(\beta_m q). \tag{6.12}$$

The case of 3D simply amounts to replacing $H(\beta_m q)$ by $G(\beta_m q)$ in every X_i where G(x) is now given by

$$G(x) = \frac{15}{64}\left\{3(x^{-1}-x^{-3}) + [3-2x^{-2}+3x^{-4}]\tan^{-1}x\right\}. \tag{6.13}$$

III) Numerical results

In this section we present numerical solutions for Hc_2 and hc_2. The method of solution involves increasing α to a value such that $\Delta^2(i\omega_0)$ equals zero.

This critical value α_c, corresponds to our desired value of the upper critical field through the relation

$$Hc_2 = \frac{2\alpha_c}{eV_F^2}, \tag{6.14}$$

and is obtained from the largest eigenvalue of the linearized gap equation. In all of our calculations in this chapter, we use a lead spectrum for $\alpha^2F(\omega)$ for which $\omega_{\ell n}$=4.83 meV and ω_{max}=11 meV, μ^*=0.0, ω_c=30 ω_{max}, and $v_F=10^6$m/s.

We will first present results for a constant EDOS and compare the 3D to the 2D case. Figure (6.1) shows the results for two different coupling strengths, T_c=0.11 $\omega_{\ell n}$ in the upper frame and T_c=0.39 $\omega_{\ell n}$ in the lower frame. The long dashed curves are for an s–wave order parameter in 3D. For all the coupling strengths in 3D we have found that s–wave in 3D gives larger values of $hc_2(0)$ than the d–wave case. For two dimensions, the dotted curves are for s–wave and the solid curves are for a d–wave order parameter. The d–wave curves are always higher than the s–wave curves in two dimensions. For these two coupling strengths, the d–wave $hc_2(t)$ curves in 3D are still higher than the d–wave curves in 2D. As the coupling strength increases, the $hc_2(t)$ curves push up to higher values at t=0 and develop an upward curvature in the intermediate region below T_c. In Figure (6.2) we show the influence of coupling strength on the d–wave case (upper frame) with constant EDOS in 2D, some s–wave curves are shown in the lower frame. The curves in terms of $T_c/\omega_{\ell n}$ are for 0.11 (lower solid), 0.21 (dotted), 0.28 (short dashed), and 0.39 (long dashed). The values of $hc_2(0)$ do not increase indefinitely. The maximum value of $hc_2(0)$ for 2D d–wave is about 1.3. For larger $T_c/\omega_{\ell n}$, $hc_2(0)$ will drop gradually to some asymptotic value. The upper solid curve in the upper frame of Figure (6.2) is for $T_c/\omega_{\ell n}$=4.10. Similar results have been

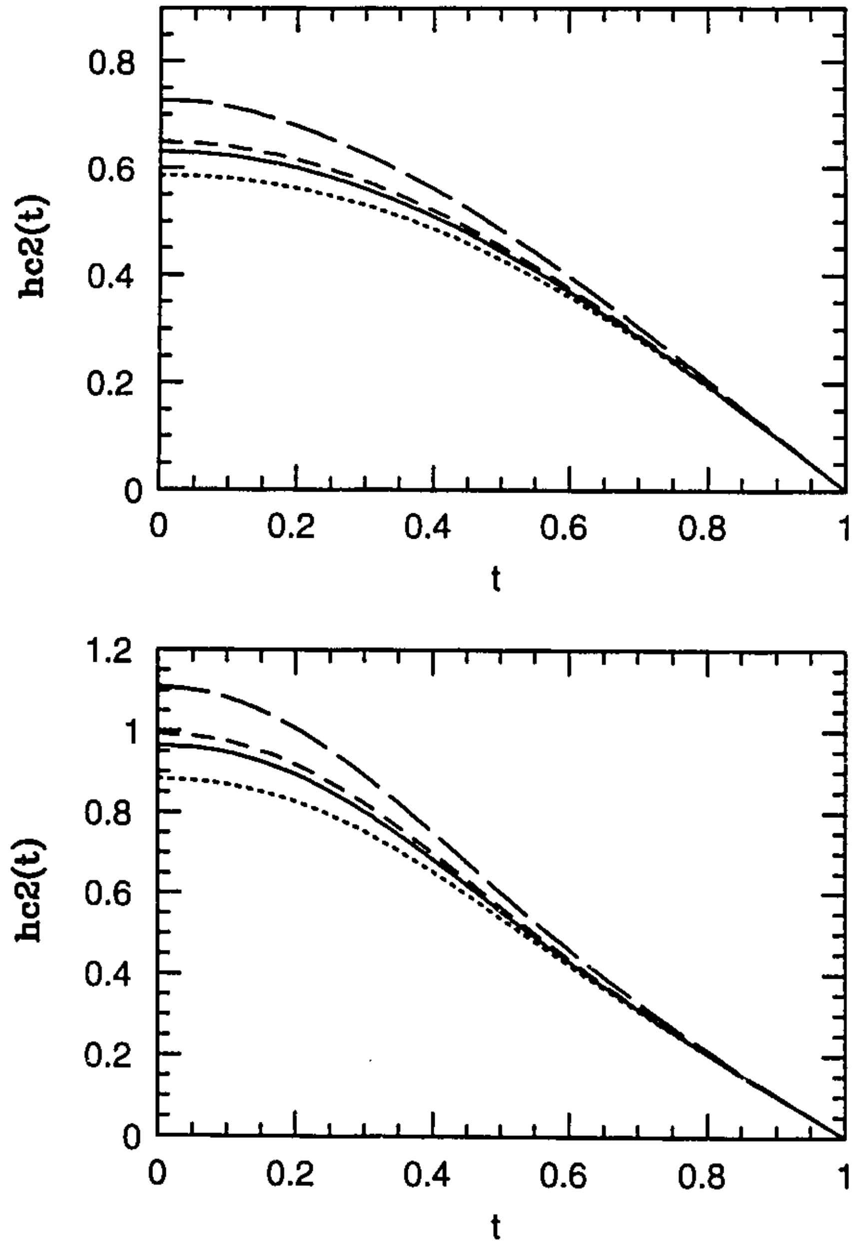

Figure 6.1: Reduced upper critical field versus reduced temperature for two different coupling strengths T_c=0.11 $\omega_{\ell n}$ (upper frame) and T_c=0.39 $\omega_{\ell n}$ (lower frame). The EDOS is constant and the curves are for 2D s–wave (dotted) and d–wave (solid) and 3D s–wave (long dashed) and d–wave (dashed curve).

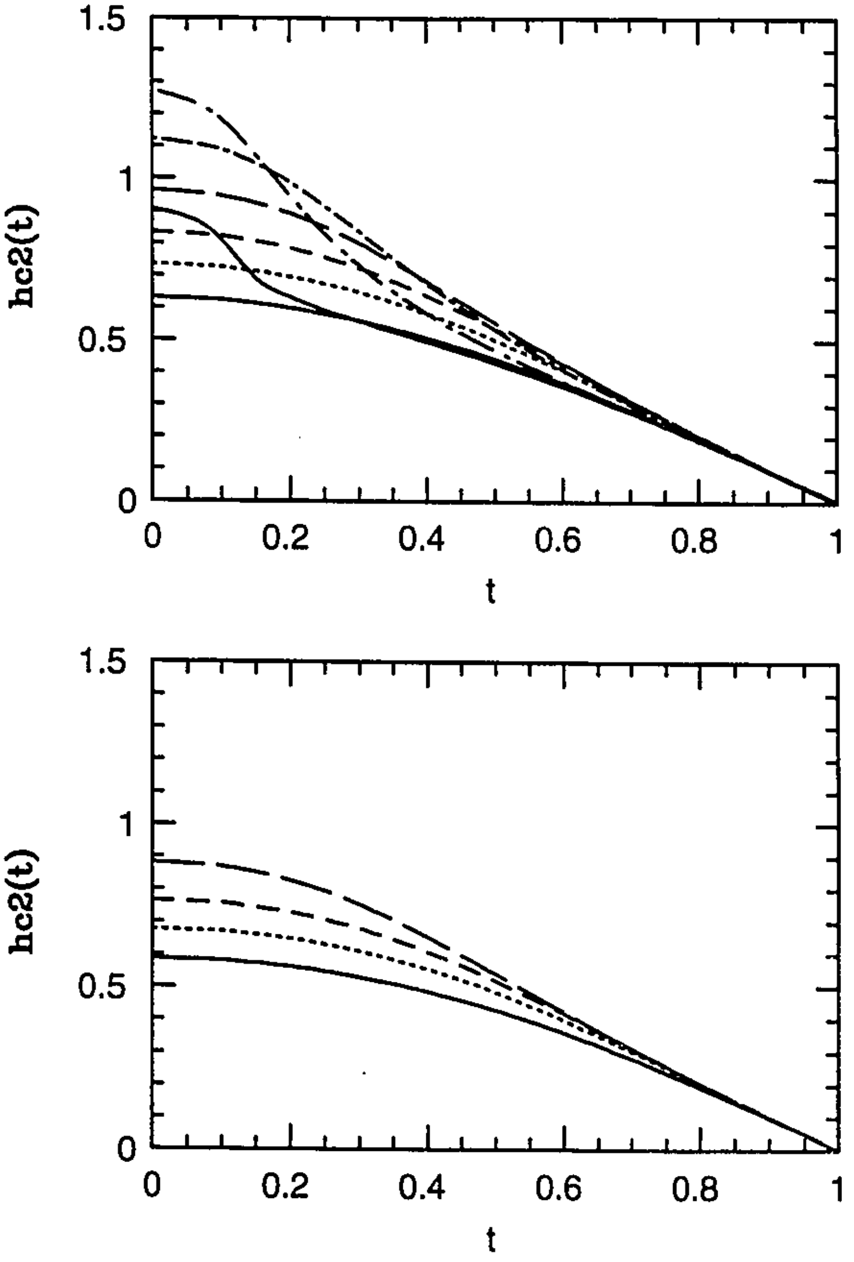

Figure 6.2: Reduced upper critical field versus reduced temperature for constant EDOS d–wave (upper frame) and s–wave (lower frame). The coupling strength is varied and the curves are for $T_c/\omega_{\ell n}$ equal to 0.11 lower solid, 0.21 dotted, 0.28 dashed, 0.39 long dashed for both frames and 0.56 dotted dashed, 0.99 dotted long dashed, and 4.1 for the upper solid curve.

calculated before for the s–wave case in 3D where it was found that the maximum in $hc_2(0)$ is about 1.5 for a lead spectrum [Marsiglio and Carbotte 1987].

We are interested in the effect of a van Hove singularity in the EDOS on $hc_2(t)$. In Figure (6.3), we show $hc_2(t)$ calculations for both d–wave and s–wave (lower frame) as the van Hove singularity is switched on. The density of states parameters are shown in the figure caption. The curves are for $T_c/\omega_{\ell n}$ equal to 0.18 (solid), 0.33 (dotted), 0.40 (dashed), 0.46 (long dashed), 0.51 (dotted dashed), and 0.64 (dotted long dashed). The solid curves are for a constant EDOS. We notice a large gain in $hc_2(0)$ coming directly from the peak in the EDOS. For comparable $T_c/\omega_{\ell n} \sim 0.4$, we see that the long dashed curve in Figure (6.2) has $hc_2(0) \sim 0.93$ and the dashed curve in Figure (6.3) has $hc_2(0) \sim 1.3$ for the d–wave case. With even a higher s value of about 11, which correspond to T_c=1.03 $\omega_{\ell n}$, we can push $hc_2(0)$ up to 3.9. This value of $hc_2(0)$ does not increase indefinately with s. Higher values of s increase the coupling strength. This in effect produces more smearing of the vHs in the EDOS and its role becomes less important. So in the limit of large s or λ, $hc_2(0)$ drops to a smaller value charactaristic of the strong coupling limit with a constant EDOS, $hc_2(0) = 0.57$ [Carbotte 1990].

Figure (6.4) shows a plot of $Hc_2(0)$ versus T_c (lower frame). The variation in T_c is accomplished by increasing s from 0.0 to 11.0. The upper frame is a log–log plot of $Hc_2(0)$ vs T_c from which we can infer that $Hc_2(0)$ is proportional to T_c^m with $m \geq 6$. In the clean limit (with the two square well model considered in section V of this chapter), the zero temperature value of $Hc_2(T)$ for a 2D s–wave superconductor with constant EDOS is given by

$$Hc_2(0) = 2\pi^2 \, e^{-\gamma}[1+\lambda(0)]^2 \, T_c^2/(eV_F^2), \tag{6.15}$$

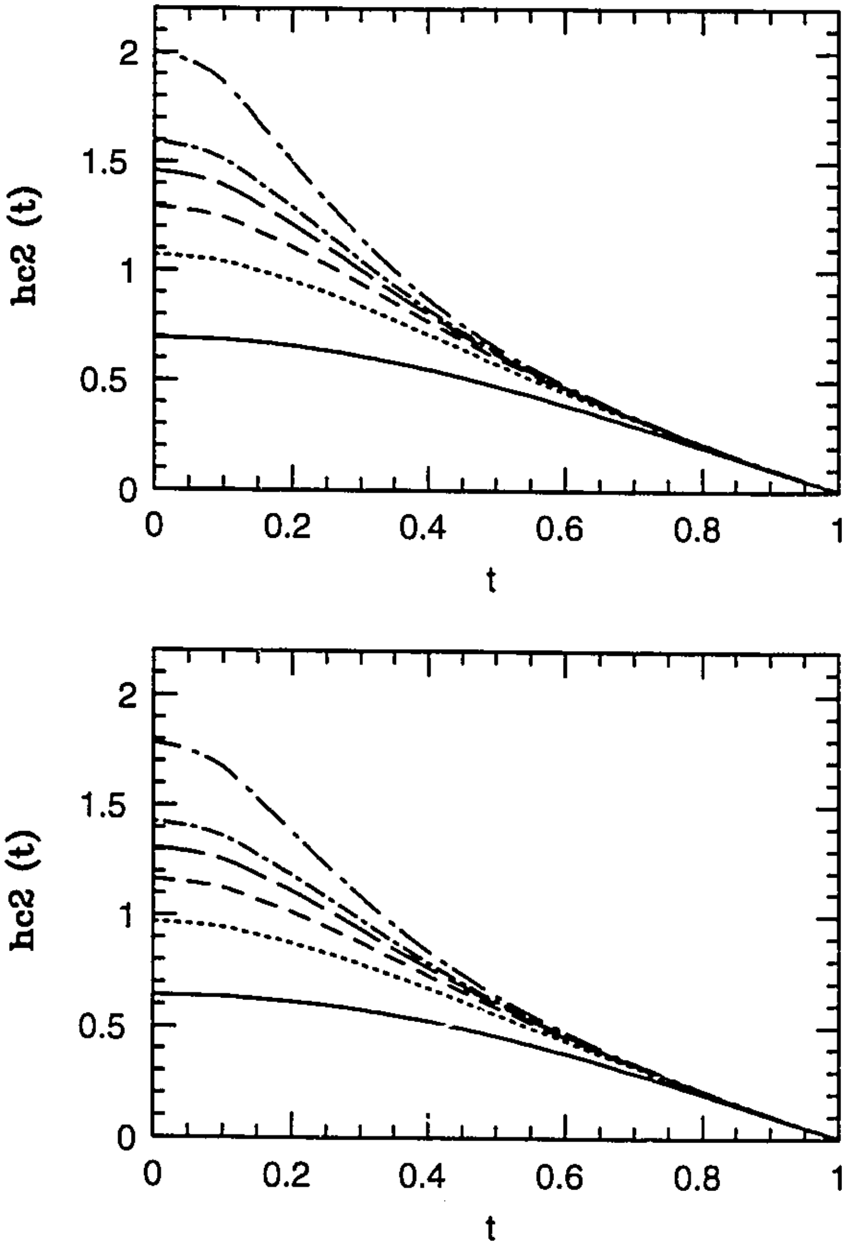

Figure 6.3: $hc_2(t)$ vs t for different s values; solid 0.0, dotted 0.25, dashed 0.5, long dashed 0.75, dotted dashed 1.0 and dotted long dashed is for s=2.0. Upper frame is for d–wave and lower frame is for s–wave.

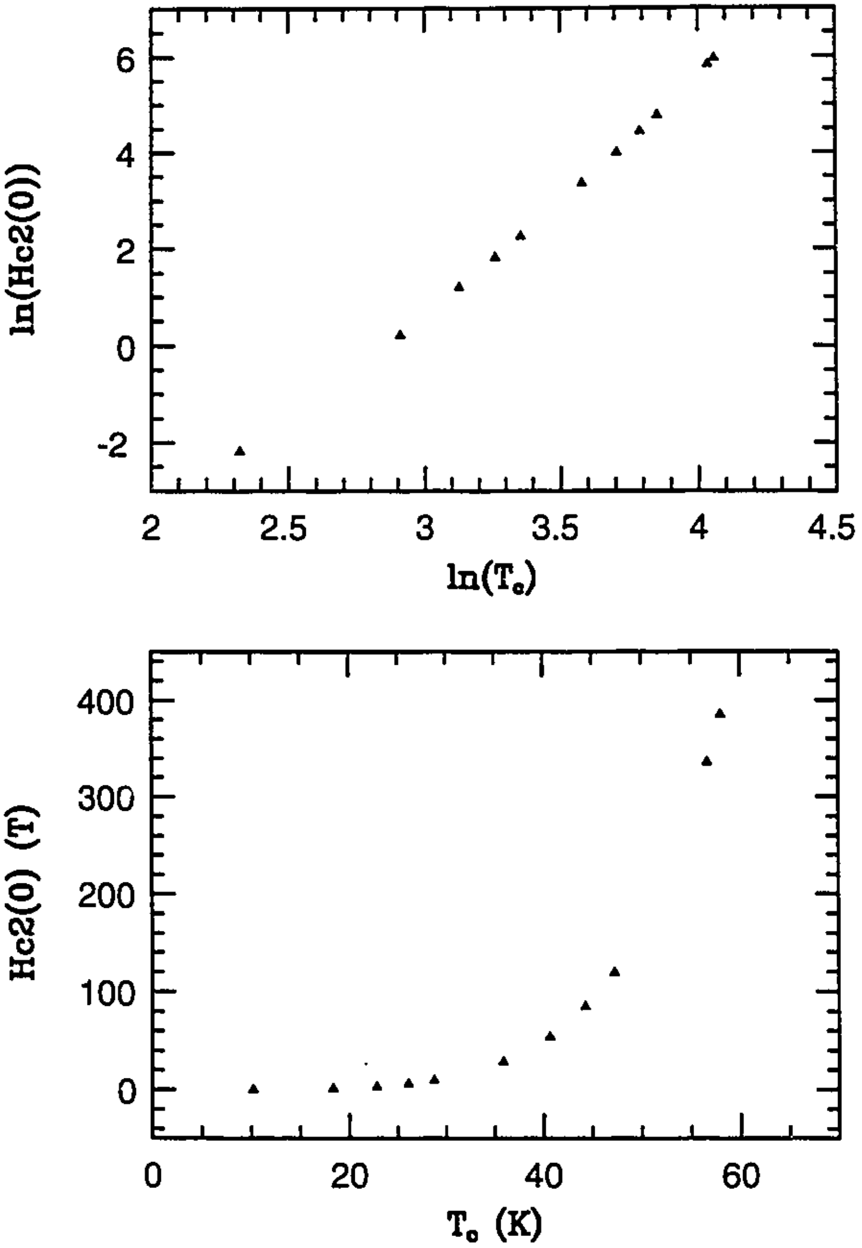

Figure 6.4: $Hc_2(0)$ vs T_c (lower frame). The lowest T_c point is for a constant EDOS ($r=1.0$, $s=0$) with $T_c/\omega_{\ln}=0.18$. The higher T_c points are for increasing values of s. The largest T_c correspond to $s=11$. The upper frame shows $\ln Hc_2(0)$ vs $\ln T_c$ for the same data.

where γ is Euler's constant. At first sight, we may only expect to see a T_c^2 law for $Hc_2(0)$ but Figure (6.4) shows a higher exponent of about 6. In the asymptotic limit of large λ, however, we have $T_c \sim \sqrt{\lambda(0)}$ and hence $Hc_2(0)$ becomes proportional to T_c^6. By increasing s dramatically we are actually going to large λ's so that the result of a T^m law with m equal to approximately 6 is justified.

The enhancement of $hc_2(0)$ is also sensitive to the position of the chemical potential from the center of the peak in the EDOS. This effect is illustrated in Figure (6.5) and Figure (6.6), in which the chemical potential δ is moved away from the centre of the vHs. In Figure (6.5), we plot $hc_2(t)$ versus t (upper frame) and $Hc_2(T)$ versus T (lower frame) with $s = 1.0$ and $T_c=0.512\ \omega_{\ell n}$. It can be seen from Figure (6.5) that $hc_2(0)$ drops dramatically from 1.6 at $\delta=0.0$ to 1.07 at $\delta=40$ meV while, on the other hand, T_c decreases only slightly from 28.7K to 27.9K. Far away from the peak in the EDOS,that is,for $\delta>90$ meV, the rate of change of $hc_2(0)$ with δ is much smaller. Figure (6.6) presents results for the same sort of calculations except with s=11. This is a much stronger coupling case as $T_c^0=1.03\ \omega_{\ell n}$. In the lower frame, we see no significant change in T_c as δ is varied from 0 to 150 meV. We notice also that the relative reduction in $hc_2(0)$ for small δ in the strong coupling case (solid to dashed curve in Figure (6.6)) is much less than that for the weaker coupling case (solid to dotted dashed curve in Figure (6.5)). A plausible explanation is that for small λ there is less smearing of the vHs and hence, $hc_2(0)$ is sensitive to small changes in δ. The reason for the increase of $hc_2(0)$ in the presence of a peak in the EDOS is that retardation effects decrease as the temperature is lowered and the weight of $\hat{N}$ contributing to the gap equation is higher. This results in a large $\alpha(0)$ value. At the same time, the mass enhancement factor increases as a function of decreasing temperature which makes retardation a bit stronger. Lowering the temperature and increasing λ work in opposite directions to increase and decrease the effective integrated $\hat{N}$ respectively.

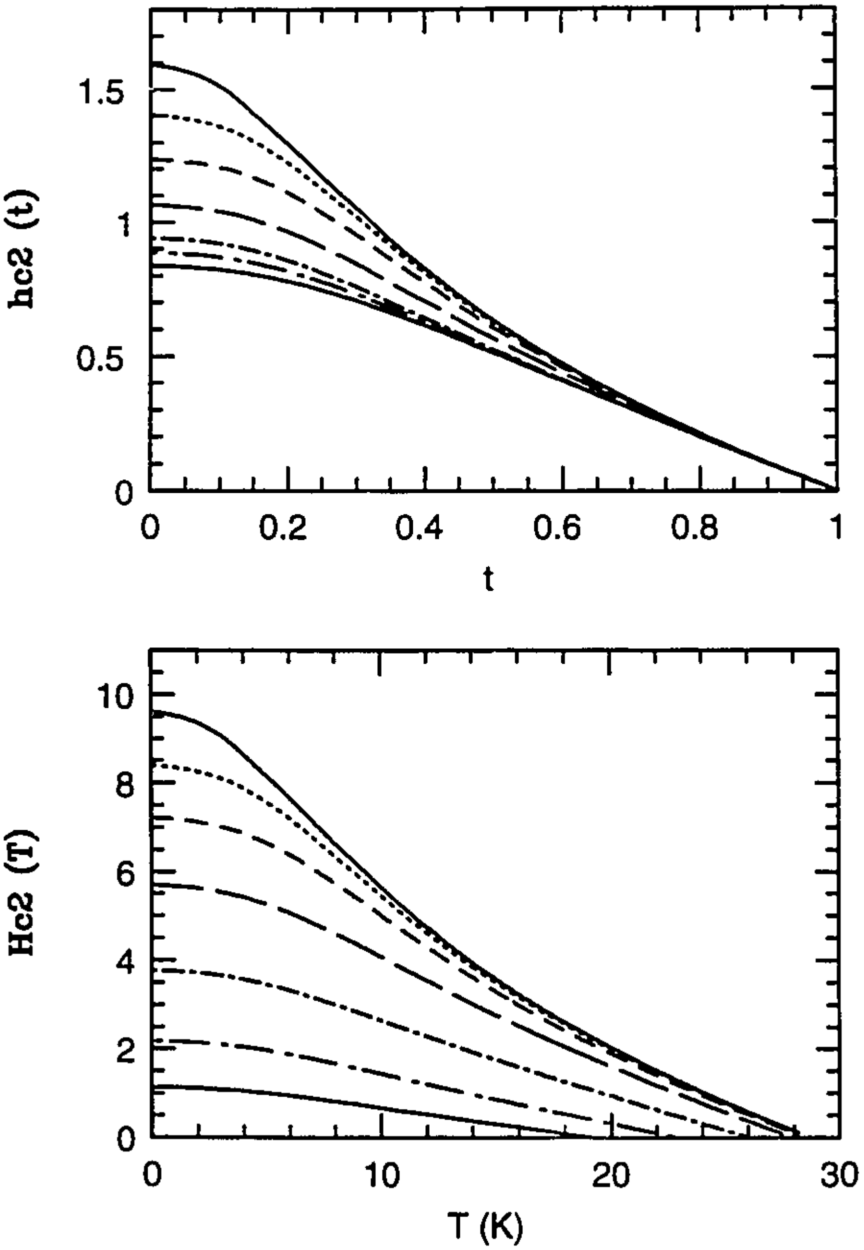

Figure 6.5: Upper frame shows $hc_2(t)$ vs t for different δ values with s=1, r=1 and E_f=1500. The curves are for δ equal to 0 upper solid, 10 dotted, 20 dashed, 40 long dashed, 90 dotted dashed, 200 dotted long dashed, and 400 meV for the lower solid curve. The lower frame is for $Hc_2(T)$ vs T for the same curves.

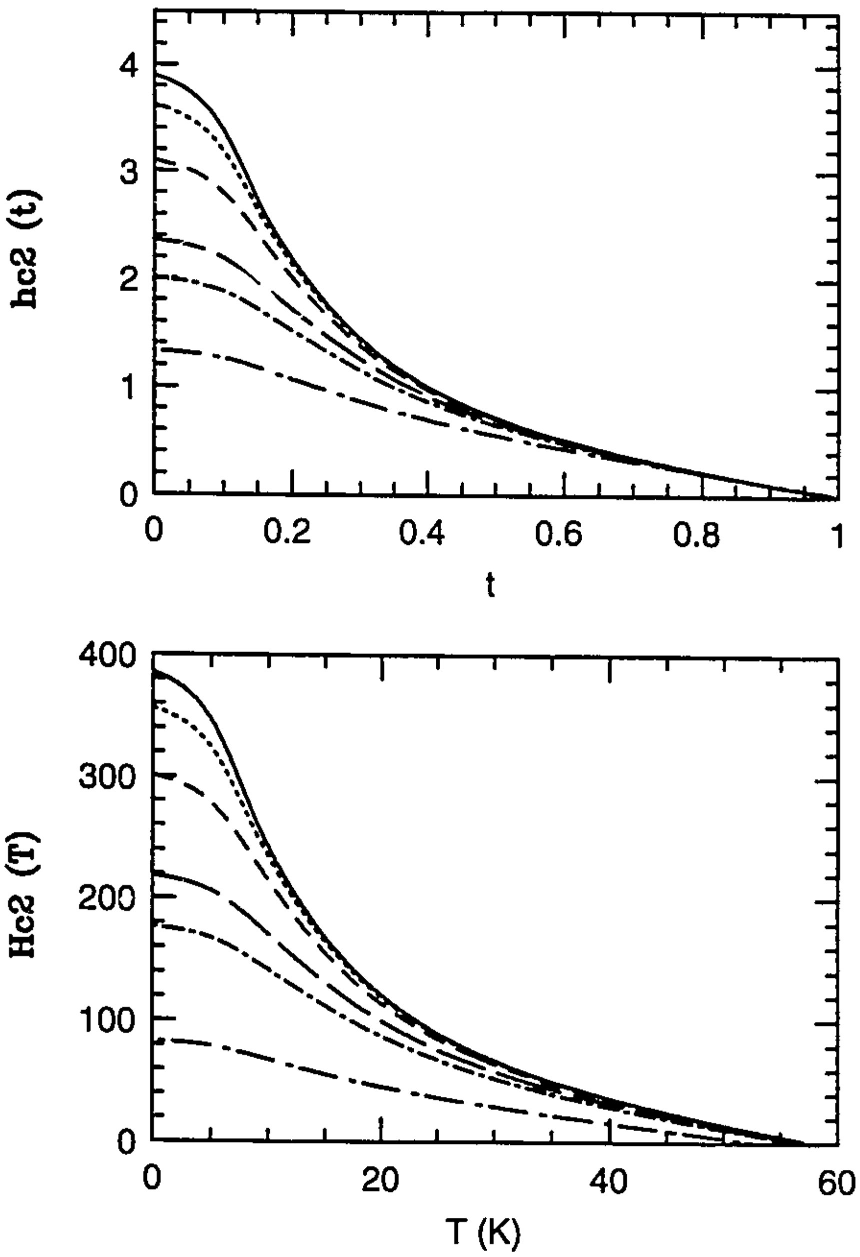

Figure 6.6: Similar to Figure (6.5) but with $s=11$. The curves are for δ equal to 0 solid, 40 dotted, 80 dashed, 150 long dashed, 200 dotted dashed and 400 meV for the dotted long dashed curve.

The net increase of $hc_2(t)$ comes from the fact that the temperature contribution in increasing $\tilde{N}$ is more dominant.

The corresponding increase of $\lambda(T)$ with decreasing temperature is shown in Figure (6.7). The upper frame is for the same case presented in Figure (6.5). The curves are for δ equal to 0 (solid), 10 (dotted), 20 (dashed), 40 (long dashed), 60 (dotted dashed), and 90 meV (dotted long dashed). The variation of $\lambda(0)$ with δ is very similar to that of $hc_2(0)$ with δ. Small changes in δ reduce $\lambda(0)$ appreciably relative to its value at T_c. Similar conclusions hold for the strong coupling case corresponding to the results presented in Figure (6.6). The curves in the lower frame of Figure (6.7) are for δ equal to 0.0 (solid), 60 (dotted), 100 (dashed), 150 (long dashed), 200 (dotted dashed), and 400 meV (dotted long dashed). Near δ=0, $\lambda(0)$ varies slowly with δ contrary to the case in the upper frame. One might infer erroneously from equation (6.15) that the temperature dependence of Hc_2 may depend on that of λ, i. e. $Hc_2(t)$ is proportinal to $[1+\lambda(t)]^2$. Although $\lambda(t)$ and $hc_2(t)$ behave similarly, we would like to stress that they are both caused by the same effect. As a matter of fact, in constant EDOS there is anticorrelation between $hc_2(t)$ and $\lambda(t)$ above zero temperature. In regular Eliashberg theory, $\lambda(t)$ and $\gamma_n(t)$ behave similarly. So $\lambda(t)$ exhibit a local minimum at t=0, while $hc_2(t)$ has a maximum at t=0 followed by a region of upward curvature. Another interesting point to make here is that $hc_2(0)$ and $\lambda(0)$ are both smooth functions and nonsingular as $T \rightarrow 0$, unlike $\gamma(T)$ described earlier in Chapter 5 which simply did not saturate for the case when the chemical potential is pinned to the vHs.

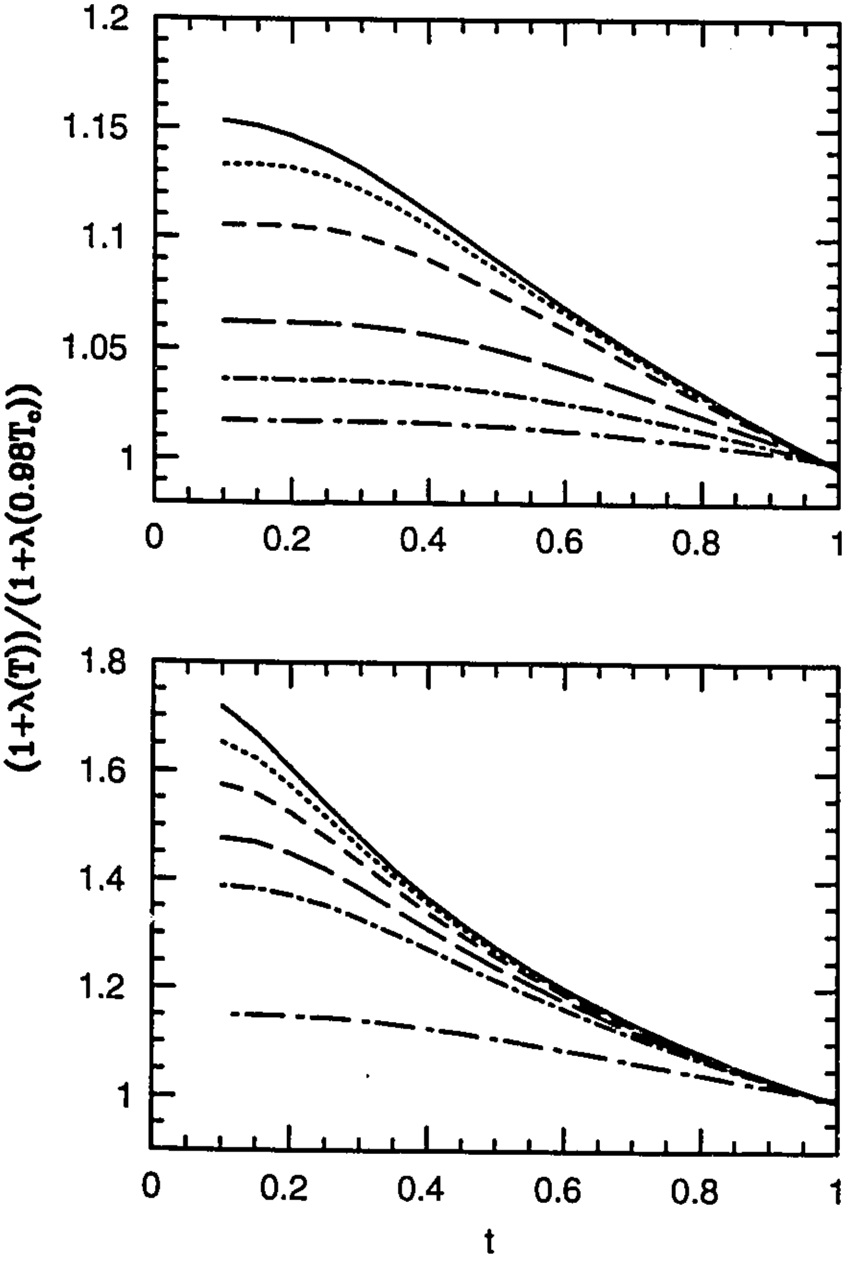

Figure 6.7: $Z(i\omega_0)$ normalized to its value at 0.98 T_c vs t. Upper frame is for s=1 and the same parameters as in Figure (6.5) and lower frame is for s=11 and the same parameters as in Figure (6.6). See text for δ values.

Next, we present our results on impurity scattering. Figures (6.8) and (6.9) show results for the effect of impurity doping in the d–wave case. The solid curve in Figure (6.8) corresponds to the upper solid curve in Figure (6.5) while the solid curve in Figure (6.9) corresponds to the solid curve in Figure (6.6). For both figures we pin the Fermi level to the vHs, at δ=0, and increase the impurity concentration. In the d–wave case, both normal and paramagnetic impurities have the same effect on T_c. As the impurity concentration increases T_c decreases at the same rate for both types of impurities. The impurity concentrations, in order of increasing concentration (decreasing T_c), are 0.0, 0.1, 0.2, 0.4, and 0.6 meV for Figure (6.8) and 0.0, 0.05, 0.1, 0.2, 0.3, 0.4, and 0.6 meV for Figure (6.9). We notice in both figures that $Hc_2(0)$ decreases with decreasing T_c and the relative decrease of $Hc_2(0)$ is more dramatic than the relative decrease in T_c. This is shown more clearly in the upper frames of both figures, where $hc_2(t)$ is reduced substantially from the solid curve, especially at t=0. We attribute this reduction to the smearing of the density of states. Also notice that this reduction in $hc_2(0)$ with impurities is not as dramatic as that resulting from the chemical potential change (Figures (6.5) and (6.6)) if the change in T_c is used as a gauge. Very similar effects are observed for paramagnetic impurity scattering for s–wave superconductors. In Figure (6.10), we show the s–wave case corresponding to the d–wave one shown in Figure (6.8). Paramagnetic impurity scattering is pair breaking and results in a reduction of both T_c and $Hc_2(0)$.

Normal impurity scattering (t^+) in the s–wave case is quite different as can be seen from Figure (6.11). Within the vHs scenario, there can be a decrease or an increase in T_c depending on the position of the chemical potential relative to the peak in the EDOS. For the case where the Fermi level is pinned to the vHs,

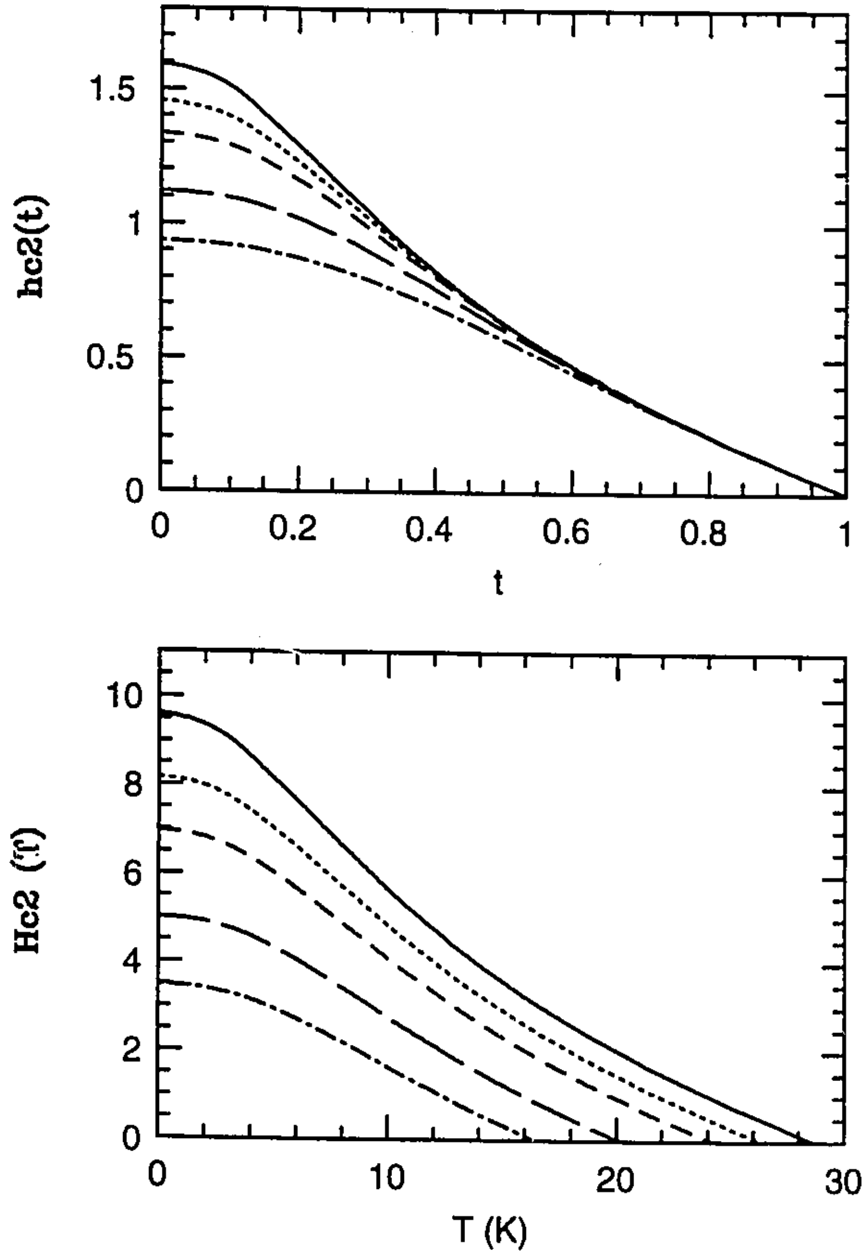

Figure 6.8: Impurity scattering t^+ for the d–wave case with s=1.0. Upper frame $hc_2(t)$ vs t with t^+=0 solid, 0.1 dotted, 0.2 dashed, 0.4 long dashed and 0.6 meV for the dotted dashed curve. Lower frame is for $Hc_2(T)$ vs T for the same curves in the upper frame.

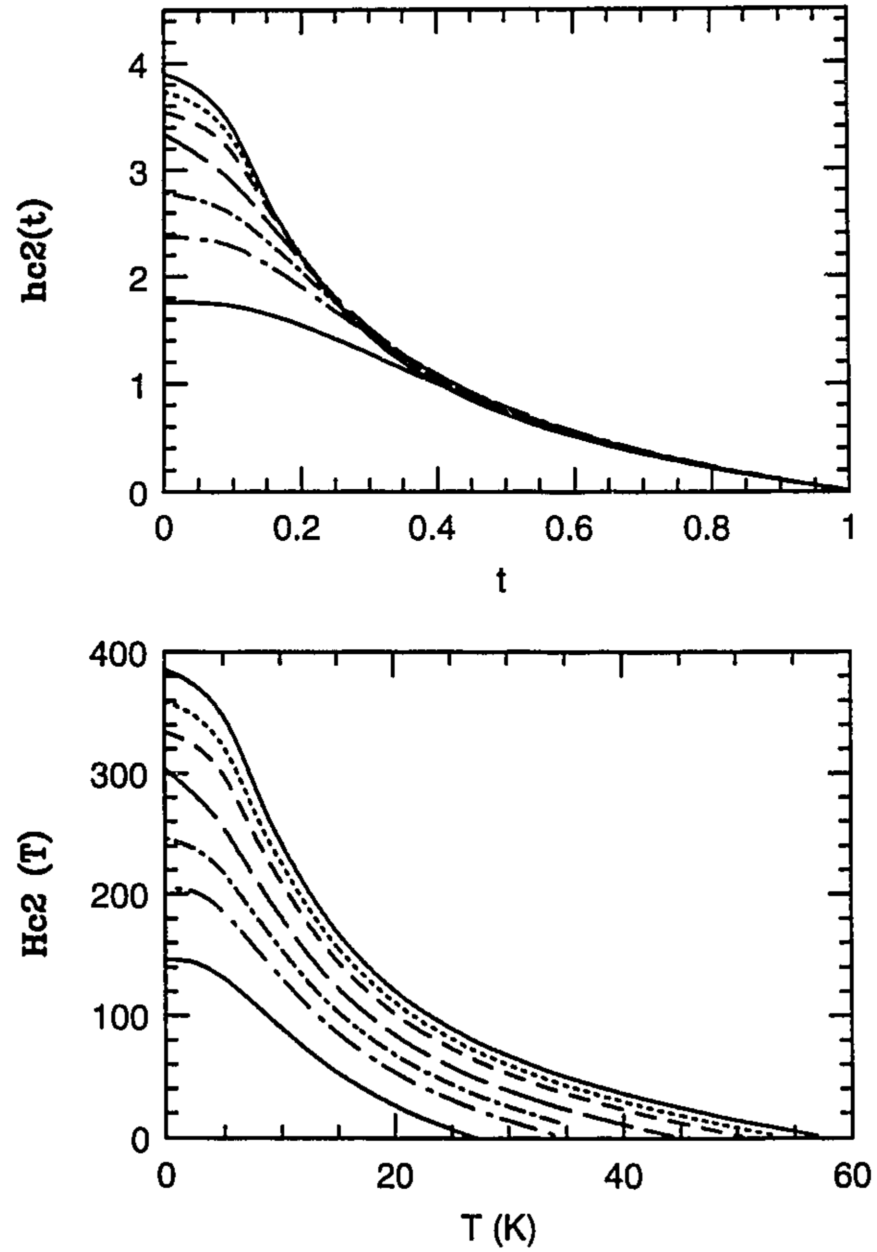

Figure 6.9: Similar to Figure (6.8) but with s=11. Upper frame, $hc_2(t)$ vs t for $t^+=0$ solid, 0.05 dotted, 0.1 dashed, 0.2 long dashed, 0.3 dotted dashed, 0.4 dotted long dashed and 0.6 meV for the lower solid curve. Lower frame, $Hc_2(T)$ vs T for the same curves shown in the upper frame.

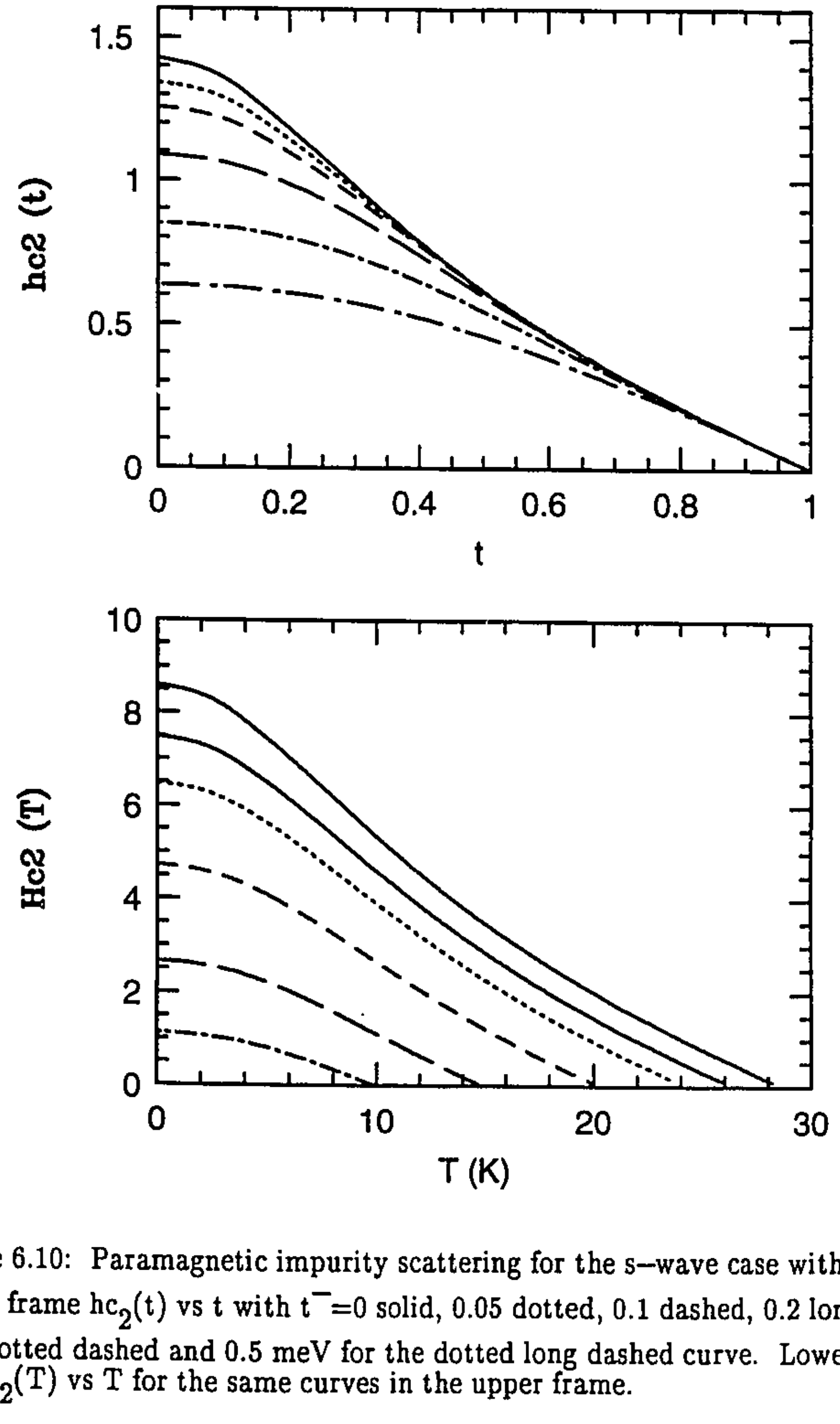

Figure 6.10: Paramagnetic impurity scattering for the s–wave case with s=1.0. Upper frame $hc_2(t)$ vs t with $t^{-}=0$ solid, 0.05 dotted, 0.1 dashed, 0.2 long dashed, 0.35 dotted dashed and 0.5 meV for the dotted long dashed curve. Lower frame is for $Hc_2(T)$ vs T for the same curves in the upper frame.

increasing t^+ always results in monotonic decrease in T_c to a lower bound given by an average background EDOS. The transition temperature is reduced in this case due to smearing of the density of states while $Hc_2(0)$ increases as can be seen in the lower frame of Figure (6.11). A similar increase in the slope of $Hc_2(T)$ at T_c also results. The net over all effect on $hc_2(t)$, however, is to reduce the $hc_2(t)$ curves especially at t=0. In the dirty limit and constant EDOS, we can show that both $Hc_2(0)$ and its slope at T_c are proportional to the normal impurity concentration t^+, and for 2D we have

$$Hc_2(0) = \frac{8\pi}{1.13}\frac{(1+\lambda)}{eV_F^2} T_c\, t^+, \tag{6.16}$$

and

$$\left.\frac{dHc_2(T)}{dT}\right|_{T_c} = -32\frac{(1+\lambda)}{eV_F^2} t^+. \tag{6.17}$$

These two expressions result in the universal number $hc_2(0)=0.69$. This is true even with a nonconstant EDOS.

IV) Experimental comparison

Most of experimental data on HTSC for $Hc_2(T)$ is near T_c and does not extend to lower temperatures. Measurements of $Hc_2(T)$ are done by dc–magnetization, ac–susceptibilities or magnetoresistance. The HTSC samples are either single crystals or magnetically aligned polycrystals. Typical slopes for Y123 are 0.46–0.71 (T/K) at 88.7K [Worthington et al. 1987], 1.9 (T/K) at 92.5K [Welp et al. 1989], 2.01 (T/K) at 92.9K [Zhang et al. 1994]. The variation of T_c in these pure samples of Y123 could be due to a number of reasons among them oxygen

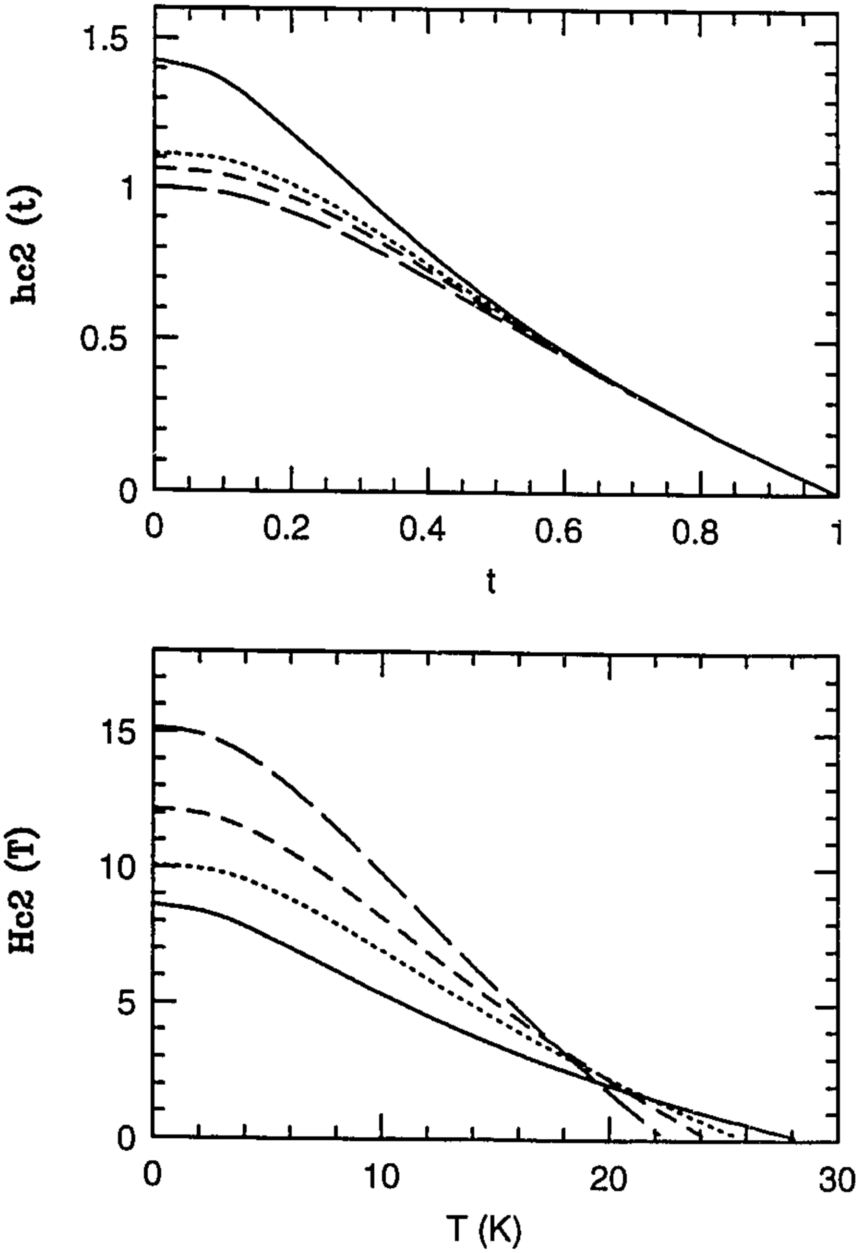

Figure 6.11: Normal impurity scattering for the same case of Figure (6.10). Upper frame $hc_2(t)$ vs t for t^+=0 solid, 5 dotted, 10 dashed and 20 meV long dashed curve. The lower frame $Hc_2(T)$ vs T for the same curves in the upper frame.

deficiency or impurities. Most of the $Hc_2(T)$ data are not well controlled in terms of oxygen or impurity content. This makes meaningful comparison with theory a very hard task. Furthermore, in our formalism, we can only calculate α_c and one has to make a good guess for V_F^2 to be able to extract $Hc_2(T)$ from α_c. In a simple model one might expect that V_F correlates with inverse of the density of states, so that a chemical potential change or even impurity doping will in principle change V_F. Controlled experiments for Y123 with Zn doping could be very useful, given a good model for V_F, in discriminating between s–wave or highly anisotropic s–wave and d–wave. Our calculations show the slope of α_c w.r.t. T at T_c rises substantially with normal impurity doping, while in d–wave there is a very slow change with impurity doping.

In the lower frame of Figure (6.12), we show $Hc_2(T)$ versus T for a $Bi_2Sr_2CuO_7$ overdoped thin film sample (squares) [Osofsky 1993] and for a $T\ell_2Ba_2CuO_6$ overdoped single crystal (triangles) [Mackenzie 1993]. These two materials are highly two–dimensional and the data are extracted from resistivity curves. Our calculations show rounding near small T and these experimental curves do not show any sign of saturation near T=0. A similar curve is obtained for $Sm_{1.85}Ce_{0.15}CuO_{4-y}$ single crystal (overdoped) [Andrade et al 1991; Dalichaouch et al. 1990]. Many authors caution that these resistivity measurements actually represent the irreversibility line. Fluctuation analysis of the raw data of SmCeCuO resulted in an $Hc_2(T)$ curve that is consistent with the WHH theory [Han et al 1992]. The upper frame of Figure (6.12) shows $hc_2(t)$ data for the 3D cubic $Ba_{1-x}K_xBiO_3$ with x=0.35 (optimum doping) single crystal [Affronte et al. 1994]. This data is also measured from resistive curves. Three dimensional fluctuation corrections to the data may still be important. The data shows a saturation near

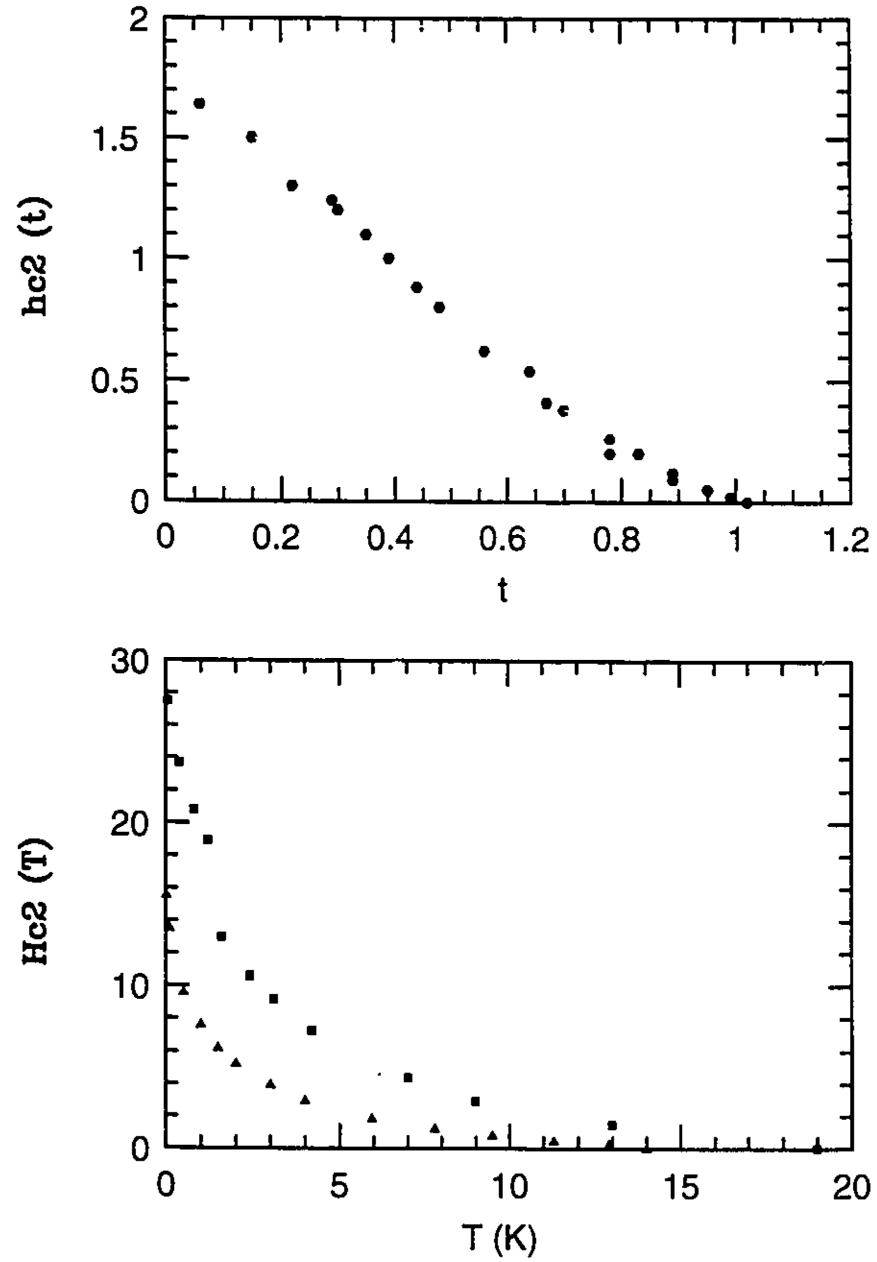

Figure 6.12: Upper frame, $hc_2(t)$ vs t for $Ba_{1-x}K_xBiO_3$, x~0.35, single crystal [Affront et al. 1994]. Lower frame, $Hc_2(T)$ vs T, $Bi_2Sr_2CuO_7$ thin film [Osofsky 1993], $T\ell_2Ba_2CuO_6$ single crystal [Mackenzie 1993].

$t\simeq 0.05$ in contrast to the 221 systems (lower frame). It is not hard to find a suitable fit for the data by invoking a nonconstant EDOS model applicable in 3D.

V) Asymptotic limits in 2D

A) Clean limit

In this section, we would like to find analytic formulas for $Hc_2(T)$ at zero temperature and its derivative (slope) with respect to temperature near the transition temperature for a BCS s–wave superconductor with constant EDOS. We will first find an expression for the slope near T_c by expanding $\chi(i\omega_m)$ in the gap equation (6.1) in terms of small powers of α and then taking the temperature derivative of α. The clean limit implies no impurity concentration, i.e. $t^+=t^-=0$. We approximate the pairing interaction (the double well model) by

$$\lambda(n-m) = \lambda\, \theta(\omega_c-|\omega_n|)\, \theta(\omega_c-|\omega_m|).$$

The gap equation then gets reduced to

$$1 = \pi T\,(\lambda-\mu^*) \sum_m \frac{1}{|\tilde{\omega}_m|}\left[1-\frac{1}{2}\,\frac{\alpha(T)}{\tilde{\omega}_m^2}\right],$$

and the omega channel is replaced by

$$\tilde{\omega}_n = \omega_n\,(1+\lambda).$$

The summations are easy to evaluate and at T_c

$$\alpha'(T_c) = \frac{-\pi^2}{N}(1+\lambda)^2\, T_c$$

where

$$N = \sum_{n\geq 0} \frac{1}{(2n+1)^3} \cong 1.05.$$

In the limit of T→0, we have

$$\pi T \sum_{m} = \frac{1}{2}\int_{-\infty}^{\infty} d\omega\,,$$

so we can write the gap equation as

$$\frac{1+\lambda}{\lambda-\mu^*} = 2\int_0^\infty dq\; q e^{-q^2} \int_0^{\omega_c} \frac{1}{\sqrt{\omega^2+\alpha(q/(1+\lambda))^2}}.$$

We perform the ω–integration and expand it in $\omega_c/\sqrt{\alpha}$ to get

$$\frac{1+\lambda}{\lambda-\mu^*} = 2\int_0^\infty dq\; q e^{-q^2} \left[\ln \frac{2\omega_c(1+\lambda)}{\sqrt{\alpha}} - \ln q\right].$$

We can use $\int_0^\infty \ln x e^{-x}\, dx = -\gamma$ and at T_c, $1+\lambda/(\lambda-\mu^*)=\ln(e^{\gamma}\omega_c/\pi T_c)$ to finally get at T=0

$$\sqrt{\alpha} = \pi\, e^{-\gamma/2}\,(1+\lambda)\, T_c.$$

The normalized upper critical field then is

$$hc_2(0) = N\, e^{-\gamma} = 0.59.$$

In the 3D s–wave case $hc_2(0)=0.73$.

B) Dirty Limit

In two dimensions we can write $\chi(i\omega_m)$ for all T as

$$\chi(i\omega_m) = \frac{1}{|(1+\lambda)\omega_n+\pi t^+|}\left[1-\frac{1}{2}\frac{\alpha(T)}{t^{+2}}\right],$$

while for three dimensions

$$\chi(i\omega_m) = \frac{1}{|(1+\lambda)\omega_n+\pi t^+|}\left[1-\frac{1}{3}\frac{\alpha(T)}{t^{+2}}\right].$$

Since the two equations differ only in a scale for $\alpha(T)$, then the 2D solution of α and its slope at T_c is the same as for the 3D case but multiplied by a scaling factor of 2/3. Then it is obvious that the ration of α'/α is the same for both dimensionalities in the dirty limit. For 3D this ratio is $hc_2(0) \sim 0.69$ and hence it is the same ratio for 2D. For completeness, we mention the solutions of $\alpha(0)$ and $\alpha'(1)$ for the 3D case [Carbotte 1990]

$$\alpha(0) = \frac{6\pi}{1.13}(1+\lambda)\, t^+\, T_c$$

$$\alpha'(T_c) = -24\,(1+\lambda)\, t^+.$$

VI) Summary

We have found that the $hc_2(t)$ is larger in 3D than in 2D. In 2D we have also found that $hc_2(t)$ for the d–wave order parameter is larger than the s–wave. Quite generally, the vHs in EDOS acts to enhance $hc_2(t)$ in a fashion similar to strong coupling effects. For d–wave and a simple vHs in the EDOS, the maximum of $hc_2(0)$ is about 4.0. This is larger than the maximum value of 1.3 attainable from strong coupling effects in constant EDOS. Furthermore $hc_2(t)$ has an upward curvature near T_c that is absent in a constant EDOS model.

Born impurity scattering in d–wave and paramagnetic impurity scattering in s–wave are quite similar; in both cases T_c and $Hc_2(0)$ are reduced. The temperature dependence of $hc_2(t)$ is also changed and $hc_2(0)$ is reduced because the slope of Hc_2 near T_c slowly increases with impurity concentration. Normal impurity scattering in s–wave is quite different from the previous two cases. Both $Hc_2(0)$ and the slope of $Hc_2(T)$ at T_c increase rapidly with normal impurity entration. Despite this, $hc_2(0)$ decreases because of smearing of the vHs in the EDOS.

In the limits of very large normal impurity concentration or very strong coupling, $hc_2(t)$ is not affected by large peaks in the EDOS. We also showed that dimensionality has no effect on the limiting value of $hc_2(0)$ in the limit of large t^+.

Chapter 7

Summary

In Chapter 2, we have presented a derivation of the Eliashberg equations, the free energy formula, the London penetration depth and the eigenvalue equation for the upper critical field, all appropriate to a general electronic band.

In Chapter 3, we gave an analytic expression for the Eliashberg equations specific to an infinite band EDOS with a damped logarithmic singularity. From these equations, we calculated the transition temperature, T_c, and the isotope effect, β, and their dependences on chemical potential and on normal and paramagnetic impurity concentrations. We show that the enhancement of T_c due to a peak in the EDOS can be an order of magnitude larger than the corresponding T_c in the absence of such a peak. We also show that the isotope effect is reduced by, at maximum, only 15% from its BCS value of 0.5. This reduction falls short of the quoted experimental values for most HTSC's. The Bardeen Stephan free energy difference formula appropriately generalized to include the damped vHs was also given in Chapter 3. From this expression, we have calculated numerically the thermodynamic critical field at zero temperature, $H_c(0)$. We find good agreement between the calculated $H_c(0)$ and its variation with normal impurity concentration and the experimental data on Zn doped Y123. The agreement is also good for the specific heat jump calculations and experimental results for the same system, as shown in Chapter 5. In the same chapter, Chapter 5, good agreement between the experimental specific heat jumps for oxygen doped Y123 and the calculated specific heat jumps modeled with a chemical potential change in the damped vHs model is found. Although the above calculations were for an s–wave superconductor, we believe that the agreement between theory and experiment reflects the presence of a peak in the EDOS although it is not indicative of the mechanism itself or of the symmetry of the order parameter. The Zn doped data may be consistent with highly anisotropic s–wave or highly anisotropic d–wave order parameters but not with very isotropic d–wave.

In Chapter 4, we have shown that, for a pure isotropic s–wave superconductor, the London penetration depth at low temperature is not consistent with recent experiments on Y123. The d–wave picture is more appropriate but still has some problems in explaining the observed insensitivity of T_c value to small variations in the impurity concentration. This is reflected indirectly in the discrepancy found between $\lambda_L^{-2}(0)$ vs T_c curves and the corresponding experimental data for thin films. This is also deduced from the $\Delta C(T_c)/T_c$ versus T_c calculations for a d–wave order parameter given in Chapter 5. The theoretical curves for $\Delta C(T_c)/T_c$ vs T_c have a downward curvature because T_c drops faster than $\Delta C(T_c)$ with impurity concentrations for an isotropic d–wave superconductor, a property that does not agree with present data.

In Chapter 5, we showed that the renormalized Sommerfeld constant, $\gamma_n(T)$, exhibits large deviations at the vHs from the standard behaviour found in the case of a constant EDOS. In regular metals, $\gamma_n(T)$ has a local minimum at T=0 and a maximum at $T \sim 0.1\ \theta_D$, where θ_D is the Debye temperature. For a logarithmic singularity, this peak shifts to T=0 and $\gamma_n(T)$ becomes a monotonicly decreasing function of T. Our calculations of γ_n do not establish unambiguously whether this peak is finite or not at T=0. In the absence of the electron–phonon interaction, we showed that $\gamma_n \sim -\ell n\, T$ and at T=0 the peak in γ_n does not saturate. We have also shown that γ_n at low T is reduced by normal impurity scattering because of density of states smearing.

In the superconducting state, the electronic specific heat, c_s at low temperature is exponentially activated for an s–wave order parameter while it is quadratic with T for a d–wave order parameter. Born scattering and resonant scattering are quite dissimilar in their effects at low temperature for a d–wave superconductor. Born scattering leaves the temperature dependence of c_s quadratic in temperature, however at T_c both types of scatterings are almost identical in their effects on T_c and $\Delta C(T_c)$.

In Chapter 6, we have shown that the upper critical field at zero temperature, $hc_2(0)$, is greatly enhanced by the presence of a simple vHs in the EDOS. The temperature dependence of the $hc_2(t)$ curves is slightly different from that obtained previously in the very strong coupling limit of the constant density of states case. Near T_c, $hc_2(t)$ has an upward curvature while with a constant EDOS $hc_2(t)$ is a straight line. The temperature dependence of $hc_2(t)$ is almost identical for both d--wave and s–wave order parameter and $hc_2(0)$ is slightly larger for a d–wave superconductor in 2D. We attribute the upper curvature in $hc_2(t)$ near T_c and the enhancement of $hc_2(0)$ for both s–wave and d–wave to an effective increase in the density of states caused by a decrease in retardation effects.

In conclusion, the modified Eliashberg theory presented here was found to be able to account for some of the observed properties of the HTSC's within a Fermi liquid framework. Some extra refinements to this mean field theory may be necessary. For example, near T_c, fluctuations may contribute important corrections to various properties like $\Delta C(T_c)$ and Hc_2. Our work supports a d–wave picture (spin fluctuations) with perhaps a nonisotropic d–wave order parameter for $YBa_2Cu_3O_7$ and also the existence of a sharp structure in the underlying electronic density of states.

Appendix A

Analytic Integrals

I) Some Integrals of interest, some of which are used in this thesis:

$$\int_{-\infty}^{\infty} d\epsilon \, \frac{1}{\epsilon^2+a^2} = \frac{\pi}{|a|} \tag{A.1}$$

$$\int_{-\infty}^{\infty} d\epsilon \, \frac{\epsilon}{\epsilon^2+a^2} = 0 \tag{A.2}$$

$$\int_{-\infty}^{\infty} d\epsilon \, \frac{\ln|\epsilon-\delta|}{\epsilon^2+a^2} = \frac{\pi}{2|a|} \ln\,(a^2+\delta^2) \tag{A.3}$$

$$\int_{-\infty}^{\infty} d\epsilon \, \frac{\epsilon \ln|\epsilon-\delta|}{\epsilon^2+a^2} = -\pi \tan^{-1} \frac{\delta}{|a|} \tag{A.4}$$

$$\int_{-\infty}^{\infty} d\epsilon \, \ln\left[\frac{\epsilon^2+a^2}{\epsilon^2+c^2}\right] = 2\pi\,\{|a|-|b|\} \tag{A.5}$$

$$\int_{-\infty}^{\infty} d\epsilon \, \frac{\ln(\epsilon^2+a^2)}{\epsilon^2+c^2} = \frac{2\pi}{|c|} \ln(|a|+|c|) \tag{A.6}$$

$$\int_{-\infty}^{\infty} d\epsilon \, \frac{\epsilon^2+a^2-c^2}{(\epsilon^2+a^2+c^2)^2} = \pi \frac{a^2}{(c^2+a^2)^{3/2}} \tag{A.7}$$

$$\int_{-\infty}^{\infty} d\epsilon \, \frac{\ln(\epsilon^2+a^2)}{(\epsilon-\delta)^2+c^2} = \frac{\pi}{|c|} \ln[\delta^2+(|a|+|c|)^2] \tag{A.8}$$

$$\int_{-\infty}^{\infty} d\epsilon \, \frac{\ln|\epsilon-\delta|}{(\epsilon-\delta)^2+c^2}\,\frac{1}{\epsilon^2+a^2} = \frac{\pi}{2|a||c|} \, *$$

$$\left\{\frac{(|a|+|c|)\ln[|c|\sqrt{a^2+\delta^2}]+\delta \tan^{-1}\frac{\delta}{|a|}}{\delta^2+(|a|+|c|)^2}\right.$$

$$\left. + \frac{(|a|+|c|)\ln\left[\frac{\sqrt{a^2+\delta^2}}{|c|}\right]-\delta \tan^{-1}\frac{\delta}{|a|}}{\delta^2+(|a|-|c|)^2}\right\} \qquad \text{(A.9)}$$

$$\int_{-\infty}^{\infty} d\epsilon \, \frac{\ln|\epsilon-\delta|}{(\epsilon-\delta)^2+c^2}\,\frac{\epsilon}{\epsilon^2+a^2} = \frac{\pi}{2|c|} \, *$$

$$\left\{\frac{\delta(\ln|c|+\ln\sqrt{\delta^2+a^2})-(|c|+|a|)\tan^{-1}\frac{\delta}{|a|}}{\delta^2+(|c|+|a|)^2}\right.$$

$$\left. + \frac{\delta(\ln|c|-\ln\sqrt{\delta^2+a^2})+(|a|-|c|)\tan^{-1}\frac{\delta}{|a|}}{\delta^2+(|a|-|c|)^2}\right\} \qquad \text{(A.10}$$

II) Full derivation of (A.9) and summary of steps leading to (A.10).

To evaluate (A.9), we use the residue method to evaluate the following integrand,

$$\oint dz \, \frac{\ln(z-\delta)}{(z-\delta)^2+c^2}\,\frac{1}{z^2+a^2}. \qquad \text{(A.11)}$$

Equation (A.9) is just the real part of (A.11), and the contour is defined by the following figure:

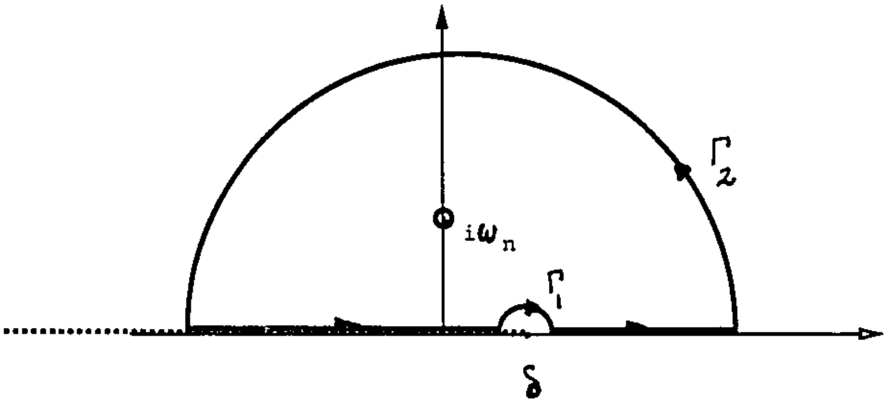

Figure (A.1)

where we assume $\delta \geq 0$ and $\ell n\, z$ has a branch for $\forall$ z such that $x<0$ and $y=0$, $z=x+iy$.

Γ_1 and Γ_2 contribute zero to (A.11) and by the residue theorem, the total contribution, r, of (A.11) is equal to

$$r = 2\pi i \left\{ \frac{1}{2i|c|}\, \ell n(i|c|)\, \frac{1}{(\delta+i|c|)^2+a^2} + \frac{1}{2i|a|}\, \frac{\ell n(i|a|-\delta)}{(i|a|-\delta)^2+c^2} \right\}. \qquad \text{(A.12)}$$

We are only interested in Re r only to get Re (A.11).

We can expand (A.12) in real and imaginary terms by using the following expansions:

$$\ell n\,(i|a|-\delta) = \ell n\,\sqrt{a^2+\delta^2} + i\left[\frac{\pi}{2}+i\,\tan^{-1}\frac{\delta}{a}\right] \tag{A.13}$$

$$\ell n(i|c|) = \ell n|c| + i\,\frac{\pi}{2} \tag{A.14}$$

but before inserting equation (A.13) and (A.14) into (A.12), we can rewrite (A.12) as

$$r = \frac{\pi i}{2|a||c|}\left\{\frac{[\delta-i(|a|+|c|)]\ell n(i|c|)-\ell n(i|a|-\delta)[\delta+i(|a|+|c|)]}{\delta^2+(|a|+|c|)^2}\right.$$

$$\left.+\frac{[\delta-i(|c|-|a|)]\ell n(i|a|-\delta)-[\delta-i(|c|-|a|)]\ell n(i|c|)}{\delta^2+(|c|-|a|)^2}\right\}. \tag{A.15}$$

The final result is

$$\mathrm{Re}\,r = \frac{\pi}{2|a||c|}\left\{\frac{(|a|+|c|)\ell n[|c|\sqrt{\delta^2+a^2}]+\delta\,\tan^{-1}\frac{\delta}{|a|}}{\delta^2+(|a|+|c|)^2}\right.$$

$$\left.+\frac{(|c|-|a|\ell n\left[\frac{\sqrt{\delta^2+a^2}}{|c|}\right]-\delta\,\tan^{-1}\frac{\delta}{|a|}}{\delta^2+(a-|c|)^2}\right\}. \tag{A.16}$$

Evaluating Re (A.11) and changing the dummy variable x to ϵ and equating Re (A.11) to (A.16) we get (A.9) identically. To evaluate (A.10), we use the follwing integrand

$$\oint_c \frac{\ell n(z-\delta)\,z\,dz}{[(z-\delta)^2+c^2][z^2+a^2]} \tag{A.17}$$

with the same contour shown in Fig. (A.1) and by using only the real part of (A.17) and the real part of the residue r_2

$$r_2 = 2\pi i \left\{ \frac{(\delta + i|c|\,\ell n(i|c|)}{2i|c|} \frac{1}{(\delta + i|c|)^2 + a^2} + \frac{1}{2} \frac{\ell n(i|a| - \delta)}{(i|a| - \delta)^2 + c^2} \right\} \tag{A.18}$$

which is rearranged in similar fashion done previously for equation (A.12), but more tedious this time, we can arrive at equation (A.10).

III) Evaluation of $\hat{N}(a,\delta)$

The definition of $\hat{N}$ used in our Eliashberg equations is given by

$$\hat{N}(x) = \frac{x}{\pi} \int_{-\infty}^{\infty} d\epsilon\, N(\epsilon) \frac{1}{\epsilon^2 + x^2}. \tag{A.19}$$

For

$$N(\epsilon) = r - \frac{s}{(\epsilon - \delta)^2 + D^2} \ell n \frac{|\epsilon - \delta|}{E_f}$$

we can scale ϵ, δ and D by E_f and use equation (A.1). For the first part we get

$$\hat{N}(x) = r - \frac{xs}{\pi E_f^3} \int_{-\infty}^{\infty} d\epsilon' \frac{1}{(\epsilon' - \delta')^2 + D'^2} \ell n|\epsilon' - \delta'| \frac{1}{\epsilon'^2 + x'^2} \tag{A.20}$$

with every

$$y' = y/E_f. \tag{A.21}$$

Using equation (A.9) for the second part, we get

$$\begin{aligned}\hat{N} = r - \frac{s\,x}{\pi {E_f}^3}\,\frac{\pi}{2x'D'}\Bigg\{&\frac{(x'+D')\ln\left[D'\sqrt{x'^2+\delta'^2}\right]+\delta'\tan^{-1}\frac{\delta}{x}}{\delta'^2+(x'+D')^2}\\ &\frac{(D'-x')\ln\left[\frac{\sqrt{x^2+\delta^2}}{D}\right]-\delta\tan^{-1}\frac{\delta}{x}}{\delta'^2+(x'-D')^2}\Bigg\}\end{aligned} \tag{A.22}$$

$$\begin{aligned}\hat{N} = r - \frac{s}{2D'}\Bigg\{&\frac{(x'+D')\ln\left[D'\sqrt{x'^2+\delta'^2}\right]+\delta'\tan^{-1}\frac{\delta}{x}}{\delta'^2+(x'+D')^2}\\ &\frac{(D'-x')\ln\left[\frac{\sqrt{x^2+\delta^2}}{D}\right]-\delta'\tan^{-1}\frac{\delta}{x}}{\delta'^2+(x'-D')^2}\Bigg\}\end{aligned} \tag{A.23}$$

which, eventually, we write as

$$\begin{aligned}\hat{N}(x,\delta) = r - \frac{s}{2D}\Bigg\{&\frac{(x+D)\ln\left[\frac{D\sqrt{x^2+\delta^2}}{E_f^2}\right]+\delta\tan^{-1}\frac{\delta}{x}}{\delta^2+(x+D)^2}\\ &\frac{(D-x)\ln\left[\frac{x^2+\delta^2}{D}\right]-\delta\tan^{-1}\frac{\delta}{x}}{\delta^2+(x-D)^2}\Bigg\}.\end{aligned} \tag{A.24}$$

Appendix B

The Eigenvalue Equation for Hc_2

I) The D–Wave Eigenvalue Equation

A) The Energy Integration

To perform the energy integration, we will use a contour integration identical to that used in Appendix A, see Figure A.1. For $\tilde{\omega}_m>0$, we will close in the upper half of the complex ϵ–plane, and for $\tilde{\omega}_m<0$, we close the contour in the lower half plane. Because of the exponential damping in equation (2.73), $e^{i\epsilon t(\mathrm{sgn}\tilde{\omega}_m)}$, the contribution from the large semicircle is identically zero. If we choose $N(\epsilon)$ as $r - s\ \ell n((\epsilon-\delta)/E_f)$, then $N(\epsilon)$ does not contain any poles in the lower and upper half planes of the ϵ–plane. When performing the contour integration, we only pick out one residue form the pole $\tilde{\epsilon}-i\omega_m=0$. The residue is

$$2\pi i s_m\, e^{-2|\tilde{\omega}_m|t}\, N_b\left[r-s\ \ell n\left(\frac{i\tilde{\omega}_m-\delta}{E_f}\right)\right] \times c$$

where c represents everything else in equation (2.73) and is pinned to the Fermi surface. Because we used $\ell n(\epsilon-\delta)$ in $N(\epsilon)$ instead of $\ell n|\epsilon-\delta|$, we shall keep only the real part of $\ell n(i\omega_m-\delta)$. This is very similar to the procedure carried out in Appendix A. The real part of $\ell n(i\omega_m-\delta)$ is $\ell n\sqrt{\tilde{\omega}_m^{\,2}+\delta^2}$. Hence, the contributing part of the residue is

$$2\pi i s_m c\, e^{-2|\tilde{\omega}_m|t}\, N_b\, \hat{N}(\tilde{\omega}_m),$$

and $\hat{N}$ is given by equation (3.18) in this case. So equation (2.73) becomes:

$$b_s\, \Delta(\mathbf{k}_F;i\omega_n) = -2\pi T\, N_b \sum_m \int \frac{d\Omega_q}{\Omega_0}\, I^2\chi(\mathbf{k}_F-\mathbf{q}_F;n-m)$$

$$\times\, \hat{N}(\tilde{\omega}_m) \int_0^\infty dt\, e^{-\alpha_1 t^2|v_{\perp F}|^2/2}\, e^{-2|\tilde{\omega}_m|t}\, \Delta(\mathbf{q}_F;i\omega_m)\, \{\ \}.$$

The curly bracket is given by:

$$\left\{\sum_{N=0}^{\infty} \sum_{j=\max(N-s,0)}^{j=N} \frac{(-is_m a_F^* t\,)^{s-N+j}}{(s-N+j)!} \frac{(-is_m a_F t)^j}{j!\,(N-j)!}\right.$$

$$\left.\times\, (s!N!)^{1/2}\, b_N\right\}$$

where s_m=sign $\tilde{\omega}_m$, $a_F=\sqrt{\alpha_1}(v_{F1}+iv_{F2})$, and α_1=eH.

We will use Fermi surface harmonics to expand the pairing potential $I^2\chi$ and the gap in the following forms:

$$I^2\chi(\mathbf{k}_F-\mathbf{q}_F;n-m) = \frac{1}{N_b}\, \lambda(n-m)(1-g\, \eta_k\eta_q),$$

$$\tilde{\omega}(i\omega_n) = \tilde{\omega}(i\omega_n) + \tilde{\omega}_1(i\omega_n)\eta_k,$$

$$\Delta(k,i\omega_n) = \Delta_0(i\omega_n) + \Delta(i\omega_n)\eta_k.$$

We also choose $<\eta_k>=0$ and $<\eta_k^2>=1$. The self consistent solution is $\Delta_0=\tilde{\omega}_1=0$, and $\tilde{\omega}(i\omega_n)$ is given by the normal state solution of equation (3.11) where $\hat{N}(x_m,\delta)$ is replaced by $\hat{N}(\tilde{\omega}_n)$ given by equation (3.18). The gap equation is then written as

$$b_s\,\Delta(i\omega_n) = 2\pi g T \sum_m \lambda(n-m)\,\Delta(i\omega_m)\,\hat{N}(\tilde{\omega}_m)\; *$$

$$\int \frac{d\Omega_q}{\Omega_0}\,\eta_q^2 \int_0^\infty dt\, e^{-\alpha_1 t^2 v_\perp^2/2}\, e^{-2|\tilde{\omega}_m|t} \times \{\,\}.$$

We dropped the subscript F for short. The following table defines some of the quantities in the previous equation and those in { } for D–dimensions.

Table B.1

D	Ω_0	$d\Omega_q$	$v_\perp$	a_{q_F}	η_q
2	2π	$d\phi$	v_F	$\sqrt{\alpha_1}v_\perp e^{i\phi}$	$\sqrt{2}\cos 2\phi$
3	4π	$\sin\theta d\theta d\phi$	$v_F\sin\theta$	$\sqrt{\alpha_1}v_\perp e^{i\phi}$	$\frac{\sqrt{15}}{2}\sin^2\theta\cos 2\phi$

B) The ϕ Integration

The curly brackets, {}, contain a factor of $e^{-i\phi(s-N)}$ and η_q^2 contains $\cos^2 2\phi$ in both cases D=2 or 3. We can perform the ϕ integration by using

$$\frac{1}{2\pi}\int d\phi\, e^{im\phi} = \delta_{m,0}$$

and can then perform the N summation to get the following

$$\int_0^{2\pi} \frac{d\phi}{2\pi} \cos^2 2\phi \Big\{\ \Big\} = \frac{1}{4}\Big\{2 \sum_{j=0}^{s} \frac{(-1)^j s! x^j}{(j!)^2 (s-j)!}\, b_s$$

$$+ \sum_{j=4}^{s+4} \frac{((s+4)!s!)^{1/2} (-x)^{j-2}}{(j-4)!j!(s+4-j)!}\, b_{s+4}$$

$$+ \sum_{j=0}^{s-4} \frac{((s-4)!s!)^{1/2} (-x)^{j+2}}{(j+4)!j!(s-4-j)!}\, b_{s-4}\Big\}$$

with $x = \alpha_1 t^2 v_\perp^2$.

The sums can be converted into associated Lagurre polynomials [Arfken 1985, eq. 13.41 p. 725] to get eventually

$$b_s\, \Delta(i\omega_n) = \frac{\pi g T}{2} \sum_m \lambda(n-m) \Delta(i\omega_m)\, \hat{N}(\tilde{\omega}_m) \int \frac{d\Omega(\theta,\phi)}{\Omega_0} f(\theta)$$

$$\int_0^{\infty} dt\, e^{-x/2}\, e^{-2|\tilde{\omega}_m| t} \Big\{2\, L_s^0(x)\, b_s$$

$$+ \frac{x^2}{[(s+4)(s+3)(s+2)(s+1)]^{1/2}} L_s^4(x)\, b_{s+4}$$

$$+ \frac{x^2}{[s(s-1)(s-2)(s-3)]^{1/2}} L_{s-4}^4(x)\, b_{s-4}\Big\}$$

with

$$f(\theta) = \begin{cases} 2 & \text{in } D=2 \\ \frac{15}{4} \sin^4\theta & \text{in } D=3 \end{cases}$$

This is the same equation as found in [Prohammer and Carbotte 1993] for the d–wave case except for the extra factor of $\hat{N}(\tilde{\omega}_m)$.

C) The Largest d–Wave Eigenvalue Equation

In our treatment of the d–wave, we will consider the coupling between only two basis functions belonging to the coefficient b_0 and b_4. For such a case, the gap equation can be written as

$$\Delta(i\omega_n) \begin{bmatrix} b_0 \\ b_4 \end{bmatrix} = \begin{bmatrix} c_1(n) & c_2(n) \\ c_2(n) & c_3(n) \end{bmatrix} \begin{bmatrix} b_0 \\ b_4 \end{bmatrix}$$

and the largest eigenvalue is

$$\Delta(i\omega_n) = \frac{c_1(n)+c_3(n)}{2} + \frac{1}{2} [(c_1(n)-c_3(n))^2+4c_2^2(n)]^{1/2}. \qquad \text{(B.1)}$$

The general expression for $c_i(n)$, i=1,2,3, is

$$c_i(n) = \pi g T \sum_m \lambda(n-m)\Delta(i\omega_m)\hat{N}(\tilde{\omega}_m)X_i(i\omega_m) \tag{B.2}$$

where

$$X_1(i\omega_n) = \int \frac{d\Omega(\theta,\phi)}{\Omega_0} f(\theta) \int_0^\infty dt\, e^{-\alpha_1/2\, t^2 v_\perp^2} e^{-2|\tilde{\omega}_n|t},$$

$$X_2(i\omega_n) = \frac{1}{2\sqrt{4!}} \int \frac{d\Omega(\theta,\phi)}{\Omega_0} f(\theta) \int_0^\infty dt\, [\alpha_1 t^2 v_\perp^2]^2\, e^{-\alpha_1/2\, t^2 v_\perp^2} e^{-2|\tilde{\omega}_n|t},$$

$$X_3(i\omega_n) = \int \frac{d\Omega(\theta,\phi)}{\Omega_0} f(\theta) \int_0^\infty dt\, L_4^0\, [\alpha_1 t^2 v_\perp^2]\, e^{-\alpha_1/2\, t^2 v_\perp^2} e^{-2|\tilde{\omega}_n|t}.$$

If we define an ordering operator of the following form

$$\hat{O}^n(z\frac{d}{dy}) \equiv z^n \frac{d^n}{dy^n}, \tag{B.3}$$

then

$$X_2(i\omega_n) = \frac{1}{2\sqrt{4!}} \hat{O}^2 \left[-2\alpha_1 \frac{d}{d\alpha_1}\right] X_1(i\omega_n) \tag{B.4}$$

and

$$X_3(i\omega_n) = L_4^0\, (\hat{O}(\left[-2\alpha_1 \frac{d}{d\alpha_1}\right]))\, X_1(i\omega_n). \tag{B.5}$$

So we only have to handle X_1 in any form we wish and then simply use (B.4) and (B.5) to find analytic expression for X_2 and X_3 respectively.

D) The X_1 Equation in 2D

In 2D, $X_1(i\omega_n)$ is given by

$$X_1(i\omega_n) = 2 \int_0^\infty dt\, e^{-\alpha_1/2\, t^2 v_F{}^2}\, e^{-2|\tilde{\omega}_n|t} . \qquad \text{(B.6)}$$

From this point on,we will let $\alpha = \alpha_1/2\, v_F^2$.

We can use an identity of the form

$$\int d^W t\, f_1(t) f_2(t) = (2\pi)^W \int d^W q\, F_1(q)\, F_2(-q) \qquad \text{(B.7)}$$

where F is the Fourier transform of f, to rewrite X_1 in a new form. If we take $f_1(t) = e^{-\alpha(t_1^2+t_2^2)}$ then $F_1(q) = (4\pi\alpha)^{-1}\, e^{-q^2/4\alpha}$ and $f_2(t) = e^{-2|\tilde{\omega}_n|t}/\pi t$ and so $F_2(q) = [2\pi^2\sqrt{4\tilde{\omega}_n^2+q^2}]^{-1}$ and we get for X_1 the expression

$$X_1(i\omega_n) = \int_0^\infty dq \left[\frac{e^{-q^2/4\alpha}}{\alpha}\right] H(q/2|\tilde{\omega}_n|) \qquad \text{(B.8)}$$

where

$$H(x) = \frac{x}{\sqrt{1+x^2}} . \qquad \text{(B.9)}$$

E) The X_1 Equation in 3D

We take the same f_1 expression as in D to get $F_1(q) = (4\pi\alpha)^{-1}\delta(q_3)\exp[-(q_1^2+q_2^2)/4\alpha]$ and for $F_2(q)$ we have

$$F_2(q) = \frac{1}{(2\pi)^3}\frac{15}{16\pi}\int \frac{d^3t}{t^2}\,(1-\hat{t}_3^2)^2\, e^{-2|\tilde{\omega}_n|t}\, e^{-i\mathbf{q}\bullet\mathbf{t}} \qquad \text{(B.10)}$$

where $\hat{t}_3=\cos\theta$ and the integrand is not spherically symmetric and hence, can not use $\mathbf{q}\bullet\mathbf{t}=qt\ \hat{t}_3$. We can rotate the coordinate system to new one which has $\mathbf{t}_3'$ parallel to $\mathbf{q}$, i.e., $\mathbf{q}\bullet\mathbf{t}'=qt'\cos\theta'$. The coordinate transformation from t to t′ is shown in Figure (B.1).

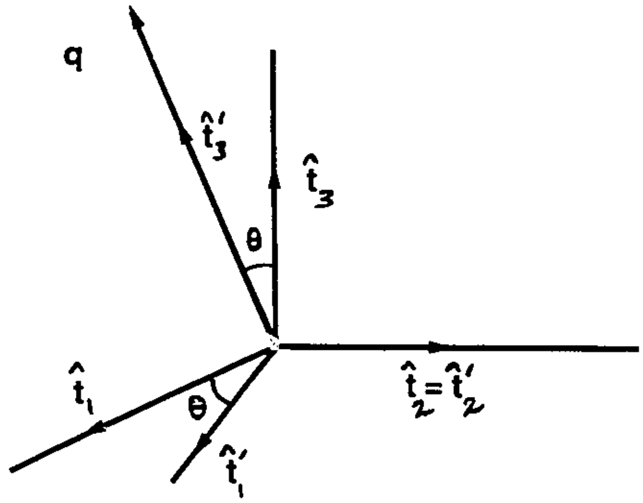

Figure (B.1)

We can set $\hat{t}_2=\hat{t}_2'$ because of cylindrical symmetry and then $\hat{t}_3$ is given by

$$\hat{t}_3 = \hat{t}_3' \cos\theta - \hat{t}_1' \sin\theta. \tag{B.11}$$

Clearly, $F_1(q)$ contains $\delta(q_3)$ which implied $\theta=\pi/2$, so we can set $\hat{t}_3=-\hat{t}_1'$ and the new expression for $F_2(q)$ is

$$F_2(q) = \frac{1}{(2\pi)^3}\frac{15}{16\pi}\int \frac{d^3t'}{t'^2}(1-\sin^2\theta'\cos^2\phi')^2 e^{-2|\tilde{\omega}_n|t'}$$

$$\times\ e^{-iqt'\cos\theta'}$$

which results in

$$F_2(q) = \frac{15}{16(2\pi)^3}\frac{1}{q}\left\{\left[\frac{3}{2} - 4\frac{\tilde{\omega}_n^2}{q^2} + 24\frac{\tilde{\omega}_n^4}{q^4}\right]\tan^{-1}(q/2|\tilde{\omega}_n|) + 3\frac{|\tilde{\omega}_n|}{q} - 12\frac{|\tilde{\omega}_n|^3}{q^3}\right\}.$$

The final expression for X_1 in 3D is

$$X_1(i\omega_n) = \int_0^\infty dq\left[\frac{e^{-q^2/4\alpha}}{\alpha}\right]G(q/2|\tilde{\omega}_n|) \tag{B.12}$$

with

$$G(x) = \frac{15}{64}\left\{3(x^{-1}-x^{-3})+[3-2x^{-2}+3x^{-4}]\tan^{-1}(x)\right\} \tag{B.13}$$

F) The X_2 and X_3 Equations

If we define T_0 as

$$T_0(z,y) = \frac{1}{y}e^{-z/y}$$

then we can show by repeated differentiation that

$$T_n = \hat{O}^n\left(-y\frac{d}{dy}\right)T_0 = (-y)^n\frac{d^n}{dy^n}T_0 = n!\,L_n^0\left(\frac{z}{y}\right)T_0(z,y)$$

for n = 0,1,2,3,4.

Similar formula for $L_n^0(x)$ exist [Arfken eq. 13.31], which reads

$$n!L_n^0(x) = e^x \frac{d^n}{dx^n} (x^n e^{-x}).$$

We also can show that

$$\alpha_1^n \frac{d^n}{d\alpha_1^n} = \alpha^n \frac{d^n}{d\alpha^n}$$

and hence, equation (B.4) simply becomes

$$X_2(i\omega_n) = \frac{1}{\sqrt{6}} \int_0^\infty dq \frac{e^{-q^2/4\alpha}}{\alpha} [2!\ L_2^0(q^2/4\alpha)]\ H(q/2|\tilde{\omega}_n|) \qquad (B.14)$$

We can also show (a bit tedious) that:

$$L_4^0 (-2y\frac{d}{dy})\ T_0(z,y) = L_4^0(\frac{2z}{y})\ T_0(z,y)$$

so

$$X_3(i\omega_n) = \int_0^\infty dq \frac{e^{-q^2/4\alpha}}{\alpha} [L_4^0(q^2/2\alpha)] H(q/2|\tilde{\omega}_n|) \qquad (B.15)$$

In 3–D, one just replaces H by G.

II) The S–Wave Eigenvalue Equation

The largest eigenvalue for the s–wave case is for

$$\Delta(i\omega_n) = \pi T \sum_m \lambda(n-m)\Delta(i\omega_m)\hat{N}(\tilde{\omega}_m)X(i\omega_m)$$

$$+ \pi\,(t^+-t^-)\Delta(i\omega_n)\hat{N}(\tilde{\omega}_n)X(i\omega_n) \qquad (B.16)$$

where we have introduced elastic impurity scattering in the standard way and

$$X(i\omega_n) = 2\int \frac{d\Omega\,(\theta,\phi)}{\Omega_0}\int_0^\infty dt\; e^{-\alpha t_\perp^2}\, e^{-2|\tilde{\omega}_n|t}\,, \qquad (B.17)$$

which follows directly from the fact that $\eta_q^2 = 1$ and the previous curly bracket is also equal to one.

If we define $\tilde{\Delta}$ as

$$\tilde{\Delta}(i\omega_n) = \Delta(i\omega_n)\,(1-\pi(t^+-t^-)\hat{N}(\tilde{\omega}_n)X(i\omega_n)),$$

then we can rewrite (B.16) as

$$\tilde{\Delta}(i\omega_n) = \pi T \sum_m \lambda(n-m)\tilde{\Delta}(i\omega_m)(\hat{N}^{-1}(\tilde{\omega}_m)X^{-1}(i\omega_m) - \pi\,(t^+-t^-))^{-1}. \; (B.18)$$

In 2D, X can be written as

$$X(i\omega_n) = \int_0^\infty dq\,\frac{e^{-q^2/4\alpha}}{\alpha}\,H(q/2|\omega_n|) \qquad (B.19)$$

and in 3D,

$$X(i\omega_n) = \int_0^\infty dq \, \frac{e^{-q^2/4\alpha}}{\alpha} \, F(q/2|\omega_n|) \tag{B.20}$$

with

$$F(x) = \tan^{-1} x. \tag{B.21}$$

Bibliography

Abrikosov, A.A., Sov. Phys. JETP 5, 1174 (1957).

Abrikosov, A.A., J.C. Campuzarro and K. Gofron, Physica **C214**, 73 (1993).

Abrikosov, A.A., L.P. Gor'kov and I.E. Dzyaloshinski, **Methods of Quantum Field Theory in Statistical Physics**, (Dover, New York, 1963).

Affronte, M. et al., Phys. Rev. **B49**, 3502 (1994).

Akis, R., Ph.D. thesis, McMaster University (unpublished 1991).

Akis, R. and J.P. Carbotte, Physics **C159**, 395 (1989).

Akis, R., F. Marsiglio and J.P. Carbotte, Phys. Rev. **B39**, 2722 (1989).

Aleksashin, B.A. et al., Physica **C 153–155**, 339 (1988).

Allen, P.B. and R.C. Dynes, Phys. Rev. **B12**, 905 (1975).

Allen, P.B. and B. Mitrovic, Solid State Physics **37**, 1 (1982).

Anderson, P.W., Science **235**, 1196 (1987).

Anderson, P.W., J. Phys. Chem. Solids **11**, 36 (1959).

Andrade, M.C. et al., Physica **C 184**, 378 (1991).

Anlage, S.M. and D.H. Wu, J. Supercon. 5, 295 (1992).

Annett, J. and N. Goldenfeld, J. Low Temp. Phys. **81**, 197 (1992)

Annett, J., N. Goldenfeld and S.R. Renn, Phys. Rev. **B43**, 2778 (1991).

Annett, J., N. Goldenfeld and S.R. Renn, in (PPHTS II 1990) p. 571.

Arberg, P., M. Mansor and J.P. Carbotte, Solid State Commun. **86**, 671 (1993); J. Phys. Chem. Solids **54**, 1461 (1993).

Ashcroft, N.W. and N.D. Mermin, **Solid State Physics**, (Holt, Rinehart and Winston, Philadelphia, 1976).

Bardeen, J., L.N. Cooper and J.R. Schrieffer, Phys. Rev. **108**, 1175 (1957).

Basov, D.N., T. Timusk, W.N. Hardy et al. (preprint 1994).

Bednorz, J.G. and K.A. Müller, Z. Phys. B64, 189 (1986).

Bonn, D.A. et al., Phys. Rev. Lett. 68, 2390 (1992).

Bornemann, H.J. et al., Physica C 185–189, 1359 (1991).

Bulaevskii, L.N. and O.V. Dolgov, Physica C 153–155, 241 (1988); Solid State Commun. 67, 63 (1988).

Carbotte, J.P., a) Rev. Mod. Phys. 62, 1027 (1990); b) in (PHTS 1990) p. 1435.

Carbotte, J.P. and R. Akis, Solid State Commun. 82, 613 (1992).

Carbotte, J.P. and E. Nicol, Physica C 185–189, 162 (1991).

Combescot, R and J. Labbe, Phys. Rev. B38, 262 (1988).

Coombes, J.M. and J.P. Carbotte, J. Low Temp. Phys. 63, 431 (1986).

Cooper, L.N., Phys. Rev. 104, 1189 (1956).

Crow, J.E. and N. Ong in (HTS 1990) p. 203.

Dalichaouch, Y. et al., Phys. Rev. Lett. 64, 599 (1990).

Daumling, M., Physica C 183, 293 (1991).

Dessau, D.S. et al., Phys. Rev. Lett. 71, 2781 (1993).

Dzyaloshinskii, I.E., Sov. Phys. JETP 66, 848 (1988).

Einzel, D. et al., Phys. Rev. Lett. 56, 2513 (1986).

Eliashberg, G.M., a) Sov. Phys. JETP 11, 696 (1960); b) Sov. Phys. JETP 12, 1000 (1960).

Emery V.J., Phys. Rev. Lett. 58, 2794 (1987).

Ernst, P. et al., Ann. Physik 2, 120 (1993).

Fisher, R.A., J.E. Gordon and N.E. Phillips, J. Supercon. 1, 231 (1988).

Franck, J.P., in (PPHTS IV 1994) to be published.

Freeman, A.J., Phys. Rev. Lett. 58, 1035 (1987).

Friedel, J., a) J. Phys. (Paris) 48, 1787 (1987); b) J. Phys. (Paris) 49, 1435 (1987).

Fröhlich, H., Phys. Rev. **79**, 845 (1950).

Ghiron, K., M.B. Salamon, M.A. Hubbard and B.W. Veal, Phys. Rev. **B48**, 16188 (1993).

Ghiron, K. et al., Phys. Rev. **B46**, 5837 (1992).

Ginsburg, V.L. and L.D. Landau, *Zh. Eksp. Teor. Fiz.* **20**, 1064 (1950).

Gopalan, S., O. Gunnarson and O.K. Anderson, Phys. Rev. **B46**, 11798 (1992).

Gor'kov, L.P., Sov. Phys. JETP **7**, 505 (1958).

Gorter, C.J. and H.B.G. Casimir, a) Phys. Z. **35**, 963 (1934); b) Z. Techn. Phys. **15**, 539 (1934).

Grimvall, G., **The Electron–Phonon Interaction in Metals**, (North–Holland, New York, 1981).

Gross, F. et al., Z. Phys. B. Cond. Matt. **64**, 175 (1986).

Han, S.H. et al., Phys. Rev. **B46**, 14290 (1992).

Hardy, W.N. et al., Phys. Rev. Lett. **70**, 3999 (1993).

Hardy, W.N. et al. (preprint submitted to Phys. Rev. Lett. 1994).

Hasegawa, Y. and H. Fukuyama, J. Phys. Soc. Jpn. **56**, 2619 (1987).

Helfand, E. and N.R. Werthamer, Phys. Rev. Lett. **13**, 686 (1964).

Helfand, E., N.R. Werthamer and P.C. Hohenberg, Phys. Rev. **147**, 295 (1966).

Heym, J., J. Low Temp. Phys. **89**, 869 (1992).

High Temperature Superconductivity (HTS 1990), edited by J.W. Lynn (Springer–Verlag, New York, 1990).

Hirschfeld, P. and N. Goldenfeld, Phys. Rev. **B48**, 4219 (1993).

Hirschfeld, P., W.O. Puttikka and D.J. Scalapino, Phys. Rev. Lett. **71**, 3705 (1993).

Hirschfeld, P., D. Vollhardt and P. Woelfle, Solid State Commun. **59**, 111 (1986).

Hirschfeld, P., P. Woelfle and D. Einzel, Phys. Rev. **B37**, 183 (1988).

Hotta, T., J. Phys. Soc. Jpn. **62**, 274 (1993).

Huang, X. and K. Maki, Phys. Rev. **B39**, 6459 (1989).

Inderhees, S.E. et al., Phys. Rev. Lett. 60, 1178 & 2445 (1988).

Inderhees, S.E. et al., Phys. Rev. Lett. 66, 232 (1991).

Ishida, K. et al., a) Physica C 185–189, 115 (1991); b) J. Phys. Soc. Jpn. 62, 2803 (1993).

Jiang, C. and J.P. Carbotte, Phys. Rev. B45, 10670 (1992).

Jiang, C. and J.P. Carbotte, Physica C 210, 325 (1993).

Jiang C., J.P. Carbotte and R.C. Dynes, Phys. Rev. B47, 5235 (1993).

Junod, A. in (PPHTS II 1990) p. 13.

Junod, A. et al., Physica C 152, 495 (1988).

Junod, A. et al., Physica C 162–164, 482 (1989).

Kamimura, H. et al., Comments Cond. Mat. Phys. 15, 303 (1992).

Keller, H. et al., Physica C 185–189, 1089 (1991).

Keller, J., K. Scharnberg and H. Monien, Physica C 152, 302 (1988).

Kim, H., G. Preosti and P. Muzikar, Phys. Rev. B49, 3544 (1994).

Kubo, K. and H. Yamanchi, Phys. Rev. B49, 1289 (1994).

Labbe, J., Phys. Scr. T29, 82 (1989).

Labbe, J. and J. Bok, Europhys. Lett. 3, 1225 (1987).

Leavens, C.R. and J.P. Carbotte, J. Low Temp. Phys. 14, 195 (1974).

Leavens, C.R. and J.P. Carbotte, Ferroelectrics 16, 295 (1977).

Lee, J.Y. and T.R. Lemberger, Appl. Phys. Lett. 62, 2419 (1993).

Lenck, St. and J.P. Carbotte, Phys. Rev. B46, 14859 (1992).

Levin, K. et al., Phys. Rev. B48, 653 (1993).

Liang. R. et al., Physica. C 195, 51 (1992).

Lie, S.G. and J.P. Carbotte, Solid State Commun. 26, 511 (1978).

Lie, S.G. and J.P. Carbotte, a) Solid State Commun. 34, 599 (1980); b) Solid State Commun. 35, 127 (1980).

Lie, S.G., J.M. Daams and J.P. Carbotte, J. Phys. (Paris) Colloq. **39**, C6 – 469 (1978).

London, F., Phys. Rev. **74**, 562 (1948).

Loram, J. and K.A. Mirza, Physica C **153–155**, 1020 (1988).

Loram, J.W., K.A. Mirza and P.A. Freeman, Physica C **171**, 243 (1990).

Loram, J.W. et al., Philosophical Magazine B **65**, 1405 (1992).

Loram, J.W. et al., Phys. Rev. Lett. **71**, 1740 (1993).

Lui, R. et al., Phys. Rev. **B46**, 11056 (1992).

Luttinger, J.M. and J.C. Ward, Phys. Rev. **118**, 1417 (1960).

Mackenzie, A.P., Phys. Rev. Lett. **71**, 1238 (1993).

Maeda, A. et al., Phys. Rev. **B41**, 4112 (1990).

Mahan, G.D., **Many–Particle Physics, 2nd edition**, (Plenum, New York, 1990).

Maki, K. in (S1969) p. 1035.

Mandle, F. and G. Shaw, **Quantum Field Theory**, (John Wiley and Sons, Chichester, 1984).

Mansor, M. and J.P. Carbotte, Phys. Rev. **B47**, 9029 (1993).

Markiewic, R.S., J. Phys. Cond. Mat. **2**, 665 (1990).

Markiewic, R.S. and B.C. Giessen, Physica C **160**, 497 (1989).

Marsiglio, F., Ph.D. thesis, McMaster University (unpublished 1988).

Marsiglio, F. and J.P. Carbotte, Phys. Rev. **B33**, 6141 (1986).

Marsiglio, F. and J.P. Carbotte, Phys. Rev. **B36**, 3633 (1987).

Marsiglio, F. and J.P. Carbotte, Phys. Rev. **B41**, 8765 (1990).

Marsiglio, F. and J.E Hirsch, Phys. Rev. **B41**, 6435 (1990).

Marsiglio, F., M. Schossmann, E. Schachinger and J.P. Carbotte, Phys. Rev. **B35**, 3226 (1987).

Martindale, J.A. et al., Phys. Rev. **B47**, 9155 (1993).

Mason, T. et al., Phys. Rev. Lett. **71**, 919 (1993).

Matheiss L.F. and D.R. Hamann, Phys. Rev. **B40**, 2217 (1989).

Mattheis, L., Phys. Rev. Lett. **58**, 1028 (1987).

Maxwell, E., Phys. Rev. **78**, 477 (1950).

McMillan, W.L., Phys. Rev. **167**, 331 (1968).

Meissner, W. and R. Ochsenfeld, Naturwiss. **21**, 787 (1933).

Migdal, A.B., Sov. Phys. JETP **7**, 996 (1958).

Millis, A.J., Phys. Rev. **B45**, 13047 (1992).

Millis, A.J., H. Monien and D. Pines, Phys. Rev. **B42**, 167 (1990).

Mirza, K.A. and J.W. Loram in **Electronic Properties of High–T_c Superconductors and Related Compounds**, edited by: H. Kuzmany, M. Mehring and J. Fink (Springer–Verlag Berlin, Heidelberg, 1990), p.93.

Mitrivic, B. (private notes).

Mirtrovic, B. and J.P. Carbotte, a) Can. J. Phys. **61**, 758 (1983); b) Can. J. Phys. **61**, 784 (1983), c) Can. J. Phys. **61**, 872 (1983).

Mitrovic B., H.G. Zarate and J.P. Carbotte, Phys. Rev. **B29**, 184 (1984).

Moler, K.A. et al. (submitted to Phys. Rev. Lett. 1994).

Momono, N. et al. to be published in proceedings of M2S–HTSC IV Grenoble, Physica C (1994).

Monien, H. and D. Pines, Phys. Rev. **B41**, 6297 (1990).

Monthoux, P. and D. Pines, Phys. Rev. Lett. **69**, 961 (1992).

Monthoux, P. and D. Pines, submitted to Phys. Rev. and to Nuovo Cimento D (dedicated to Prof. Fausto Fumi).

Monthoux, P., D. Pines and A.V. Balatsky, Phys. Rev. Lett. **67**, 3448 (1991).

Monthoux, P. and D.J. Scalapino, Phys. Rev. Lett. **72**, 1874 (1994).

Morel, P. and P.W. Anderson, Phys. Rev. **125**, 1263 (1962).

Nagi, A.d.S. and Yutaka Okabe, Phys. Rev. **B28**, 1320 (1983).

Nakamura, Y.O., N. Matsuda and Y. Shiina, Solid State Commun. **81**, 923 (1992).

Nam, S.B., Phys. Rev. **156**, 470 (1967).

Nambu, Y., Phys. Rev. **117**, 648 (1960).

Newns, D.M. et al., a) Comments Cond. Mat. Phys. 15, 273 (1992); Phys. Rev. **B45**, 5714 (1992).

Norman, M.R., Phys. Rev. **B37**, 4987 (1988).

Novel Superconductivity, (NS 1987), edited by: S.A. Wolf and V.Z. Kresin (Plenum, New York, 1987).

Nuss, M.C. et al., Phys. Rev. Lett. 66, 3305 (1991).

O'Brien, Mary C.M., Am. J. Phys. 61, 688 (1993).

Onnes, H.K., Leiden Comm., 1206 (1911).

Osofsky, M.S. et al., Phys. Rev. Lett. **71**, 2315 (1993).

Pao, C.–H. and N.E. Bickers, Phys. Rev. Lett. **72**, 1870 (1994).

Perez–Gonzalez and J.P. Carbotte, Phys. Rev. **B45**, 9894 (1992).

Pethick, c.J. and D. Pines, Phys. Rev. Lett. **57**, 118 (1986).

Phillips, N.E. et al., Physica **B148**, 360 (1987).

Phillips, N.E. et al., Phys. Rev. Lett. **65**, 357 (1990).

Phillips, N.E. et al., to be published in proceedings of M2S–HTSC IV Grenoble, Physica C (1994).

Physical Properties of High Temperature Superconductors I, (PPHTS I 1989), edited by D.M. Ginsberg (World Scientific, Singapore, 1989).

Physical Properties of High Temperature Superconductors II, (PPHTS II 1990), edited by D.M. Ginsberg (World Scientific, Singapore, 1990).

Physical Properties of High Temperature Superconductors III, (PPHTS III 1992), edited by D.M. Ginsberg (World Scientific, Singapore, 1992).

Physical Properties of High Temperature Superconductors IV, (PPHTS IV 1994), to be published.

Pickett, W.E., Phys. Rev. **B21**, 2897 (1980).

Pickett, W.E., Rev. Mod. Phys. **61**, 433 (1989).

Pines, D. J. Phys. Chem Solids **54**, 1447 (1993).

Pines, D., Physica C **185–189**, 120 (1991).

Pint, W., Physica C **168**, 143 (1990).

Pint, W., E. Langmann and E. Schachinger, Physica C **157**, 415 (1989).

Pond, J.M. et al., Appl. Phys. Lett. **59**, 3033 (1991).

Porch, A. et al., Physica C **214**, 350 (1993).

Progress in High Temperature Superconductivity (PHTS 1990), edited by R. Nicolsky (World Scientific, Singapore, 1990).

Prohammer, M. and J.P. Carbotte, a) Phys. Rev. **B42**, 2032 (1990); b) Physica B **165–166**, 883 (1990).

Prohammer, M. and J.P. Carbotte, Phys. Rev. **B43**, 5370 (1991).

Prohammer, M., A. Perez–Gonzalez and J.P. Carbotte, Phys. Rev. **B47**, 15152 (1993).

Radtke, R.J., K. Kevin, H.–B. Schüttler and M.R. Norman, Phys. REv. **B48**, 15957 (1993).

Rainer, D. and G. Bergmann, J. Low Temp. Phys. **14**, 501 (1974).

Rainer, D. and F.J. Culetto, Phys. Rev. **B19**, 2540 (1979).

Remschnig, K. et al., Phys. Rev. **B43**, 5481 (1991).

Reynolds, C.A., B. Serin, W.H. Wright and L.B. Nesbitt, Phys. Rev. **78**, 487 (1950).

Rickayzen, G., **Theory of Superconductivity**, (Wiley, New York, 1965).

Rieck, C.T., Ph.D. thesis, Hamburg (unpublished 1991).

Rieck, C.T., D. Fay and L. Tewordt, Phys. Rev. **B41**, 7289 (1990).

Rieck, C.T., Th. Wölkhausen, D. Fay and L. Tewordt, Phys. Rev. **B39**, 278 (1989).

Romero, D.B. et al., Phys. Rev. Lett. **68**, 1590 (1992).

Salamon, M.B. in (PPHTS I 1989) p. 39.

Salamon, M.B. et al., Phys. Rev. Lett. **69**, 1431 (1992).

Scalapino, D.J. and N. Bulut, Phys. Rev. Lett **67**, 2898 (1991).

Scalapino, D.J., E. Loh and J.E. Hirsch, Phys. Rev. **B34**, 8190 (1986).

Schachinger, E. and J.P. Carbotte, J. Low Temp. Phys. **42**, 81 (1981).

Schachinger, E. and J.P. Carbotte, Phys. Rev. **B43**, 10279 (1991).

Schachinger, E., J.M. Daams and J.P. Carbotte, Phys. Rev. **22**, 3194 (1980).

Schachinger, E., M.G. Greeson and J.P. Carbotte, Phys. Rev. **B42**, 406 (1990).

Schachinger, E., B. Mitrovic, and J.P. Carbotte, J. Phys. F12, 1771 (1982).

Scharnberg, K. and R.A. Klemm, Phys. Rev. **B22**, 5233 (1980).

Schilling A., H.R. Ott and F. Hulliger, Physica **C 161**, 626 (1989).

Schneider, T. and H. Keller, Phys. Rev. Lett. **69**, 3374 (1992).

Schneider, T. and M.P. Sörensen, Z. Phys. **B81**, 3 (1990).

Schossman, M. and J.P. Carbotte, Phys. Rev. **B39**, 4210 (1989).

Schossmann, M. and E. Schachinger, Phys. Rev. **B33**, 6123 (1986).

Schrieffer, J.R., **Theory of Superconductivity**, (Addison Wesley, Redwood City, 1964).

Schultz, H.J., Europhys. Lett. **4**, 609 (1981).

Shen, Z.X. et al., Phys. Rev. Lett. **70**, 1553 (1993).

Shiba, H., Prog. Theor. Phys. **40**, 435 (1968).

Shiba, H., Prog. Theor. Phys. **50**, 50 (1973).

Sigrist, M. and T.M. Rice. Z. Phys. **B68**, 9 (1987).

Sigrist, M. and T.M. Rice. J. Phys. Soc. Jpn. **61**, 4283 (1992).

Superconductivity (S 1969), edited by R.D. Parks (Marcel Dekker Inc., New York, 1969).

Tsuei, C.C. et al., Phys. Rev. Lett. **65**, 2724 (1990).

Tsuei, C.C. et al., Phys. Rev. Lett. **69**, 2134 (1992).

Ulm, E.R., J.T. Kim and T.R. Limberger (preprint).

van Veenendaal, M.A. and G.A. Sawatzky, Phys. Rev. **B49**, 1407 (1994).

Varma, C.M., A.J. Millis and S. Sachdev, Phys. Rev. **B37**, 4975 (1988).

Varma, C.M., K. Miyake and S. Schmitt–Rink, Phys. Rev. **B34**, 6554 (1986).

Volovik, G.E. and L.P. Gor'kov, Sov. Phys. JETP **61**, 843 (1985).

Voronin, V.I. et al. in (NS 1987) p. 875.

Weber, W., Phys. Rev. Lett. **58**, 1371; 2154(E) (1987).

Wegner, F. and S. Östlund, Phys. Rev. **B47**, 5977 (1993).

Wells, B.O. et al., Phys. Rev. **B46**, 11830 (1992).

Welp, U. et al., Phys. Rev. Lett. **62**, 1908 (1989).

Wermbter, S. and L. Tewordt, Phys. Rev. **B46**, 12061 (1992).

Williams, P.J., Ph.D. thesis, McMaster University (unpublished 1990).

Williams, P.J. and J.P. Carbotte, Phys. Rev. **B39**, 2180 (1989).

Wollman, D.A. et al., Phys. Rev. Lett **71**, 2134 (1993).

Worthington, T.K. et al., Phys. Rev. Lett. **59**, 1160 (1987).

Wühl, H. et al., Physica **C 185–189**, 755 (1991).

Xing, D.Y., M. Liu and C.D. Gong, Phys. Rev. **B44**, 12525 (1991).

Yip, S. and A. Garg, Phys. Rev. **B48**, 3304 (1993).

Zhang, D.N. et al., Phys. Rev. **B49**, 1417 (1994).

Zhang, H. and H. Sato, Phys. Rev. Lett. **70**, 1697 (1993).

Zhou, C. and H.J. Schultz, Phys. Rev. **B45**, 7397 (1992).

Zarate, H.G. and J.P. Carbotte, Solid State Commun. **52**, 449 (1984).